ANALYSIS OF LIPID STORAGE IN *C. ELEGANS* ENABLED BY IMAGE PROCESSING AND MICROFLUIDICS

A Dissertation
Presented to
The Academic Faculty

by

Maria Elena Casas

In Partial Fulfillment
of the Requirements for the Degree
Doctor of Philosophy in Chemical Engineering in the
School of Chemical and Biomolecular Engineering

Georgia Institute of Technology
May 2017

ANALYSIS OF LIPID STORAGE IN *C. ELEGANS* ENABLED BY IMAGE PROCESSING AND MICROFLUIDICS

Approved by:

Dr. Hang Lu, Advisor
School of Chemical and Biomolecular Engineering
Georgia Institute of Technology

Dr. Julie Champion
School of Chemical and Biomolecular Engineering
Georgia Institute of Technology

Dr. Ho Yi Mak
Division of Life Science
Hong Kong University of Science and Technology

Dr. Le Song
Computational Science and Engineering
College of Computing
Georgia Institute of Technology

Dr. Mark Styczynski
School of Chemical and Biomolecular Engineering
Georgia Institute of Technology

Date Approved: March 17, 2017

To my parents, Barbara and Jose Casas, my love, Michael Aguilar, and to all of those who could not see me make it to the end, Abuelito Playa, Abuelita Mima, Orto, and Tata.

Where to begin but at the end… Where to end but at the beginning…

ACKNOWLEDGEMENTS

First and foremost, I would like to thank my family especially my parents, Barbara and Jose Casas for their never wavering enthusiasm, support, encouragement, and love. They always emphasized how important, fulfilling, and life-changing an education could be. For that, I am eternally grateful. I also want to thank my two younger brothers, Eduardo and Andres Casas, for pushing me in school to be the best that I can be, even if that was so they could re-use my school projects. They have provided a listening ear, advice, and humor all along this process and throughout my life. When I first began graduate school, my niece, Sophia, was born, and as I have gone through this journey I have seen her grow. I want to thank her for the happiness she spreads with her never-ending curiosity of the world, and how it works. I hope seeing me in this role helps inspire the future scientist in her. Next, I would like to thank my boyfriend of 6 years, Michael Aguilar, for everything he has done to help me get to this point. He has not only loved me unconditionally through good experimental days, and bad ones, but supported me emotionally, nutritionally, and intellectually. This Ph.D. would not have been possible without all of the home made dinners, chores, and pep talks he provided and did more than his fair share of. Meeting him at the beginning of orientation at Georgia Tech, and having him be by my side throughout this whole journey, has made each and every day brighter.

Earning a Ph.D. is a daunting task, and could not have been possible without the support and guidance of my advisor, Dr. Hang Lu. Through many obstacles and digressions, she has stood by me and believed in me even when others did not. She pushed

me every day to be the best scientist and critical thinker I have ever been. I want to thank her for her patience with me and for letting me experience the hardships and joys of science.

I want to thank my committee members, Dr. Mark Styczynski, Dr. Julie Champion, Dr. Le Song, and Dr. Ho Yi Mak, for all the input and guidance through my many years in this program that has led to the culmination of this thesis. I also want to especially thank my committee member Dr. Ho Yi Mak, from the Hong Kong University of Science and Technology, for being a great collaborator that was willing to generously share invaluable biological insight and expertise throughout my Ph.D.

Along with my advisor and committee members, I would like to thank past and present Lu Lab members for all of their knowledge and advice that has substantially contributed to the work done in this thesis. There are a few lab members that I would especially like to thank: Dr. Jeffrey Stirman, now a postdoctoral fellow at the University of North Carolina at Chapel Hill, for showing me the ropes when I first joined the lab; Dr. Adriana San-Miguel Delgadillo, now a professor at North Carolina State University, for always being a role model, helping me brainstorm about my project, and making me feel welcomed; Dr. Guillaume Aubry, for always having the patience with me to discuss any and all topics about my project to great lengths; Dr. Ivan Caceres and Daniel Porto, who without, I could not have completed my Chapter 2; Dr. Hyewon Lee, now a researcher at Korea Research Institute of Bioscience and Biotechnology, for developing, characterizing, and refining the microfluidic device that helped make Chapter 3 and 4 possible; Dr. Thomas Levario and Emily Jackson-Holmes, who allowed for me to test my ideas on their model systems, contributing to the completion of Chapter 4; Yun-Hsuan “Stellina” Lee, for being a helping hand during long experimental days for results included in Chapter 3;

Clayton Wilbanks, QuocAnh Vu for being my undergraduate mentees who assisted me in my research; and Tel Rouse and Weipeng Zhou, who are always willing to listen and chat about the most recent developments about our projects. I would also like to additionally thank those that help with corrections to this thesis as well: Weipeng Zhou, Emily Jackson-Holmes, and Michael Aguilar.

In addition to the lab members, there are those that get unnoticed that are who allow for the lab to continue running smoothly every day. I would like to thank Eric Anderson, Kathie Watkins, Courtney Fox, and Christine Alberico for allowing me to run my experiments without thinking about who is running the lab and making sure we have everything we need at arm's length. In addition to our own lab space, I routinely used core facilities for imaging and would like to thank Andrew Shaw, and especially Aaron Lifland, for their microscopy knowledge and experimental design advice.

I would like to thank my various funding sources for the financial support they provided throughout my research: National Institute of Health Biomaterials Training Grant, National Science Foundation Graduate Research Fellowship, the Georgia Institute of Technology President's Fellowship, and the Goizueta Foundation Fellowship. With regards to the NIH Biomaterials Training Grant, I would like to especially thank Dr. Johnna Temenoff for allowing for me to rotate in her laboratory, giving me my first scientific experiences in graduate school. With regards to the Goizueta Foundation, I want to especially thank Jorge Breton for always advocating for me for all the awards and opportunities in and outside of campus, that help influence students who may not have scholarly encouragement at home.

I would like to thank my high school AP biology teacher, Mrs. Estrella Gonzalez, for inspiring me to pursue degrees that interfaced between biology and engineering. Her passion for the topic is contagious and her lectures on genetics lead me to where I am today.

Because getting through this process takes more than academic support, I would like to thank all of the social support I have received. I want to thank my core graduate school, and now life-long, friends, as we call ourselves, MATLAB ME: Drs. Matt Mistilis, Abiola Shitta, Timi Fadiran, Lindsay Arnold, Andy Peters, and Brennen Mueller. I want to thank all of you for your support and encouragement from qualifying exams to graduation, and for making graduate school and Atlanta an enjoyable and wonderful place. Lastly, I would also like to thank all of my Atlanta friends that I have met throughout these years, especially my wine nights' girls that have kept me sane and well hydrated, with nights to routinely wine, dine, and chat about science and non-science alike.

TABLE OF CONTENTS

LIST OF TABLES

LIST OF FIGURES

LIST OF ABBREVIATIONS AND TERMS

C. elegans	*Caenorhabditis elegans*
E. coli	*Escherichia coli*
D. melanogaster	*Drosophila melanogaster*
CGC	Caenorhabditis Genetics Center
PDMS	Polydimethylsiloxane
LD	Lipid droplet
NGM	Nematode growth media
GFP	Green Fluorescent Protein
M9	Buffer used for washing *C. elegans* from plates
M9-triton	M9 with added 0.01% Triton-X surfactant
OP50	Strain of *E. coli* typically used to feed *C. elegans* in the laboratory
HB101	Strain of *E. coli* alternatively used to feed *C. elegans*
PCR	Polymerase chain reaction
ER	Endoplasmic reticulum
EMS	Ethyl methane sulfonate
Ado-Cbl	Adenosylcobolamin, an active forms of vitamin B_{12}
Me-Cbl	Methylcobalamin, another active form of vitamin B_{12}
mESCs	murine Embryonic Stem Cells

SUMMARY

Obesity is a serious health issue plaguing 72 million Americans[1]. While the genetic origin of obesity has yet to be fully understood, the risk of this serious health issue has been linked to fat and lipid storage[2]. The nematode, *C. elegans*, is a convenient model to understand key lipid droplet storage mechanisms conserved through evolution, which can give insight towards pathways in humans[3]. Fat in *C. elegans* is primarily stored in organelles called lipid droplets, which can be imaged *in vivo* through the transparent animal[4]. However, current imaging and analysis methods for lipid droplets are labor intensive and time consuming. Microfluidics can provide a solution to this problem by enabling high-throughput imaging and screening[5,6]. Engineering methods and tools to improve object quantification would also dramatically enhance the ability to study lipid droplets. The purpose of my thesis is to use microfluidics, image processing, and manipulation of diet to further understand fat storage in *C. elegans*. This can be accomplished through powerful methods such as genetic and diet screening, and automated quantification of lipid droplet phenotypes, thus my aims are as follows:

In my first aim, we developed an image processing method to automatically distinguish lipid droplet phenotypes in *C. elegans*, and conduct an automated forward genetic screen for *C. elegans* mutants that suppress the lipid droplet phenotype of *atlastin*. Current methods for characterizing lipid droplet phenotypes are labor intensive, time consuming, and pose a difficult image processing challenge due to the high density of overlapping objects. Therefore, to analyze the lipid droplet size distribution, we developed a parameter-free algorithm that can automatically detect and quantify lipid droplets using the principles

of granulometry. This analysis takes only seconds, two orders of magnitude faster than done before. We were able to distinguish the size differences of fluorescently labeled lipid droplets in wild type and *atlastin* mutant strains. Applying our method, we were able to conduct a forward genetic screen that successfully isolated a worm with a suppressor mutation, confirming that the developed platform is capable of automatically classifying and sorting mutants of interest. This algorithm is generalizable and can be applied toward other densely packed structures in different organisms.

In my second aim, I conducted a pilot diet screen with genetically varied *E. coli* fed to *C. elegans* and developed methods to characterize differences in phenotype populations. To further understand dietary effects on fat storage, I developed a workflow that allowed for the imaging and analysis of many different diet conditions. In analyzing a subset of an *E. coli* single-gene knockout library, I found changes in metabolic differences that contributed to altered lipid droplet phenotypes. The metabolite propionic acid, which has been linked to regulate food intake in humans and potentially help combat the obesity epidemic[7,8], was shown to have a dramatic effect in decreasing the size of lipid droplets in worms.

In my last aim, I developed an integrative method to selectively recover worms from reversibly bonded microfluidic devices with the ability to conduct individual animal analysis after high magnification imaging. By combining array microfluidic devices with a biocompatible hydrogel system to maintain animals in position and recover selective animals of interest, it was possible to conduct experiments, such as genetic screens on lipid droplet morphology, without active components and additional software and hardware. The vast applicability of this method was demonstrated by applying this technique to three

different model systems, *C. elegans*, *D. melanogaster*, and stem cell aggregates. In recovering these animals, a new realm of experimental hypotheses can be investigated.

In summary, this thesis shows that the development of platforms using microfluidics and image processing could facilitate genetic and diet screens allowing for the discovery and understanding of components vital to lipid metabolism and storage in *C. elegans*. We envision that these approaches will enable additional studies of fat storage unfeasible with traditional methods.

CHAPTER 1. INTRODUCTION

This thesis investigates the use of image and data analysis as applied to the high throughput imaging of *C. elegans* lipid droplet phenotypes. Additionally, an integrative system that combines microfluidics, pressure clamps, and a hydrogel solution will be used to further the selective recovery single animals of various organisms, including *C. elegans*, while allowing the use of high throughput imaging. The utility of this system can also be utilized in combination with the analysis of lipid droplets phenotypes in *C. elegans*.

1.1 *C. elegans* as a model organism

Caenorhabditis elegans (*C. elegans*) is a non-hazardous soil dwelling nematode that is transparent and measures only 1 mm in length as an adult[9]. In nature, the nematode is most commonly found in soil and within rotting fruit in temperate environments, where its diet is composed of microbes such as bacteria[10]. The body is cylindrical in shape and contained within a long tough cuticle which surrounds the pseudocoelom and the tissues of the animal which include the intestine which spans the length of the body[11]. Other tissues include a pharynx and grinder that properly digest the bacterial diet, musculature along the body walls for efficient undulating wave motions which allow for locomotion, and a nervous system of exactly 302 neurons which has been entirely mapped in the only complete connectome of any organism[12]. Because the *C. elegans* population is mostly self-fertilizing hermaphrodites, the progeny of homozygous worms are isogenic, or genetically identical, allowing for ease of culture of various strains, and increased statistical power in experiments[9]. The nematode reproduces quickly with a life cycle of approximately 3 days, and can be easily cultured on agar plates seeded with *E. coli* as the food source for

laboratory maintenance, which is amenable to conducting high throughput studies in a short span of time[9]. *C. elegans* are also easily genetically manipulated through the estimated 17,800 distinct genes that can be mutagenized using chemicals or ionizing radiation, as well as genetically crossed with other mutant strains[9,13].

In a laboratory setting all of these properties lead to a simple organism that can be cultured easily and quickly allowing for consistent complex experiments. Since the introduction of *C. elegans* to the model organism research community[9], the number of laboratories utilizing this system has flourished in the past five decades spanning studies from the nervous system to aging to metabolism. Many Noble prizes have been awarded for rigorously characterization of varying aspects of *C. elegans* including cell lineage (2002)[14–18], RNA interferences (RNAi) use (2006)[19–21], and the use of green fluorescent protein (GFP) for labeling structures for visualization through the optically transparent body (2008)[22,23].

1.1.1 Why C. elegans?

At a glance, *C. elegans* may appear to be very different from humans. However, there are many genes, processes, and pathways that are conserved between *C. elegans* and humans[24]. *C. elegans* is a simple multicellular organism with a great genetic homology to humans with 60-80% of genes having an ortholog in *C. elegans*[25]. Many biological characteristics that are essential to problems in human biology are conserved evolutionarily and can be investigated using *C. elegans*[24]. These include but are not limited to studies in aging[26–28], behavior[29–31], learning[32,33], development[29,34,35], nerve function[36–38], metabolism[39–41], and fat storage[42–46]. *C. elegans* research provides a basis of biological

information in a tractable system that is complex enough to be a whole organism that can interact with the environment and stimuli, but simple enough to conduct a large amount of studies in an inexpensive and efficient manner[24,25].

Furthermore, for this thesis, the ability to fluorescently tag structures within the worm body and image them through the optically transparent body is of great advantage because it allows for ease of visualization without harming or disturbing the worm. In this study, the fluorescently tagged structures are lipid droplets which are the primarily fat storage vesicle in *C. elegans*[4]. The lipid droplets are distributed throughout the intestine and can be imaged using conventional fluorescent microscopy.

1.1.2 Imaging C. elegans

To gain information from the transparent nematode, imaging is performed. There are various methods used to image *C. elegans*. The most common method is manually picking worms on to agar pads on glass slides that are then mounted on microscopes for imaging[47]. However, this is a labor intensive task that requires individual selection of the worms that will be imaged. Additionally, immobilizing the worms to produce better images is essential. This leads to a labor intensive and time intensive method to image *C. elegans*. An improvement on worm imaging uses microfluidic technology that is capable of manipulating the worm with precision[48].

Microfluidics is an emerging technology that deals with the manipulation of small volumes of fluids in the nanoliter scale that can be applied for precise control of small organisms such as *C. elegans* due to the small dimensions and inherent laminar flow[48–52]. Microfluidics greatly benefited from the microelectronics industry where the creation of

masks through photolithography allows for small precisely patterned structures on masters to be molded into devices using soft lithography[52]. The ability to study lipid droplets in *C. elegans* is enhanced by imaging using microfluidics, which significantly increases throughput[48].

High throughput imaging of *C. elegans* can be easily accomplished with a microfluidic device by using pressure to introduce a solution containing *C. elegans* into the channels[48]. Pressurizing a closed channel creates a valve on a single layer device that allows for the flow channel to be closed, causing the worm to be stopped[5,6]. In a serial loading device, worms are introduced in a single file, making it is easy to image the worms in a very high throughput manner[5,6]. These devices can also have multiple outlets where sorting of specific worms can be accomplished[5,6]. When using the device in conjunction with custom MATLAB and LabVIEW programs, control of the various pressurized valves as well as the microscope and camera allow for automated high throughput imaging[48,53]. There are also parallel loading devices where a whole array of worms can be loaded at once[54,55]. This does not necessarily allow for precise sorting, but if the goal is to image a large population, an array device can also be suitable. The precise location of the worms in individual traps allows for locating the worm faster and in a predictable fashion. A simple epi-fluorescence microscope can be used to image the worm in the device in both bright-field and in fluorescence mode, and programs can allow for the capture of images along the z plane through the worm, creating a z-stack image. As compared to traditional methods where worms are individually mounted, the use of microfluidics greatly enhances the speed of capturing the images and is amenable to automation and decision making when sorting specific worms.

1.2 Conserved Fat Storage Pathways from *C. elegans* to Humans

1.2.1 Obesity

Obesity is a prevalent problem in the United States that is becoming a global epidemic[2,56]. Although trends have stabilized in the last ten years[57], the percentage of both men and women in the United States who are considered obese is still high at above 30%, which corresponds to approximately 72.5 million adults[1,57]. Recent studies have shown that these numbers may be inaccurate, and the true percentage of people that should be classified as obese is twice the current percentage at over 60%[56]. Risks for health issues such as type 2 diabetes, coronary heart disease, cancer, Alzheimer's disease, reduced life expectancy, and osteoarthritis are all increased with obesity[56–58]. Fat distribution within the body also contributes to various risk levels for diseases[2]. For example, individuals with more abdominal fat rather than subcutaneous fat have a higher risk of developing diabetes and metabolic complications[2]. The evidence has shown that obesity can occur when there is an energy imbalance between the amount of energy intake as food and amount of energy consumed, which results in accumulation of fat[2]. However, energy is not the only contributing factor; there are genetic components to fat accumulation and storage that are not yet fully understood[58].

1.2.2 Fat Metabolism

Homeostasis of energy is maintained through a complex system between the nervous system and sites of fat storage. Therefore, fat storage may be related to the genes that encode the molecular components that are involved[3]. The main energy storage tissue in mammals is white adipose tissue, which secretes signals that regulates food intake and

energy pathways[59]. One type of energy source is glucose, which gets processed in the liver where it is phosphorylated, and then metabolized into four different components: triglycerides, fatty acids, glycogen, or energy[60]. Other factors that contribute to the regulation of fat are leptin, which is secreted in proportion to fat mass, and insulin, which controls the balance of energy through regulation of glucose uptake and storage[3]. To understand fat regulation, many factors have to be considered including interactions between tissues, signaling pathways, feeding behavior, uptake of nutrients and fat storage[3].

1.2.3 C. elegans as fat storage model

Using *C. elegans* as a model for fat storage may not be apparent, especially because worms do not have leptin or adipose tissue[3]. However, intake, digestion, and the metabolism of food, as well as the maintenance of an energy balance are such fundamental processes to life that the study of fat storage translates between *C. elegans* and humans[3,42,43]. Fat regulatory research in *C. elegans* has shown that there are a number of loss-of-function mutations that cause an increase in fat storage[46]. These genes can underlie obesity in human homologues[46]. Similarly, there are genes that contribute to a decrease in fat storage, and these genes can be investigated in the drug development industry to treat obesity and other diseases[46]. Additionally, lipids are essential components to fat storage and the proteins that help make, metabolize and transport fats are highly conserved as well as the genes that encode for these proteins[44]. Major fat regulatory pathways, such as β-oxidation is found in the worm to break down fatty acids similarly to humans[61]. Another common model for fat storage studies are mice because they are mammals, have leptin, and have adipose tissues[3]. However, beyond the genetic complexity of mice, longer generation time, and their more labors intensive maintenance, analysis of pathways is done

by looking at known genes that contribute to fat regulation, making it difficult to discover new genes that contribute to fat storage[44]. The study of *C. elegans* is an ideal model for fat storage because manipulation of genes is simple, and unbiased screens can be accomplished[42–44]. This has allowed for genes that are required for proper energy balance to be found in *C. elegans* where homologous genes are then seen in mice, such as the gene for adipogenesis[44].

1.3 Lipid Droplets

Lipid droplets that accumulate fat are stored in the intestinal and hypodermal cells of *C. elegans*[3], and they are thought to originate from the endoplasmic reticulum (ER), but the exact mechanism is still unknown[62]. The morphology of lipid droplets consists of a core of lipids, containing triglycerides and cholesteryl esters, that are enveloped by a monolayer of phospholipids embedded with associated proteins[63]. The composition of the droplets have been analyzed using gas-chromatography/mass spectrometry, and the results indicate that the majority of molecules are triglycerides, with a range of saturated, monounsaturated, and polyunsaturated fatty acids, similar to mammals[3]. Because energy needs are always fluctuating, lipid droplets are dynamic and undergo respective changes according to these needs[45]. Lipid droplet morphology can provide a vast amount of information that can lead to detection of new genes and pathways affecting overall fat storage and accumulation.

1.3.1 Lipid Droplet Visualization Techniques

Methods to visualize lipid droplets within *C. elegans* include staining of live or fixed animals with dyes that are lipophilic such as Nile Red, Oil-Red-O, BODIPY, and Sudan Black[64–69]. These lipophilic dyes label lipid droplets and allow for estimation of fat

content, however animals are typically fixed, and recovery of phenotype and animal are not possible, therefore use of these methods for genetic screens is not recommended. Another method to determine lipid droplet phenotype is through the technique coherent anti-Stokes Raman scattering (CARS)[70] or stimulated Raman scattering (SRS)[71], which detect C – H bond vibrations in the lipids. Although this system is amenable to screens because it is label-free for lipid imaging[65,70,71], the systems are not common and difficult to integrate into fully automated systems.

For the purposes of this thesis, lipid droplets are visualized by utilizing transgenic expression of lipid droplet markers in live animals. There are various proteins that localize to the lipid droplet surface such as diacylglycerol acyltransferase (DGAT-2), which is a triglyceride synthesis enzyme[72]. Our collaborator, Ho Yi Mak, generated the strains used in this thesis, by creating single copy transgenes that expressed green fluorescent protein (GFP) fused to the *C. elegans* ortholog of DGAT-2, and showed the functionality of the construct by assessing that lipid droplet expansion is supported[72,73]. Because it is transgentically manipulated, there is no need to stain or fix the animals, therefore, the lipid droplets are visible under fluorescent light from the cultured plate. The ability to easily visualize and image lipid droplets through fluorescent imaging in live animals allows us to start addressing the question as to how the size of lipid droplets are regulated.

1.3.2 Changes in lipid droplet morphology due to mutations in atlastin

Atlastin is a protein encoded by the gene *atln-1*, which is one of the genes responsible for the rare genetic disorder hereditary spastic paraplegia (HSP)[74,75]. The main symptoms of this disease are slow progress weakness and spasticity, or stiffness, of the

lower limbs due to nerve damage[74–76]. An estimated 10,000-20,000 individuals are affected by this disease in the United States[76]. There is high variability in the manner in which this disease manifests itself, as well as many subtypes, and the disease is even variable among family members[76]. Because of this, it is very difficult to diagnose, therefore the number of individuals affected by this disease is not clear[76]. Hereditary spastic paraplegia has not been fully characterized, and there are many unknowns, including the full functionality of *atlastin*, which has been identified as one of the many genes involved in HSP[74–80]. It is currently known that *atlastin* is a GTPase required for homotypic membrane fusion, and mostly manifests in the formation of the endoplasmic reticulum (ER) membrane[74,77–80]. When *atlastin* is depleted, the ER becomes unbranched with a lack of interconnections between membranes[80]. This phenotype has been observed, not only in humans, but in *Drosophila*, and *C. elegans* as well, which both have orthologue to the human *atlastin*[80,81].

The ER is also responsible for formation of lipid droplets, thus it is not surprising, that *atlastin* also causes changes to lipid droplet formation and sizes, changing how fat is stored[80]. Phenotypic changes are observed in *C. elegans*, with the *atlastin* mutation (*a015*), where lipid droplets are reduced in size, and the ER appears less organized and branched[80]. To gain further knowledge about this gene, studies on the mechanism in which *atlastin* affects lipid droplet formation have been conducted[80]. For example, forward genetic screens have been conducted where changes in appearance of the ER morphology have been observed to identify mutants. This can also be accomplished by observing and quantifying the lipid droplet phenotypes in *C. elegans*[80]. In observing changes in lipid droplet formation and sizes, it is possible to gain knowledge about the function of *atlastin*[80]. The pathway in which *atlastin* functions has not been fully characterized, therefore genetic

screens have been conducted to help determine other genes that may interact with *atlastin*[78–80]. To date, there have not been any extragenetic mutations identified that can completely suppress *a015*. In addition to a lipid droplet and ER morphology changes, it has been observed that in *C. elegans* a mutation in *atlastin* causes decreased brood size at elevated temperature. This will be a criteria used later in this thesis to possibly identify novel mutants through the use of a forward genetic suppressor screen that quantifies lipid droplet size distribution changes between potential mutants.

1.3.3 Lipid droplet morphology changes due to changes in diet

In addition to changes of lipid droplet morphology due to genetic changes that alter lipid droplet expansion, manipulation of diet changes the morphology of lipid droplet sizes in worms[45,82]. For example, Zhang, *et al.* showed that by feeding the worm two different types of *E. coli* (OP50 and HB101) commonly used in the laboratory to feed *C. elegans*, it was possible to see a significant size increase in lipid droplets in worms fed OP50 versus HB101[45]. The results of these studies indicate that when *C. elegans* have a varied diet, lipid droplet morphology can change[45]. However, the analysis on a broader scale would need to be done in a more robust and less labor intensive way than the current method where lipid droplets are stained and manually annotated[45,82].

The variations in food contribute differently to a worm's metabolism and may up regulate or down regulate a gene that contributes to fat storage and distribution. Performing the experiments using microfluidics allows for higher throughput, and thus a greater number of worms can be imaged giving more statistically power to the results. In Chapter 3, I will explore the use of the *E. coli* Keio Knockout Collection[83] that provides a method

to systematically test the effect of varying diet in a precise way. This library contains a single-gene deletion of 3,985 of 4,309 genes, which are all nonessential, in *E. coli* K-12 strain BW25113[83]. A platform to be able to feed the *C. elegans* the various knockouts from the *E. coli* library can help determine the metabolites that cause changes in *C. elegans* lipid droplet distribution.

1.4 Image processing for biological analysis

The application of image processing to a myriad of biological problems has increased the classification ability of phenomenon, which was once only characterized by qualitative measurements through visual inspection[53,84–86]. This field combines the biological imaging with data processing, and is called 'bioimage informatics'[84]. Currently, classification of *C. elegans* mutants using 'bioimage informatics' has been applied to fields such as behavior analysis, neuron localization, and muscle striation for age determination[53,84–86]. There are different ways of quantifying images, including the use of feature extraction techniques and clustering algorithms[87–89]. The most difficult component to correctly classify and quantify images is based on the selection of appropriate features. Phenotypes in the worm with overall textural difference such as muscle tissue aging[64], have different features that describe the image, as compared to other applications such as detection of neurons that are composed of a couple of pixels[53]. Features used to detect textural differences include the Haralick features that measures the overall entropy of the image[64].

For the purposes of this thesis, the quantification of lipid droplet sizes is critical to determine phenotypes, and this can be done by using various image processing methods mentioned previously. The ability to automatically distinguish overall differences within

the lipid droplet phenotype would greatly decrease the time necessary to analyze the worm as well as provide a way to classify different phenotypes in a statistically significant way. Current methods for determining variations in lipid droplet phenotypes are labor intensive, time consuming, and have potential for error. This creates a difficult and tedious problem when attempting to create a vast lipid droplet phenotype library for classification methods such as support vector machine. Additionally, segmentation methods require a ground truth or approximation of a ground truth, which is the observed and annotated phenotype that will be analyzed. In the case of lipid droplets, the approximation of the ground truth is obtained through manual annotation of individual lipid droplet. To best optimize the parameters in segmentation methods obtaining the ground truth may be tedious or not possible when very small structures are present such as what can occur with lipid droplet morphologies[90]. Therefore, in addition to these segmentation and classification methods, another algorithm category exists using the principles of granulometry[91] where the phenotype of the image is neither determined by segmentation or clustering, which will be introduced in Section 1.4.3.

1.4.1 Classification algorithms

To classify difference in these features, there are methods used that cluster the data in order to determine if an image is different from the control scenario. These methods include Support Vector Machine (SVM) and Principle Component Analysis (PCA)[53,85,86,92]. In using SVM, the algorithm must be supplied with a training set of images to classify future images[53,84]. This method is very robust, but compilation of a training set may be tedious, and can introduce bias[53,88]. In contrast, the use of PCA provides a simpler unbiased way to classify images through analysis of clusters formed by the linear

combination of the features in order to increase the variance[88]. However, due to the simplicity of PCA, complex phenotypes with subtle differences may not be appropriately classified.

1.4.2 Segmentation algorithms

Beyond feature extractions and clustering algorithms, analysis of images with distinct objects can also be performed using segmentation methods[93–96]. These methods include but are not limited to edge detection methods, global and local thresholding, watershed implementation, and Hough transform[94,96]. In using these algorithms, the ability to properly segment the objects in the image depends on the edge gradient, image sharpness, as well as the parameter values chosen for each method that are optimized toward a ground truth[94,96].

For edge detection, one common algorithm is Canny edge detection that has 3 parameters to optimize which include a threshold as well as Gaussian filter edge parameters[97]. The disadvantage of using Canny edge detection is that if the objects are overlapping, or have poorly defined edges with shallow gradients, the algorithm may cluster objects together, improperly identifying the structures[98]. For global and local thresholding, the Otsu method is common which binarizes the image to minimize the interclass variance between the black and white pixels[99]. However, using a single threshold can create incorrectly labeled structures if the image background is not uniform, if structures are overlapping or if edges have shallow gradients as with edge detection[100].

Using watershed implementation to determine structures is also a common segmentation method that is more complex than detecting edges or a single threshold[101].

Watershed functions by determine the local minima of the gradient of the image, where the algorithm imitates how a drop of water would flow between distinct minima to form edges[101–103]. This algorithm has parameters that need to be determined *a priori* which include the connectivity between segments that are selected by using a distance transform[102]. Although this method is very sophisticated, the ability to determine the proper parameters for optimal segmentation can be tedious and take multiple iterations.

Lastly, the Hough transform can be used to accurately determine circular objects in an image[104–108]. This algorithm has up to five different parameters that can be optimized and these include the minimum and maximum radius range to be analyzed, the circularity sensitivity factor that affects how much the objects need to approximate a circle to be detected, and edge threshold level[104,106,107]. Optimizing this number of parameters would not be amenable to analyzing biological structures with unknown object sizes as what is seen in genetic screens. To determine the proper phenotype, a method must be used that can easily adapt and not have parameters to optimize with each phenotypic change.

1.4.3 Granulometry

Developed in the 1960s by mathematician Georges Matheron[91], the approach of granulometry has been used to determine the size distributions of objects in binary images. Although the original application was for sedimentary research[91,109], the application in biological research is still mostly unexplored. Briefly, this algorithm uses morphological openings and closings of increasing sizes to determine the prominent structures in the image without determining individual objects, which is conceptually similar to digitally sieving an image[91]. The output of this algorithm is the size distribution, however in order

for the algorithm to output meaningful biological information, more modifications to the software must be done.

To address this, we developed a method that uses the principles of granulometry along with other modifications. Using the basis of granulometry is advantageous over the segmentation and classification algorithms because *a priori* knowledge of the structures is not necessary, the edges of the objects do not need to be well defined or non-overlapping, and because the various size ranges are being scanned, there are no parameters that need to be optimized to determine the sizes of the objects[91]. This is critical to conducting genetic screens on structures such as lipid droplets, where the phenotype of the various animals imaged will be unknown and changing between each animal. The algorithm will be further analyzed and validated in Chapter 2 when analyzing both lipid droplets which are circular structures, and the ER which helps identify porosity and is even harder to quantify compared to lipid droplets.

1.5 Recovery of animals from microfluidic devices

In *C. elegans* research, there has been great adoption of the use of microfluidic devices to increase the throughput of imaging[48]. To conduct high-throughput genetic screens, devices have been traditionally made where an inlet and outlet connect the channel where worms are flowed through[5,6,48]. This allows for serial imaging of worms, and potential sorting mutants of interest[5,6,48]. Although automation is not necessary to conduct these screens, software and hardware developments must be accompanied with these devices in order to properly operate the microfluidic devices[48]. On or off chip valve actuation controls the flow and allows for worm recovery at the outlet of the device[48].

Additionally, due to variety of microscope setups and software that may or may not be tuneable, customization can be tedious and difficult for non-experts. Devices also exist that allow for high-throughput imaging through passive parallel loading in arrays[54,55], but these devices do not have a systematic method to selectively recover animals of interest. This is not advantageous for experiments such as genetics screens where individual mutants must be recovered and cultured to allow for the production of new progeny to ensure the preservation of the mutant strain.

To address these challenges and broaden the adoption of microfluidics to laboratories without extensive software and hardware expertise, the ability to reversibly bond microfluidic devices is necessary. In addition to the reversibility of the device, the animals must not move from the respective positions to assure proper registration with previous images acquired. This can be accomplished by utilizing a substance within the device channels that prevents movement of the animals, such as a hydrogel. However, the hydrogel has two important properties it must meet: 1) the hydrogel must not harm the animal due to the condition that the animal may need to lay progeny, and 2) the hydrogel must have a low enough viscosity to flow through small constrictions, but stiff enough to hold animals in position.

1.5.1 Reversible bonding of microfluidic devices

The ability to reversibly bond microfluidic devices, instead of the permanently bonding devices through oxygen-plasma, can be of great advantage when access to the device channels is needed[110]. Applications such as cell patterning, or surface functionalization may be common applications[110–112]. Recovery of single animals from

microfluidic devices is currently possible through serial loading and unloading through tubing[5,6,48], however, animals such as worms, may swim or stick to the tubing, which may change the order of the worms during unloading. If a device is highly complex with many layers, or sections, fabrication may be labor intensive and have a high rate of error, therefore, reversibly bonding the device can facilitate cleaning or replacement[110,113]. There are currently four different techniques for reversibly bonding which include bonding by: 1) mechanical strength using clamps or vacuum, 2) magnetism strength, 3) intermediate adhesive layer, and 4) oxygen-plasma[110].

With vacuum, a seal is made through aspiration, and high working pressures can be reached, however, additional space and changes to the devices must be made to accommodate this mode, and a wide array of channels are not suitable for this method[111,113,114]. Using magnetism also allow for high pressures, however, the assembly of the device becomes much more complex and reduces the ability to use simpler geometries and lower density structures[115,116]. With an adhesive layer, there are additional steps involved, and biocompatibility issues, or leaching of the chemical into the liquids in the channel can also be a concern[117–120]. The adhesive may not necessarily be ideal for higher magnification imaging where the surface of the coverslip must be thin and transparent to not obstruct the objective and light path into the device[117–120]. It is possible to use oxygen-plasma to partially bond the devices, however, there is a high degree of difficulty to maintain conditions that will reversibly and not permanently bond the device, the adhesion strength of this method is low, and this process is mostly suitable for static conditions where high pressures or moving volumes of fluid are not necessary[121,122].

In this thesis, we will be using high magnification imaging, as well as high density device structures and perfusion through the device, therefore, we will explore the use of the bonding through mechanical strength by screwing two clamps made of a clear stiff substrate between the surface of the PDMS and the glass slide[121,123,124]. The ability to reversibly compression seal devices can potentially lower the cost of use of microfluidic devices due to not needing a plasma chamber for bonding. Various substrates used to compression seal are glass, plexiglass, and acrylic[123,124]. Additionally, most applications for reversibly bonded devices using compression sealing are typically chemicals or small particles or cells suspended in the media[121,123,124]. Larger organisms such as *C. elegans* that can swim, or *Drosophila* embryos that are delicate to pressure, are more difficult for loading on to a device that is reversibly bonded using a compression seal.

1.5.2 Hydrogel solutions for organism handling in microfluidic devices

Due to the small dimensions of channels in microfluidic devices, it can be challenging to flow hydrogel solutions for various applications. Because of this, lower viscosity hydrogels must be utilized that are amenable to flow, however this reduces the amount of structural integrity available by the hydrogel. Coupled with microfluidics, hydrogel solutions are mostly used to immobilize organisms that are in suspension, or are mobile[125,126]. Various mechanisms to circumvent these challenges include UV curing of hydrogels and combining chemicals, or changing temperature to increase the cross-linking density of the polymer[125–129].

A common material used is agarose, which is biocompatible and can change stiffness properties with temperature[130–132]. Agarose solutions routinely need elevated temperatures

to dissolve in solution, and elevated temperatures are necessary to maintain the solution liquefied[130–132]. Agarose is typically solidified at room temperature, however, low-melting point agarose is a great alternative that remains liquid at 37°C, which is body temperature and amenable to cell culture[133]. Polymer solutions can also be used that alter the stiffness properties with temperature[130,131]. Hydrogels are solutions that upon activation are capable of retaining water within a structure[134]. Various methods to change the properties of hydrogels include the use of physical stimuli such as UV light for cross-linking, or chemical stimuli, such as changes in pH[134–141]. The disadvantage of hydrogels is that the activation of the hydrogel may not be biocompatible, and the curing of these solutions may cause harm to the organisms within the device. The use of UV light, for instance, may cause for mutations to occur in *C. elegans*[142].

One interesting polymer that functions opposite of most temperature sensitive polymers is Pluronic F127. Pluronic is a block-co-polymer that transitions from solution to hydrogel as the temperature reaches the critical gelation temperature at ~4°C for a 25% w/v concentration. The gelation of the polymer increases the viscosity of the polymer from 100 to 1000 times and can be reversed to form back into solution once place below the critical gelation temperature[125,143–145]. This polymer has been used for the immobilization of *C. elegans* with the addition of beads for added stiffness[125,126], and has been shown to have very low levels of cytotoxicity as it has been used in many clinical applications[146,147]. However, due to the high heat exchange rate of microfluidic devices, Pluronic will gel quickly at room temperature. Therefore, to maintain the Pluronic in solution, experiments must be performed within a cold room. The advantage of this system is that cooling *C. elegans* to 4°C for the brief time to flow this solution into the device does not affect

morphological phenotypes, and because the gelation occurs at room temperature, the *C. elegans* are able to stay within physiologically biocompatible temperatures throughout the gelation process[125,126].

Lastly, the combination of two liquid chemicals that combine and solidify is an alternative that can be used in microfluidic devices. For instance, the solutions of sodium alginate, and calcium chloride cross-link once in contact, and solidify to stiffness based on the concentration of chemical in each solution[148,149]. These chemicals are both biocompatible, and form a non-reversible gel at room temperature[148,149]. This solution allows for no temperature change or stimuli to affect the organisms within the device.

In Chapter 4, the use of low-melting point agarose, Pluronic, and the combination of sodium alginate and calcium chloride will be explored. Additionally, this method is not limited to *C. elegans* and will also be applied to two other model systems, *D. melanogaster* embryos and stem cell aggregates, to better demonstrate the vast applicability and broad advantage of this system.

1.6 Thesis Outline

The challenges in the field of *C. elegans* lipid droplet research can begin to be addressed through the use of various technologies and methods discussed in this thesis. In using microfluidics, image processing, automated quantification, and selective animal recovery, this thesis aims to advance the knowledge of how fat storage is affected due to both genetic and dietary changes through the analysis of lipid droplet morphologies. To determine genetic effects on lipid droplets through a screen, it is necessary to develop a method that is able to automatically quantify lipid droplet phenotypes that can analyze

overlapping objects without the need to change settings at each sample. To determine the effect of diet changes on fat storage, it is necessary for a method to be streamlined to test many bacterial diets, while maintaining the ability to differentiate between subtle population differences. Finally, for selective recovery of single animals from microfluidic devices, it is necessary to develop a system that allows for easy manipulation of the organisms within the microfluidic device, without harming the organism and maintaining the precise locations for longitudinal studies that correlate imaging with further analysis.

The chapters of this thesis are organized to build upon the work from previous chapters and expand upon the information and knowledge that can be gathered concerning lipid droplet phenotypes in *C. elegans:*

In Aim I (**Chapter 2**), we developed a modified granulometry algorithm that detects overlapping, mostly circular, objects through a semi-quantitative textural analysis of the object size distribution. This was applied toward various morphologies in lipid droplet phenotypes and structural analysis of endoplasmic reticulum in *C. elegans.* We show that one of the main advantages of the modified granulometry algorithm as compared to other segmentation methods, such as edge detection or Hough transform, is that our algorithm is parameter-free, eliminating the need for *a priori* knowledge of the size range. I used this algorithm to conduct an automated high-throughput genetic screen of lipid droplet size distribution phenotypes in *C. elegans*, where *a priori* knowledge of the sizes is unknown and varies between each animal. This allowed us to identify lipid storage mutants approximately 500 times faster than previously capable.

In Aim II (**Chapter 3**), we used the modified granulometry algorithm developed in Aim I and applied it to determine the phenotypic changes in lipid droplet morphology due to dietary changes. In addition to analyzing the lipid droplet phenotype of worms, I developed a pipeline to be able to handle various dietary conditions and image a large sample size in a high-throughput manner. Because the lipid droplet morphological changes due to diet changes were more subtle than genetic changes, additional analysis was developed using the output of the algorithm developed in Aim I. The methods created in this aim were used on a portion of an *E. coli* knockout library, where more of the library can easily be analyzed using these developed techniques. From the small subsection analyzed, I found genes in *E. coli* that caused changes in the metabolic composition of the *C. elegans* diet, where the metabolite that robustly caused a decrease in lipid droplet size was propionic acid.

In Aim III (**Chapter 4**), we used the microfluidic device and imaging process discussed in Aim II, and developed a method to selectively recover animals of interest without active components or additional software. In Aim I, a microfluidic device was used to serially sort mutants, however, the complexity of the software and device may slow possible adoption of this method to analyze *C. elegans* phenotypes. To address this, I developed an integrative method where existing array microfluidic devices are used to image, however, instead of irreversibly bonding the devices, the devices are held with compression using an acrylic clamp. With the addition of a hydrogel that solidifies within the device after imaging, this device can be opened, individual animals remain in position and can be selectively recovered. This can allow for further studies because the animal can now develop and produce progeny to further study the phenotype observed. This allows for

mutagenesis screens with the use of existing microscopy software, without intervention of software or active components. Finally, to show translatability, I also applied this technique to *Drosophila melanogaster* embryos, as well as stem cell aggregates. This allows for easy recovery of single animals after imaging and culture within a microfluidic device where the investigation of new developmental phenotypes is now practical and achievable.

Finally, in **Chapter 5**, I summarize the contributions of this thesis, as well as suggest future work that is a clear extension of the work accomplished for the three different aims.

For clarity, the work in Chapter 2 was done in collaboration with Dr. Ivan Caceres and Daniel Porto of the Lu Lab. Dr. Ivan Caceres developed the first generation of the modified granulometry algorithm which I continued using and modifying as experiments required. Daniel Porto was involved in the initial validation of the algorithm and development as well. The work in Chapter 3 was done with the collaboration of Dr. Ho Yi Mak at the Hong Kong Univeristy of Science and Technology, where he provided strains used as well as valuable biological, experimental, and analytical input. The device used in Chapter 3 was masterfully characterized and developed by Dr. Hyewon Lee, of the Lu Lab.

Lastly, the work in Chapter 4 was accomplished along with Dr. Thomas Levario for the *D. melanogaster* embryo experiments and imaging, and Emily Jackson-Holmes for the stem cell aggregate experiments and imaging. All the *C. elegans* strains used in this thesis were provided by Dr. Ho Yi Mak, as well as the *E. coli* knockout library that was created by the Wanner and Mori labs in Keio University in Japan. As with work in any lab, incremental advances to device design, automation algorithms, microscopy set ups, pre-fabricated silicon masters are due a great deal of gratitude. This thesis would not be possible

without all of the work accomplished and passed down by members of the Lu Lab. The intentions of this thesis are to provide new methods and applications where better imaging, quantification, and analysis of changes in lipid droplets will lead to advances in the realms of fat storage and metabolism.

CHAPTER 2. PARAMETER-FREE ANALYSIS OF DENSELY PACKED OBJECTS FOR HIGH-THROUGHPUT SCREENS

The following work in this chapter was performed in collaboration with Ivan Caceres (ICC) and Daniel Porto (DP) from the Lu lab and Dr. Ho Yi Mak's laboratory at Stower's Institute for Medical Research and the Hong Kong University of Science and Technology, China. The algorithm was developed by ICC, experiments, including validation were conducted by MEC, and data curation was done by DP and MEC. Visualization was completed by MEC.

2.1 Introduction and Motivation

While performed effortlessly by people, object recognition remains a highly complex computational problem[85]. Variance in object shape and size, non-uniform intensity, low signal to noise ratio, and occlusion are all contributing factors to the complexity of the process. Images and instances requiring detection and analysis of a large number of objects compound these issues even further. In analyzing biological images, these circumstances are a frequent and common occurrence and are pivotal issues limiting large-scale screening, rapid analysis and quantification.

Segmentation algorithms have been widely used in biological image analysis many problems including quantification of cellular phenotypes[6,150–153], real-time genetic screening[154], laser surgery[155], behavior analysis[156], lineage tracking[157–159], and MRI analysis[160]. Common methods include global and local thresholding, edge detection, watershed implementations, machine learning, template matching, active contour and

snake algorithms, image transforms, and Gaussian mixture model techniques[97–99,101,104]. The field of image processing as applied to biological structures commonly uses segmentation algorithms such as edge detection and thresholding; however, analyzing many objects is difficult, often due to size variations and high degrees of object occlusion. Segmentation methods can easily incorrectly combine objects in images with densely packed overlapping objects and noise from out of focus light and other confounding elements which leads to errors in segmentation. For example, the analysis of *C. elegans* fat storage can suffer from these challenges due to the need to determine the size range of hundreds to thousands of lipid droplets that are spread three-dimensionally throughout the intestine of the worm. Many segmentation methods also require the optimization of parameters with the use of manually annotated images, which can be labor intensive and subjective. This would hinder the use of these algorithms for the analysis of unknown phenotypes, such as during a screen where morphological changes are unpredictable. Hence, there is a need for a nonparametric unsupervised analysis to characterize objects, such as lipid droplets, in an image without *a priori* knowledge of the structures. This analysis method would enable unbiased quantification of properties that are difficult and time consuming to obtain.

To address these needs, we utilized the principles of granulometry, along with pre-processing steps, and noise reduction through thresholding in our algorithm for the analysis of lipid droplet organelles in *C. elegans*. In analyzing lipid droplets in the model organism *C. elegans*, we can test our algorithm against a complex problem where object size variability and occlusion occurs. *C. elegans* are a comparatively simple multicellular eukaryote of up to 1 mm in length and are widely used in biological studies due to their

compact genome, isogenic progeny, short life cycle, and transparency, which allow the imaging of internal structures[9,161,162]. Additionally, processes such as metabolism and fat storage are regulated by pathways and genes that are highly conserved between *C. elegans* and higher order organisms, such as humans[3]. Lipid droplets, which are the organelles that predominantly accumulates fat, are commonly studied as they are essential components to fat storage that help produce, metabolize, and transport fat[3,44]. Lipid droplets are stored in the hypodermis and distributed throughout the intestine of *C. elegans*[163]. The lipid droplets are spherical vesicles that appear clustered together and overlapping making the image processing, particularly the segmentation process, difficult and inefficient. Current imaging and analysis methods for studying lipids are time consuming and tedious where manual measurements of hundreds to thousands of individual lipid droplets are quantified to determine the size distribution and characterize the lipid droplet phenotypes[45,66,67,164]. Thus, the current analysis standard is low throughput, labor intensive, and prone to human error, which stunts the potential for growth, exploration, and attainable knowledge in the research area.

There is an opportunity to use granulometry, a morphological processing algorithm traditionally applied to in sedimentary research[165–170], to analyze and characterize images that are difficult for segmentation methods to process, such as images with overlapping lipid droplets. Structuring elements are used to perform the morphological processing that semi-quantitatively determines the size distribution of lipid droplets in the image[171]. To obtain the size distribution, the granulometry algorithm is analogous to the repeated sieving of grains or particulate. In this sieving, the mesh shape and size correspond to the structuring element used for the operation and with the increase in size of the mesh the

number of particulates that fall through are quantified. As this mesh size is repeatedly increased, larger particles are removed until eventually all particles are processed.

Similarly, granulometry uses a series of morphological opening operations with structuring elements of increasing size to filter objects from an image, however due to difference in structuring element shape and objects in the images, the algorithm also has inherent noise associated with the size distribution that is output. As objects are removed, the resulting loss in pixel intensity from the image is computed, allowing the algorithm to quantify information about various sized objects without the need to segment foreground from background pixels, and simultaneously mitigating the effect of occluded objects. The resulting size distribution is then composed of various peaks that correspond with the sizes of the objects in the image where not all peak perfectly correspond with the objects in the image due to intensity and shape differences.

Previously, granulometry has been used in more simple biological applications. These applications include: red blood cell imaging, neuron cell body identification, and cell size estimation[172–174]. In these applications, the images do not include many occluded objects, and the contrast and edge gradient is high; therefore, the objects are easier to binarize because of the low noise and the cleaner backgrounds with even illumination. Since it is based on intensity differences which can fluctuate greatly between images, granulometry has perhaps not been more widely applied to different biological structures because of this inherent noise. In addition to intensity fluctuations, the inherent noise of the images is due to the differences between the structuring element shape and the objects in the image as well as background artifacts like auto-fluorescence or out-of-focus light.

Thus, smaller peaks in the size distribution may be present that are remnants of previously sieved objects.

To address the intensity fluctuations, the image must be pre-processed such that the objects for analysis are more uniform in intensity and distinct from the background. Additionally, the predominant size of the objects in the image is determined through the application of a threshold that is based on the distribution's mean which allows us to also circumvent the effects of the inherent noise. The resulting distribution is based on intensity differences, and so to relate the intensity to biologically relevant information and associate images with a descriptive histogram showing the frequency of various sizes, a pseudo-count is determined. This pseudo-count is calculated by dividing each bin by the area of the structuring element used to determine the amount of intensity associated with the specified size. This allows for meaningful population distributions to be computed and compared where information is not hidden by accumulation of noise from each individual's distribution or intensity values. Therefore, the modified granulometry algorithm can be used to determine biologically relevant size information.

In this work, we propose a parameter-free algorithm that semi-quantitatively determines the size distribution of densely packed objects by applying the principles of granulometry. We show that our method can estimate the size distribution of lipid droplets as accurately as conventional methods, but two orders of magnitude faster and without user input (Figure 2-1). Combining this algorithm with microfluidics and epi-fluorescent imaging makes it now possible to perform automatic real-time on-chip classification of lipid droplet mutants during a forward genetic screen on a comparatively inexpensive imaging system with an increased throughput that is 500 times faster than was previously possible.

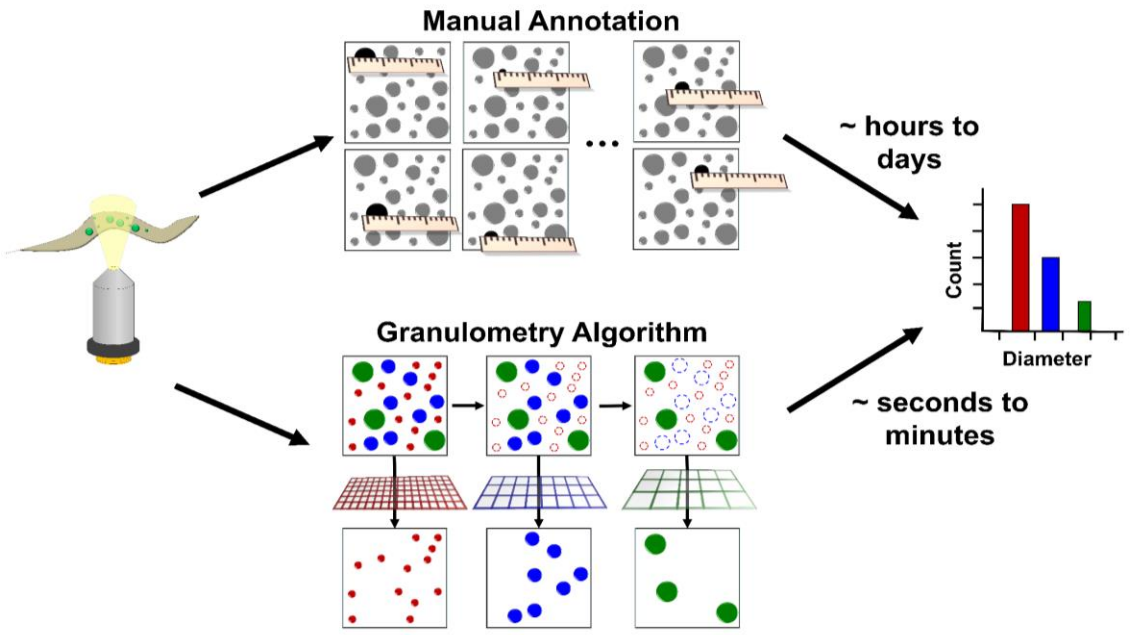

Figure 2-1. Granulometry conceptualized. *C. elegans* lipid droplets are imaged and traditionally annotated manually to acquire phenotype information based on lipid droplet diameter distribution, which can consume multiple hours per animal, whereas the modified granulometry algorithm provides similar results as the conventional methods without user input by applying a digital sieve of increasing sizes. Analysis time per worm is reduced by two orders of magnitude

2.2 Materials and Methods

2.2.1 C. elegans culture, mutagenesis, imaging, and manual lipid characterization

The strains utilized in this study were: *hjSi56*[*vha-6p*::3xFLAG-T*EV*-GFP::*dgat-2*::*let-858* 3'UTR] IV; *hjSi224*[*vha-6p*::*dhs-3a* cDNA::GFP-TEV-3xFLAG::*let-858* 3' UTR]. Strains were cultured and maintained on agar plates grown at a temperature of 20°C using established protocols[9]. A standard concentration (50mM) of ethyl methanesulfonate (Sigma Aldrich) was used to chemically mutate *a015;hjsi224* animals to perform a F2

suppressor screen of the *atlastin* lipid mutant, *a015*[175]. More detailed information about the protocol can be found in Appendix B.

Manual characterization of *C. elegans* lipids utilized the software program Imaris 6.2.1 for 3D reconstruction, lipid diameter measurements, and lipid intensity analysis[164]. Manual lipid characterization was performed in Klemm *et al.* and was used in this work for comparison to results from custom software analysis[164]. Imaging for manual lipid analysis was performed using a spinning disk confocal microscope (Ultraview, Perkin Elmer) and digital CCD camera (Orca-R2, Hamamatsu) controlled through the Volocity software (PerkinElmer) as described in Klemm, *et al*[164]. Images of multiple focal planes were acquired during imaging using a step distance of 0.25 µm for a total distance of 8 µm.

On-chip imaging of animals for genetic screening was performed using a custom built epi-fluorescent compound microscope with a digital CCD camera (Luminera Infinity-3) and a 100x/1.25NA Plan Achromatic objective (PA100X). Animals were anesthetized using a 35-50 mM concentration of tetramisole which was also used as the buffer solution during device operation. Images were acquired on-chip using a step distance of 1 µm for a total distance of 40 µm.

All animals whether screened in device or imaged manually were inspected during their L4 stage of development.

2.2.2 Microfluidic device fabrication and automated system operation

Single-layer microfluidic devices were fabricated using conventional soft lithography methods using the elastomer polydimethylsiloxane (PDMS, Dow Corning

Sylgard 184)[176]. Silicon wafers and SU-8 photoresist (Microchem) were used to create master molds and were subsequently treated with tridecafluoro-1,1,2,2-tetrahydrooctyl-1-trichlorosilane vapor (United Chemical Technologies) as in previous work[154]. Devices were similarly fabricated by thermally bonding two thin layers of PDMS, each with a different ratio of elastomer to cross linker, to allow for valve flexibility. These PDMS layers were a height of approximately one mm (25:1 ratio) and three mm (10:1 ratio) for the base and second layer respectively. After curing, fabricated devices were cut and prepared for tubing before irreversibly being bonded to cover glass using oxygen plasma.

The single-layer device used in this work operates similarly to previous designs, utilizing pressure driven flow and on-chip actuation of PDMS valves to obstruct fluid flow and selectively route *C. elegans* into various channels for loading, imaging, and sorting[6,53,153,177]. Devices were designed with a channel width and height of 40 μm, similar to the width of an L4 animal.

All system control software was written and performed using MATLAB®. The software controlled a custom built pressure box that was connected to the microfluidic device through PE tubing and 20 gauge metal pins (McMaster Carr, Inc.) connected to the device[48]. The epi-fluorescent microscope utilized was a custom built microscope that had a stepper motor that moved the objective turret in order to obtain z-stack images. The illumination used a high power blue LED array (Enfis UNO AIR BLUE-465, Circular LED Light Engine, 100 Blue LEDs) and the images were captured using the camera that was also connected to software to allow for automation. During the screen, both a bright field and fluorescent image were captured, using the bright field image to identify if the worm

was in the correct head first orientation. The sequence of the automation of the screen is available in Appendix B.3.

2.2.3 Synthetic image creation and software validation

Synthetic images were created in MATLAB® using disk shaped structuring elements of two, five, and ten pixels. The number of objects for each size was determined so that the total area between all three object sizes was kept equal. Additionally, object location and intensity (where specified) was randomized in order to create a set of 100 unique images for our testing library. While random, location was constrained to prevent object overlap with one another. Similarly, intensity values for lipids were constrained between 1 and 255 and were kept uniform throughout each individual object. Object area was calculated using the total number of pixels contained in the respective structuring element used to create it.

Bead images were created by preparing standard microscope slides using varying concentrations of 1.019±0.032, 2.063±0.067, 4.358±0.113 μm sized beads (Fluoresbrite® Fluorescent Microscpheres, Polysciences, Inc.). Beads were fluorescently labeled with GFP. For software validation, bead sizes were manually measured to determine a ground truth for the quantity of lipids and lipid distribution profile, respectively. Only sizes corresponding to relevant biological ranges were used for synthetic images or bead analysis.

2.2.4 Analysis of nematode lipid distribution using granulometry principles

Lipid droplet analysis was performed off-chip and on-chip for confocal and epi-fluorescent microscope images respectively. Size distribution for images was determined using a four step process involving image stack conversion and preprocessing, granulometry, size analysis, and normalization. All structuring elements used for morphological operations in this study were flat and disk shaped; all image analysis software was programmed in MATLAB®. Confocal nematode images analyzed in this study were identical to manually evaluated images used in Klemm, *et al*[73]. Example of pre-processed image for both confocal and widefield microscopy images are available in Appendix A.1, and more detail on the specific mathematical operations can be found in Appendix A.2-A.4.

Granulometry relies on the use of sequential morphological openings. A morphological opening is defined as an erosion followed by a dilation of the image. The erosion and dilation are applied to the image using a defined structuring element shape. For the analysis of lipid droplets, a disk shape is used, and it is applied to the pre-processed image (Figure 2-2A). The erosion applies the minimum value of the whole pixel intensity neighborhood encompassed by the structuring element for each pixel in the image. Similarly, in a dilation the maximum intensity of the neighborhood is applied. As structuring elements change in size, objects in the image become eroded, and if eliminated, the dilation would not restore the droplet. Conversely, if a droplet is not entirely eliminated, but only reduced in size during the erosion, the dilation will apply the maximum intensity for the size of the structuring element used, restoring the original size of the droplet. These sequential morphological operations allow for the calculation of the size differences in the

object. As shown in Figure 2-2, the yellow-orange droplet in the top right corner is still present after the erosion because the droplet is larger than a structuring element disk with a radius of 5 pixels (Figure 2-2B). This image then undergoes dilation of the same 5 pixel radius disk structuring element, where a similar process is applied, however the maximum value of the neighborhood is applied. This restores the approximate original size of the structures in the image where smaller elements were eliminated, and thus dilation restores the shape of structures larger than the structuring element disk applied. In Figure 2-2C, the yellow-orange droplet in the top right corner in the erosion image is close to becoming eliminated. Because the dilation applies the maximum intensity value to the size of the structuring element, which in this case is a radius of 11 pixels, the droplet is restored in size. In using a larger structuring element radius size of 16 pixels, the yellow-orange droplet on the right corner is completely eliminated, indicating that the lipid droplet is smaller than this size (Figure 2-2D). Thus, when the image is dilated, a droplet is not present and has been eliminated. The other larger droplets in the image, such as the red droplet on the top left corner has not had the size affected through this process. These images demonstrate that the larger lipid droplets do not have a change in intensity or size until the structuring element can encompass the entire lipid droplet without detecting edges.

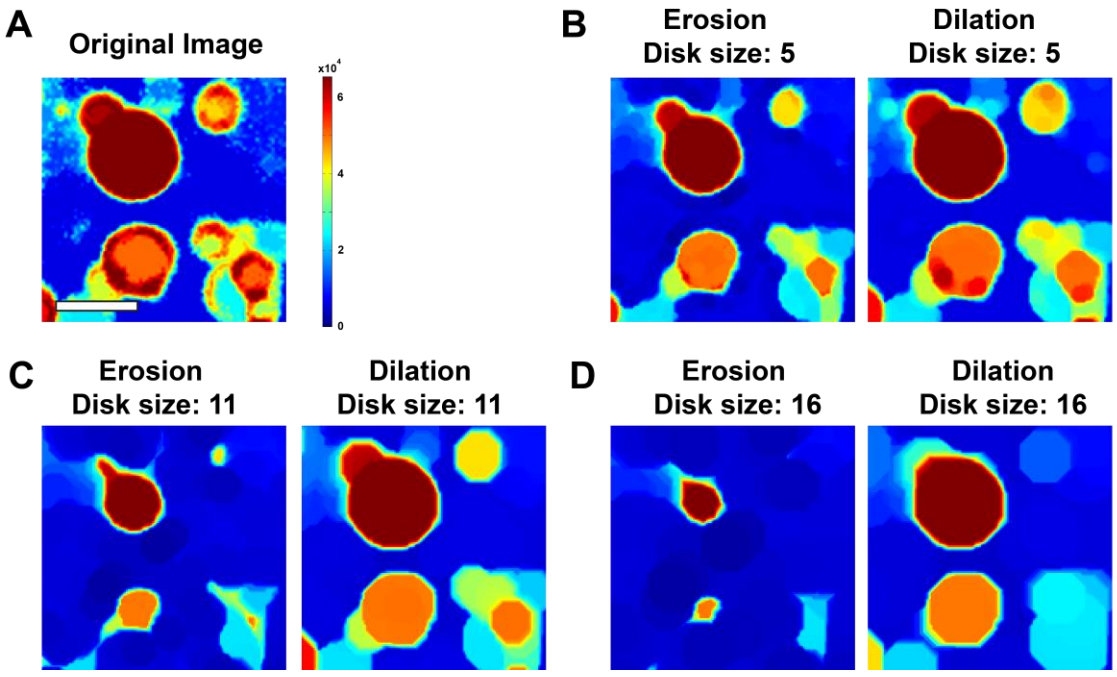

Figure 2-2. Morphological opening example depicted using lipid droplet image. A) Shows the original processed image before undergoing the granulometry process through sequential morphological opening. The image was adjusted to jet colormap to best show lipid droplets with higher intensity. B) Shows an example where the original image has undergone an erosion with a disk structuring element radius of 5 pixels. C) Shows the same process as in A, but with a larger structuring element disk size of 11 pixels in radius. D) Shows the same process in A, but with a larger structuring element disk size of 16 pixels in radius. A more detailed set of sequential images with a step size of 1 pixel in radius is available in Appendix A.5. (Scale bar = 50px = 3.2um)

2.3 Results and Discussion

2.3.1 Modified Granulometry Algorithm for Parameter-free Object Size Analysis

To solve the challenging problem of quantifying overlapping lipid droplet in *C. elegans* without *a priori* knowledge of size distribution, we developed a modified granulometry algorithm (Figure 2-3, Figure 2-4). First, the algorithm pre-processes the image to improve the signal-to-noise ratio using smoothing and contrast adjustment. This allows for images with out-of-focus light, such as those obtained from an epi-fluorescent

microscope, to be analyzed more accurately compared to raw images. To pre-process the image, built-in functions from the MATLAB® Image Processing Toolbox were used. For the smoothing component, anisotropic diffusion is applied to the image, followed by top hat filtering to emphasize the foreground, and subtraction of the image produced through bottom hat filtering to eliminate background artifacts. Then, the algorithm contrast adjusts the image by histogram equalization of the intensities as well as saturating the highest and lowest 1% of the intensities to increase the contrast of the output image. Lastly, holes produced in the image are filled to contain a uniform intensity to be analyzed during the traditional granulometry portion of the algorithm that follows (Figure 2-3 B). After this first step, the image can undergo various different image processing techniques to extract object information, however, the specific preprocessing functions were chosen to best suit the granulometry process.

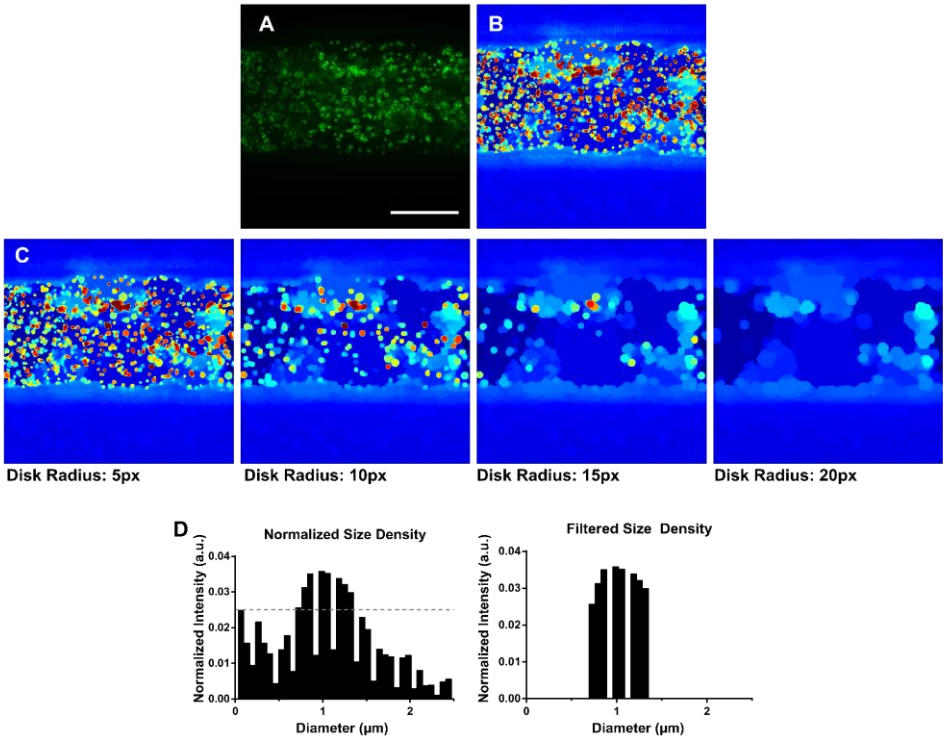

Figure 2-3. Representative images and lipid droplet size distribution outputs from granulometry. A) Raw image shows lipid droplets from a WT *C. elegans* (All images at same scale. Scale bar = 20 μm) B) WT image of lipid droplets after pre-processing. Image is contrast adjust such that lipid droplets are the highest intensity shown in warmer colors, which allows for the modified granulometry algorithm to sieve the high intensity droplets of different sizes. C) Images of WT through various morphological openings in the granumoletry process of 5, 10, 15, and 20 px. As the morphological openings progresses more droplets have been removed from the image. D) Pattern spectrum output from the modified granulometry algorithm shows the predominant sizes of objects in the image based on intensity. A threshold is applied at the mean plus the standard deviation of the intensity in order to show the predominant size of objects in the image.

Second, the traditional granulometry procedure is applied to the smoothed and contrast adjusted image. Morphological openings with disk structuring elements of sequentially increasing radius (Figure 2-3 C, Figure 2-4) are then applied to the image. The intensity loss is recorded at each structuring element size increment, resulting in a pattern spectrum of the image. The pattern spectrum is analogous to a histogram of the number of

objects that fall through the sieve after each size increase resulting in a size distribution. Because granulometry digitally filters the image as opposed to segmenting objects, overlapping and adjacent objects are individually analyzed as opposed to incorrectly being detected as a cluster with a much larger size. Additionally, granulometry does not require optimization of parameters, thus sets of images with varying structure sizes can be analyzed.

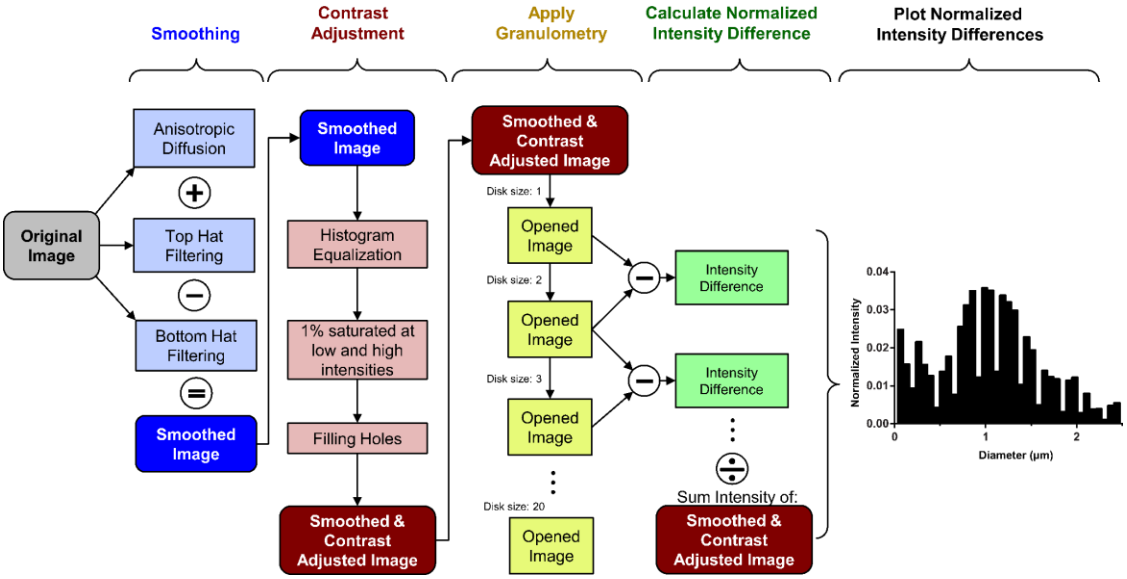

Figure 2-4. Algorithm flowchart. Algorithm showing all of the steps necessary to perform the pre-processing of the image (smoothing and contrast adjustment) as well as the granulometry and normalization steps necessary to calculate the size distribution of objects in an image.

Third, a threshold is applied to the pattern spectrum to emphasize the principal size distribution that corresponds to the prominent objects in the image (Figure 2-3 D). This empirical threshold was calculated by determining the bins from the pattern spectrum that were one standard deviation over the mean bin intensity. In calculating the threshold, the first and second bins with pixel radius of 1 and 2 were discarded because noise was prominent in those bins and biological structures could not be properly analyzed with the

structuring element approximation of a disk with radius of 1 and 2 pixels (Figure 2-5). The threshold also serves the purpose of identifying the principle size distribution of objects in the image. Granulometry produces a noisy pattern spectrum that may have distributions overlap based on the intrinsic intensity variations in the images rather than actual object size differences; therefore, the threshold is advantageous when comparing distributions of different images.

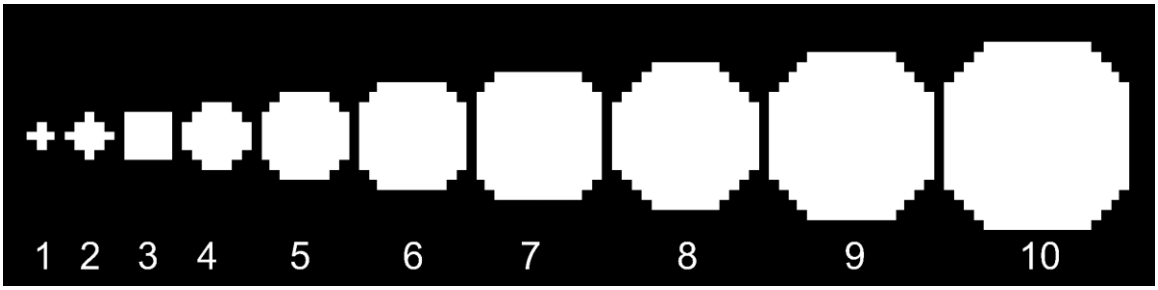

Figure 2-5. Structuring element sizes with increasing disk size from 1 to 10

Last, the pattern spectrum is normalized by dividing each bin by the total structuring element area of the disk used for the morphological operations of that bin. The output is an estimate of the relative quantity of objects for each diameter. For instance, a bin that corresponds to structuring element disk of a radius of 5 has a total intensity captured in that bin size 552 A.U., which is the divided by this area of 69 pixels. This indicates that there are approximately 8 objects of radius size 5 in the bin. The pre-processing of the image causes for the lipid droplet to have similar intensities, thus, this normalization allows for a semi-quantitative method to determine the number of objects in an image. This can be accomplished without having to segment or identify individual objects, and it occurs in a relatively rapid timescale of seconds. In calculating this pseudo-count of objects, the number of objects detected and their corresponding sizes can be

compared to conventional manual annotation methods. This algorithm has three main advantages over traditional manual annotation: 1) there is a great deal of time saved due to the algorithm being two orders of magnitude faster than manual annotation, 2) there is a decrease in bias and human error, and 3) the algorithm facilitates the ability to incorporate automated analysis to be performed unsupervised.

2.3.2 Validation of Algorithm using Synthetic and Microscopy Images

We first tested the accuracy of our method to properly estimating object size distribution in an image by applying the algorithm to synthetic images. We generated a synthetic image library with densely packed, overlapping disks of three different sizes and random intensity values (Figure 2-6A). Our method yielded accurate results for object distribution by size, with an average error of roughly 1% for each size (Figure 2-6B), and a total cumulative error of 3.46±1.72% (Figure 2-7A), demonstrating our ability to accurately determine the number of disks in an image without individual segmentation. In addition to disks, synthetic libraries with varying sizes were also created for square and rhombus shapes. The cumulative mean error for the square and rhombus shapes were 1.51±0.99% and 9.41±1.48%, respectively, demonstrating that the granulometry algorithm can also accurately determine size distributions of varying shapes (Figure 2-7B).

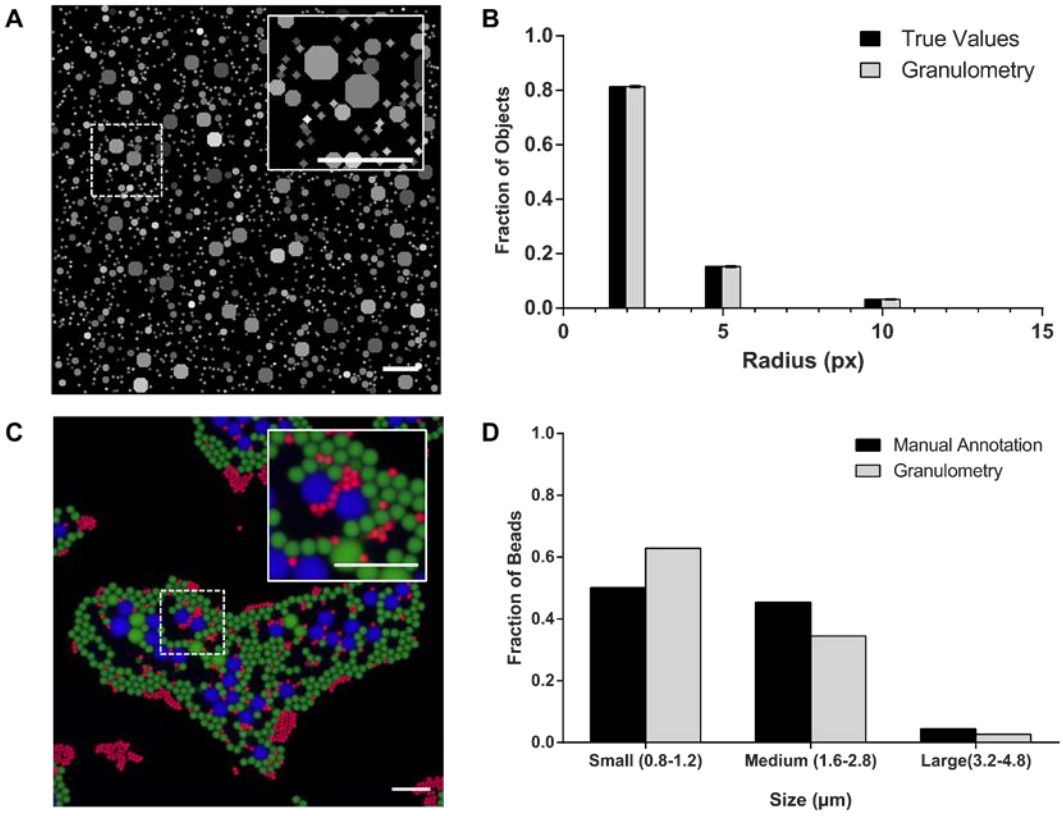

Figure 2-6. Validation of granulometry algorithm using synthetic and confocal microscopy beads for size reference. A) Representative synthetic image with disks of varying diameters (2, 5, 10 px) and varying intensities (1-255), insert shows structuring elements are not perfect disks but a close approximation. (Scale bars = 50 px) B) Synthetic image validation shows that granulometry is very accurate when objects are similar to structuring elements used in morphological openings. (n=100 images) C) Representative confocal image of clustered beads of varying intensities, colors, and diameters, insert shows how edges are not as well defined as in the synthetic images. (Scale bars = 10 µm) D) Results show that the hand annotated value of the diameters in the image closely follow that of the modified granulometry algorithm, indicating that although each method has inherent error partially due to the gradient at the edges, the modified granulometry algorithm diameters are similar to the hand annotated diameters. (n = 25 images)

To address the source of discrepancies between algorithm results and actual object distribution, we looked at two possibilities: object proximity and intensity differences between objects. One source of error in our method is the close proximity between objects, where neighboring or overlapping objects are considered a single object. To test how much

of the error is due to this problem, we tested our method on new synthetic images with no overlapping objects. When we analyzed these images, our method yielded an improved accuracy with a total cumulative error of 0.76±0.58% (Figure 2-7A). To determine how much of the error is due to intensity variation, we tested our method on a library of synthetic images of objects with uniform intensity. With this library of images, the error was almost eliminated, with a reduced cumulative error of 0.02±0.01% (Figure 2-7A). These findings indicate that the two main sources of error in our method are object proximity and intensity variation.

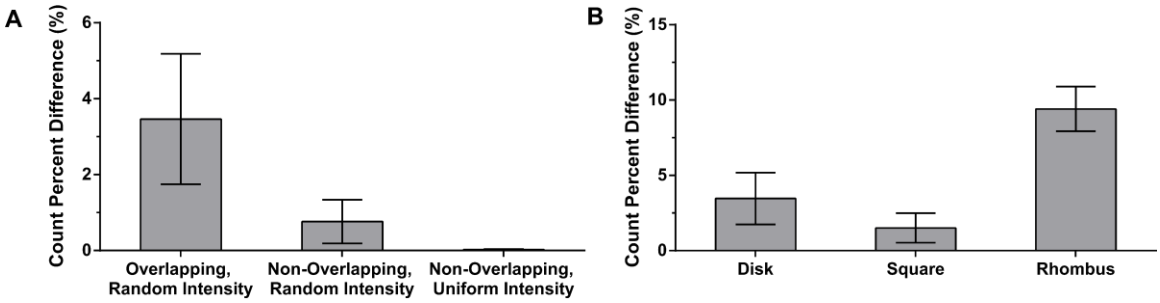

Figure 2-7. Algorithm error source. A) The interobject distance was tested and the error in the number of objects detected was calculated from the defined parameters of the synthetic image. The least amount of error is seen when uniform intensity is used and there is no touching or overlapping objects. The error is less than 0.25% for any of these scenarios so it can be concluded that a small portion of the error for the algorithm is due to the proximity of objects, and more so from changes in intensity. The changes in intensity is corrected in the algorithm by preprocessing the image to have a more uniform intensity for the foreground which includes the objects to be measured. B) In addition to disks, the algorithm can also be used to analyze other shapes such as squares and rhombi. The cumulative mean error of the number of objects detected is less than 10% for each of the different sizes, demonstrating that the algorithm can also be used on other structures other than disks with similar accuracy.

We next tested the ability of our method to characterize objects in real microscopy images, and tested a set of confocal images of micron-sized fluorescent beads (Figure 2-6C, Table 2-1). Densely packed beads were imaged to determine how the algorithm will

perform with images that have objects with edge imperfections due to imaging effects, and objects that are not identical to the structuring elements used during morphological openings. Figure 2-6D displays the average number of objects for the maximum projection images of fluorescent beads using our method versus the manually measured values, which is considered the ground truth. This comparison shows that our algorithm is capable of distinguishing amongst the three bead diameter sizes in the mixed population (Figure 2-6D), showing that the algorithm can determine the size distributions in an image with a high density of objects and edges without sharp gradients. As in synthetic image experiments, errors between computational analysis and manually measured values are attributed to the density and close proximity of objects (fluorescent beads). To characterize this effect, we created image libraries of bead with specific diameters and assessed the accuracy of our analysis method (Figure 2-8A, Table 2-2). In analyzing beads with size ranges from 0.5 μm to 5 μm, the standard deviation for each of the different sizes is less than 1 μm of the stated manufacturer's size range (Figure 2-8B, C). This minimal overlap between the size distributions of the various bead sizes demonstrates that the sizes are accurately discernable when using granulometry. Thus, even when analyzing images with objects limited to a specific size, results of granulometry based methods are still prone to report slight inaccuracies in size distribution (Figure 2-6D).

Table 2-1. Manufacturer's bead size specifications

Bead Color in Image	Size (μm)	Std. Dev. (μm)
Red	1.01	0.032
Green	2.063	0.067
Green	4.458	0.281
Blue	4.358	0.113

Table 2-2. Single-size bead population analysis

Specified Bead Size (µm)	Mean Diameter (µm)	Std. Dev. (µm)	N (# of images)	Range (µm)
1.5	0.71	0.1	31	0.6-0.8
1.0	1.1	0.4	46	0.6-3.6
2.0	1.9	0.3	25	1.2-3.2
3.0	2.7	0.5	46	1.6-3.8
5.2	5.3	0.4	19	4.6-6.8

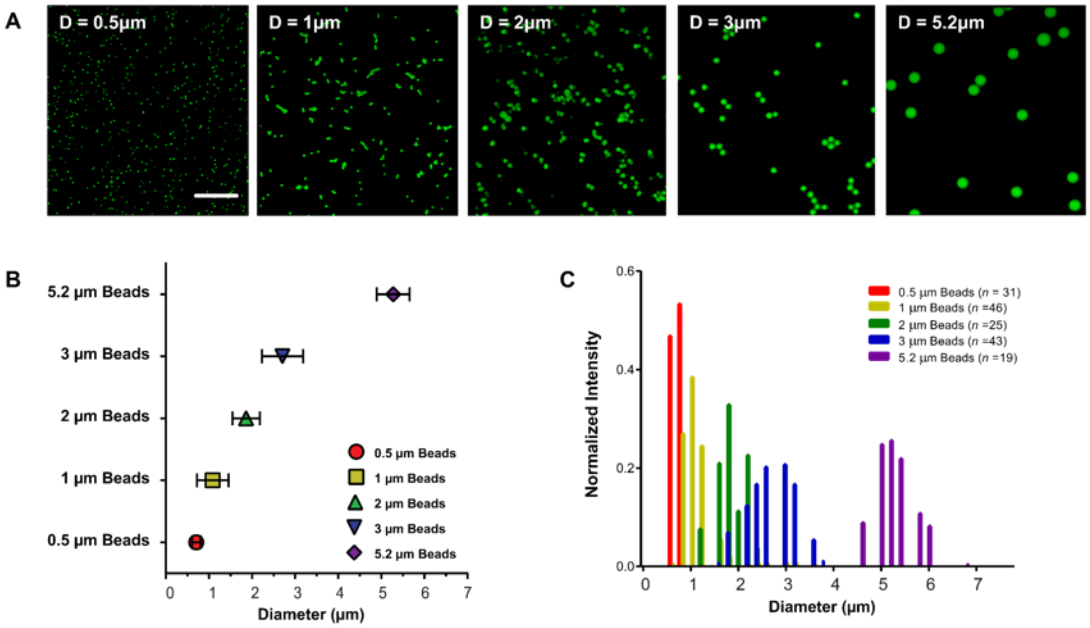

Figure 2-8. Validation of algorithm using single-sized bead population. A) Representative images of fluorescent beads imaged with increasing sizes where the diameter is indicated on the top left corner. The beads were selected to be in the biologically relevant size range of the lipid droplets in *C. elegans*. (Scale bar = 20 µm) B) Mean diameter size for the individual bead populations were calculated using granulometry, and the manufacturer's stated diameter matches up closely with that of the analyzed diameter. C) Full distribution results from granulometry show the size ranges for the beads detected. This shows that various sizes are discernable when using granulometry.

2.3.3 Characterization of Wild Type and Lipid Mutant Populations Mimics Known Distributions

After validating our proposed method using objects of known sizes, we tested the ability of our algorithm to characterize lipid droplet sizes in *C. elegans* wild-type and *atlastin* mutant (*a015*) populations. Alleles used in this study were previously described in Klemm, *et al.* and are known to exhibit different distributions of lipids ranging from 0.2 μm to 4 μm[164]. Figure 2-9 displays the results of applying our method to characterize and discern differences between lipid distributions for both wild-type (Figure 2-9A) and *atlastin* (Figure 2-9B) mutant populations where the maximum diameter evaluated was at 40 pixels which corresponds to 2.56 μm in diameter. Inspecting morphological operations between the two populations demonstrates the ability of granulometry to selectively remove objects of specific sizes from biologically relevant data (Figure 2-9 Aii-iii, B ii-iii). Examination of the *atlastin* mutant image reveals that by approximately 0.5 μm, most lipids have been removed (Figure 2-9ii), while lipids in the wild-type image are still present at 1 μm (Figure 2-9Aii). These observations are reflected in the average filtered size density (Figure 2-9C) computed for both populations, demonstrating smaller lipid droplets for *atlastin* populations (0.25 μm-0.7 μm) compared to wild-type populations (0.77 μm-1.4 μm). The average lipid distribution profile for both populations is shown in Figure 4D and displays the percentage of lipids specific to each diameter size with peak components at 0.38 μm (~35%) and 0.96 μm (~13%) for *atlastin* and wild-type, respectively. Our results correspond with the values from manual curation, thus, our method was successfully validated for more complex applications.

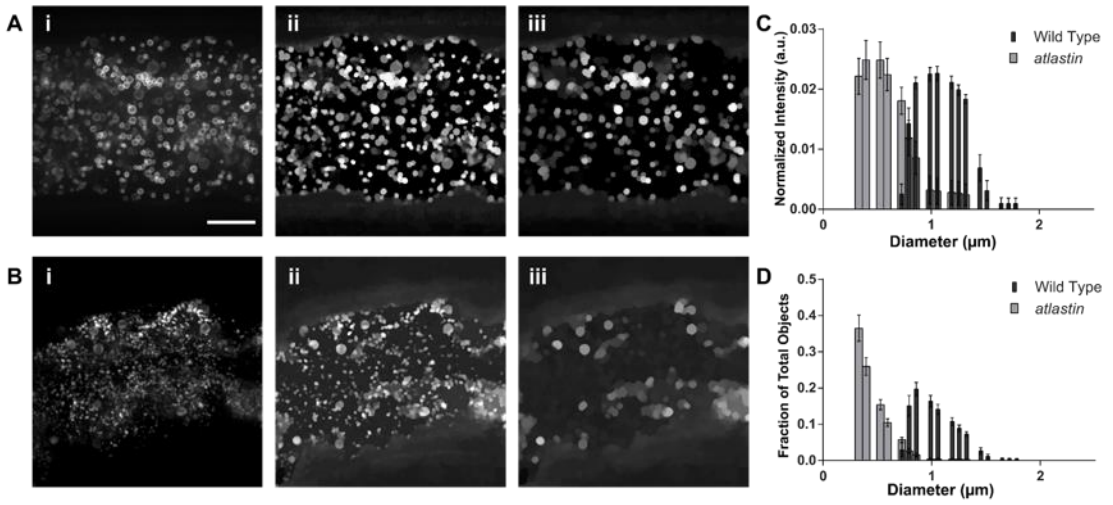

Figure 2-9. Representative images of lipid droplets with wild type and *atlastin* phenotypes with corresponding granulometry outputs. A) Representative confocal image of *C. elegans* wild type animal (hjSi56) with GFP labeled lipid droplets which are large enough to see edges by eye. (Scale bar = 10 μm) B) Representative confocal image of C. elegnas *atlastin* animal (*a015;hjSi56*) with GFP labeled lipid droplets which appear small and it is difficult to detect one individual lipid droplet. A, B) Wild type (A) and *atlastin* (B) lipid droplet phenotype through various morphological openings in the granulometry algorithm (scale bar = 10 μm). A ii,B ii) shows a morphological opening at 0.5 μm, and the right most panels show a morphological opening at 1.0 μm. In the *atlastin* (B, iii), there are very few lipid droplets left after the larger morphological opening, however in the wild type (A, iii) right panel, many lipid droplets are still visible, indicating that there are lipid droplets larger than 1.0 μm present. C) Shows the normalized intensity distribution which is the resulting output from the granulometry algorithm for both the wild type (WT, 1.1 μm ± 0.015 μm) and *atlastin* (*a015*, 0.61 μm ± 0.017 μm) populations. (n=14, mean ± SEM) D) Shows the percent of total objects which is derived from C, but it's a pseudo count to the number of lipid droplets in each of the size bins calculated by dividing the intensity by the size of the structuring element used to perform the morphological operation for that bin size. (Wild type, 1.03 μm ± 0.015 μm, n=14; *atlastin*, 0.46 μm ± 0.012 μm, n = 14; mean ± SEM)

Comparing computational results to hand measured data demonstrates the versatility of our process to discern differences in structures, which in this case are lipid droplet differences between nematode populations. Our analysis method estimates a clear distinction in lipid size for *atlastin* and wild-type animals as seen in Klemm, *et al*.[164], which is the most important aspect of the analysis for this application. The size range returned

from computational analysis deviates slightly when compared to manual measurements, but the slight deviation does not affect the conclusions and classifications of the phenotypes. The change in size is a consequence of filtering the returned size density of each animal to reduce noise while limiting results to principal lipid droplet sizes. As such, the size range for the *atlastin* mutant population is increased from 0.2 μm - 1 μm (manual) to 0.3 μm - 1.3 μm (computational), while the wild-type population shows a decrease from 0.4 μm – 2 μm (manual) to 0.77 μm - 1.8 μm (computational)[164].

Another difference between our analysis and manual measurements is the concentration of lipid sizes observed per population. Klemm, *et al.*[164] show through their analysis that lipids 0.4 μm in diameter comprise approximately 30% of total lipids measured for *atlastin* mutant populations; our results indicate that the largest lipid concentration is at 0.33 μm and 37% of total measured objects. Similarly, Klemm *et al.* report that 1 μm lipids comprise 25% of all measured lipid droplets for wild-type populations while our results estimate that the most frequent size is 0.86 μm which makes up 20% of lipids. Differences between lipid distribution profiles between computed and manually measured results are attributed to computational bias of our method for smaller diameter objects, non-uniform lipid intensity, and optical limitations due to imaging resolution. However, because the analysis is done 500 times faster than previously possible with the manual annotation, the ability to obtain resulting lipid droplet size distributions in correct biological range for two different populations expands the complexity of experiments that can be performed on these phenotypes.

During analysis, returned filtered size density is normalized by area of the structuring elements in order to estimate quantities of lipid droplets in the image. This

creates a bias for smaller diameter objects because of the low number of pixels in small structuring elements. As seen during our previous experiments using synthetic images, non-uniformity of objects can also lead to discrepancies between measured and computed quantities. To measure the extent of non-uniformity between images as well as nematode populations, we measured the average intensity per lipid for four different wild-type and *atlastin* mutant images (Figure 2-10). Analysis demonstrates that intensity of lipid droplets does not vary according to size within each population (Figure 2-10B-D); however, comparison of the wild type and *atln-1* population reveals a much broader lipid intensity range for *atlastin* (Figure 2-10F). While the mismatch does not appear to significantly bias results distinguishing the two populations, it explains discrepancies between calculated and measured values. Another potential source of error in analysis is the optical limitations caused by the physical properties of our microscopy system. The resolving power of the confocal microscope utilized for imaging is approximately 0.2 μm, placing many lipid droplets commonly seen in the *atlastin* population under the optical resolution of the system. Consequently, any objects smaller than this resolution captured in images using this system cannot be verified as true lipids. Therefore, while the size distribution of lipid droplets for the *atlastin* population is known to be smaller than that of the wild-type population, the exact distribution is unknown.

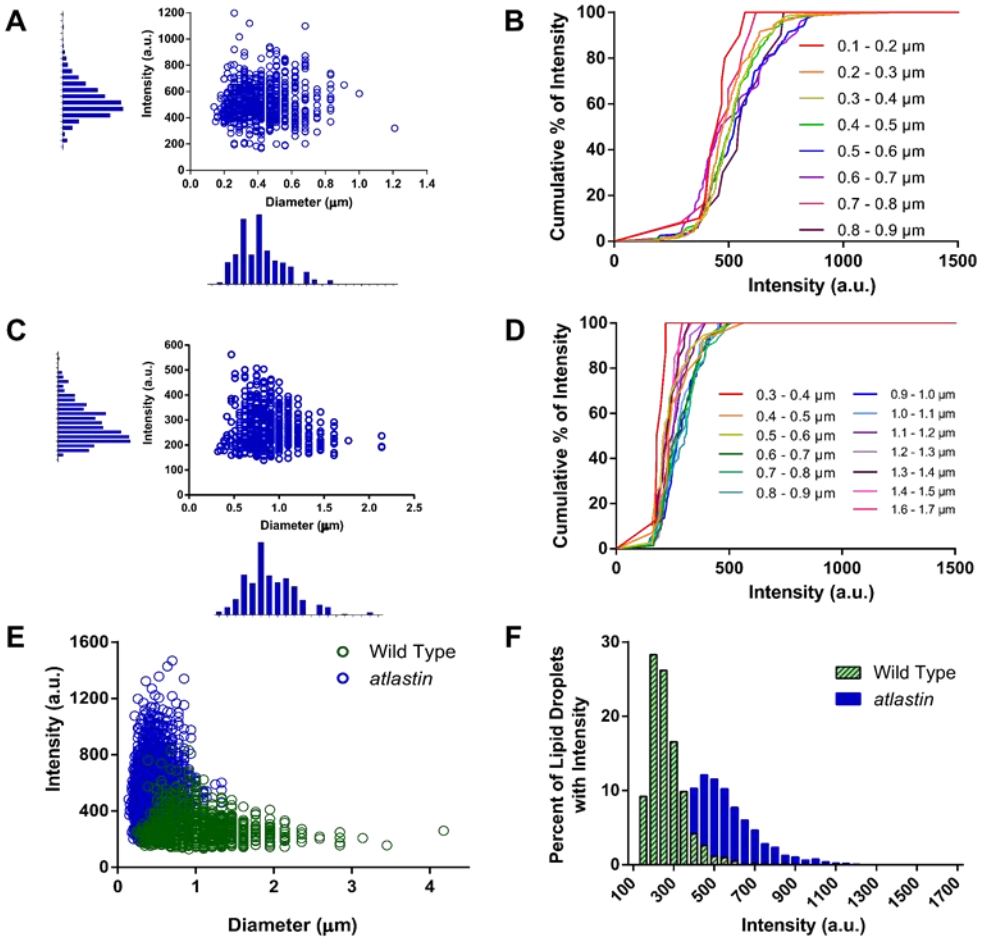

Figure 2-10. Lipid droplet intensity distribution analysis shows even intensities throughout various lipid droplet size intervals but differences in population intensities. A, C) Scatterplot comparing intensity to lipid droplet size for a representative image of the *atln-1* (A), and wild type (C) population shows distribution of intensities have a Gaussian distribution which does not skew the modified granulometry algorithm. B,D) Cumulative percent of intensity is plotted for the same image in (A) and (C), respectively, for each 0.1um interval of lipid droplet size in the image. The variation in intensity is shown not to vary with size due to the narrow distribution, i.e. the smaller droplets are not brighter than the larger droplets, thus it does not skew the modified granulometry algorithm. E) Scatterplot of lipid droplet size versus intensity for the wild type and *atln-1* population (n=4 each) shows that the *atln-1* population had a larger variation and higher intensity compared to the wild type population, which shows the preprocessing of the images is necessary to eliminate this difference in intensity. F) Histogram comparison of images from (E) plotting intensity versus the fraction of lipid droplets shows that the wild type population has a narrower and lower intensity compared to the *atln-1* population, however both populations the same fraction of lipid droplets in the respective median intensities showing that the

majority of droplets fall within an intermediate intensity thus the modified granulometry algorithm is not skewed to different sizes since the variations in intensity is a Gaussian distribution.

2.3.4 Characterization of Low Fidelity Images for Characterization of Wild Type and Lipid Mutant Populations

To test the characterization ability of our granulometry approach with lower fidelity techniques, we analyzed epi-fluorescent microscopy images of both wild type and *atlastin* populations. Because the lower fidelity images would be ideal quickly capture variations of lipid droplets in a genetic screen where the phenotypes encountered are unknown, we evaluated a maximum lipid droplet diameter size of 6 μm to encompass larger potential phenotypes. The current standard for manually measuring the size of lipids involves annotating 3D reconstructions of acquired images from many focal planes. This method requires high fidelity imaging, such as confocal microscopy, in order to accurately recreate a 3D image. Our proposed method, however, analyzes the maximum projection of an image stack, eliminating the need for 3D reconstructions and high fidelity imaging along with it. Compared to confocal images, epi-fluorescent images have more out-of-focus light, leading to larger objects, more overlap, and poor contrast for lipid droplet edges. The wild type lipid droplets (Figure 2-11A, B) can be partially manually annotated, whereas for the *atlastin* mutant, the smallest lipid droplets are beyond the resolution of the microscope used (~0.2um). This led to clusters of droplets being annotated as a single object, leading to highly inaccurate manual annotation. It was therefore impossible to acquire an accurate ground truth for the lipid droplet size distributions in these sets of images.

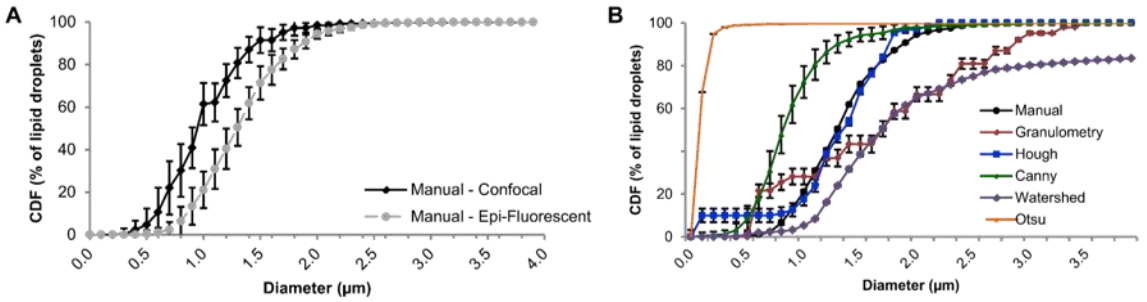

Figure 2-11. Differences between manual size annotation between high and low fidelity images, and granulometry compared to other segmentation methods when analyzing low fidelity images. A) Manual annotation of confocal and epi-fluorescent images of the same wild type strain with larger droplets was conducted and the cumulative distributions is plotted. It is expected that there would be a slight shift to the right from confocal to epi-fluorescent images due to the out of focus light contributing to a larger perceived lipid droplet, however, this shift is small enough that the strains are comparable between the confocal and epi-fluorescent images, especially when comparing to the mutant strain *atlastin* which has much smaller droplets shifted by more than 0.5 μm to the left. B) Cumulative distributions of lipid droplet sizes using various methods when analyzing epi-fluorescent images. The manual annotation and the granulometry methods line up most closely when compared to other methods. Because epi-fluroescent images have a great deal of out of focus light this becomes are much more difficult task compared to confocal images.

Although manual annotation of the images was difficult, our method was still able to detect lipid droplets and discern a difference between size distributions in the two populations. Manual annotation of both the confocal and epi-fluorescent images was conducted and a slight increase in lipid droplet sizes were observed (Figure 2-11A). Because of the low quality of the images and the out-of-focus light, the resulting distributions are different from the manually annotated confocal images where the diameters of the lipid droplets are larger using epi-fluorescent images. However, this difference does not change the classification of the wild type lipid droplets with respect to the *atlastin* lipid droplets. Our method, even when analyzing low quality images that are difficult to annotate, was still able to distinguish between the two populations in these low

quality images. The ability to extract meaningful information from low quality images captured on low cost system increases the breadth of application of our algorithm and allows for a wider array of experimental possibilities.

2.3.5 Convergence of the Modified Granulometry Algorithm

To determine the number of samples necessary that defines the lipid droplet size distribution of a population of worms, a convergence analysis was conducted. The lipid droplet phenotype, from either a wild type or *atlastin* population of worms, as well as the differences between confocal and widefield microscopy images were explored. We determined the average distribution of the population by calculating the mean and standard deviation of the normalized intensity at each bin corresponding to the different lipid droplet sizes. We then calculated the percentage of bins from a population distribution of a grouping of a randomized number of worm images necessary to obtain 95% of the bins within 1 standard deviation from the overall population distribution. This randomization was conducted 10 times and the average values were used to determine the number of worms necessary for convergence. For a wild type lipid droplet phenotype imaged by confocal microscopy 5 worms are necessary (Figure 2-12A), and for the *atlastin* lipid droplet phenotype only 4 worms are needed (Figure 2-12B). When imaging using widfield microscopy, and increased amount of out of focus light is captured. Because of this, the phenotype becomes more difficult to analyzed. Although the images may not appear to show clear lipid droplets, such as in the confocal images, the modified granulometry algorithm is still able to calculate the lipid droplet size distribution for both the wild type and *atlastin* lipid droplet phenotypes. For a wild type lipid droplet phenotype using widefield microscopy 17 worms are necessary, and for the *atlastin* lipid droplet phenotype

24 worms are needed. These number of worms are very reasonable as it is recommended to obtain a population of at least 30 worms to calculate robust statistics on the variations between populations. More worms are necessary for the widefield images to converge as compared to confocal images because the out of focus light captured in the images that causes for more heterogeneity in individual worm images, however, with enough worms the population distribution converges. This further demonstrates that the modified granulometry algorithm is capable of analysing both high and low fidelity images.

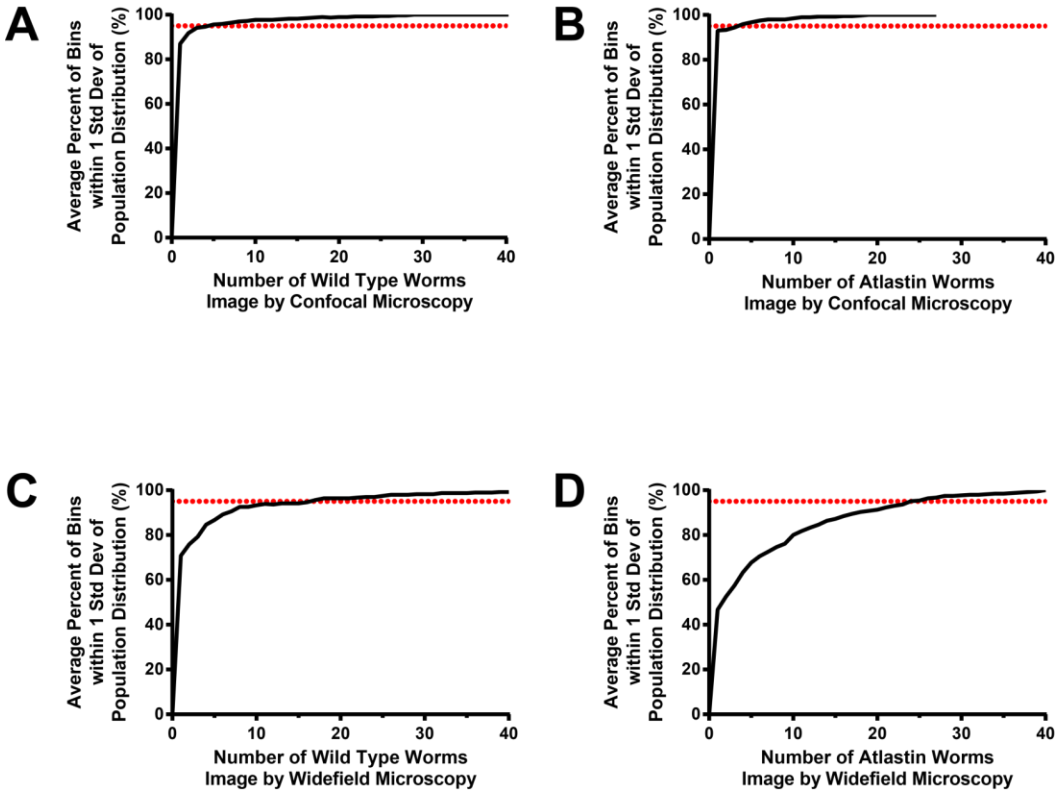

Figure 2-12. Convergence of granulometry distribution for different worm strains and imaging modalities. Convergence was calculated by determining the average population distribution and determining the number of worms that were averaged that had bins within 1 standard deviation of the mean of each bin for the population distribution. The red line indicates that 95% of the bins are within the 1 standard deviation of the average population distribution. A) Shows the convergence of using granulometry on confocal microscopy images of wild type lipid droplet phenotype. B) Shows the convergence of using granulometry on confocal microscopy images of

***atlastin* mutant lipid droplet phenotype. C) Shows the convergence of using granulometry on widefield microscopy images of wild type lipid droplet phenotype. D) Shows the convergence of using granulometry on widefield microscopy images of *atlastin* mutant lipid droplet phenotype. Generally, less worm lipid droplet size distributions are necessary to have the lipid size distribution converge when using confocal images as compared to the widefield images. In analyzing the various phenotypes and imaging modalities the maximum number of worms necessary for the distribution to converge in the different conditions was for the *atlastin* phenotype imaged using a widefield microscope, and only 24 worms are necessary for the population to converge to where 95% of the bin mean falls within 1 standard deviation of the population distribution.**

2.3.6 Comparison of Modified Granulometry Algorithm to Segmentation Methods

To test that our method is advantageous over other image analysis methods, we compared our results to commonly used segmentation methods, including Canny edge detection[97], watershed[101], and the Hough transform[104]. All these methods have more than one parameter and these parameters were optimized by comparing results to manually annotated confocal images. For instance, the Canny edge detection method has 3 parameters to optimize which include thresholds and Gaussian filter edge parameters[97], and the Hough transform has 5 parameters to optimize which include radius range, a circularity sensitivity factor, and thresholds[104,107]. With optimized parameters for various methods, we analyzed both wild type and *atlastin* phenotype lipid droplet images. The pre-processed image was used for these methods to allow for direct comparison with the modified granuometry algorithm. As compared to the manual annotation (Figure 2-13A) which we take as our ground truth, granulometry (Figure 2-13B), canny edge detection (Figure 2-13C), and the Hough transform (Figure 2-13D) all are able to clearly distinguish between the two phenotypes. Additionally, when comparing all of the segmentation methods tested, the modified granulometry algorithm performs as accurate as or more accurate to the other methods when analyzing both wild type (Figure 2-13E) and *atlastin* (Figure 2-13F)

confocal images, all without adjusting any parameters for these results. Our modified granulometry method performed similar to the segmentation methods, however, is much more advantageous to use because these results can be obtained without adjustment of parameters, making for a much more universal method to quantify sizes of objects in images.

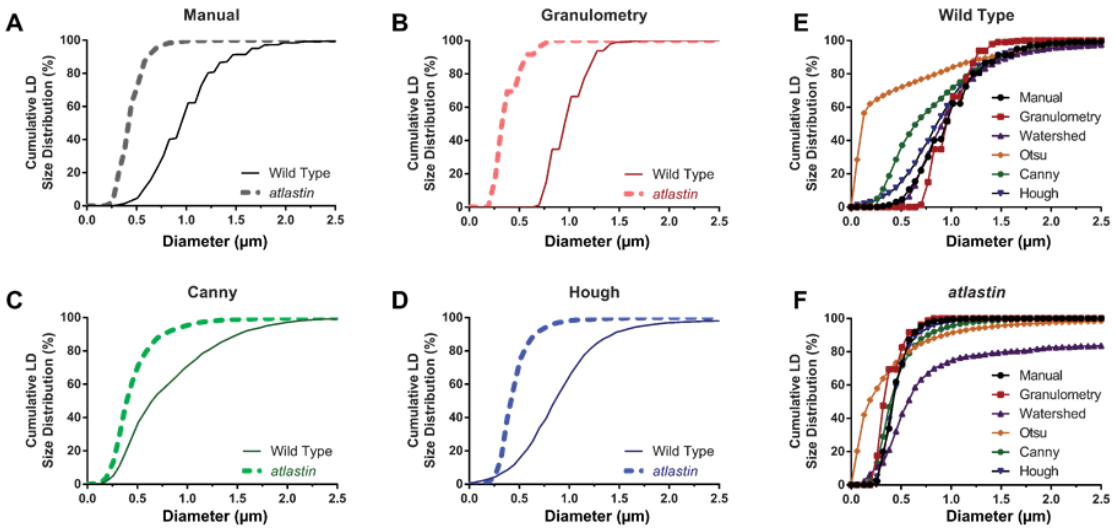

Figure 2-13. Granulometry algorithm comparison to segmentation methods for analysis of wild type and *atlastin* phenotypes. For automatic screening purposes, the difference between two populations must be detected. In addition to performing similarly to other segmentation methods for detecting a difference between the two populations, granulometry is the only one without the need for parameter optimization, which is better suited to perform a screen since potential phenotypes are unknown. (Dashed line indicates the mutant *a015*;hjSi56, and the solid line indicates wild type N2;*hjSi56*). A) Shows the manual annotation data, B) shows the granulometry results which do not need any parameters to be adjusted between phenotypes; C) shows the canny edge detection results, where 4 parameters had to be optimized between the two lipid droplet phenotypes; D) shows the hough transformation results which are similar to the manual annotation results, however 5 different parameters had to be optimized to accomplish this accuracy. E, F) Cumulative distribution of lipid droplet diameters from a representative wild type (E) and *atlastin* (F) animal show that the modified granulometry algorithm outputs a similar or better diameter distribution to other segmentation methods when compared to the manual annotation, which is regarded as the diameter distribution, when analyzing a confocal image of lipid droplets.

As mentioned earlier, our method is parameter free and can be applied to detect objects in any image, regardless of the imaging conditions. This is a key property for analyzing epi-fluorescence images, as they lack ground truth distributions. This makes it very difficult to optimize parameters for segmentation methods, disallowing the use of these methods. We manually annotated epi-fluorescent images of wild type animals and determined the modified granulometry algorithm performed similar to other methods (Figure 2-11B), however, the optimization that took part in the other methods could not be accomplished for the *atlastin* phenotype because it is not currently possible to accurately annotate the images using the epi-fluorescent images. In contrast, because our method is parameter-free, it can still be used to characterize these sets of low quality images, and can distinguish between the different lipid droplet phenotypes.

2.3.7 Modified Granulometry Approach Enables Real-Time Characterization and Forward Genetic Screening of C. elegans in Search of Lipid Mutations

The modified granulometry algorithm is able to quantify epi-fluorescent images which allows us to perform the first automated lipid droplet phenotype screen to our knowledge. Our method is ideal to conduct a forward genetic screen for two main reasons. First, it is parameter-free and can be used to characterize images without prior knowledge of the ground truth. Second, our method highly increases the throughput of phenotyping biological samples. The time required to acquire an epi-fluorescent stack images is approximately 10 seconds, compared to the more than 120 seconds with a point scanning confocal microscope. Combined with the time requirement difference between manual annotation and our automated method, the overall time required to analyze one sample is reduced from 6 hours to approximately 30 seconds.

With the ability to perform characterization of *C. elegans'* lipid distribution within seconds and without parameter optimization, we performed an automated forward genetic screen of over 3,000 animals using a microfluidic platform coupled with customized automated software. The threshold used for the software to sort a suppressor mutant was chosen based on the ROC curve calculated from a library of epi-fluorescent images (Figure 2-14). We performed this screen using microfluidics (Figure 2-15) and software automation at an average throughput of 80 worms per hour, averaged over 3 separate mutagenesis experiments.

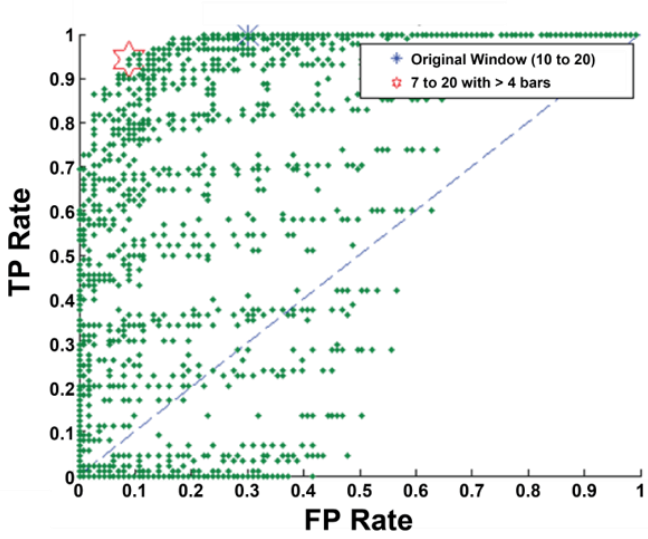

Figure 2-14. ROC curve determined the most optimal threshold to determine if a given worm image was from the wild type or *atlastin* population. This was calculated by analyzing the granulometry output from epi-fluorescent images of both populations. As shown on the graph, the original window used was 10 to 20 px which is in the top quadrant indicating a low false positive rate and high true positive rate. Other window ranges that also could be utilized are 7 to 20 px which would result in similar true positive rates. (wild-type *n = 88, atlastin n = 114,* accuracy 92.7%)

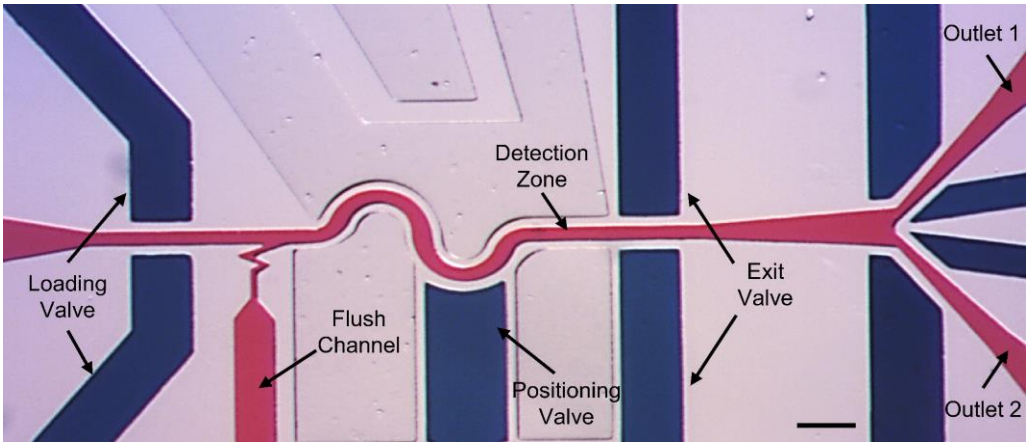

Figure 2-15. Device utilized for screen with various parts labeled. Red – fluid flow channel, Blue - pressure actuated valves. (Scale bar = 150 µm)

Our system isolated 22 potential mutants that suppress or partially suppress the *atln-1* small lipid droplet phenotype. We then imaged these animals using confocal microscopy to reduce the number of potential suppressor mutants, and one of the alleles *a211* is shown in Figure 2-16. The mutant, GT211 (*a211)*, has a suppressor mutation causing a lipid droplet phenotype similar to wild type (Figure 2-16A) and the molecular lesion of *a211* was identified by sequencing[178]. These results demonstrate that combining the granulometry algorithm to detect mutants with microfluidics to image animals makes automatic screening of *C. elegans* for different lipid droplet phenotypes possible. To our knowledge, this is the first automated high-throughput genetic screen of lipid droplet phenotypes in *C. elegans*. With the ability to analyze low quality images, and rapidly quantify lipid droplets in thousands of worms, the ability to test many perturbations that affect lipid droplet phenotypes including effects of diet, drugs, and environment, expands greatly.

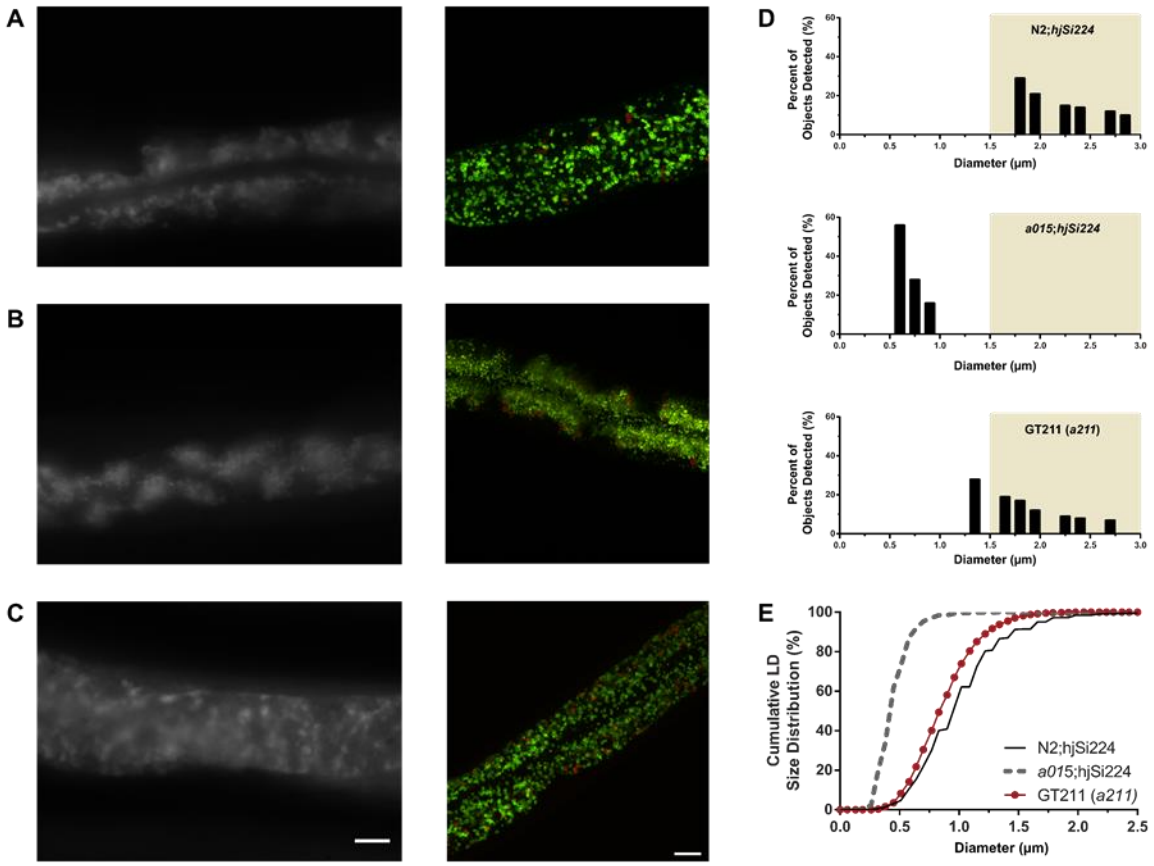

Figure 2-16. Automated genetic screen results in the identification of an *atlastin* suppressor mutant. A-C) Representative image of wild type (A), *atlastin* (B), and a211 (C) animal on epi fluorescent microscope (left) and confocal microscope (right). The epi-fluorescent image is considerably blurrier, creating a harder image processing problem to measure and segment individual droplets, as compared to the confocal image. D) Granulometry results show that the lipid droplets are within the window (shaded region) used during the *atlastin* suppressor screen from 1.5 µm to 3 µm in diameter for the wild type (top) and the suppressor found during the screen (bottom), however the *atlastin* (middle) granulometry results show smaller lipid droplet diameter range which is outside of the window threshold for sorting. E) Cumulative distribution of lipid droplet diameters from a representative wild type, *atlastin*, and *a211* animal show that the modified granulometry algorithm outputs a similar for lipid droplet distribution between the wild type and *a211* mutant found during the forward genetic screen, indicating that a mutant was found that suppresses the *atlastin* phenotype and phenocopies wild type with large lipid droplets. (Scale bars = 10 µm)

2.3.8 Brood Size Analysis for Forward Genetic Screen, using Granulometry for Phenotype Characterization

In addition to applying the modified granulometry algorithm to an online automated screen, a separate forward genetic suppressor screen was conducted, and the algorithm was applied for phenotype characterization. Currently, all known suppressors of *atlastin* lipid droplet phenotypes have been the result of intra-genic mutations. However, the benefit of finding an extra-genic mutation is that we would be able to better determine how *atlastin* interacts with other genes. The only extra-genic mutation that has been found, thus far, was due to a change in brood size that was observed[178]. At 25ºC, *atlastin* has a reduced amount of progeny, however a mutation that increases the brood size would be favorable. The majority of mutations that cause an increase of brood size at 25ºC also cause a suppression of small lipid droplets, and the phenotype more similarly approximates that of wild type. Mutants with such a profile are typically intra-genic, thus the goal is to find a mutant with an increased brood size, but no change to lipid droplet size distribution when compared to *atlastin*.

In order to increase the probability of finding an extra-genic mutation, a forward genetic screen was performed. An *atlastin* population was mutagenized using EMS, and 10 P0s, which are the generation of worms that underwent mutagenesis, were picked on to 25 large agar plates each. After 2-3 generations, the entire plate was divided into 4 sections, and put on different plates, adding up to 100 plates with potential mutations. These plates were then chunked, which includes taking a 2.5 cm x 2.5 cm square sample of agar with worms from the original plate, to a new plate with fresh food while being cultured at 25ºC. By culturing the populations at 25ºC, a selection pressure is applied, and the mutants with

a high brood size have a higher probability of a greater number of worms on the plate, being chunked to future plates. This process was repeated for 4 months, until over 20 chunks had occurred.

To determine if an extra-genic mutation had been found, the brood size for different chunked populations were qualitatively analyzed. Typically, brood size analysis is determined by picking a gravid adult, allowing for eggs to be laid for a specified amount of time, and then individual eggs are counted. Because of the large amount of plates and how labor intensive this procedure would be, the whole plates were analyzed in a different manner. A custom set up (Figure 2-17) with a large field of view was created to allow for imaging of a whole 6 cm NGM plate. From mixed age population plates, 9 worms in the L4 stage from each of the 100 plates were picked and 3 were placed on each plate, totaling to 300 plates. These worms were cultured 25^{o}C and allowed to self for 4 days allowing for the majority of the worms to pass egg laying time. Most of the worms on the plate would then be the progeny of these picked worms, and they would not yet have progeny of their own. Each of these plates were then imaged at low magnification, and the amount of progeny on the plate was qualitatively assessed from each image rating from 1-5, with 1 as low to no progeny, and 5 as a large amount of progeny (Figure 2-18). The average of the 3 plates was taken as the rating for the day for each plate. This was repeated twice, and the sum of the two ranks was used to determine how the various populations were then ranked in order from highest brood size to lowest (Figure 2-19). The top candidates with higher brood size as compared to *atlastin*, where then picked for further analysis.

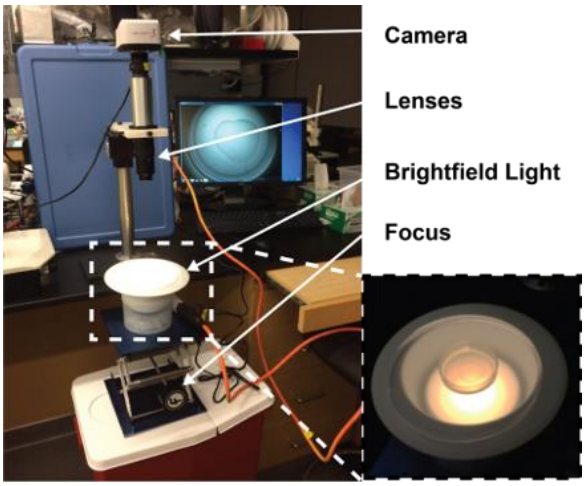

Figure 2-17. Custom imaging set-up with extended field of view for whole plate imaging

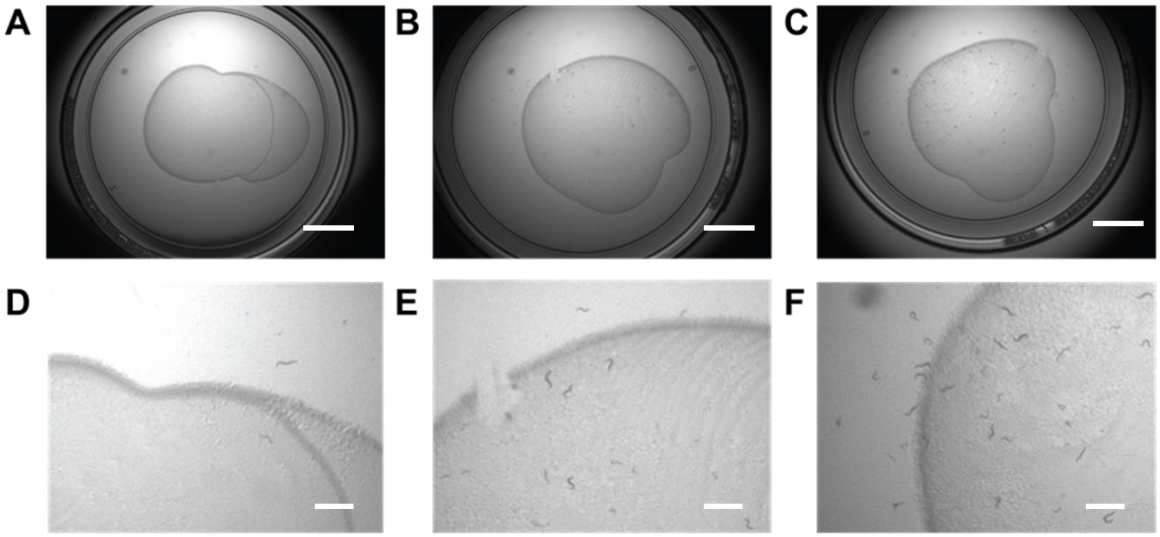

Figure 2-18. Example images of low, medium, and high brood size identification. A, B, C) Show the full 6cm plate on the extended field of view set up. The various plates are representative images of plates classified as low (A), medium (B), and high (C). D, E, F) Shows a region of the plate imaged above zoomed in 4x. It is visible to see the amounts of worms present for each classification low (D), medium (E), and high (F). (A, B, C: Scale bar = 1 mm; D, E, F: Scale bar = 200 μm)

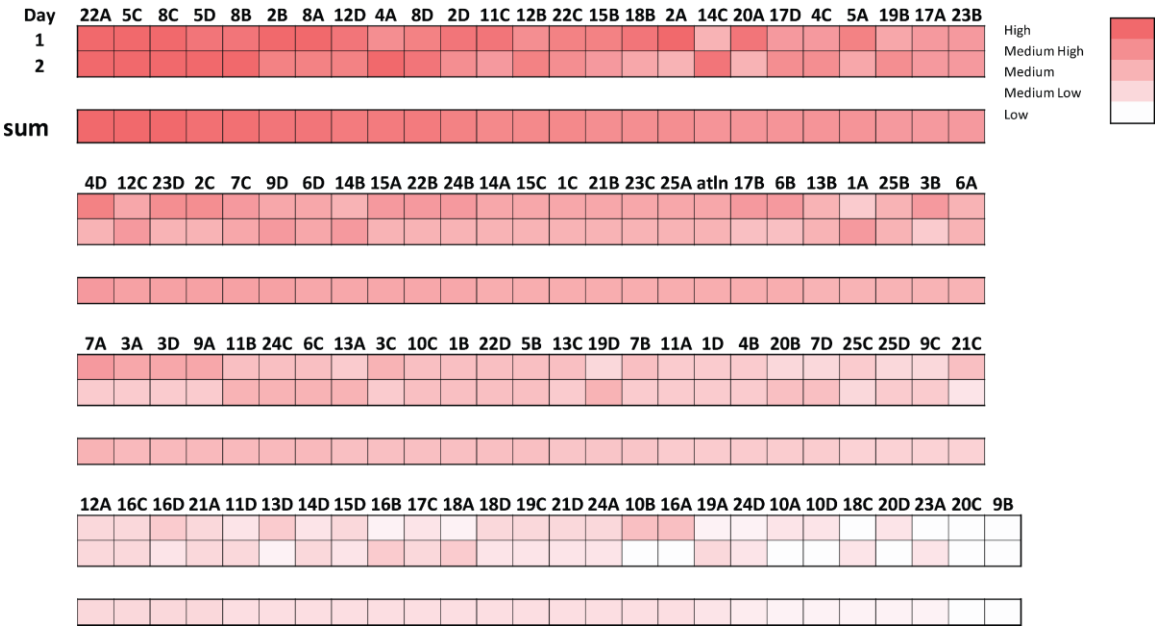

Figure 2-19. Resulting brood size assessment for round 1 of analysis. Intensity signifies the qualitative amount of progeny on the plate with most intense signifying high, and least intense signifying low. Each square is an average of 3 different plates, and the sum of this assessment on two different days was used to determine the rank order of the various populations.

A second round of brood size analysis was conducted where the top populations were qualitatively reassessed. The top 44 populations that had higher brood size compared to *atlastin* had 3 L4 worms each picked on to individual plates and allowed to self for 4 days. These populations had the number of progeny qualitatively assessed similar to the previous method with whole plate imaging (Figure 2-20A). The individual populations that were identified in the top 2 categories with the highest brood size where then chosen for imaging to determine if the population had suppressed the lipid droplet phenotype (Figure 2-20B).

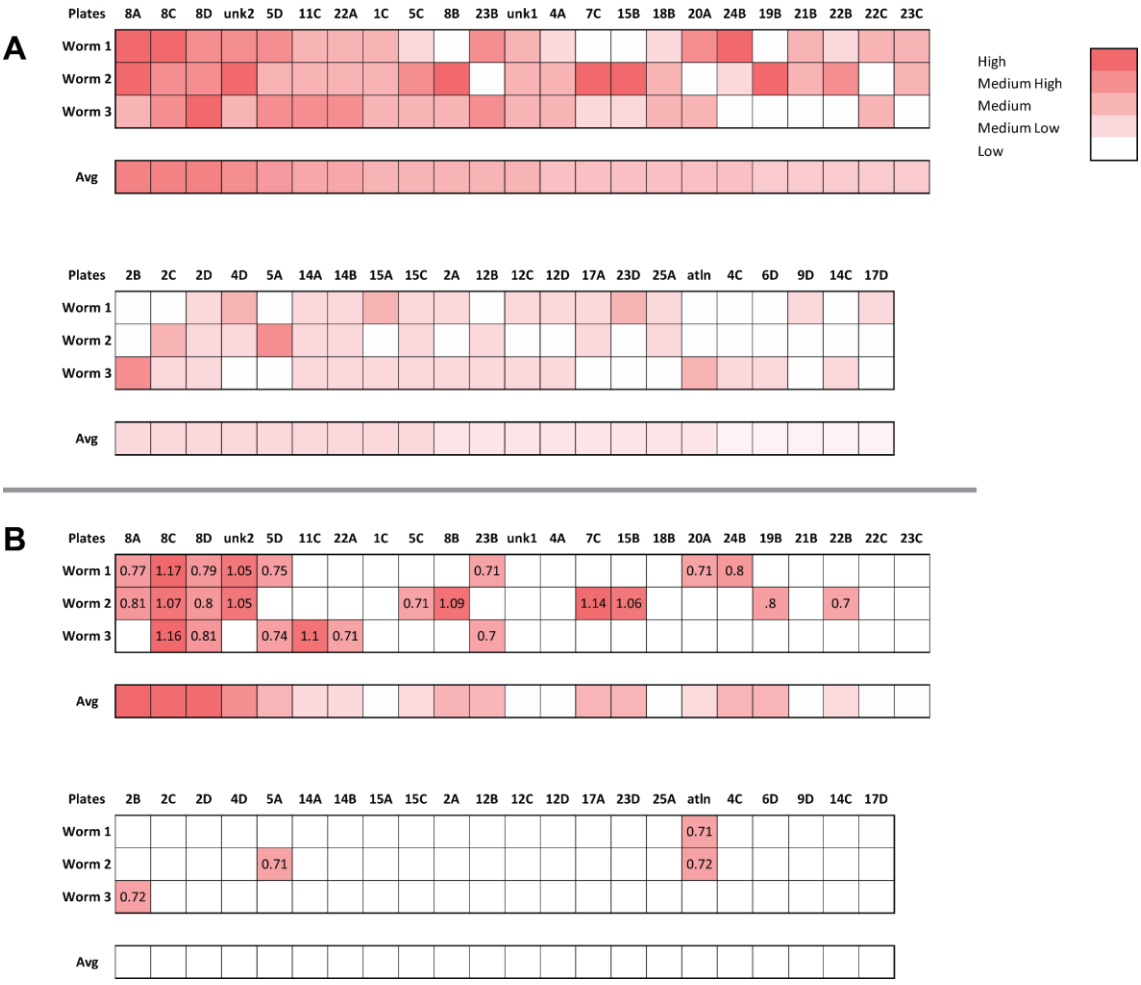

Figure 2-20. Resulting brood size assessment for round 2 of analysis coupled with lipid droplet size phenotype. A) Shows the brood size rating of each individual worm for round 2, and how they corresponded to each plate. They are ranked in order where the average of the brood size assessment for the 3 different worms is calculated. B) The top 26 potential mutants that fall in the medium-high and high rating are highlighted, and the numbers inside of the squares correspond to the average lipid droplet diameter size in µm as determined by the modified granulometry algorithm. A total of 8 populations, signified by individual squares, have higher brood size than *atlastin* with similar lipid droplet size range of approximately 0.7 µm.

The goal was to determine the mutant populations with high brood size but no change in lipid droplet phenotype. In total, 26 different populations were imaged in the L4 stage using a spinning disk confocal. After imaging, and analyzing the images using the modified granulometry analysis, 3 distinct lipid droplet size categories were determined

when compared to *atlastin*, which has an average lipid droplet size distribution of 0.7 μm in diameter (Figure 2-20B). The first category had lipid droplet size distribution with a mean of 1 μm, which suggests the worm populations have a lipid droplet size distribution similar to wild type. This indicates, that these populations have a high probability of having an intra-genic mutation and will not be further studied. There was a total of 9 populations in this category. The next category was composed of populations with small lipid droplets, but distinctly different from *atlastin* because the lipid droplets spanned the whole width of the intestine, unlike *atlastin*, as well as had a larger lipid droplet diameter of 0.8 μm with rings that were visible. Although these populations are likely partial suppressors, they have also previously been classified as intra-genic mutations when this phenotype is observed, therefore these populations will not be further investigated. A total of 9 populations were in this category of an average lipid droplet size of 0.8 μm. The last category was composed of populations that were identified with a high brood size, however, no discernable change in lipid droplet size was observed or quantified when using the modified granulometry algorithm. The average lipid droplet diameter of these populations were approximately 0.7 μm, which fall in the same range as the *atlastin* mutant population. A total of 8 distinct populations were determined to be in this category that have a high probability of having an extra-genic mutation which would lead to new information about *atlastin*.

To follow-up, these 8 populations had the brood size qualitatively assessed once again. In this iteration, 10 individual worms from each plate, totaling to 80 plates, were allowed to self as previously described, and this procedure was repeated twice. As can be seen in Figure 2-21, the average brood size was assessed for each worm population, and then averaged. The average of the average of the two trials per population was then

summed, and ordered from greatest brood size to least. From these 8 populations, 7 populations displayed an increase in brood size when compared to *atlastin* when cultured 25^{o}C (Figure 2-21). These 7 populations will then be sequenced in the *atlastin* region to determine if the observed brood size changes were due to an extra-genic mutation. The function and gene-gene interaction of *atlastin* and other genes is still greatly unknown, thus the ability to begin determining the series of genes that may interact with *atlastin* opens new potential explanations for phenomenon that are observed, and opportunities to further explore how *atlastin* may function in other organisms.

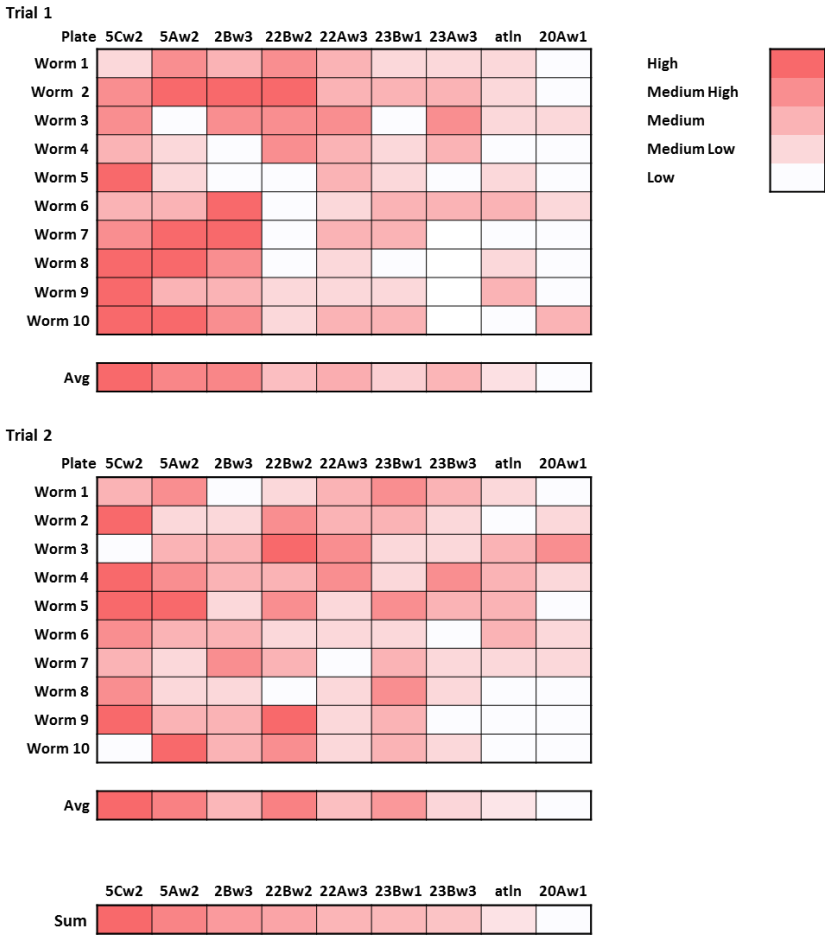

Figure 2-21. Resulting brood size assessment for round 3 of analysis. Brood size rating for 10 worms for each of the 8 populations being further analyzed, in

addition to *atlastin*. The two trials were independently summed, and the average brood size for each population over 10 worms was calculated. The sum of these two averages was then computed, and only population 20Aw1 showed a smaller brood size as compared to *atlastin.* These 7 populations will undergo further analysis to determine if the larger brood size is due to an extra-genetic mutation in *atlastin.*

2.3.9 Texture Characterization of the Endoplasmic Reticulum Shows Modified Granulometry Algorithm Quantifies Non-Uniform Porosity

Beyond detecting sizes of densely packed objects in images, the modified granulometry algorithm can also detect differences in texture such as porosity variations. Texture in an image is difficult to define and quantify thus it is typically described qualitatively. For example, manually quantifying irregular porosity can be arduous since multiple features can be used to describe one pore. Additionally, many textural analysis outputs consist of abstract values such as the entropy, homogeneity, and correlation of the image, which typically are difficult to couple with biologically relevant meaning. To show that the modified granulometry algorithm can distinguish between two textures, we analyzed the endoplasmic reticulum (ER) of *C. elegans*. The ER is an important structure to characterize because lipid droplets are primarily formed in the ER and morphological changes may lead to advances in fat storage studies[73,78,79]. Due to the mesh-like structure of the ER, it is difficult to determine a numerical representation or measurement to describe the phenotypes (Figure 2-22A, B). We examined the difference between the wild type and *atlastin* mutant and qualitatively observed that the wild type strain appears to have a more organized mesh, whereas the *atlastin* strain is more disorganized in the mesh appearance. The pattern spectrum output from the modified granulometry algorithm correlated the respective mesh-like appearances with smaller pore sizes for the wild type strain, and larger pore sizes for the *atlastin* strain (Figure 2-22C). Because of the difficulty to optimize

parameters to a non-uniform mesh, other segmentation methods are not capable of capturing the differences seen between the two phenotypes (Figure 2-22D, E), however, granulometry is not only able to capture the porosity differences, but the differences are vast enough (Figure 2-22F) that a threshold could be theoretically determined to conduct an automated screen. The modified granulometry algorithm was therefore able to quantify morphology of the ER that until now did not have a sole quantitative measurement to discern populations. This method can potentially be used to quantitatively determine new mutants through automated genetic screens.

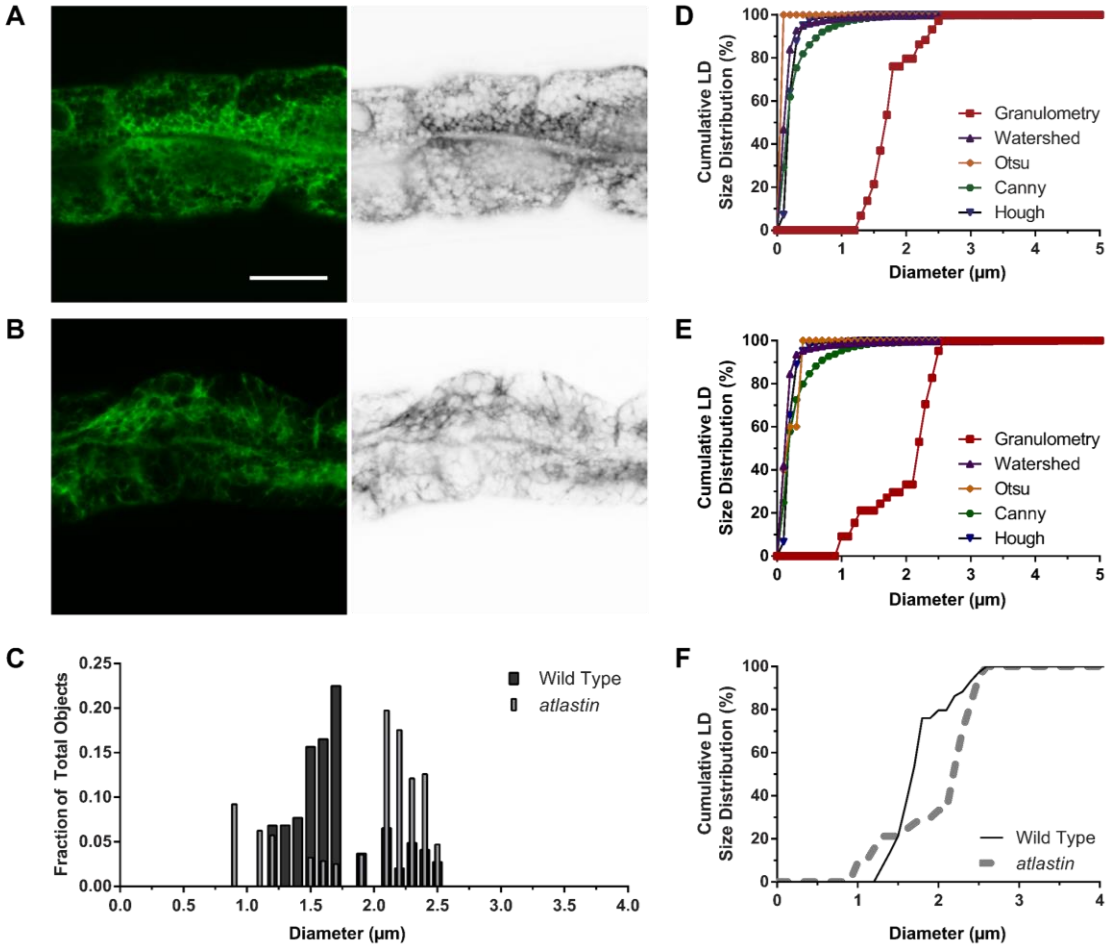

Figure 2-22. Granulometry can determine differences in porosity as seen with endoplasmic reticulum phenotype differences. A, B) Confocal (left) and inverted

color (right) image of the endoplasmic reticulum(ER) of the *C. elegans* for wild type (A) and atlastin (B), where the *atlastin* phenotype appears to have larger holes in the mesh compared to wild type, however it is difficult to use a singular metric to describe the two different phenotypes, and differentiate between them. (scale bar 10 μm) C) Granulometry output of the ER mesh for wild type and *atlastin* shows that the algorithm is able to detect textural differences, which allow for a quantitative way to determine the difference between the two phenotypes. The wild type animal appears to have a more organized ER mesh with smaller holes, thus the granulometry classified more small pores as compared to the *atlastin* mutant which had a larger, less organized mesh, which is depicted as larger potential pores. D-F) The resulting cumulative distribution plots for the various segmentation methods were used to analyze the ER mesh, however because it is a texture, there is no defining geometric feature to optimize to. F) Using the same parameters as before, granulometry is the only method that can analyze the mesh and give semi-quantitative porosity sizes, and a defining difference can be seen between the wild type distribution and the mutant distribution, where the wild type has smaller organized structures thus the distribution is shifted left, and the mutant structures are larger, and thus the distribution is shifted right. (All images at same scale, Scale bar = 20 μm)

2.4 Conclusions

We described a parameter-free algorithm for unbiased quantification of objects and textural differences in morphological phenotypes in the timescale of seconds. This algorithm, based on granulometry, enabled rapid semi-quantitative analysis of densely packed objects and characterization of irregular pore structures that lack prior quantitative representation. We demonstrated that our granulometry based method is capable of charactering object size and percentile quantity in synthetic and real images. Our method is capable of estimating the size differences of a large number of highly dense objects. We also demonstrated that this technology can be applied to determine differences in *C. elegans* lipid droplets which previously have been shown to have size distributions ranging from 0.5 μm to 7 μm within both wild-type and mutant populations[45,164]. This method is broadly applicable and suitable for use with images from any microscope showing densely packed objects, such as *C. elegans* strain with stained or fluorescently labeled lipid

droplets. We demonstrated that lipid droplet size distributions computed through our algorithm are comparable to results from manually measured values from previous works. We also showed that the throughput to phenotype an animal increased by over two orders of magnitude from hours to seconds. This approach yielded substantial benefits in animal throughput and experiment duration, enabling the first real-time automated genetic screen of lipid droplets in *C. elegans* resulting in the recovery of a lipid droplet mutant (*a211*). Additionally, we demonstrated the capability to perform genetic screens on low fidelity images, circumventing the need for expensive confocal microscopy systems which not all laboratories have easy accessible to.

Using this method, we delivered a technological means to quickly characterize images densely packed with objects for real-time analysis. Compared with other image processing techniques, the results using our algorithm demonstrated an enabling improvement in the detection of unknown structures. Our method does not require *a priori* knowledge of the structures or parameter optimization for detection allowing for animals to be phenotyped quickly. These advantages are well suited to detect mutations during screens when higher throughput characterization can allow for a greater number of animals to be analyzed, potentially finding more mutations than previously possible. Our software is flexible and easily modified to characterize objects of various sizes and shapes, making our algorithm applicable to other biological systems or processes. In addition to biological structures, this algorithm can be applied to non-biological applications such as particles, crystals, and mesh characterization. Beyond *C. elegans*, we envision that our algorithm can potentially be applied to the phenotypic profiling of other biological structures in model organisms such as *Drosophila melanogaster*, *Danio rerio*, and *Arabidopsis thaliana*.

CHAPTER 3. AN INTEGRATIVE HIGH-CONTENT APPROACH TO IDENTIFY DIETS THAT CAUSE LIPID DROPLET PHENOTYPE CHANGES IN *C. ELEGANS*

The following work in this chapter was performed in collaboration with Dr. Ho Yi Mak's laboratory at Stower's Institute for Medical Research and the Hong Kong University of Science and Technology, China.

3.1 Introduction and Motivation

Food storage, intake, digestion, and the metabolism are fundamental processes to life that translate between humans and many model systems. However, the complexity of higher order organisms and their diets create a challenge in studying the genetic origin and the effects of individual metabolites on fat storage. *C. elegans* is an ideal model to explore the effects of diet on fat storage because the majority of fat is stored in lipid droplets throughout the intestine, and many components that relate to human metabolisms are conserved[3,72,163,179]. These components include similar nutritional requirements such as essential amino acids and vitamins, as well as major mechanisms that regulate lipid uptake, transport and storage[7,179–182]. Additionally, homologous pathways that regulate energy include peroxisomal β-oxidation and the breakdown mechanism of the fatty acid propionate[7,179–182]. In nature, *C. elegans* reside in rotting fruits that provide varied diets, whereas, in the laboratory setting, the diet of *C. elegans* is composed of only *E. coli.* Since both *C. elegans* and *E. coli* are both genetically tractable, analysis of this bacterial-host

interaction can be used to identify nutrients and metabolites that contribute to fat storage changes.

Determining how changes in diet contribute to different lipid droplet morphologies provides insight to fat storage. With thousands of available clones, the K12 *E. coli* Keio Knockout Collection provides a further means to systematically test the effect of varying diet. A streamlined method to feed the *C. elegans* the various knockouts from the *E. coli* library can help determine the metabolites that cause changes in *C. elegans* lipid droplet distribution. Previously, Zhang, *et al.* has showed that the vaccenic acid difference in two different types of *E. coli* fed to worms, OP50 and HB101, contributed to changes in lipid droplet size[183]. Watson, *et al.*, fed the *E. coli.* Keio Knockout Collection to *C. elegans* to determine dietary effects on life history traits[180], and Khannan, *et al*., used this library to determine *E. coli* deletion mutants that enhanced dauer formation in *C. elegans*[184]. A complimentary addition to these studies would be to determine the effect of this same library on the lipid droplet phenotypes.

Due to the small diameter of lipid droplets (1 μm size range)[73], changes in phenotype are difficult to observe using conventional dissecting microscopes. Therefore, to efficiently quantify fat storage changes through variations in lipid droplet size distributions, high magnification microscopy is necessary. Quantification of the phenotype also requires for immobilization of the animals to properly image the structures. Because of the large amount of dietary conditions to test, the imaging process must be conducted in a high-throughput manner. These issues create a great challenge because to perform this dietary screen immobilization of each animal, and analysis of many animals for each condition

must be accomplished to qualitatively determine subtle differences in lipid droplet morphology at the population level.

To address these needs, we proposed an integrative approach that can image and quantitatively assess the differences in lipid droplet phenotypes. To increase imaging throughput and allow for precise position of immobilized worms, we utilized a microfluidic array device that passively load worms[55]. To characterize the lipid droplet phenotypes, we applied the modified granulometry algorithm developed in Chapter 2. Next, to best differentiate among different populations, we calculated various biologically relevant metrics from these distributions. This provided high-content information about the quantitative differences in lipid droplet phenotypes produced by changes in diet. The ability to easily handle, image, and quantify the lipid droplet phenotypes while using high magnification microscopy in a reduced time frame can greatly increase the knowledge available on fat storage in *C. elegans* and can potentially be applied to higher level organisms in further studies.

3.2 Methods and Materials

3.2.1 C. elegans strains and culture

All *C. elegans* strains were cultured at 20^{o}C on nematode growth medium (NGM) agar plates seeded with OP50 *E. coli* for general culture using standard methods[9]. Mutant strain used for all imaging was *dhs-28;hjSi224* [vha-6p::*dhs-3a* cDNA::GFP-TEV-3xFLAG::let-858 3' UTR] which has larger lipid droplets than wild type strain when grown on the *E. coli* knockout library to facilitate image analysis and lipid droplet diameter quantification. This strain was created by crossing VS8 *dhs-28*(hj8)X from the CGC with

hjSi224[*vha-6p*::*dhs- 3a* cDNA::GFP-TEV- 3xFLAG::let-858 3'UTR] provided by Ho Yi Mak, using standard procedures. The crossing result was confirmed by sequencing through Eurofins MWG Operon, LLC using standard procedures. This worm strain (*dhs-28;hjSi224*) was fed on the various *E. coli* knockouts by seeding different plates with dried *E. coli* with ~150-200 eggs from an age-synchronized population of *dhs-28;*hjSi224 through bleaching. Worm populations for imaging were then cultured at 20^{o}C for 60 hours until reaching the L4 stage and then imaged by washing with M9 for introduction into the microfluidic device.

3.2.2 dhs-28 mutation facilitates lipid droplet size analysis

The worm strain used for all the experiments was chosen to be *dhs-28;hjSi224* instead of the wild type strain to facilitate lipid droplet size measurements. When wild type worms are fed the control strain from the Keio Library, the starting size for droplets is already very small (<1 μm), which creates a much harder problem to see when the effect from the clones is a smaller lipid droplet phenotype. To circumvent this, we imaged worms with the *dhs-28* mutation, which causes accumulation of fat, and thus larger lipid droplets to form, due to the mutation in the second to last step for fatty acid catabolism in the peroxisomal β-oxidation pathway. In starting with a larger lipid droplet size, changes in both larger and smaller lipid droplet size can be quantified more accurately and easier.

3.2.3 E. coli strains and culture

E. coli OP50 used for worm culture was obtained from the CGC. The Keio *E. coli* deletion collection clones were provided by Ho Yi Mak, and stored at -80^{o}C. This library contains a single-gene deletion of 3,985 of 4,309 genes, which are all nonessential, in *E.*

coli K-12 strain BW25113[83]. The clones were grown in 2x YT media (Appendix C, C.1) containing 50 µg/ml kanamycin in sterile 15 mL test tubes by filling to 3 mL of media. A sterile pipette tip was used to scrape the frozen cultures from the 96 well plate, and the pipette tip was placed in the media during culture. The cultures were slightly angled in a test tube rack in a shaker incubator with 250RPM at 37°C for 16 hours for overnight culture. For plate seeding, 250 µl of this overnight culture was seeded on to 6 cm NGM agar plates and allowed to dry overnight. The control population of the Keio *E. coli* deletion collection is the parent strain without any deletions. This parent strain was transformed using standard protocol and cloning vector pBBR122 (Mo Bi Tec) to include kanamycin resistance which allows for growth of all strains in the same media. (Cloning vector pBBR122 provided by Lindsay Arnold and Rachel Chen). Plate 1 of the Keio collection was screened twice. When cultured, 8 strains from a single row were cultured with two replicates of the parent strain with kanamycin resistance.

3.2.4 Device Fabrication

Microfluidic devices were fabricated by soft lithography techniques using 1-layer SU-8 molds[176]. Briefly, conventional photolithography was used to create the pattern by spinning a 35 µm thick layer of SU-8 photoresist (Microchem, Newton, MA) on a 4-inch wafer, then exposing the resist to UV for curing through the mask of the pattern, and the unexposed SU-8 is removed through chemical development. The master mold is then treated overnight with silane vapor ((tridecafluoro-1,1,2,2-tetrahydrooctyl)-1-trichlorosilane; United Chemical Technologies) to promote simple release of the polydimethylsiloxane (PDMS) (Dow Corning Sylgard 184, Midland, MI) during molding. To obtain devices with a thickness of ~1mm, a thin mixture of PDMS (20:1 base:cross-

linker weight ratio) was degassed and poured over the mold and allowed to cure for 20 minutes at 75^{o}C, and then a second mixture (10:1 base:cross-linker weight ratio) of ~5mm thick was poured over the previously semi-cured mixture for mechanical integrity and placed at 75^{o}C overnight. The various chips were then cut with a scalpel and the access holes were punched with 20-gauge needles (McMaster-Carr, Elmhurst, IL) at the inlet and outlet. The PDMS was then bonded to glass cover slips using plasma-activation for 30 seconds.

3.2.5 Microfluidic device operation and imaging

For each experiment, the devices were prepared as stated in Lee, *et al*[55]. Briefly, devices are slightly pressurized with M9 to removed air bubbles. Then, previously synchronized L4 animals are washed from the NGM plates with M9 solution, and aspirated into a 3 mL syringe (Becton, Dickinson and Company). The syringe is placed vertically with the tubing closest to the bottom to allow for worms settle down the tubing, and a syringe pump is flowed in at 2.5-5 mL/hr. Once the devices had approximately 75% of the traps loaded the tubing from the syringe to the device is compression sealed, and the syringe is changed to a 200mM solution of tetramisole. The tubing is unclamped and the immobilizing solution is flowed in at 2.5-3.5 mL/hr for approximately 3-5 minutes. The tubing between the syringe and the devices is then clamped, the syringe is removed, and the device is placed on a microscopy stage holder.

For imaging all worms in the devices, a PerkinElmer UltraVIEW VoX spinning disk confocal (PerkinElmers, GT EBB Microscopy Core, Aaron Lifland) was used along with Volocity software, and a Hamamatsu FLASH 4 sCMOS version 2 spinning disk

detector. Using the ASI XY motorized stage, a scan image was taken of the whole device area using bright field with a 10x 0.3NA air objective by selecting the top left corner and bottom right corner to encompass the whole array, allowing the system to scan the entire span of the device. Without moving the position of the device, the objective turret was lowered and then switched to the 60x 1.49NA oil objective and the immersion oil was added to the objective. The objective turret is then raised to the bottom of the coverslip and focused using the bright field setting. Using the 10x scanned image to identify worms in the L4 stage, the stage is automatically moved using the Volocity software to the locations of the worms in the x,y, and z planes. The field of view was placed on intestinal cells 1, 2, and partially 3, where the end of pharyngeal bulb is used as a reference for the beginning of intestine. Approximately 50-75 worms are selected for each device using the Volocity software, and once all of the worms have been selected, the imaging system automatically captures a z-stack of 33 slices at 0.25 µm step size using the 488 nm laser, and a bright field reference image is taken at the middle plane for each worm.

3.2.6 Streamlined experimental process from E. coli culture to C. elegans imaging

The process begins by synchronously growing one column of 8 different *E. coli* deletion mutants from the library overnight in liquid culture, in addition to the control strain with kanamycin resistance, to culture the various strains in the same media. The various *E. coli* populations are then seeded to 5 plates each and allowed to dry overnight. Then, while the *E. coli* clones are grown, a large mixed population of *C. elegans* is cultured, and then bleached once the *E. coli* plates are dry, and an equal number of eggs (~200) are seeded on each plate. The worms are cultured for 60 hours at 20ºC until they are in the L4 stage. These steps are continuously repeated for 12 different days to complete the 96 well plate.

While the worms and *E. coli* are cultured, and once the first population of *C. elegans* reaches the L4 stage, imaging is also conducted.

For imaging, worms fed one condition are loaded into a microfluidic device using a syringe. Then, a bright field reference image at 10x is captured of the whole device to facilitate locating worms using a PerkenElmers UltraView Vox Spinning Disk Confocal microscope. Next, the magnification is changed to 60x and the region to each worm to image is manually selected for approximately 50-70 worms, and this step takes approximately 12 seconds per worm. Next, using the built in software, a z-stack of each worm is captured automatically. During the imaging, the next microfluidic device is loaded with the next set of worms fed a different knockout. These steps are repeated 10 times per day, where the control is imaged both at the start and end of imaging in addition to the 8 knockouts in the column grown.

3.2.7 Dietary supplementation of metabolites

To perform the supplementation experiments, the *E. coli* and *C. elegans* were cultured as stated before, however, before seeding the *E. coli* on the NGM plates, metabolites were added before pouring the plates. For the propionic acid experiments either 1, 20, or 40 mM were added, and for the vitamin B_{12} experiments 8×10^{-7}, or 6.4×10^{-6} mM were added. Plates were allowed to dry overnight, and *C. elegans* eggs were seeded on the plate and allowed to grow for 60 hours at 20^{o}C before imaging. Imaging was conducted with the same procedure as previously described and the comparison was performed between the knockouts and the control with supplemented metabolites, and those without.

3.2.8 Lipid droplet diameter distribution quantification and analysis

Quantification of lipid droplets were performed using the procedure stated in Chapter 2. Briefly, the z-stacks for each worm are captured, a maximum intensity image is calculated, and then pre-processed using smoothing and contrast adjustment. Then the image undergoes the granulometry algorithm which is composed of a series of morphological openings and closings with increasing sized disk structuring elements. The output is a distribution based on the diameters of the lipid droplets in the image. To obtain a population distribution, the distributions for each worm are summed by computing the average of each bin in the distribution throughout the population.

3.2.9 Statistical analysis for population comparisons

All statistical comparisons were performed between one population that was fed a clone, and another population that was fed the control vector. Statistics were calculated using Kruskal-Wallis comparison's test and Dunn's correction for multiple comparisons. The Kruskal-Wallis comparisons test is the nonparametric analysis analogous to ANOVA. The mean ranks of each population fed different foods were independently compared to the mean rank of each control. Two controls were imaged for each imaging day, with one as the first set, and the second as the last set. All statistical tests were performed on GraphPad Prism version 6.02.

3.2.10 E. coli knockout verification using PCR and sequencing

We verified the following clones in the Keio Knockout Collection were the correct gene and not cross contaminate: *btuR, prpC, prpR, tonB*. Locus-specific upstream and

downstream primers for the 4 genes were obtained from a supplemental table in Baba, et al., and truncated to the first 40 base pairs for purchase from Eurofins MWG Operon, LLC. PCR reactions were carried out in 250 µL micro-centrifuge tubes. Each clone was independently streaked to an LB medium agar plates with kanamycin from the frozen stock and incubated overnight at 37^{o}C. Using a pipette tip, an isolated colony was selected from each gene, and cultured in LB medium for overnight hours at 37^{o}C without shaking. For a 50 µL reaction, 1 µL of the *E. coli* liquid culture was used along with 25 µL of OneTaq 2x Master Mix polymerase, 1 µL of each of the 10 µM concentration primers, and 22 µL of deionized water. Reactions were run for with a start of 95^{o}C for 30 seconds and then followed by 30 cycles of 95^{o}C for 30 seconds, 60^{o}C for 45 seconds, and 68^{o}C for 1 min, plus 68^{o}C for 5 min. PCR products were analyzed by 1.5% agarose gel electrophoresis using 0.5 x Tris-acetate buffer. The 4 genes, *btuR, tonB, prpC¸and prpR*, along with the empty vector were analysed. Bands for the empty vector were ~400bp smaller than that of each knockout, which indicates that the knockouts have the kanamycin cassette in the correct location. The PCR products for each knockout strain were also sequenced, and the presence of the kanamycin cassette in the correct location was confirmed. More details on the confirmation of the genotype of the knockout strains investigated is available in Appendix C.3.

3.3 Results and Discussion

To study dietary effect on fat storage, we need to quickly and efficiently image a large number of animals fed various foods since metabolism is sensitive to day-to-day variability. We performed a pilot dietary screen as a proof of concept integrating the methods of microfluidics[55], and lipid droplet size analysis algorithm from Chapter 2. We

imaged and analyzed lipid droplets in worms as a means to determine the phenotype exhibited due to the changes in diet. The process to culture various *E. coli* strains to provide varied diet to the animals, and then image the various conditions with above 50 worms per condition is non-trivial. Additionally, changes in lipid droplet size distribution are not necessarily easily distinguishable by only one defining metric, such as the mean, therefore more metrics must be computed and compared to determine lipid variation due to diet changes.

3.3.1 Parallel imaging and culture process for bacterial diet pilot screen

To overcome the throughput challenge, we optimized a process where the timing of each step is precisely calculated, and various steps were nested and performed in parallel in order to increase productivity and the number of conditions possible to image in each day (Figure 3-1). The diet variation was accomplished by feeding the first plate of the Keio *E. coli* Consortium Library, which contains 96 deletion mutants of the protein-coding genes. High magnification imaging of lipid droplets is necessary to quantify subtle changes in phenotypes; however, the field of view does not permit for many worms to be imaged simultaneously, thus single worms are selected for each image. Imaging of a whole plate is accomplished in 12 days of imaging. In total, including both the loading of the devices and the imaging, the time per day is approximately 4.5 hours, per column. A total of approximately 6,000 worms are imaged in the 12-day span for 96 different conditions. Using these steps, we can successfully image all of the conditions in a small timespan, assuring that conditions are as close as possible, greatly reducing the introduction of outside factors.

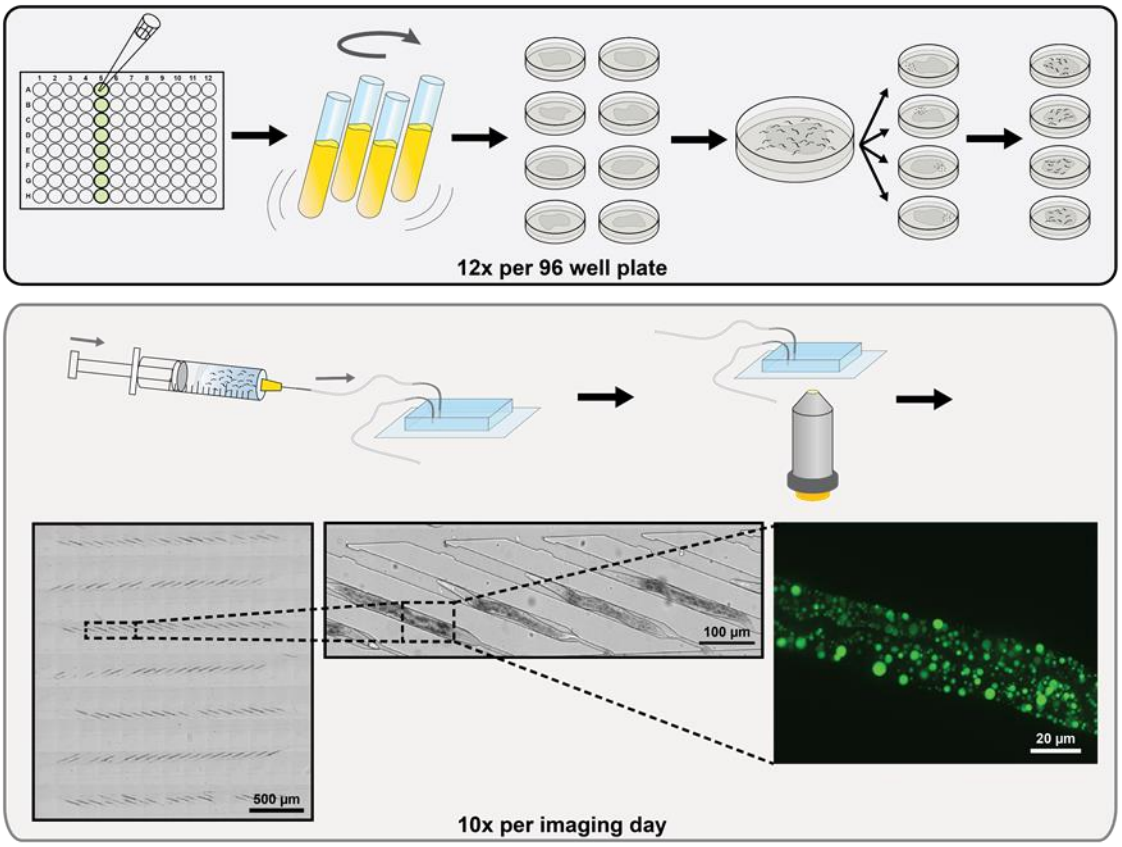

Figure 3-1. Imaging procedure for high throughput imaging of *E. coli* knockouts. There are various preparatory steps that must be accomplished in parallel. From one column, the *E. coli* are grown synchronously from the frozen 96 well cultures. NGM plates are seeded with *E. coli* knockouts and then a large *C. elegans* population of one strain is bleached and the plates are seeded with eggs that grow until L4 stage. These steps are repeated one time per day for 12 days in order to image the whole 96 well plate. Each knockout is then imaged in a worms array microfluidic device and a bright-field image is captured for easy worm location identification. Magnification was changed to 60x where the field of view is chosen by using Volocity and worms in the L4 stage are selected. Once all worms are selected, z-stacks are captured for each worm. Shown is a maximum projection of a sample z-stack image captured. While the z-stack images are being captured automatically through the Volocity software, the next set of worms are being flowed into the next microfluidic device. These steps are repeated 10 times per day to image all of the 8 clones in the column in addition to two controls.

3.3.2 Lipid droplet phenotype analysis due to diet changes

To determine the lipid droplet phenotypes of the various conditions, we developed a system for data analysis where the quantification of phenotypic differences for the population level are calculated. For the first part of the analysis, we previously developed a method to efficiently analyze lipid droplets in *C. elegans*, as discussed in Chapter 2. Due to inherent worm heterogeneity in distributions, a population distribution is calculated to compare phenotypes by obtaining the average of each population (Figure 3-2A).

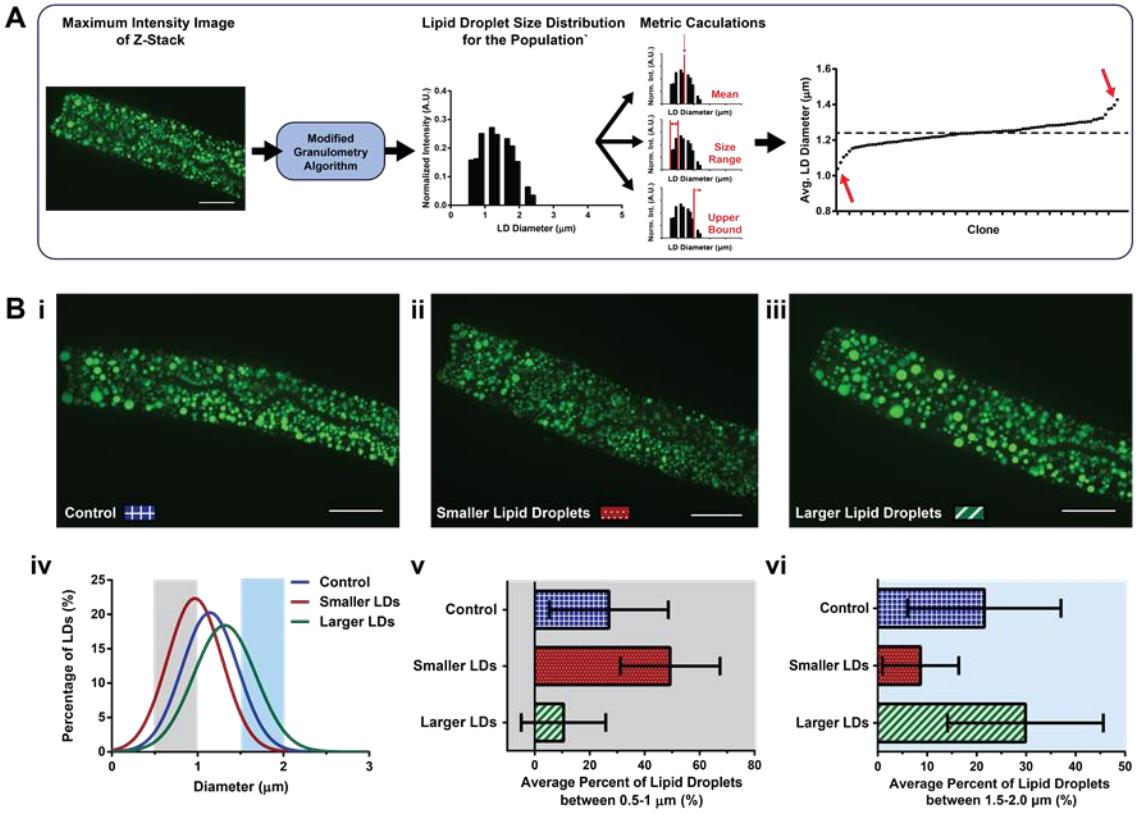

Figure 3-2. Flow chart for image analysis. A) Shows the overall analysis method to quantify lipid droplet size distributions between populations. Z-stacks are captured where 33 slices are captured at an 8 μm depth with 0.25 μm step size. These z-stacks are then flattened using the maximum projection of the image. The maximum intensity image is analyzed using a granulometry algorithm where the lipid droplet

diameter distribution is calculated. From the population average lipid droplet size distribution, 50 different features are calculated that describe the distribution including mean, and percentage of lipid droplets in various size ranges. These features are calculated for each diet condition as well as the control. A sample feature is plotted where the average lipid droplet diameter for each population is calculated by obtaining the average of the population distribution. All of the average sizes are plotted from least to greatest, where the solid line represents the average of the control, and the dotted lines represent 1 standard deviation away from the control. (Scale bar = 20 μm) B) i-iii show representative images of worms fed the control (i), a population with small lipid droplets (ii), and a population with larger lipid droplets (iii). iv) The lipid droplet size distributions were calculated using granulometry, and a Gaussian fit was applied. The gray shading indicates the data in (v), and the blue shading indicates the data in (vi). v) Shows one of the features calculated, the average percentage of lipid droplets between 0.5 to 1 μm, and how the phenotype with the smaller lipid droplets can be easily distinguished from the control and the phenotype with larger droplets easier than when comparing distributions in (iv). vi) Shows complimentary data to (v), where a different feature, the average percentage of lipid droplets between 1.5 to 2 μm is plotted, and the difference between the phenotype with larger lipid droplets can more easily be distinguished from the control and the phenotype with smaller lipid droplets. (Scale bar = 20 μm)

To determine if a diet has contributed to changes in lipid droplet phenotypes, lipid droplet size distribution at the population level must be quantitatively different between populations. In addition to the mean of the distribution, various metrics were calculated to determine differences between populations that include features such as the average percentage of lipid droplets in a certain size range. Figure 3-2B (i-iii) shows representative images of a worm fed various food conditions contributing to smaller lipid droplets (Figure 3-2B ii), or larger lipid droplets (Figure 3-2B iii) as compared to the control diet (Figure 3-2B i). The lipid droplet size distribution of each of these three populations have overlapping area (Figure 3-2B iv). Between the small lipid droplet curve and the control curve there is a 75% overlap in area, and between the large lipid droplet curve and the control curve there is an 79% overlap in area. These plots are depicting extreme cases;

therefore, this indicates that only determining differences based on the distribution and averages may mask other metrics that better differentiate the populations.

One metric that can quantitatively distinguish the three populations is the average percentage of lipid droplets that are between 0.5 and 1 μm in diameter. This size range is most emphasized when a population has predominantly small lipid droplets (Figure 3-2B v). Another feature that is complimentary to the previous metric is the average percentage of lipid droplets that are between 1.5 and 2.0 μm in diameter. When comparing this metric, the population with much larger lipid droplets is clearly visible (Figure 3-2B vi). Thus, quantifying the differences with these two metrics instead of the mean of the population helps better phenotype the population. In comparing the populations using these different metrics, it is possible to identify the populations to further investigate that deviate the most from the control (Figure 3-3). This process was repeated for the 96 conditions imaged, which were then compared to the control for the various measures (Appendix C.2).

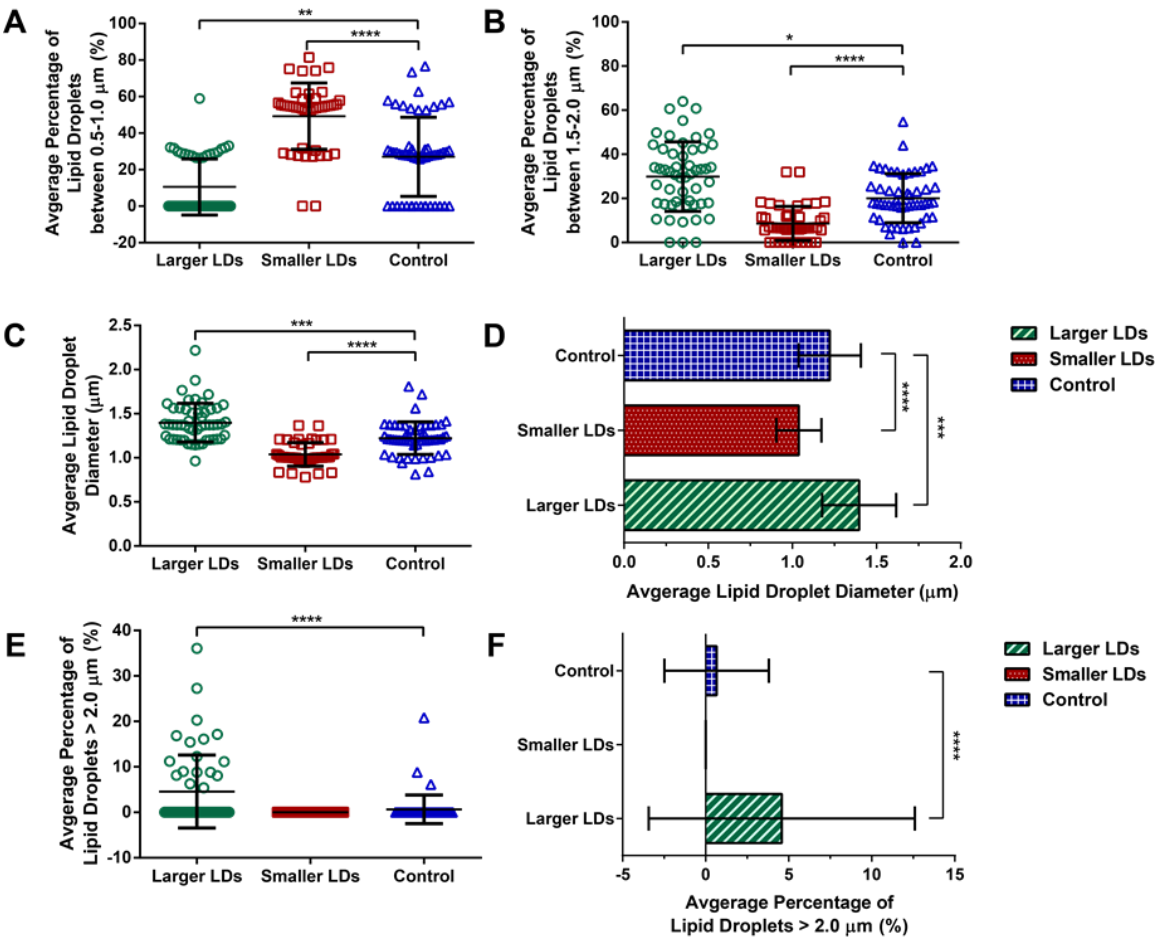

Figure 3-3. Lipid droplet phenotype characterization. A) Shows the average percentage of lipid droplets that are in the smaller range of 0.5 to 1.0 µm. This information is also in Figure 3-2B (v), however, here each individual symbol represents the value for one worm. The number of worms that have a higher percentage in this category also correspond with the phenotype that is characterized as smaller lipid droplets. B) Shows the average percentage of lipid droplets in the larger size regime of 1.5 to 2.0 µm. This mirrors the information in Figure 3-2B (vi), where each individual symbol represents one worm. The number of worms that have lipid droplets in this larger size range is much greater in the phenotype characterized as larger lipid droplets. Even though there is still overlap with the control, there is much less overlap with the smaller lipid droplet category, allowing for distinct differentiation between the two populations. C) Shows the average lipid droplet diameter, and this mirrors the information in Figure 3-2B (iv). In only looking at individual worms, each population has a great deal of overlap where worms from different populations have similar lipid droplet size ranges. D) Shows the same information from C, where only the mean is plotted. E) Shows an additional feature of the average percentage of droplets over 2 µm. Here, the distinction between the larger LD population and the other populations is most apparent. The smaller LD population although may have some overlap when

looking at only the mean, none of the worms had lipid droplets in this larger regime, making it possible to differentiate between the different populations. F) Shows the information in E, and how using this metric of the average percentage of lipid droplets over 2 μm can show the difference in population lipid droplet size distribution more clearly as compared to the mean lipid droplet size. (All comparisons made with respect to the control. n> 30, * significance at p<0.05, ** significance at p<0.01, * significance at p<0.001, **** significance at p<0.0001)**

To determine potential *E. coli* knockout clones from the 96 well plate that contribute to significant changes in lipid droplet morphology, we compared the lipid droplet distributions of populations fed different clones to the control diet for various features. Listing the resulting population mean lipid droplet diameter value for each diet from least to greatest shows that there are both clones above and below the mean diameter of the control diet (Figure 3-4A). Notably, as compared to the control diet, the clone that contributed to the smallest mean diameter showed a reduction of up to 16.3%, and the clone with the largest mean diameter showed an increase of up to 14.5% (Figure 3-4A). However, the majority of the populations lie along the same mean lipid droplet diameter as the control diet (Figure 3-4A). Therefore, only analyzing the mean diameter size of lipid droplets for a population can occlude other potential interesting clones.

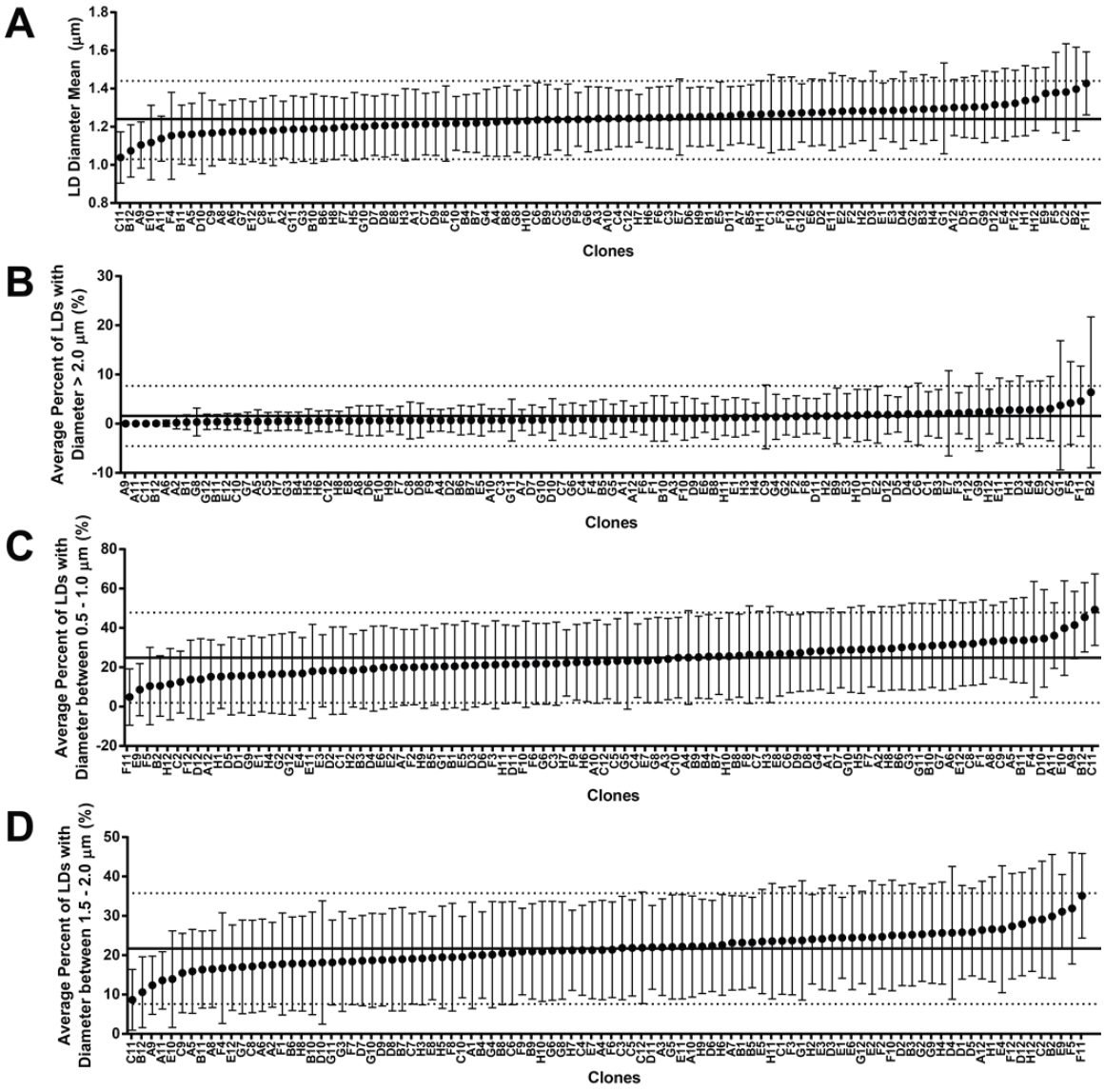

Figure 3-4. These graphs depict examples of the variation of various features throughout all the clone diets in the plate for one trial. The clones are ordered from least to greatest value for each feature, where the solid line represents the average value of the feature for all the controls, and the dotted line represents the standard deviation of said feature values for all of the controls. Bars represent the standard deviation. A) Shows the mean lipid droplet diameter size where the lowest clone was C11 and the highest clones were B2 and F11 indicating that these clones were the most significantly different to $p<0.05$ from the mean LD size as compared to the control. B) Shows the average percentage of droplets that have a diameter of greater than 2 µm for each population. There are clones that had 0% of lipid droplets in this size range (A11, C11, and A9), and clones that had a much great percentage of lipid droplets in this size range such as B2, as compared to the control. C) Shows the percentage of lipid droplets that are between 0.5 and 1 µm in diameter, where F11 had the least amount of droplets in this small size range indicating that many of the

lipid droplets in F11 are in a larger size window, whereas C11 was greater than the control by more than 1 standard deviation indicating that C11 has a higher percentage of the lipid droplets in a smaller size as compared to the control. D) Shows the average percentage of lipid droplets with diameters that are between 1.5 to 2 µm in diameter, where C11 had the smallest percentage of lipid droplets in this size range, as compared to F11 which had the largest percentage of lipid droplets as compared to the control. In comparing these various features, it can be suggested that C11 has many lipid droplets in the smaller size (0.5-1 µm) range and much less in the larger size range (1.5-2 µm), as compared to F11 which is the opposite. These two clones are examples of potentially interesting hits due to their distance from the control mean in various features.

Metrics that can be concealed by the mean include changes in the proportion of lipid droplets on the larger or smaller tails of the distribution, as compared to the control. For instance, the proportion of larger lipid droplets in a population may not be substantial enough to skew the mean size; therefore, we also analyzed values beyond measure of central tendency. To achieve a more thorough phenotypic profile of a population, we also calculated the average percentage of lipid droplets that have a diameter above 2 µm. Typically, the control has approximately 1.6% of the lipid droplets analyzed in this larger size range. In comparing the effect of the 96 clones, there are populations that had no lipid droplets (0%) in this size range (A11, C11, A9), as well as populations that had more than 4 times the percentage of larger droplets, such as worms fed clone B2 from plate 1 (Figure 3-4B). This metric is biologically relevant because it leads to the hypothesis that worms fed clones that increase the proportion of larger lipid droplets may not be able to properly breakdown all of the fat in the diet affected by the *E. coli* mutation.

We also explored features that determine the percentage of lipid droplets within a specified size range, between 0.5 and 1.0 µm, that correlates with an abundance of smaller lipid droplets (Figure 3-4C) and, between 1.5 – 2.0 µm, that correlates with an abundance of larger lipid droplets (Figure 3-4D). The distributions for these two size ranges were

complimentary. Clones that contributed to phenotypes with a much greater amount of smaller lipid droplets, typically had the least amount of large lipid droplets, and vice versa. This indicates that the populations imaged did not have a bimodal distribution in the lipid droplet sizes, exhibiting phenotypes with more continuous size ranges of lipid droplets.

We note that when comparing all of the clones to the mean of the control for the various metrics the majority of the clones on the plate have mutations that very minimally affect the metabolism of the worm. The results are consistent with the notion that a majority of mutations in *E. coli* did not cause a change in the lipid droplet size distribution in *C. elegans.* Although the majority of the clones do not contribute to a lipid droplet size change that drives the value beyond the standard deviation of the control, there are potentially interesting conclusions that can be drawn from the few clones that do cause substantial changes in the lipid droplet size that will be discussed in Section 3.3.4 and 3.3.5.

3.3.3 Reproducibility of the integrative approach

To determine the clones that can cause significant changes in lipid droplet size, we first must analyze whether the changes in lipid droplet morphology are reproducible. Because all of the imaging cannot be performed in one day and lipid droplet morphologies are heterogeneous, this is an important aspect of our approach. We conducted a reproducibility test that demonstrates the powerful ability of our integrative approach to culture, image, and analyze the lipid droplet phenotypes from different days. To accomplish this analysis, two independent trials of the pilot screen for plate 1 of the Keio *E. coli* Consortium library were fed to the worms, 2 months apart. The various features previously calculated per population were compared between the two trials.

Due to inherent variation, the control populations imaged will have a standard deviation for each feature. As shown in Figure 3-5A, reproducible populations of interest will be plotted beyond the region encompassing one standard deviation away from the mean control feature value. This increases the confidence that one has identified clones that contributes to a change in lipid droplet size and distribution.

As observed in Figure 3-5B, C, and D, almost all clones fall in the region indicating that the dietary effect of the clone is reproducible. This suggests that the feature values calculated for the dietary effect of each clone demonstrate the underling lipid droplet phenotype of the population. Figure 3-5B shows the mean lipid droplet size for two trials, where majority of the clones that are within one standard deviation, but not all clones. In particular, there are a few clones that fall beyond one standard deviation away, on both the larger lipid droplet region (B2, F11), and smaller (C11) lipid droplet region.

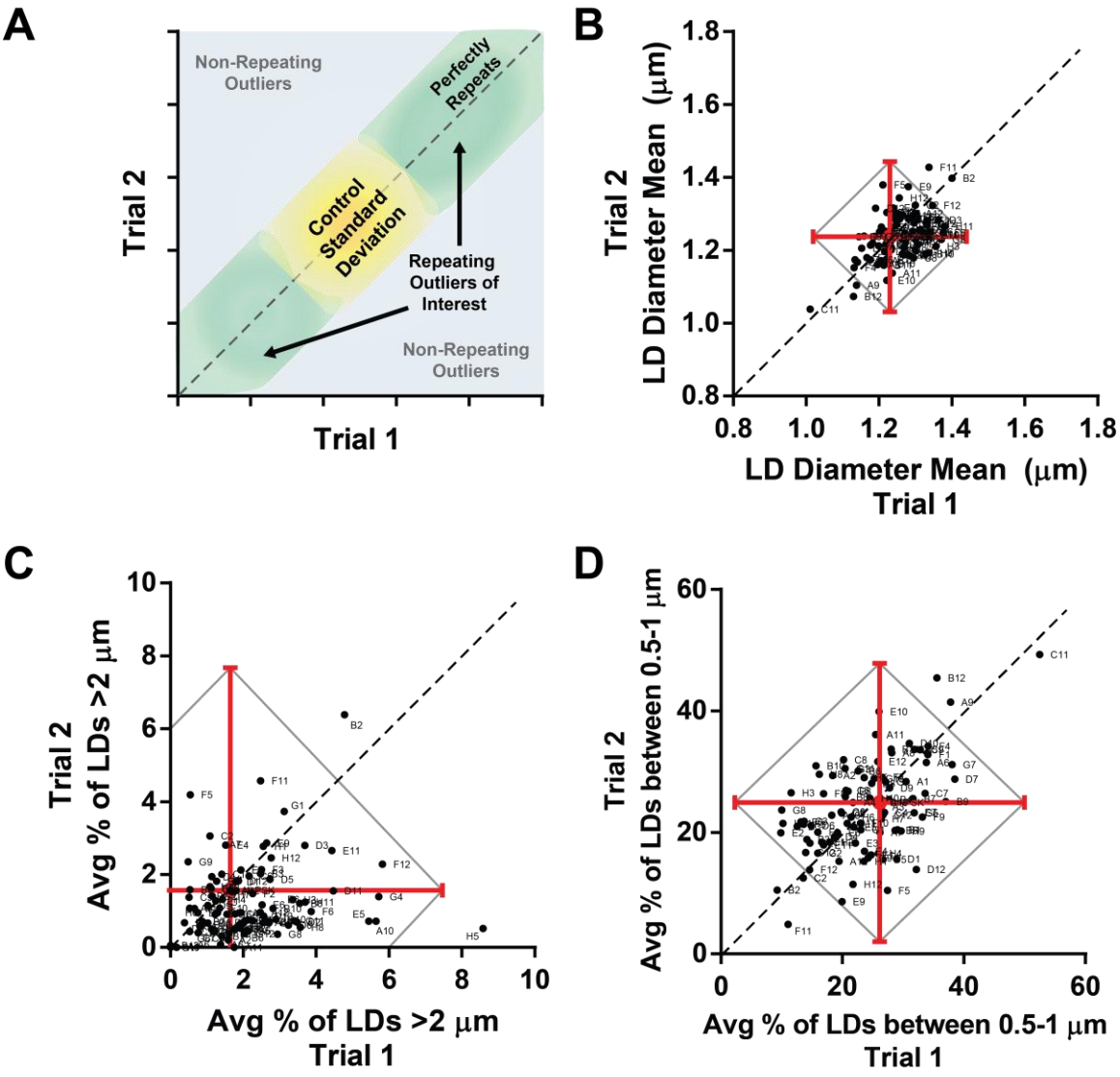

Figure 3-5. Analysis of reproducibility between trials. Due to the heterogeneity between worms as well as batch to batch variation in imaging, a reproducibility analysis was conducted. A) Shows how to interpret the various graphs for reproducibility. Alone the line y=x, it would be assumed that the two trials have perfectly repeated for each of the various features, as indicated by the dotted line. The yellow region signifies the average of the control for the feature plotted for each of the two trials, and size of the region is defined by the standard deviation away from the mean. The green regions signify clones that did repeat but lay outside of one standard deviation away from the mean of the control indicating a potentially interesting clone. The blue background region signifies the area that will contain clones that did not repeat and had a high value for one trial and a low value for another trial. For the subsequent graphs, each dot represents the value for each of

the populations fed a different clone for each of the two trials. B) Shows the means of the clones in the 96 well plate as well as the control mean at the center of the red cross and one standard deviation from the control mean as shown by the black circle. The majority of the clones are within the circle, however there are 3 clones (C11, B2, F11) outside of this range that lie along the line indicating that they have appeared beyond the value of the control for multiple trials with similar values. C) shows each individual clone where the value of the average percentage of lipid droplets over 2 µm per population have been plotted. There is one clone, B2, that is farthest from the majority of the clones along the circle indicating one standard deviation away from the control. D) shows the average percentage of lipid droplets with a diameter between 0.5-1 µm per population, where there are two clones (C11, F11) with populations outside of one standard deviation of the control value for this feature.

Repeating this analysis with the average percentage of lipid droplets over 2 µm in diameter, shows only an upper bound. Because the majority of the clones, along with the control, have close to 0% of lipid droplets in this range (Figure 3-5C), most clones do not show a different phenotype pertaining to changes in the proportion of larger lipid droplets. The dietary effect of clone B2, however, repeatedly shows that larger lipid droplets are present due to the percentage of lipid droplets over 2 µm in diameter that is considerably larger than the control. This is also apparent when analyzing the percentage of smaller lipid droplet in the range of 0.5 to 1.0 µm, where B2 is also observed to have much less lipid droplet phenotype in this smaller range as compared to the control (Figure 3-5D). Additionally, a clone that has consistently caused a change in lipid droplet sizes is C11, which displays a decrease in lipid droplet size. In analyzing both the mean lipid droplet size, and the percentage of lipid droplets in the range of 0.5 to 1 µm of the population, C11 has fallen beyond the standard deviation of the control, indicating a smaller lipid droplet phenotype.

3.3.4 Clones identified that alter lipid droplet size

To verify the validity of the phenotypic differences due to various clones, analysis on lipid droplet size variation was performed on single day results. Because of the heterogeneity of the lipid droplets in the worm and inherent biological variation, comparison to the population fed the control of the same day allows for the most robust comparison. This comparison does not add an increase in variation due to day to day batch variability. In comparing the populations that were fed the clones from column 2 of the 96 well plate, the average lipid droplet diameter shows a consistent trend among most strains as compared to both of the controls imaged, however, a few clones, including B2, do contribute to a statistically significant change in the average lipid droplet diameter (Figure 3-6A). These results are consistent, and even more apparent, when analyzing other metrics such as the percentage of lipid droplets in the 0.5 to 1 μm range (Figure 3-6B), and in the 1.5 to 2.0 range (Figure 3-6C), where B2 is the only statistically significant different clone when compared to the control for the single day of imaging. The trends on all three metrics agree in that the clone B2 contributes to a phenotype with a greater proportion of larger lipid droplets.

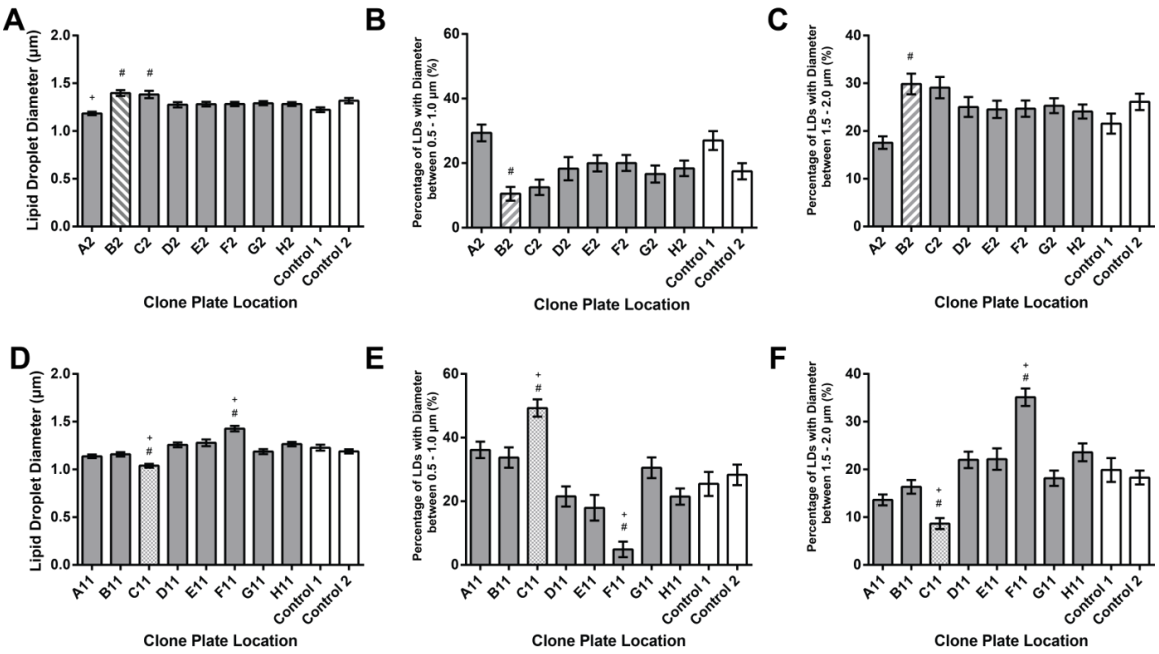

Figure 3-6. Comparisons of populations sets fed different *E. coli* clones that were imaged on the same day are compared through various metrics. Values plotted are mean ± SEM. + depicts statistically significant differences with $p < 0.01$ between the population fed said clone and the first control of the day, Control 1. # depicts statistically significant differences with $p < 0.01$ between the population fed said clone and the second control of the day, Control 2. For sample size, n>30 for each population. White bars indicate the population fed the control vector. Gray bars indicate the different populations fed clones from the same column in the plate. Hashed or spotted patterned bars signify the clones that will be further analyzed using a supplementation experiment. The hashed bars highlight the clone that resulted in a population with phenotypically larger lipid droplets, while the spotted patterned bars highlight the clone that resulted in a population with smaller lipid droplets, when comparing both to each control. A, B, C) shows comparison for the imaging of column 2 of Plate 1 of the Keio collection. D, E, F) show comparisons for the imaging of column 11 of Plate 1 of the Keio collection. A, D) Show the mean lipid droplet diameters for each population, B, E) show the percentage of lipid droplets that are within the size range with the smaller lipid droplets of 0.5 – 1.0 µm in diameter, and C, F) show the percentage of lipid droplets that are within the size range with the larger lipid droplets of 1.5 – 2.0 µm in diameter. Comparing the clones to each of the controls, populations B2, F11, and C11 are statistically significantly different for all different metrics. Clones B2 and F11 results in phenotypes with larger lipid droplets, whereas clone C11 results in smaller lipid droplets.

This analytical approach was applied to the populations fed clones from column 11 of the 96 well plate. Here, we show that both clones C11 and F11 cause drastic changes on lipid droplet size as compared to the control, in the opposing ways. In comparing the mean lipid droplet size, percentage of lipid droplets from 0.5 to 1 μm in diameter, and 1.5 to 2 μm in diameter, clone F11 is shown to contribute to a phenotype with a greater proportion of larger lipid droplets (Figure 3-6D, E, F). In analyzing these same metrics, clone C11 is shown to significantly decrease the lipid droplet size of the population (Figure 3-6D, E, F) by almost doubling the amount of smaller lipid droplets typically seen in the control. Because the controls were imaged on the same day, the statistical significant different in lipid morphology due to these diets is independent of day to day variability. This indicates the differences measured are valid, and the effects of some of these clones will be further analyzed. This analysis was also conducted for each of the columns imaged as shown in Appendix C.2, where the most significant differences were due to clones C11 and B2.

3.3.5 Metabolites contribute to changes in lipid droplet morphology tested through supplementation

To further test the clones that resulted in the most statistically significant difference in lipid droplet morphology, a supplementation experiment was conducted. The two clones of interested that were investigated are B2 and C11 from Plate 1, which cause an increase and decrease in lipid droplet size, respectively.

3.3.5.1 *tonB* diet causes a lack of vitamin B_{12}

For the clone B2, the gene affected is *btuR*. The gene *btuR* encodes for a protein that is involved in the synthesis of adenosylcobalamine from cob(II)yrinate a,c-diamide,

which has effects on the quantity of vitamin B_{12} produced. Therefore, to test the effect of lipid droplet changes, the diet was supplemented with vitamin B_{12}. In Watson, *et al*, the effect of vitamin B_{12} was also explored and an additional gene of *tonB* was tested as a gene involved in vitamin B_{12} synthesis[180]. Because *btuR* and *tonB* are both involved in this pathway, we further explored the effect of *tonB* on lipid droplets as well.

To supplement the diet, two different active forms of vitamin B_{12} were added independently to the agar plates at various concentrations. The two forms are adenosylcobalamin (Ado-Cbl), and methylcobalamin (Me-Cbl), where in the vitamin B_{12} synthesis pathway Ado-Cbl is converted into Me-Cbl[180]. Figure 3-7 shows representative images of worms fed the different clones: empty vector, *btuR*, *tonB*, with supplementation of Ado-Cbl at three different concentrations. Worms fed on the *tonB* diet without any added metabolite exhibited a dramatic difference in lipid droplet phenotype; however, when supplemented with Ado-Cbl, the lipid droplets appeared similar to the lipid droplets from the worms fed the empty vector.

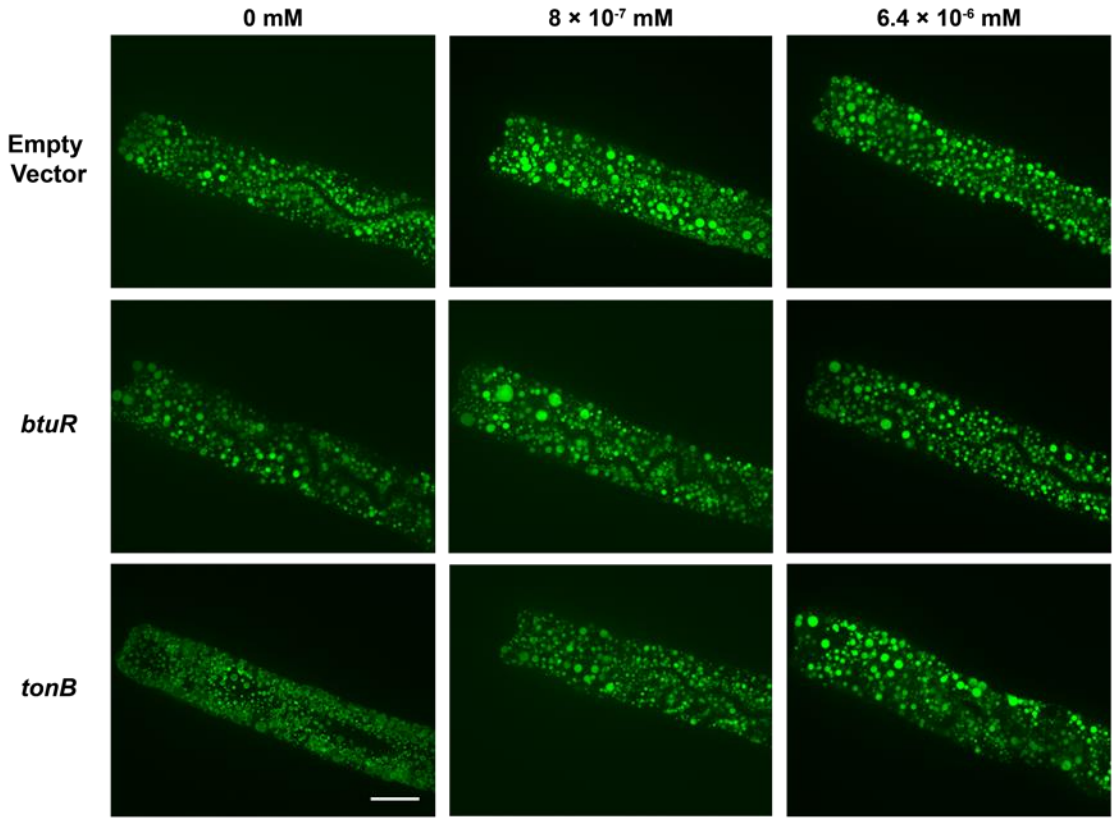

Figure 3-7. Representative images of lipid droplets in worms fed on plates supplemented with Ado-Cbl. Different concentrations of Ado-Cbl were added in addition to feeding the worms the empty vector diet, the *btuR* diet which corresponds with the previously identified B2, and the *tonB* diet, which also corresponds with synthesis of vitamin B_{12} similar to that of *btuR*. (All images at the same scale. Scale bar = 20 µm)

Two different trials were completed where the worm diet was supplemented with Ado-Cbl, and each time similar results were obtained (Figure 3-8). The mean lipid droplet diameter for worms fed on the *tonB* diet were significantly reduced; however, when supplemented with either 8×10^{-7} mM (Appendix C.4) or 6.4×10^{-6} mM of Ado-Cbl (Figure 3-8A, D), there was no significant difference from the lipid droplets for worms fed the empty vector. While the *btuR* diet still contributed to a significantly larger lipid droplet size as compared to the empty vector diet, the addition of Ado-Cbl to the *btuR* or empty vector

diet, did not contribute to a significant difference in lipid droplet mean size in the worms (Figure 3-8 A, D). Two additional features were calculated where the phenotype difference of worms fed *tonB* was even more apparent. When comparing the percentage of lipid droplets in the size range corresponding to smaller lipid droplets between 0.5 to 1.0 μm, the *tonB* diet contributed to an almost 4-fold change in the amount of lipid droplets present from 0.5 to 1.0 μm in diameter (Figure 3-8 B, E). As a compliment to this feature, the percentage of lipid droplets in the size range of 1.5 to 2.0 μm, which corresponds to larger lipid droplets, was significantly reduced in the *tonB* diet as compared to worms fed the empty vector or *btuR* (Figure 3-8 C, F). The addition of Ado-Cbl to the *tonB* diet contributed to a more than 10-fold change in the percentage of larger lipid droplets from 1.5 to 2.0 μm. This reduction in size was reversed when the *tonB* diet was supplemented with Ado-Cbl (Figure 3-8 C, F); however, as compared to the worms fed the empty vector and *btuR*, the percentage of lipid droplets in this larger size range was still reduced.

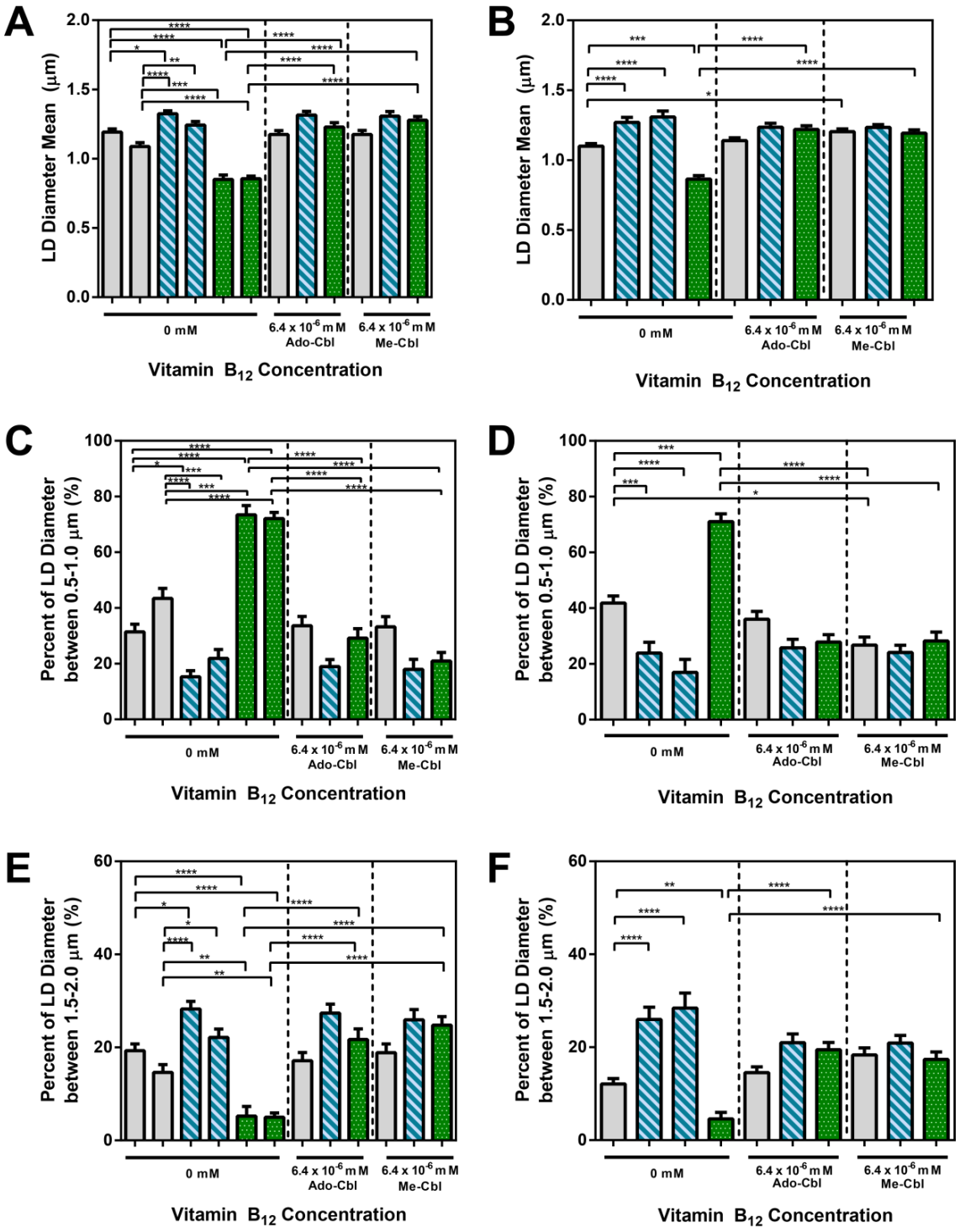

Figure 3-8. Results of two repeated experiments with supplemental metabolite enrichment of Ado-Cbl and Me-Cbl, where the *E. coli* was cultured from individual colonies that were confirmed to have the knockout present through sequencing. A, D) Two different trials showing the mean lipid droplet size for a population fed the various conditions, where the population fed *tonB* with no supplement had a

decreased lipid droplet size. When the plates is supplemented with either 6.4 x 10^{-6} mM Ado-Cbl or 6.4 x 10^{-6} mM Me-Cbl, the population fed *tonB* has lipid droplets where the mean increases substantially, reaching similar size as the worms fed the empty vector without supplementation. In comparing the population fed *btuR*, without supplementation, the mean lipid droplet diameter is significantly larger as compared to the population fed the empty vector without supplementation. B, E) Two different trials showing the average percentage of lipid droplets between 0.5 – 1.0 µm for a population fed the various conditions. Worms fed *tonB* have a significant increase in the amount of lipid droplets in this smaller size range as compared to the worms fed the empty vector. With the addition of metabolites, the percentage of smaller lipid droplets decrease to levels similar to the empty vector without supplementation. In comparing worms fed *btuR*, there is a significant decrease in the average percentage of lipid droplets between 0.5 – 1 µm when compared to the worm population fed the empty vector without supplementation. C, F) Two different trials showing the average percentage of lipid droplets between 1.5 – 2.0 µm for a population fed the various conditions. Worms fed *tonB* have a significant decrease in the percentage of lipid droplets in this larger size range, which compliments the results in B, E where the majority of the lipid droplets are in a smaller size range. Worms fed *btuR* have a significant increase in the average percentage of lipid droplet sizes between 1.5 and 2.0 µm when compared to the population fed the empty vector without supplementation. When the plates are supplemented with Ado-Cbl or Me-Cbl, the percentage of LDs in this larger size range approximates that of the worms fed the empty vector. It can be inferred that the knockout *tonB* results in a diet deficient in vitamin B_{12} form of Ado-Cbl or Me-Cbl, and thus supplementation at the 6.4 x 10^{-6} mM level returns lipid droplet size and morphology to that of the empty vector which does not have this deficiency. (n> 30, * significance at p<0.05, ** significance at p<0.01, * significance at p<0.001, **** significance at p<0.0001).**

When comparing within each diet, only *tonB* had a significant change in lipid droplet mean when comparing the two different trials of feeding a population *tonB* with the added metabolite Ado-Cbl (Figure 3-9 A, D). For the smaller size range of 0.5 to 1.0 µm, the percentage of lipid droplets is greatly reduced only in the worms fed the *tonB* diet as compared to the non-supplemented diet (Figure 3-9 B, E). Similarly, for the larger size range of 1.5 to 2.0 µm, adding the metabolite to the *tonB* diet significantly increased the percentage of lipid droplets in this size range as compared to no addition of supplement (Figure 3-9 C, F).

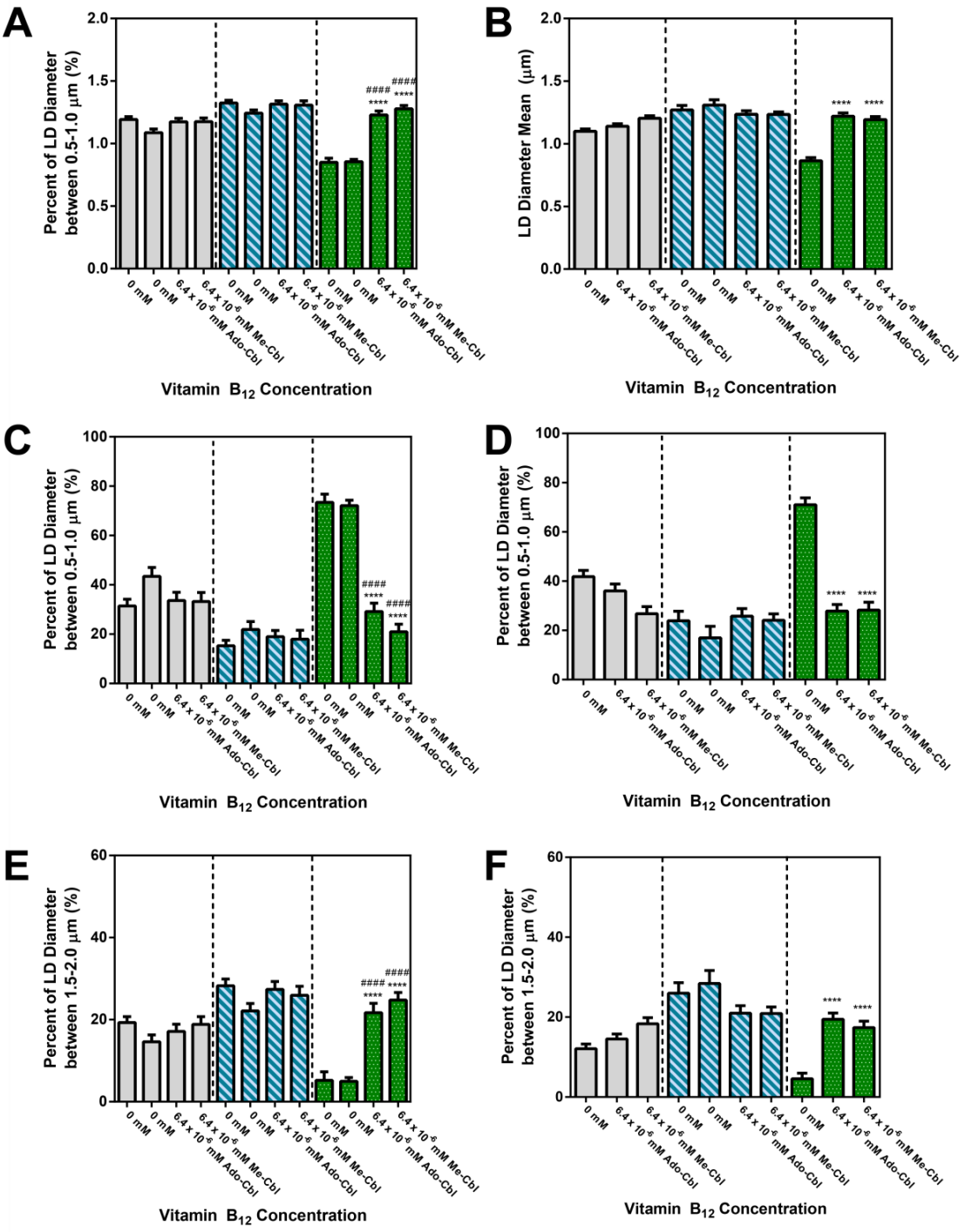

Figure 3-9. Results of the same two repeats grouped according to the various *E. coli* diets supplemented with Ado-Cbl or Me-Cbl, where the knockout gene of the individual colonies of *E. Coli* were confirmed using sequencing. A, D) Two different trials showing the mean lipid droplet size for a population fed the various

conditions, where the population fed *tonB* with supplementation was significantly different compared to the population fed *tonB* without supplementation. The other two diets did not contribute to a significant difference in mean as compared to the sets not supplemented. B, E) Two different trials showing the average percentage of lipid droplets between 0.5 – 1.0 µm for a population fed the various conditions. Worms fed *tonB* have a significant decrease in the amount of lipid droplets in this smaller size range as compared to the worms fed *tonB* without supplementation. C, F) Two different trials showing the average percentage of lipid droplets between 1.5 – 2.0 µm for a population fed the various conditions. Worms fed *tonB* with supplementation have a significant increase in the percentage of lipid droplets in this larger size range, which compliments the results in B, E. (n> 30, * significant difference versus the first set without supplementation (0 mM), # significant difference versus the second set without supplementation (0 mM). One symbol represents significance at p<0.05, two represents significance at p<0.01, three represents significance at p<0.001, and four represent significance at p<0.0001)

The same lipid droplet morphology changes and trends seen by worms fed *tonB* were also observed when the diet was supplemented with the other active form of vitamin B_{12}, Me-Cbl, as compared to worms fed Ado-Cbl (Figure 3-8, Figure 3-9, Figure 3-10). An additional two independent repeat for each condition was conducted and the results are available in Appendix C. 4. We can infer that the changes in lipid droplet morphology are independent of the vitamin B_{12} form. Additionally, the decrease in lipid droplet size of worms fed *tonB*, is repeatable, as is the increase in lipid droplet size when the worms fed *tonB* are supplemented by either Ado-Cbl or Me-Cbl. Knowing that *tonB* is involved in the synthesis of vitamin B_{12} as a transporter, knocking out this gene in *E. coli* may cause a decrease in the quantity of available vitamin B_{12}. This relates to worm metabolism because the deficiency in vitamin B_{12} is reversed with the artificial addition of vitamin B_{12}, as indicated with the increase in lipid droplet size. The increase in size corresponds to similar size ranges as the worms fed on the empty vector without vitamin B_{12} supplementation. These results also suggest that having an excess quantity of vitamin B_{12} does not necessarily contribute to a dramatic lipid droplet change. Only the deficiency in vitamin

B_{12} causes for a reduction in lipid droplet size. Because the larger lipid droplet phenotype of *btuR* was not affected by this addition, it also leads to the inference that vitamin B_{12} may have already been in excess for this knockout or it may not have been what caused the lipid droplet size change.

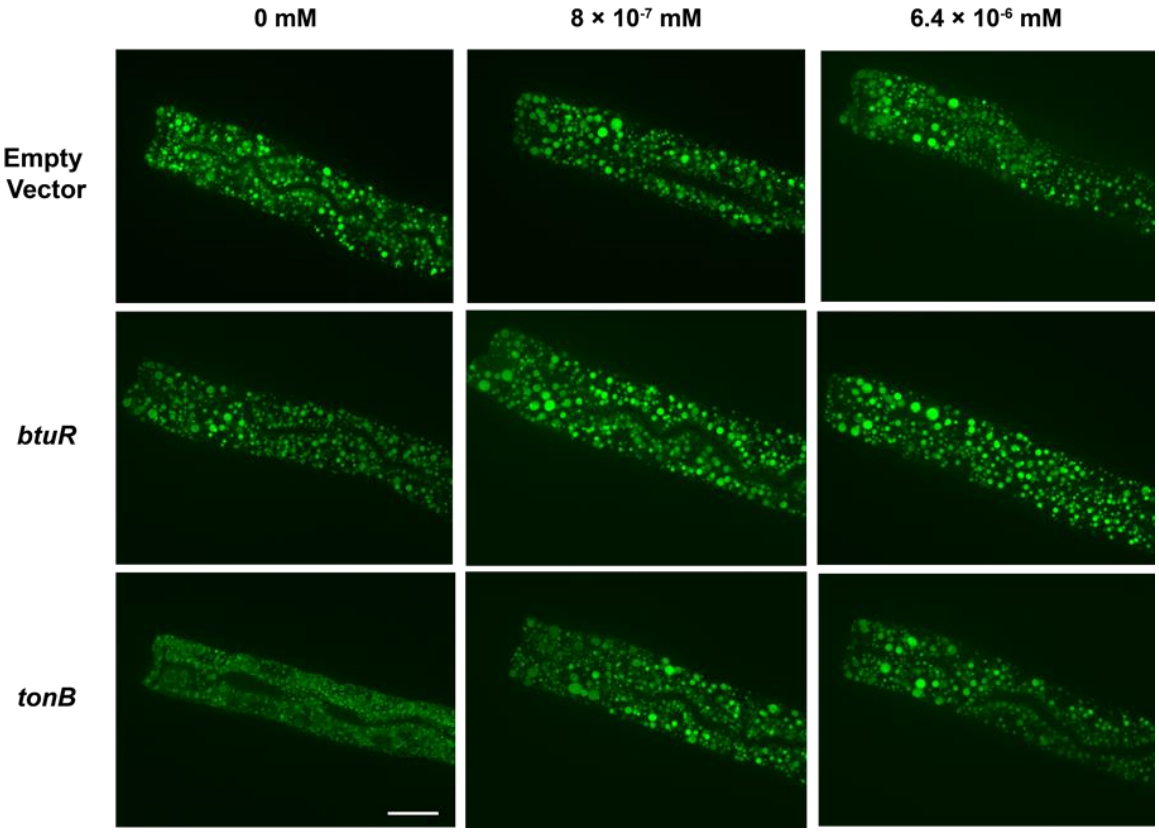

Figure 3-10. Representative images of lipid droplets in worms fed on plates supplemented with Me-Cbl. Different concentrations of Me-Cbl were added in addition to feeding the worms the empty vector diet, the *btuR* diet which corresponds with the previously identified B2, and the *tonB* diet, which also corresponds with synthesis of vitamin B_{12} similar to that of *btuR*. (All images at same scale. Scale bar = 20 µm)

3.3.5.2 *prpC* diet causes an accumulation of propionic acid

For the clone C11, the gene affected is *prpC*. The gene *prpC* is involved in catabolism of short chain fatty acids and catalyzes the Claisen condensation of propionyl-

CoA and oxaloacetate[7,185]. This deletion causes changes in the quantity of propionic acid in the *E. coli*[185], and in turn propionic acid was chosen as the metabolite to supplement the diet. In Watson, *et al.*, the Keio *E. coli* Consortium library was screened to determine variations in *C. elegans* life history traits, where propionate metabolism was explored[180]. In addition to *prpC*, the gene *prpR* is also involved in the propionic acid pathway[180]. Therefore, along with *prpC*, *prpR* was also investigated in the second round of analysis.

Similar to the vitamin B_{12} supplementation tests, we conducted the supplementation tests using propionic acid. Figure 3-11 shows representative images of worms fed the different clones: empty vector, *prpC*, *prpR*, with supplementation of propionic acid at four different concentrations. The *prpC* deletion in *E. coli* causes for *C. elegans* to have a reduced diameter of lipid droplets, which is accentuated when propionic acid is added to the agar, but difficult to visualize the change (Figure 3-11). The lipid droplets of worms fed the *prpR* diet more closely resemble that of the empty vector; however, when adding propionic acid, both the empty vector diet and the *prpR* diet have a reduction in lipid droplet sizes (Figure 3-11).

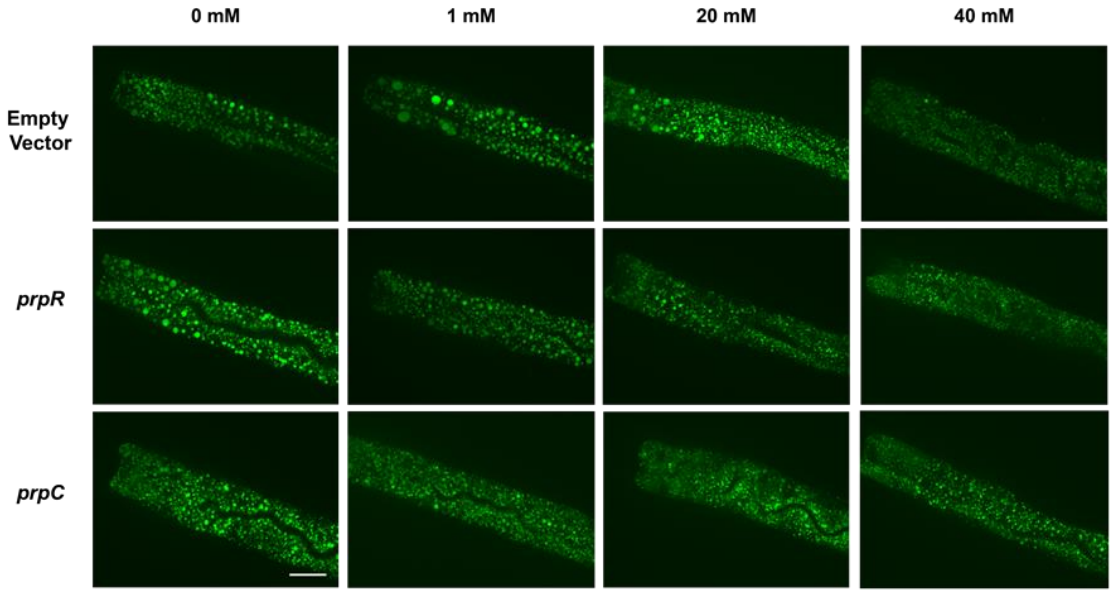

Figure 3-11. Representative images of lipid droplets in worms fed on plates supplemented with propionic acid. Different concentrations of propionic acid were added in addition to feeding the worms the empty vector diet, the *prpC* diet which corresponds with the previously identified C11, and the *prpR* diet, which also corresponds with the catabolism of propionic acid, similar to that of *prpC*. (All images at same scale. Scale bar = 20 µm)

Two different trials were completed where the worm diet was supplemented with propionic acid, and each time similar results were obtained. As compared to the empty vector without supplementation, the mean lipid droplet size for worms on the diet of *prpC* robustly showed a statistically significant reduction in size (Figure 3-12A, D). In contrast, worms fed the *prpR* diet without supplementation did not have a significantly different lipid droplet size distribution from worms fed the empty vector without supplementation; however, when supplementation is added, there is significant decrease in the mean lipid droplet size (Figure 3-12A, D). Worms fed with the empty vector, *prpC*, or *prpR*, with the propionic acid supplementation to concentrations of 20 mM (Appendix C.4) or 40 mM (Figure 3-12B, E) had a significant increase in the amount of lipid droplets in this smaller size range as compared to the worms fed the empty vector without addition of propionic

acid, and a significant decrease in the percentage of lipid droplets in this larger size range (Figure 3-12C, F). This indicates the majority of the lipid droplets are in a smaller size range.

Even though there is variability in the lipid droplet sizes in the worms fed the empty vector, the addition of propionic acid still caused a robust response with decreasing the size of the lipid droplets in multiple repeats, and the decrease in lipid droplet size for worms fed *prpC* showed an effect beyond the typical variability of the empty vector. An additional two independent repeat for each condition was conducted and the results are available in Appendix C. 4. When either the *prpC* or *prpR* diet is supplemented with 20 or 40 mM, the size of the lipid droplets significantly decreases to approximately the same level, even though the lipid droplets from the worms fed *prpC* were already significantly smaller without any supplementation. This indicates that the reduction in size for the worms fed *prpC* may have reached a lower limit in how small the lipid droplets can become from propionic acid supplementation. This is recapitulated when analyzing the percentage of lipid droplets in the smaller size range (Figure 3-12 B, E), where both worms fed *prpC* and *prpR* have a similar percentage of lipid droplets in the smaller size range, must be greater than that of the empty vector. Because of the great number of lipid droplets in the smaller size range, when observing the percentage of lipid droplets in a higher size range of 1.5 to 2.0 μm, most of the droplets do not fall in this category (Figure 3-12C, F). Furthermore, when comparing the lipid droplets sizes within each diet, the effect of propionic acid is even more apparent (Figure 3-13). In analyzing the mean lipid droplet size, the addition of 20 to 40 mM propionic acid decreased the mean sizes of lipid droplets (Figure 3-13A, D), and increased the percentage of lipid droplets in the smaller size range of 0.5 to 1.0 μm

(Figure 3-13B, E), to the point that when determining the percentage of lipid droplets in the larger size range, both *prpC* and *prpR* practically have no lipid droplets in this size range (Figure 3-13C, F). This leads us to infer that the knockout *prpC* is causing and accumulation of the metabolite propionic acid. Thus, the propionic acid is working alongside the effects of the *prpC* diet which already has an elevated amount as compared to the empty vector.

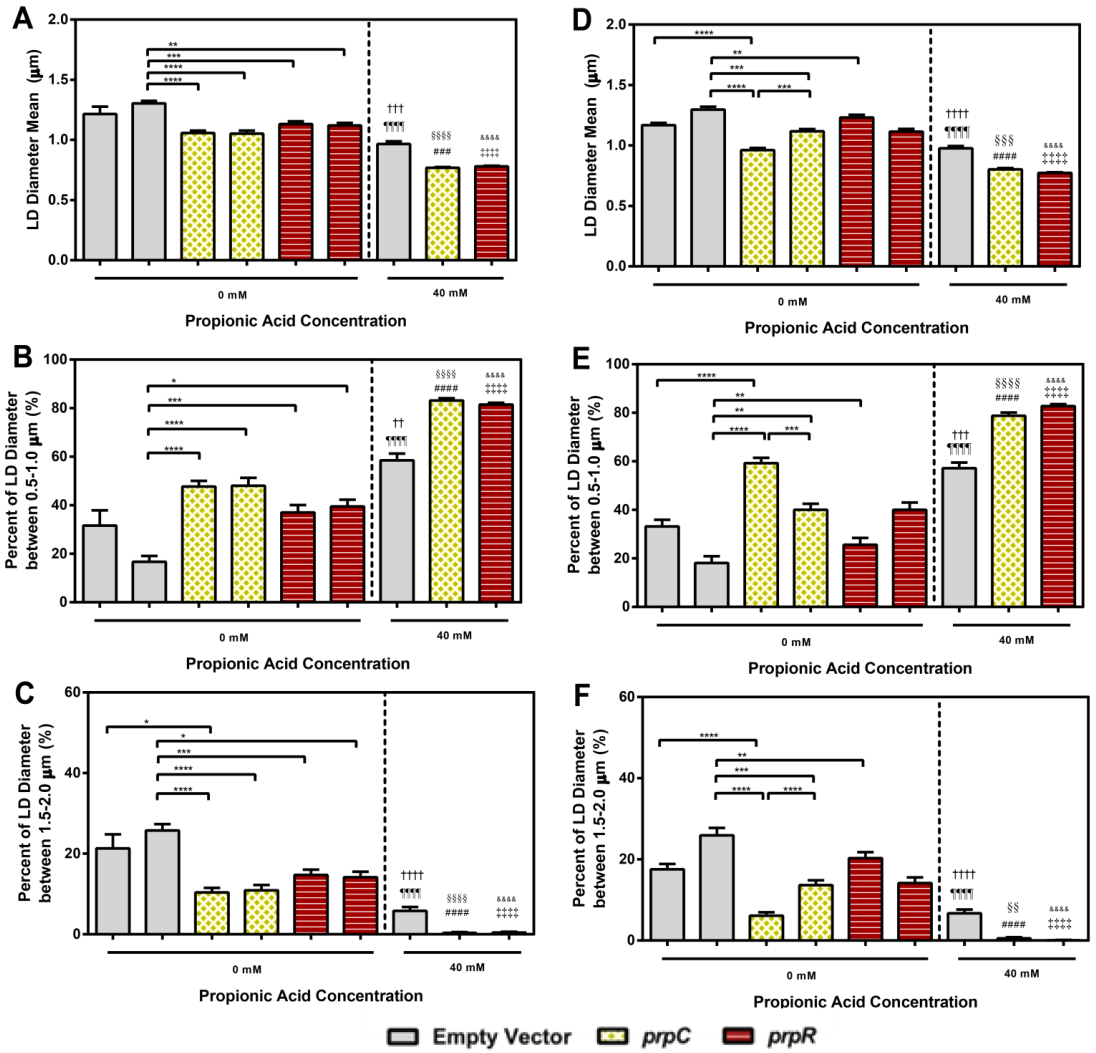

Figure 3-12. Results of two repeated experiments with supplemental metabolite enrichment of propionic acid, where the *E. coli* was cultured from individual colonies that were confirmed to have the knockout present through sequencing. A,

D) Two different trials showing the mean lipid droplet size for a population fed the various conditions, where the all three populations that were fed either the empty vector, *prpR*, or *prpC*, showed a significant reduction in LD size when fed the 40 mM concentrations. B, E) Two different trials showing the average percentage of lipid droplets between 0.5 – 1.0 µm for a population fed the various conditions. C, F) Two different trials showing the average percentage of lipid droplets between 1.5 – 2.0 µm for a population fed the various conditions. (n> 30; * significance level vs bracketed conditions, † significance level vs the first empty vector 0 mM PA, ¶ significance level vs the second empty vector fed 0 mM PA, § significance level vs the first set of *prpC* fed worms at 0 mM PA, # significance level vs the second set of *prpC* fed worms at 0 mM PA, ‡ significance level vs the first set of *prpR* fed worms at 0 mM PA, '&' significance level vs the second set of *prpR* fed worms at 0 mM PA ; 1 symbol = p<0.05, 2 symbols = p<0.01, 3 symbols = p<0.001, 4 symbols = p < 0.0001). An additional set of two independent repeats were conducted, and the results correspond with these trials, and are available in Appendix C.4.

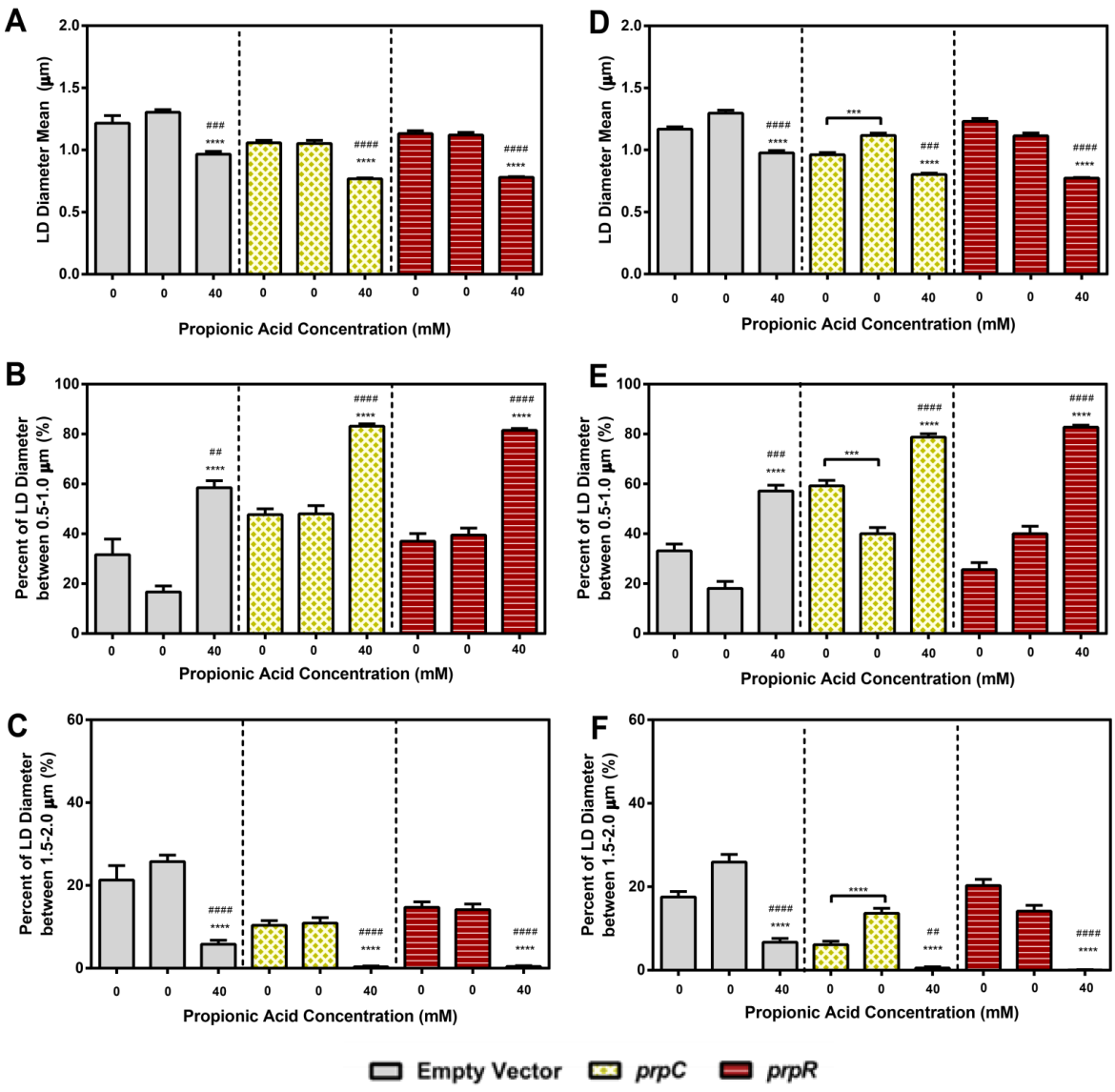

Figure 3-13. Results of the same two repeats grouped according to the various *E. coli* diets supplemented with propionic acid, where the knockout gene of the individual colonies of *E. Coli* were confirmed using sequencing. A, D) Two different trials showing the mean lipid droplet size for a population fed the various conditions, where all diets, empty vector, *prpC*, and *prpR* show a significant decrease in lipid droplet mean diameter when supplemented at the 40 mM concentrations. B, E) Two different trials showing the average percentage of lipid droplets between 0.5 – 1.0 µm for a population fed the various conditions. Similar to the mean lipid droplet information, worms fed all three diets exhibited a statistically significant increasen droplets in the smaller size range of 0.5 to 1 µm indicating that the lipid droplets of each of the populations decreased in size with a concentration of 40 mM. C, F) Two different trials showing the average percentage of lipid droplets between 1.5 – 2.0 µm for a population fed the various conditions. Complimentary to the results in B, and E, in C and F we see that there is a significant decrease in the

percentage of lipid droplets in the larger size range when supplemented with propionic acid as compared to no supplementation. (n> 30, * significant difference versus the first set without supplementation (0 mM), # significant difference versus the second set without supplementation (0 mM). One symbol represents significance at p<0.05, two represents significance at p<0.01, three represents significance at p<0.001, and four represent significance at p<0.0001). An additional set of two independent repeats were conducted, and the results correspond with these trials, and are available in Appendix C.4.

In literature, it has been shown that the *prpC* gene is responsible for propionate catabolism[7,8,180,182]. Therefore, the breakdown of propionic acid is hindered in the knockout resulting in an accumulation of the metabolite. Similar conclusions have been seen in studies that have been trying to increase the production for propionyl-CoA by knocking out *prpC*[185]. The resulting mean lipid droplet sizes calculated through the supplementation experiments support the inference that *prpC* causes an accumulation of propionic acid. When the worms were fed the empty vector and supplemented with propionic acid the worms phenocopied the smaller lipid droplet phenomenon when propionic acid is artificially added. The gene knockout *prpR* does not have a significant difference in lipid droplet size as compared to the worms fed the empty vector when both are not supplemented. Because *prpR* shows a similar phenotype to that of *prpC* when supplemented, it shows that the reduction in size of lipid droplets is predominantly due to the increase in propionic acid.

3.4 Conclusion

Using an interspecies systems biology approach with *C. elegans* and the bacterial diet of *E. coli*, we determined two metabolites that alter lipid droplet size and morphology. Additionally, a methodology was established that allowed for the imaging and analysis of population variations in lipid droplet phenotypes in a systematic way. We conducted a pilot

diet screen where the first plate in the Keio *E. coli* Consortium library was fed to *C. elegans* and the variations in the lipid droplets were observed. In this first plate, we were able to identify two different knockouts, *prpC* and *btuR*, that contributed to a change in the lipid droplet morphology. The knockout *prpC* is involved in the propionate metabolism pathway, and *btuR* is involved in the vitamin B_{12} synthesis pathway. From the identification of these two different knockouts, an additional two knockouts, *prpR* and *tonB*, were tested because they are each involved in the respective pathways.

We identified that the knockout *tonB* contributed to a dramatic change in smaller lipid droplets that can be recovered with the supplementation of vitamin B_{12}. This indicates that the *tonB* knockout contributed to a vitamin B_{12} deficiency that was restored with supplementation. In addition to causing lipid droplet morphology changes in *C. elegans*, the deficiency of vitamin B_{12} can have a severe impact on human health. Deficiency in vitamin B_{12} can lead to various diseases such as methylmalonic acidemias, which is an autosomal recessive disorder of amino acid metabolism, and homocystinuria, which is another hereditary metabolism disorder[186–188]. These disorders are not fully understood in the array of health consequences it leads to in humans. In using this model, we were able to move one step further in characterizing the effects of vitamin B_{12} deficiency which may provide a means for additional studies or treatments in vitamin B_{12} deficiencies.

In addition to vitamin B_{12}, we also identified the effect of propionic acid on lipid droplet morphology. The pilot diet screen identified *prpC* as a diet that decreased the size of lipid droplets robustly. In performing supplementation experiments with propionic acid, it was inferred that the contributing factor to the decrease in lipid droplet size was the accumulation of propionic acid. The deletion of the *prpC* contributes to a lack of propionate

breakdown, and thus the accumulation is sufficient to affect the metabolism of the *C. elegans* as well. Beyond changes in *E. coli*, or *C. elegans* metabolism, propionic acid has shown to lower the fatty acid content in the liver and plasma of humans, as well as reduce food intake with the potential to improve the sensitivity of tissue to insulin[189]. An increase in the production of propionic acid in the microbiota of humans may also be beneficial for the prevention of obesity and type 2 diabetes[7,8]. Currently, the mechanisms in which propionic acid may contribute to health effects in humans is not entirely understood, however propionic acid is an important metabolite when considering nutritional effects to physiology. The decrease in fatty acid content in humans mirrors what is seen in *C. elegans* where the smaller lipid droplets may also be indicative of an overall reduction of fatty acid content.

Further studies must be conducted to determine the true link between these identified metabolites and fat storage. These two metabolites, however, are only the results of a pilot screen where 96 diet conditions were explored. With the ability to complete the entire knockout library using the methodology developed, it will be possible to determine more metabolites that may causes changes in lipid droplet phenotypes that had previously not been implicated with fat storage and metabolism. The discoveries from analyzing the entire knockout library will lead to a new array of dietary conditions that contribute to changes in metabolism that can be explored in *C. elegans* as well as higher order organisms. These discoveries can help continue to unravel the complicated network of dietary effects on metabolism.

CHAPTER 4. SELECTIVE RECOVERY FROM REVERSIBLY BONDED MICROFLUIDIC DEVICES FOR SINGLE ANIMAL ANALYSIS OF *C. ELEGANS, DROSOPHILA* EMBRYOS, AND STEM CELL AGGREGATES

The following work in this chapter was completed in collaboration with Dr. Thomas Levario for the portion including *D. melanogaster* embryo imaging, and Emily Jackson-Holmes for the portion including murine stem cell aggregates.

4.1 Introduction and Motivation

Developments in microfluidic platforms have enabled integration, automation, and high-throughput operation for applications in the biological sciences[190,191]. Due to the small scale and tuneable features of microfluidics, various organisms such as *C. elegans, D. melanogaster*, and cells can be easily manipulated[190,191]. One of the main features of microfluidic devices is the ability to control the fluid flow within the device to conduct automated experiments[6,191,1926]. However, automating experiments can be a complex problem due to the issue of having to customize camera, microscope, and valve actuation software[6]. The ability to conduct an automated genetic screen as done in Chapter 2 is not easily done when the microscope system does not easily allow for customizable setup. Semi-automated experiments are possible by controlling the microfluidic device valve actuation with one computer, and obtaining images with a microscopy system with a separate computer; however, this method is tedious, and decreases the advantages of being able to automatically sort individual animals. A system that is capable of loading a large

number of animals, allowing for imaging on a system, and then facilitating recovery of selected animals from the device, would provide a means to eliminate the complication of interfacing microfluidic control with microscopy systems. An additional challenge of conducting automated screens, is that the analysis and decision making for sorting an animal must be done online, often one of the factors that can decrease throughput. In using a system where individual animals can be selectively chosen after imaging, the analysis of the phenotype can be done offline, where the dependence of the throughput of the experiment is not bottlenecked by analysis time. To accomplish this, it would be advantageous to position or arrange the animals for imaging and then be able to selectively recover specific animals to further study the phenotype or genotype. Another challenge is that incorporating automation between the microfluidic and microscopy systems require expertise in both software and hardware. A method that could increase throughput, without needing software and hardware customization would be more accessible and could greatly impact biological studies. Existing microfluidic designs allow for imaging of animals, however, selective recovery of individual animals after imaging or stimulus in a microfluidic device is difficult.

To address these issues, we have developed a method to selectively recover single animals from microfluidic devices without software integration or traditional on-chip sorting. We have combined two independent existing technologies: compression sealing of microfluidic devices and biocompatible hydrogels. The compression sealing allows for the microfluidic device to be reversibly sealed to a glass coverslip instead of permanently bonded as is traditionally done. The reversible seal allows for access to the various chambers or areas with the animals. To ensure the animals remain individually positioned

in the device and do not get dislodged when unsealed for recovery, we have incorporated the use of biocompatible hydrogels that assist in maintaining the animals in the positions. The hydrogel must have the ability to flow through the device, however, the hydrogel must be rigid enough to maintain animals in position, creating a delicate balance between viscosity and stiffness to consider. Without this hydrogel, the animals will become easily dislodged, losing the positioning and ability for identification. This combination of a reversibly bonded device with hydrogels allow for simple integration into many biological laboratories where selective recovery from a microfluidic device is needed.

4.2 Methods and Materials

4.2.1 C. elegans strain, culture, device loading, and imaging

*C. elegans s*trains used for experiments were *hjSi224 [vha-6p::dhs- 3a cDNA::GFP-TEV- 3xFLAG::let-858 3'UTR]* and *a015;hjSi224* provided by Ho Yi Mak. Strains were cultured at 20^{o}C on nematode growth medium (NGM) agar plates seeded with OP50 *E. coli* using standard culture methods[9]. For synchronization of the population, standard bleaching methods were applied, and eggs were seeded on to NGM plates and allowed to grow for 48-54hrs until reaching L4 stage for efficient trapping in the microfluidic array device. To load the device, the device was first primed with ethanol (Sigma Aldrich) to remove all air bubbles, and then washed with M9 with 0.01% Triton X-100 (Sigma Aldrich). Next, the worms were washed from the agar plate using M9 with Triton as a surfactant to reduce the amount of sticking to the tubing and PDMS walls. The worms were flowed in using a syringe pump set at 2.5 mL/hr. To immobilize the worms,

200 mM solution of tetramisole in M9 was flowed through the device after loading for 2 minutes.

Then, worms were loaded with Pluronic F127 (Sigma Aldrich) at 25% w/v concentration a 4^{o}C cold room for 5 minutes at a rate of 3 mL/hr, and then the device was taken to room temperature for the hydrogel to solidify. Next, the compression seal was removed to have access to the coverslip below the device. Imaging was performed using the PerkinElmer UltraVIEW VoX spinning disk confocal microscope, where a stitched image of the whole device was first captured using a 10x objective in bright-field, and then the object was switched to a 60x/1.49 NA oil objective for high resolution imaging. Individual worms were identified for imaging manually, and z-stacks were captured for each worm, imaging 33 slices for a depth of 8 μm at a step distance of 0.25 μm. A maximum projection image was used for all worm lipid droplet analysis using the algorithm in Chapter 2 to determine the lipid droplet phenotype.

4.2.2 Drosophila melanogaster strains, culture, device loading, and imaging

Histone2AV-GFP (Histone-GFP; Bloomington stock center) expressing flies were used for all experiments where the cells were visualized using fluorescence. The preparation of embryos was done using standard preparation protocols[193]. Briefly adult flies were placed on a fresh apple cider agar plate for 2 hours at 25^{o}C to collect synchronized embryos. To remove the chorion membranes, live embryos were soaked in 2.5% sodium hypochlorite (bleach active ingredient; Clorox) for approximately 1 minute. To remove the bleach solution, the embryos were then rinsed with 10 mL of deionized water, and then the embryos were suspended in 15 mL of phosphate-buffer saline solution

(PBS; VWR) buffer with 0.3% Triton X-100 (Sigma Aldrich). For embryo loading, the microfluidic device was mounted on a dissecting microscope and then primed with PBS with Triton X-100 to eliminate air bubbles. Using slight positive pressure (~6psi) the embryos are loaded in the device.

Once the embryos are properly loaded after approximately 5 minutes of loading, the solution is changed to 1.5wt% sodium alginate in deionized water. This solution is flowed through for 2 minutes, and then quickly switched to 100 mM calcium chloride solution for 30 seconds. The solution is then switched back to sodium alginate for 30 seconds, and then calcium chloride for another 30 seconds. Repeating the alternating steps of the two solutions allows for areas to become cross linked in the interface, however still allowing flow for a few seconds. Due to the changes in viscosity and cross linking, there may be a few bubbles introduced. Then the embryos can be imaged by removing the bottom piece of the compression seal to have access to the coverslip.

For time-lapse confocal microscopy, the imaging was performed on a UltraView PerkinElmers spinning disk confocal microscope We first imaged the device at 10x in bright-field to easily identify the location of the embryos. Next, the magnification was switched to a 40x/1.3 NA oil objective. Using an environmental chamber, the temperature of the chip and embryos was maintained at 25^{o}C, and images were acquired every 60 seconds for a total of 3 hours. To determine the slice where imaging took place, the focal plane was placed at ~80µm in from either the anterior or posterior end closest to the coverslip. After imaging, the embryos were removed from the device by removing the glass slide and carefully recover the embryos with the identities still known. To reduce dehydration when the coverslip was removed to recover the embryos, FC40 oil (Sigma

Aldrich) was applied to the entire device while the embryos were recovered using a platinum wire pick.

4.2.3 Stem cell aggregate culture, device loading, staining, and imaging

The culture, device loading, and staining of stem cell aggregates was conducted by Emily Jackson-Holmes of the Lu Lab. Briefly, mouse embryonic stem cells (mESCs, D3 cell line) were formed into aggregates by centrifugation into 400 μm agarose (OmniPur, EMD Millipore) microwells placed within a 12 well polystyrene plate(Corning, Inc.)[194]. Cells were seeded at a density of 1.2 million cells per microwell insert to yield aggregates of 1000 cells and allowed to form for 18-24 hours. Prior to each experiment, the device, needles, and tubing were autoclaved, and the device was primed using 70% ethanol to remove air bubbles. A solution of 1 mg/ml of bovine serum albumin (BSA, Millipore) was then flowed through the device and incubated for 30 minutes to passivate the surfaces. For aggregate loading and perfusion, a 200 μL pipette tip was placed in the device inlet. To prevent rapid settling of aggregates during loading, aggregates were resuspended in 1.05 g/mL Percoll (Sigma Aldrich). To load aggregates, the solution with aggregates was pipetted into the inlet and loaded through gravity-driven flow. Following loading, the devices were placed in an incubator and perfused using a syringe pump at a flow rate of 10 μL/hr. Phase contrast images were captured at day-1 and day-5 of culture using an EVOS microscope (Life Technologies). For on-chip immunofluorescent staining, all solutions were perfused through the pipette tip inlet driven by gravity driven flow. Aggregates were immunostained with nuclear stain Hoechst 3342, Oct-3/4, and Nanog to observe loss of pluripotency.

Before imaging, 1% low melt agarose (Sigma Aldrich) solution was perfused through the device using gravity while in the incubator to maintain the solution at 37^{o}C for 30 minutes. The device was removed from the incubator, solidifying the agarose at room temperature for 5 minutes. To capture a reference image of the aggregate locations in the device the bottom compression seal was removed, and using the UltraView PerkinElmers spinning disk confocal microscope, a stitched image of the whole device was captured using a 10x objective in bright-field. Next, the coverslip was removed along with the pipette at the inlet and the top portion of the compression seal. Using a 1mL pipette tip, individual aggregates were aspirated from the device and added into 250 μL microcentrifuge tubes containing approximately 100 μL of 1% agarose solution with a 1:40,000 dilution of 500 nm, red fluorescent beads. The beads were included to register the multiple imaging angles and reconstruct a properly aligned 3D rendition of the aggregate in future work that will be conducted by Emily Jackson-Holmes. To image samples, a Zeiss Lightsheet Z.1 microscope with a 20x water immersion objective and 405 nm (for Hoechst), 488 nm (for Nanog), and 561 nm (for Oct-3/4) laser lines was used. Z-stacks of single aggregates were captured with Multiview using 3 different angles of imaging separated by 120^{o}. The z-stack step size was 5 μm for all images captured.

In using a pipette tip with BSA, the aggregates can be recovered by applying suction at the desired trap. The liquid is then expelled to recover the individual aggregate. For lightsheet imaging, the liquid to best use is the low melt agarose to better load the capillary used for imaging.

4.2.4 Microfluidic Device Fabrication for C. elegans, D. melanogaster, and stem cell aggregates

Microfluidic devices were fabricated by soft lithography techniques with various feature thicknesses[176]. The *C. elegans* worm array was fabricated from a two-layer SU-8 (Microchem, Newton, MA) mold; the first layer was 13 μm, which is the height of the step utilized to maintain the worms in the traps, and the second layer was 31 μm, for a total height of 44 μm throughout the device. The *D. melanogaster* embryo array device was fabricated from a two-layer SU-8 master (total device thickness: 250 μm). The stem cell aggregate device was fabricated from a three-layer SU-8 master with respective feature heights of 200 μm, 100 μm, and 200 μm, for a total height of 400 μm. All master molds were treated overnight with silane vapor ((tridecafluoro-1,1,2,2-tetrahydrooctyl)-1-trichlorosilane; United Chemical Technologies) to promote simple release of the polydimethylsiloxane (PDMS) (Dow Corning Sylgard 184, Midland, MI) during molding. For rigidity under the compression seal, a mixture of PDMS (10:1 base:cross-linker weight ratio) was degassed and poured over the mold and allowed to solidify at 75^{o}C overnight. The various chips were then cut with a scalpel and the access holes were punched with 20-gauge needles (McMaster-Carr, Elmhurst, IL) at the inlet and outlet.

4.2.5 Compression Seal Fabrication

The compression seal used for this application consisted of two ¼" thick clear acrylic pieces (McMaster Carr, Inc.). The design of the compressions sealing pieces was made using AutoCAD, where the original microfluidic device was used as a template to determine the locations of the inlets and outlets of the device. To cut the acrylic, the

AutoCAD design was imported to Adobe Illustrator and printed using a laser cutter. The acrylic was then cleaned with ethanol to eliminate residual dust. The device was assembled using 80 thread nuts and 1' long bolts (McMaster Carr), tightened using a hex screwdriver.

To seal the microfluidic device, we first prepared a clean microfluidic device with entry and exit ports punched, and applied the coverslip to the feature side of the device as is normally done in traditional bonding. Next the top, pre-cut, acrylic sheets was aligned with the exit and entry ports, and the second sheet was placed below the glass coverslip assuring that the screw holes were aligned for the top and bottom sheet. To tighten and seal the clamp, screws were threaded through the holes and hex nuts are tightened with a screw driver until just tight. Care must be taken not to over-tighten, as this can result in breaking of the coverslip or feature deformation. The pins with tubing were then placed in the entry and exit ports and the device was degassed with ethanol before loading.

4.2.6 Hydrogel Solution

For the *C. elegans* experiments, the Pluronic F127 (Sigma Aldrich) solution was prepared at 25% w/v in deionized water, where the suspension was agitated at 4^{o}C until dissolved. For the *Drosophila melanogaster* embryo experiments, the sodium alginate (Sigma Aldrich) solution was prepared at 1.5wt% in deionized water and the calcium chloride (Sigma Aldrich) solution was prepared to 100 mM in deionized water. For the low melting point agarose (Sigma Aldrich), a 1% w/v solution was prepared by boiling deionized water to dissolve the agarose, and then temperature was reduced to 37^{o}C before being flowed in the devices with stem cell aggregates.

4.3 Results and Discussion

This platform utilizes two custom built, laser-cut transparent acrylic pieces, which act as a compression seal to hold the PDMS microfluidic device to either a cover slip or glass slide using screws (Figure 4-1A). The acrylic piece is cut to have inlet and outlet ports available for pins or tubing. This system has the potential to be applied to many different types of microfluidic devices, for various types of organisms. This compression seal provides the ability to reversibly seal the microfluidic device to the glass substrate, without using plasma bonding, and thus making the inside of the microfluidic device accessible. However, to fully benefit from the high-throughput ability of array devices, using compression sealing must be combined with a method to maintain the animals in position for selective recovery. Due to hydrophilicity of glass, the water-based solutions in microfluidic devices will typically come out of the device and on to the glass surface so the animals will be no longer indexed in their array location. The use of a hydrogel solution would prevent the animals from becoming dislodged by maintain the animals in the microfluidic device making the identify of each animal easily determined.

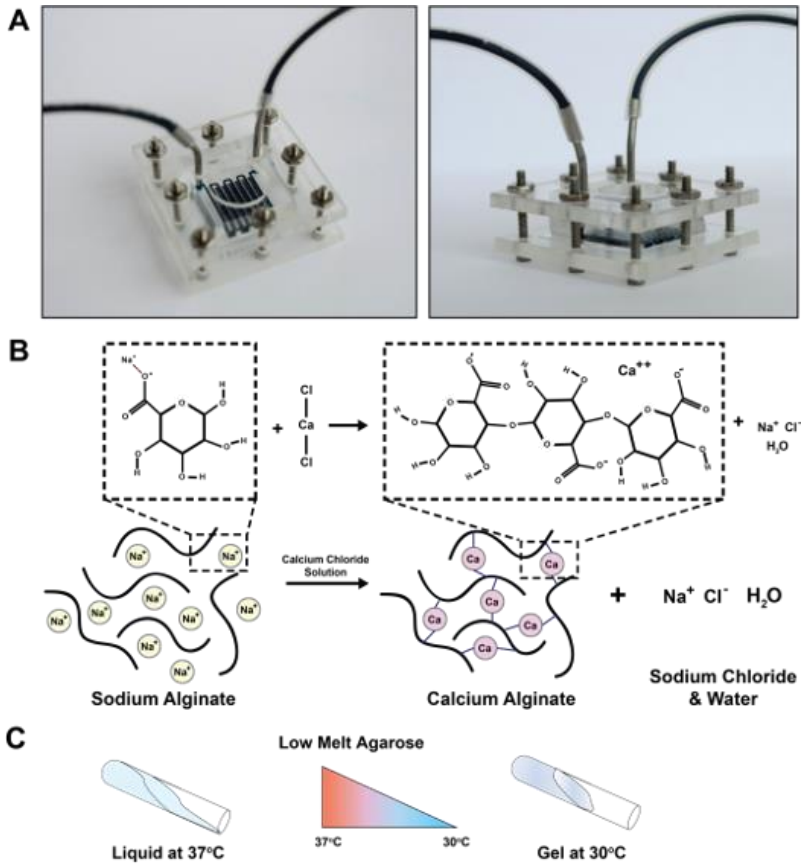

Figure 4-1. Device and hydrogel overview. A) Two different angles are shown of an assembled microfluidic device and compression seal, where the device is pressed to the cover slip by the custom laser cut two acrylic pieces, with screws and nuts to hold the pieces together. B) Chemical structure of the hydrogel that is loaded into the device to maintain the animals in position. Sodium alginate is first loaded, and then a solution of calcium chloride is subsequently added, causes for the hydrogel to cross link forming calcium alginate and salt solution to form. C) Depiction of the hydrogel solution used for cell aggregates, where at 37ºC the low melt agarose is low viscosity and can flow through the device. When the temperature is decreased to at least 30ºC or less, the solution solidifies, and is higher viscosity stopping flow in the device. The higher viscosity holds the animals in the array to allow for selective recovery.

To avoid using surface treatments of the glass surface, and to maintain the indexed locations of animals in array devices, the addition of a hydrogel solution is advantageous to recovering animals in the precise location after imaging or stimuli. Surface treatment of the glass slide to be hydrophobic is not desired because residual chemicals may cause

unwanted biological effects, and may cause for the surface to not seal properly. It also does not ensure that the animals will remain arrayed. Additionally, in creating a surface that is hydrophobic, the wetting of the surfaces to degas the device may become much more difficult leaving bubbles that hinder device operation. The hydrogels used to recover various animals may vary in composition and gelation temperature, but the principle is similar.

To recover organisms that are typically cultured at room temperature, and to avoid heat shock or irradiation of animals with UV light, a hydrogel solution is used where sodium alginate is cross linked by calcium chloride (Figure 4-1B). This provides a stable biocompatible structure when the glass slide is removed from the microfluidic device, and the solutions can flow through the devices at room temperature until gelation occurs within the device when the two solutions become in contact. To recover model systems that are cultured at higher temperatures such as 37^{o}C, low melting point agarose can be substituted (Figure 4-1C). The low melting point agarose has the ability to be a low viscosity, flowing solution at 37^{o}C; in contrast, at room temperature the agarose will solidify in seconds to minutes. Lastly, a third solution that has the ability to flow through a device with low viscosity is the thermosensitive hydrogel Pluronic F127[126,145,146,190,195]. This solution at 4^{o}C is a low viscosity liquid, and at room temperature the solution solidifies into a gel. The challenge with flowing solutions that gel or solidify is that the solutions typically have high viscosities that either make it difficult to flow through the smaller dimensions of a microfluidic devices, or the higher viscosity causes for an increased pressure to be applied that causes the animals to be dislodged from the defined positions in the devices. A balance between stable structure that will retain the animals in their positions, and a structure that

can flow through the device is carefully adjusted for each of the various organisms and device designs.

The following study explores the use of these techniques with 3 different organisms, including *C. elegans* worms, *Drosophila melanogaster* embryos, and murine embryonic stem cell (mESC) aggregates. The variation in size and rigidity of these organisms/cells causes for different pressure and temperature requirements that are necessary to recover the individual animals. For *C. elegans,* the long tubular structure of the body is easily deformed so reduced pressure must be applied for both loading the worms and flowing the hydrogel. Additionally, their small scale of approximately 50 μm at the L4 stage causes difficulty in precise recovery. Furthermore, the worms are sensitive to higher temperatures above 25^{o}C, but are unharmed in temperatures as low as 4^{o}C, providing boundaries for the allowable gelation properties for the hydrogel used with this model system. Therefore, the Pluronic solution is best suited for *C. elegans* recovery. For *D. melanogaster* embryos, a higher pressure can be applied because the embryos are ellipsoids that have more rigidity as compared to the worms. The larger scale of approximately 500 μm in length and 200 μm in height allow for easier recovery than that of the *C. elegans*. However, due to high temperature sensitivity, the gelation for this organism must take place at room temperature to assure there are no developmental changes due to changes in temperature. Therefore, the combination of the sodium alginate with the calcium chloride solutions will be used for the *D. melanogaster* embryos. Lastly, for the mESC aggregates, the aggregates are very easily deformable, and thus a very low pressure is necessary for both loading of the aggregates and flowing of the hydrogel solution. Because of the delicate nature of the aggregates, recovery from the device must be gentle. The aggregates are

typically cultured at 37°C; thus, the hydrogel solution best suited for this application is the low melting point agarose. The flexibility of this system is demonstrated by using these three different organisms and device designs with the same technique of compression sealing and adding a hydrogel to selectively recover animals.

4.3.1 C. elegans recovery from modified worm array microfluidic device

To selectively recovery *C. elegans,* an array microfluidic device was passively loaded with up to 140 worms into one single device (Figure 4-2A). The design used was slightly modified from a previous array device[55]. The advantage of the array device is that no moving components or software is necessary, and a large number of worms can be easily imaged with the defined locations in the device traps. One challenge in using a compression seal to reversibly bond the device is the difficulty in applying sufficient pressure to seal the device without collapsing the device features. To address this, we incorporated an air pocket ring around the device (Figure 4-2B) that can deflect and collapse without affecting the device channels. This portion of the device acts as a gasket that allows for variability in the pressure applied where the serpentine channel does not collapse. Another challenge in using pressure to reversibly bond this microfluidic device is that the restriction channels on the devices are already very narrow (Figure 4-3A, B). Thus, when mechanical pressure is applied, the restrictions can close, not allowing flow or loading to occur. Additionally, if the restrictions do not close, due to the smaller slender shape of *C. elegans*, pushing with higher viscosity fluid can cause the worms to squeeze through the restriction channel in the original worm array device[55] because the height is equivalent to the whole channel (Figure 4-3C).

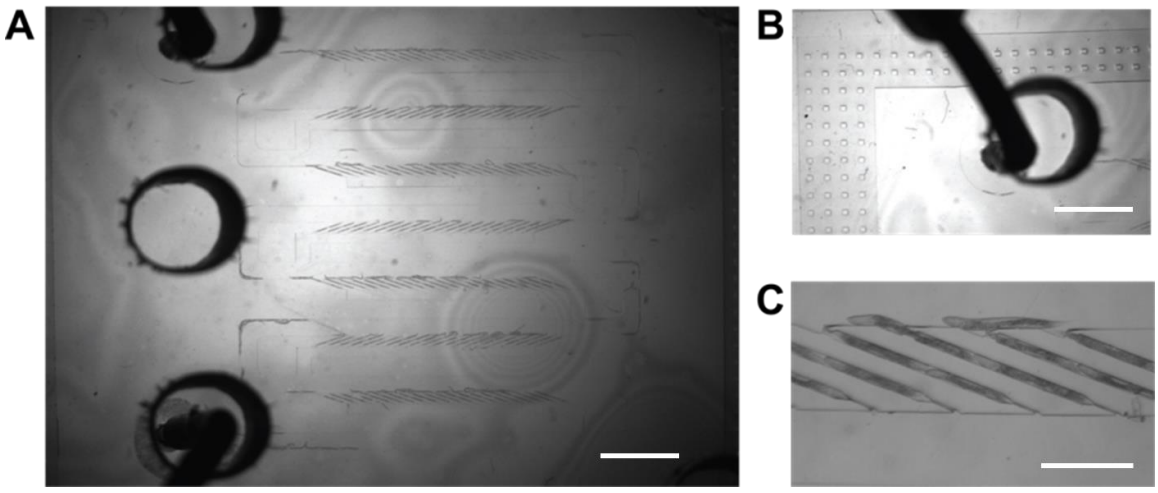

Figure 4-2. Worm array microfluidic device loaded with the use of a compression seal. A) Shows a worm array device fully loaded while using a compression seal to reversibly seal the device. (Scale bar = 2 mm) B) Shows the outer ring that is used as an air pocket to dampen the effects of the mechanical pressure due to the compression seal. This area acts as a pseudo-gasket that can collapse to still allow for the main device channels to remain open, allowing for less precision when applying pressure to seal the device. (Scale bar = 2mm) C) Shows a zoomed view of the worms in the microfluidic array device. (Scale bar = 500 μm)

To remedy these issues, a slight modification to the array design was made, where a second layer feature was added. A step was included in the restriction channel to allow flow, but stop the worm from squeezing through the resistance channel (Figure 4-3D). This step has a broader width (Figure 4-3E) as to not collapse when the pressure from the compression seal is applied, and a shallower opening, that is a third of the overall height of the device (Figure 4-3F), where flow still occurs so worms can load, but when viscous hydrogel solution is applied the worms do not push through. No significant change in the loading was detected between the previous design and the modified design with an extra step. With the addition of the step, hydrogel solution is able to flow through and the majority of the worms stay in their traps (Figure 4-4A). The ability to trap over 100 worms

in this device, image the worms, and then properly select worms of interest for further testing was then investigated.

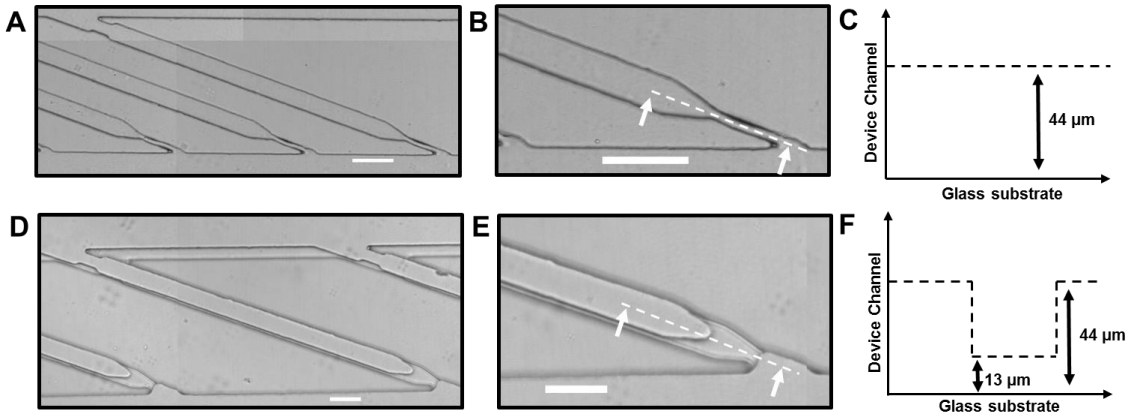

Figure 4-3. Worm device restriction modification. A, B, C) Show the original worm array design with 1 SU-8 layer. A) Shows a worm channel with the opening for loading to the serpentine, and the restriction which narrows. B) Shows a zoomed version of the restriction from the original design, where the dotted line indicates the depth profile shown in C. C) Indicates the device channel was one depth at 44 µm. D, E, F) Show the modification to the worm array design. E) Shows a worm channel with the opening to the serpentine, and the restriction with a broader and more shallow opening, where the dotted line indicates the depth profile shown in F. F) Indicates the device channel was made to two depths where the overall device is at 44 µm, however the restriction is more shallow at 13 µm, preventing the worms from flowing through when higher pressure is applied to flow viscous fluid. (All scale bars = 100 µm)

To test the ability to selectively recover worms of interest from the modified worm array device, we imaged and selectively recovered worms showing a variation in phenotype. We selected to use Pluronic[126,144,145], a block-co-polymer, that is liquid at 4^{o}C, and solid at room temperature. Worms can withstand short instances of time at 4^{o}C and physiological changes have not been observed[125,126]. The population of worms cannot be loaded while already in a Pluronic solution because cool temperatures are necessary for the Pluronic to be in a liquid phase, and at these decreased temperatures the worms have

decreased mobility. The worm bodies become straight in morphology which decrease the ability of the worms to properly load into the individual channels. A mock screen was performed where changes in lipid droplet size were selected. The device was loaded with a wild type population that was mixed with *atlastin* mutants, that causes for a decrease in lipid droplet size[73]. To identify the differences in lipid droplets, higher magnification imaging was performed. After the imaging, the device was opened by removing the coverslip (Figure 4-4B) and the worms were maintained in the various traps (Figure 4-4C, i). Under a dissecting microscope, 0.5 μL of M9 is used to a select worm and dislodged the worm from the trap without disturbing adjacent trapped worms (Figure 4-4C, ii). For recovery, the selected worm is aspirated into a pipette and placed on to an NGM plate, where the worm can lay progeny (Figure 4-4C, iii). The majority of the population had the wild type phenotype with larger lipid droplets (Figure 4-4D) as determined quantitatively through analysis (Figure 4-4E). Only few worms had the *atlastin* phenotype with smaller lipid droplets (Figure 4-4F), that quantitatively showed a reduced lipid droplet size as compared to wild type (Figure 4-4G). These *atlastin* worms in the population were then recovered, and allowed to lay progeny. The progeny of the recovered worms were then reimaged, and were confirmed to be from the *atlastin* population identified by the smaller lipid droplet distribution quantified using the granulometry algorithm from Chapter 2.

The timespan of the loading, imaging, and recovery is on the order of approximately an hour for the device, where over 100 worms are imaged. The worms remain viable in this span of time and can withstand many more hours within the device so long as they do not become dehydrated because the Pluronic stays gelled at room temperature. Therefore, to prevent dehydration the analysis of the phenotype must be done after imaging but before

removing the glass slide. The timespan of processing and phenotyping the images do not require a reduction in time as compared to previous experiments. This gives flexibility to the amount of analysis and quantification necessary to properly phenotype the worms.

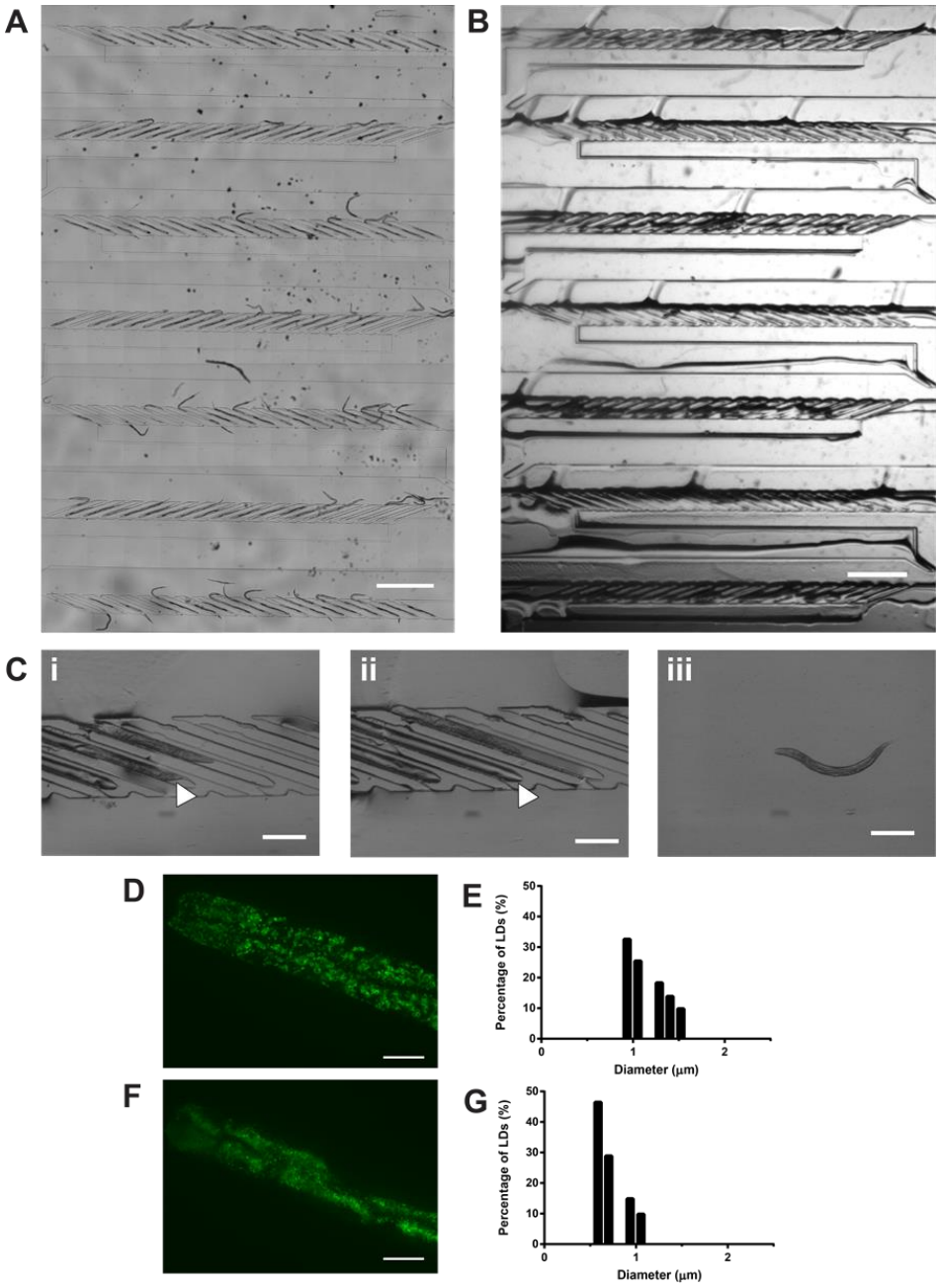

Figure 4-4. Recovery of select worms from worm array device. A) Device loaded with a mixed population of worms, where the Pluronic hydrogel has already been introduced, and the compression sealing sheets have been removed. (Scale bar =

1mm) B) Shows the same device in A once the cover slip is removed. The hydrogel causes for refraction to not allow easy visualizing of the worms. C) At higher magnification it is possible to see that worms are present in the traps after the coverslip has been removed. The white arrow indicates the worm that was selected for recovery (i), and the same trap is seen empty after the recovery (ii), and the worm is recovered on to an NGM plate (iii). (Scale bar = 100 μm) D) Shows a representative image with the wild type lipid droplet. (Scale bar = 20 μm) E) Shows the granulometry output of the lipid droplet distribution for the wild type worm in D. F) Shows a representative image of an *atlastin* mutant with smaller lipid droplets, which was targeted for recovery. (Scale bar = 20 μm) G) Shows the granulometry output of the lipid droplet distribution for the worm in F, where the lipid droplets are smaller.

The proof-of-concept experiment using a mock screen shows the ability of this procedure to be utilized for any screen of choice. The advantage of this selective recovery system over a serial sorting system is the ease of manipulating the device without having any external pumps or valves. This system can be imaged on most microscopes with upright or inverted configurations, and the ability to recover mutants of choice is precise, as compared to the serial sorting device where worms must be flushed with a great amount of solution and there is a chance that the worm may become adhered to the tubing and not necessarily flow through in the order sorted. With our system, one can be confident that the phenotype observed during imaging is the phenotype that is recovered and later analyzed. Although it is a batch process, while one device is being imaged, the next device can be prepared, and thus lost time is minimized. This system is self-contained, and due to not requiring automated controls, or pumps, would be a great addition to laboratories that conduct screens. Additionally, select ablation, or optogenetics can also be performed and selected phenotypes could be recovered for further analysis. The universality of this method allows for a larger audience to utilize this device and conduct complementary studies in many fields.

4.3.2 Drosophila melanogaster embryo imaging and selective recovery

Next, we explored the use of this technique with *D. melanogaster* embryos in microfluidic devices. *D. melanogaster* embryos are a model that can be used to study developmental genetics by monitoring pattern formation and morphogenesis[49]. As compared to imaging embryos on pad, current studies of *D. melanogaster* embryos in microfluidic devices allow for precise orientation and the ability to analyze the effects of various stimuli on development[49,196]. Studies where embryos are imaged and then allowed to develop through larvae and fly stages have only been possible thus far when imaging on pad[197]. The combination of reversibly sealing a microfluidic device with biocompatible hydrogel now allows for the ability to benefit from the advantages of microfluidics, but allow for longitudinal studies.

For the recovery of *D. melanogaster* embryos, various steps are taken as seen in Figure 4-5. First, the microfluidic device[196] was loaded with embryos in PBS and Triton X solution (Figure 4-5A). The device was held in place with the compression seal and a hole in the acrylic located in the area of the array to facilitate loading by prodding the PDMS with a pipette tip as stated in Levario, *et al*[196]. Because exposing *D. melanogaster* embryos to cold treatment causes abnormalities[198], the Pluronic solution could not be used. Instead, we used sodium alginate with calcium chloride, which gels at room temperature once the two solutions become in contact. Quickly flowing solutions of sodium alginate and then calcium chloride allowed for the hydrogel to become crosslinked once in the device (Figure 4-5B). Once all of the hydrogel has cross-linked, the device can be removed from the compression seal by removing all of the outside screws (Figure 4-5C). At this point the device is held in place, and the coverslip is available for high resolution imaging. After

imaging, the coverslip is removed and the device features and embryos in the traps are accessible (Figure 4-5D). Using a platinum wire, the hydrogel structure can be removed from the PDMS and placed on an agar plate (Figure 4-5E), and applying slight pressure releases each embryo from the hydrogel (Figure 4-5F). Here, all of the embryos are still in place; therefore, the identity of each embryo is known and can be associated with the appropriate image. The embryos can be easily manipulated or moved to individual plates for further analysis. Because the emrbyos are still developing within the egg, the timespan to phenotype and recover the embryos can be as long as two days. However, like the recovery of worms, the embryos must not become dehydrated; therefore, the coverslip must stay on the device until recovery decisions for specific embryo phenotypes have been completed. This assures that viable embryos can be recovered and develop as expected.

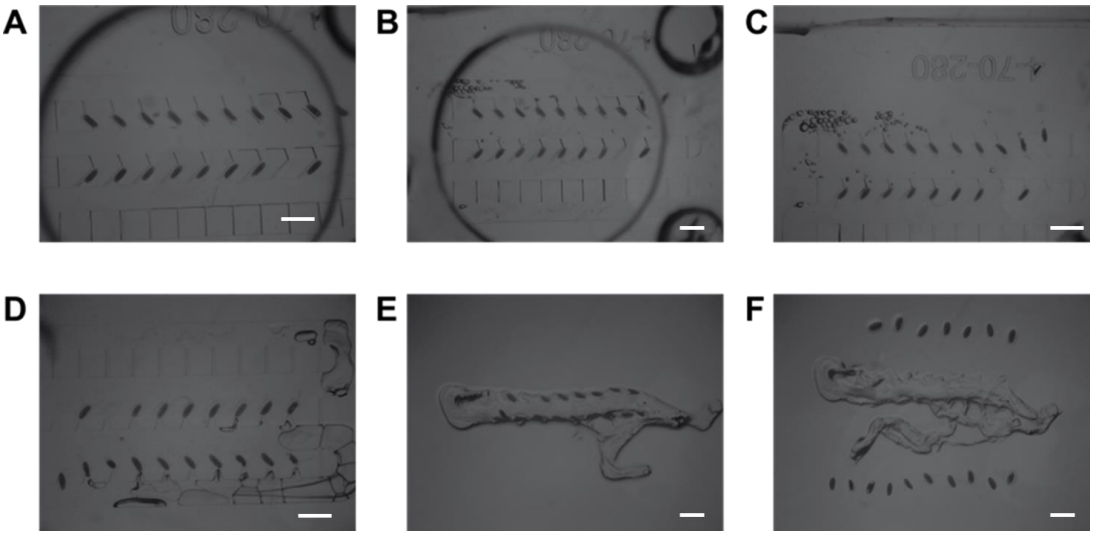

Figure 4-5. Selective recovery procedure for *D. melanogaster* embryos. A) The device is held together using the compression seal, and the embryos are loaded in the individual traps. B) Once embryos are loaded, a solution is added where alternating sodium alginate and calcium chloride are loaded until gelation occurs throughout the device. Due to the gelation, there may be formation of bubbles during this process. C) Once the hydrogel has solidified, the compression seal can be removed, and the device with be maintained adhered to the coverslip, so standard

microscopy images can be captured. D) After imaging, the coverslip is then removed and FC 40 oil is added to the exposed device to prevent dehydration of the embryos and hydrogel solution. E) Using a metal pick, the whole hydrogel structure can be removed from the device and placed on an agar plate, maintaining the embryos in the identifiable positions. F) Using the same pick, the embryos are removed from the hydrogel by applying slight pressure to the bottom interface between the embryos and the hydrogel. This allows for precise identification of the embryos to occur for further longitudinal studies. (All scale bars = 1 mm)

To show that we can identify select embryos from imaging through postembryonic development, a device was loaded and filled with a hydrogel solution as stated previously (Figure 4-6A), imaged on a spinning disk confocal microscope, and then embryos were allowed to hatch after recovery. The developing embryos were imaged for 3 hours, and embryos had both normal and abnormal development as seen by the histone::GFP marker on the nucleus during stage 4 through gastrulation and beyond (Figure 4-6B). The individual embryos were then recovered with known identities (Figure 4-6C, i), where the correlation between the images and the specific embryo could be assessed. The embryos were allowed to develop for 2 days on an agar plate at 25ºC (Figure 4-6C ii), and the missing embryos were determined to be embryos that hatched into viable larvae, which were found on the same plate (Figure 4-6D). Non-surprisingly, the embryos that hatched had been identified with normal development when previously imaged and embryos that showed poor development as seen by the delamination of nuclei during development did not hatch (Figure 4-7).

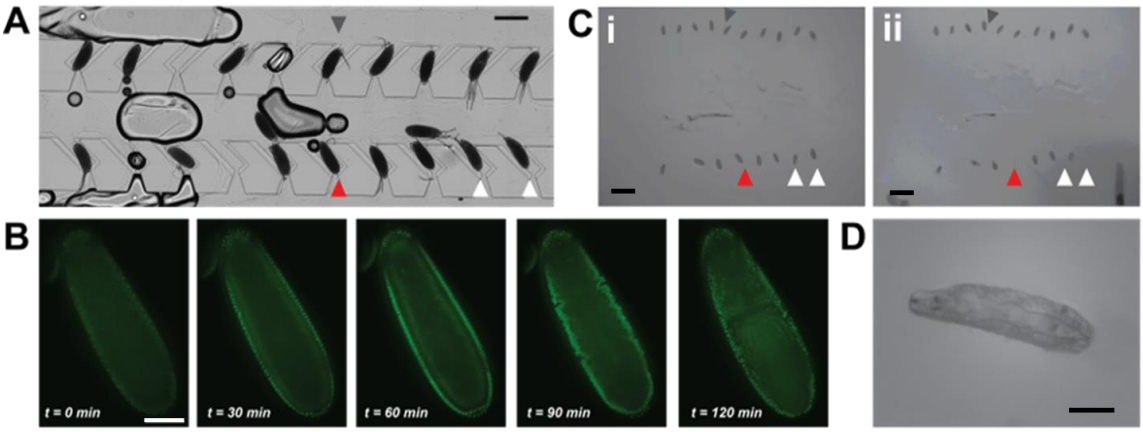

Figure 4-6. Imaging and recover of select *D. melanogaster* embryos. A) Device overview of the embryos that will be imaged, after the hydrogel solution has been loaded. The white arrows signify embryos that after recovery hatched, and the red arrow signifies the embryo that hatched and images were used for this figure. (Scale bar = 500 µm) B) The embryo identified with the red arrow in A, is imaged for 2 hours where normal development is visible through the nuclear divisions from stage four, where furrow formation and typical development is visible. (Scale bar = 100 µm) C) i) Shows the embryos recovered from the device after imaging, and ii) shows the same plate 48 hours later, where 3 embryos are missing indicating that the specific embryos hatched. (Scale bar = 1 mm) D) After being loaded in the device and imaged, the hatched larvae are found on the plate showing typical morphology of normal development with visible mouth hooks and standard locomotion. (Scale bar = 250 µm)

The manual manipulation of *D. melanogaster* embryos can be difficult, and the ability to utilize the microfluidic device for placement and identification, but still be able to recover the specific embryo is of great advantage. Perturbations or mutations can be studied from development in the embryo, and then analysis on the larvae or developed fly can be done where the developmental change can be linked to phenotypic changes in the fly later on in the lifespan. Because this platform is independent of strain, and the microfluidic device allows for the easy manipulation and stimulation of the embryos, the number of experimental conditions that can be easily done expands. The main advantage of this system over a serial device that images the embryos and allows for proper sorting

of select phenotypes is that in developmental experiments, many hours are necessary to identify mutations. In this device, embryos can be imaged in parallel, analysis for selecting the proper mutant can still take place, and the embryo can be recovered to further analyze the individual or the future population.

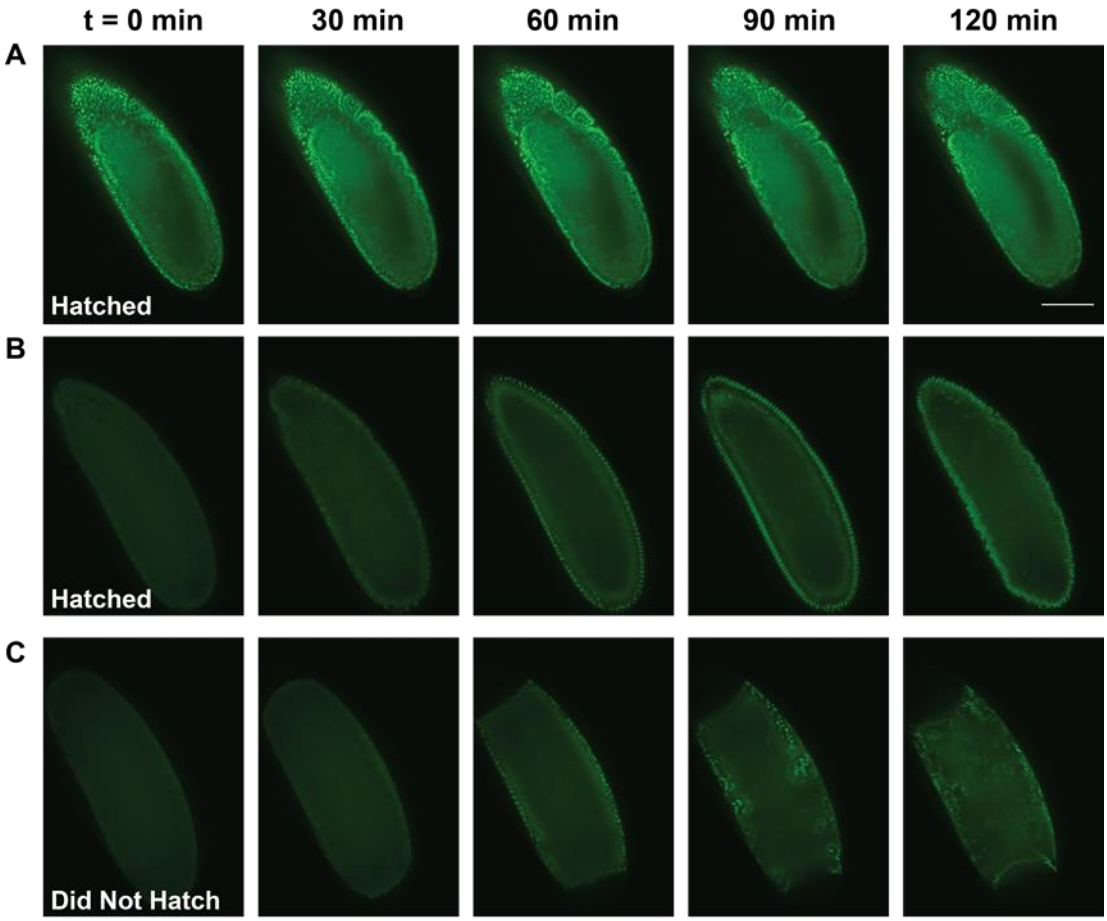

Figure 4-7. Developmental time-lapse of *D. melanogaster* embryos, where the embryos were recovered and hatching was correlated with proper nuclear division. A, B) Show example images two different embryos that were imaged for 2 hours in the microfluidic device, selectively recovered, and determined the embryos had hatched. C) Shows an example of an embryo that did not hatch, where the nuclear delamination was indication that the embryo was not undergoing proper development. (All images at same scale. Scale bar = 100 μm)

4.3.3 Stem cell aggregate imaging, select recovery, and analysis

To further demonstrate the applicability of our method, we applied our technology to stem cell aggregate recovery. In performing the various steps of our method, there are additional challenges when handling stem cell aggregates that are not present with the other organisms explored in this chapter. The most challenging aspect of handling the cell aggregates is that the aggregates although large, can be easily deformed. Thus, when filling the microfluidic device with a hydrogel solution for recovery, the hydrogel viscosity needs to be low enough to flow through the device but must prevent the aggregates from squeezing through the device restriction channels at the back of each culture chamber. However, the viscosity must be high enough to immobilize aggregates for selective recovery.

Because the aggregates need to be cultured at 37^{o}C, we took advantage of a different hydrogel for this application. Low melt agarose is liquid at 37^{o}C and can flow through the devices if maintained at 37^{o}C. The agarose then solidifies at room temperature within a few minutes. This is advantageous to using the two hydrogel cross-linking method stated earlier. Since the two hydrogel cross-linking system gels on contact, the two fluids must be flowed through the device at a faster rate, and switching between solutions must be done quickly. This may cause for the aggregates to deform, squeezing through the restrictions of each chamber. However, in using the low melt agarose, only one solution is flowed through the device, and it can be done at a slow rate because the agarose is liquid while the device and the solution are maintained in the incubator at 37^{o}C. The reason the low melt agarose cannot be used with the previous organisms stated is that 37^{o}C would heat shock both *D. melanogaster* as well as *C. elegans*, and if experimental procedure calls

for the recovery of these organisms, having a step that can cause damage to the organism is not ideal. The various systems and biocompatible hydrogels used are summarized in Table 4-1.

Table 4-1. Summary of model system with respective biocompatible hydrogel used for selective recovery

Model System	Hydrogel	Gelation Temp (°C)
C. elegans worms	Pluronic F127	> 4°C
D. melanogaster embryos	Sodium Alginate + Calcium Chloride	Once in contact, room temperature
mESC aggregates	Low Melt Agarose	< 37°C

The device is loaded with previously formed day-1 stem cell aggregates, where the compression seal does not hinder the ability of the device to be completely loaded with a single aggregate per culture chamber (Figure 4-8A). The aggregates were then cultured in the device for 5 days (Figure 4-8B) allowing for the aggregates to grow in each culture chamber (Figure 4-8B). To recover the aggregates, similarly to how the device is loaded and perfused, low melt agarose at 37°C is loaded into the pipette at the inlet, while in the 37°C incubator the agarose is slowly driven via gravity driven flow for approximately 10 minutes. Next, when the device is removed from the incubator the agarose solidifies within a couple of minutes. This allows for the removal of the coverslip with all the aggregates staying in the respective chambers in the PDMS device (Figure 4-8C). Without the addition of the hydrogel, the aggregates have a tendency to easily move from the chambers to the serpentine, losing the specific positioning that allows for the selective and precise recovery of a particular aggregate. To isolate individual aggregates for further analysis, a 1 mL pipette with PBS is used to aspirate the aggregate in the specific chamber desired (Figure

4-8D). This causes no harm to the aggregates, and can be easily achieved without additional training. Because the aggregates have been fixed to facilitate antibody staining, the temperature does not have to remain at 37^{o}C and the imaging and recovery time are not critical. The prevention of dehydration can be accomplished even when the coverslip is removed with the addition of liquid agarose above the traps.

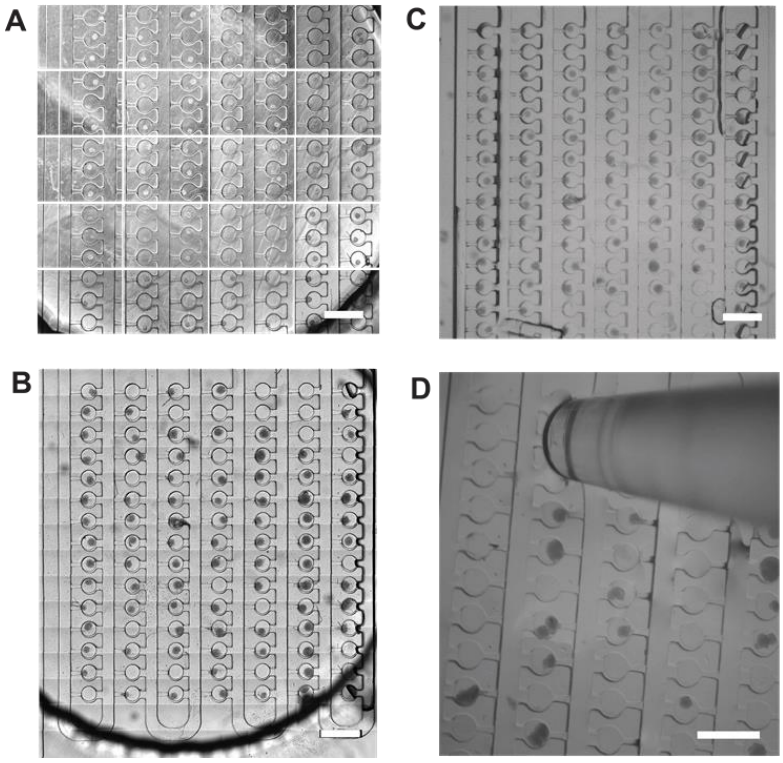

Figure 4-8. Stem cell aggregates stay in traps throughout culture in the compression sealed device even after the hydrogel solution is flowed through and the coverslip is removed. A) Shows a compilation of images to show an overview of a loaded device with day-1 stem cell aggregates. B) Shows an overall image of the same device imaged in A after 5 days of culture. C) Shows the same device from A and B after the hydrogel has been added and the coverslip has been removed. In comparing A, B, and D, it is possible to note that no stem cell aggregates were lost in the process. D) Shows the method in which aggregates are selectively recovered from a device by using a pipette tip to aspirate individual stem cell aggregates. (All Scale bars = 1 mm)

To validate this ability to selectively recover single aggregates from the device without damaging the aggregates, we chose three distinct positions in the device to show the selectivity of the method. These three positions included two positions that are in close proximity to each other, in order to demonstrate that the recovered aggregates do not need great separation to be selectively recovered. The third position chosen was located in the middle of the device where all the traps around the aggregate of choice were filled. This position shows that only the particular aggregate and no other aggregates are recovered through this selective recovery method (Figure 4-9A i, ii, iii). Aggregates loaded at day-1 (Figure 4-9B) remained in their traps through day-5, and increased in overall size as expected (Figure 4-9C). Using the pipette method previously stated, these individual aggregates were recovered on to a coverslip with a PBS droplet without showing any signs of damage (Figure 4-9D). This assures that post culture analysis can be performed.

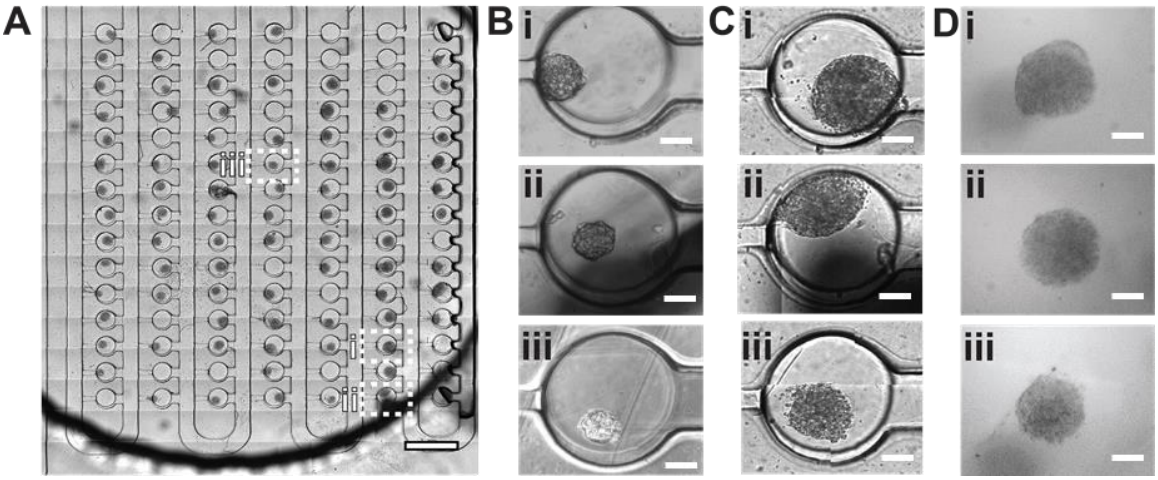

Figure 4-9. Selective recovery of individual stem cell aggregates. A) Shows an image of the device loaded with stem cell aggregates after 5 days of culture, where three locations were outlined to show aggregates that were recovered. (Scale bar = 1 mm) B) Shows three different day-1 aggregates from three different locations in the device as shown in A. (Scale bar = 100 μm) C) Shows the same aggregates in B on day-5 of culture. (Scale bar = 100 μm) D) shows the same three aggregates individually recovered and undamaged on to a droplet of PBS on a coverslip. The

proximity of aggregates i and ii shows that there is great accuracy in the selectivity of aggregates, even if traps are near each other. Aggregate iii was a third example where the aggregate was in the middle of the device where there were aggregates loaded in all traps around and only one aggregate was recovered from the correct location. (Scale bar = 100 μm)

Next, the individual aggregates that were recovered from the device could also be easily imaged on the lightsheet microscopy system (Figure 4-10). The advantage of being able to image on the lightsheet microscope compared to traditional confocal microscopes, is that the aggregate can be easily rotated and imaged from multiple viewpoints because the aggregates are mounted in agarose on a capillary. The staining of various nuclear pluripotency markers including Hoechst, Nanog, and Oct-3/4 can be seen from various angles to better phenotype the specific aggregate. Further analysis and image processing can quantitatively determine the variations in these aggregates, where the increased information from various sides of the aggregates will enhance current phenotypic conclusions that are determined through traditional one sided imaging.

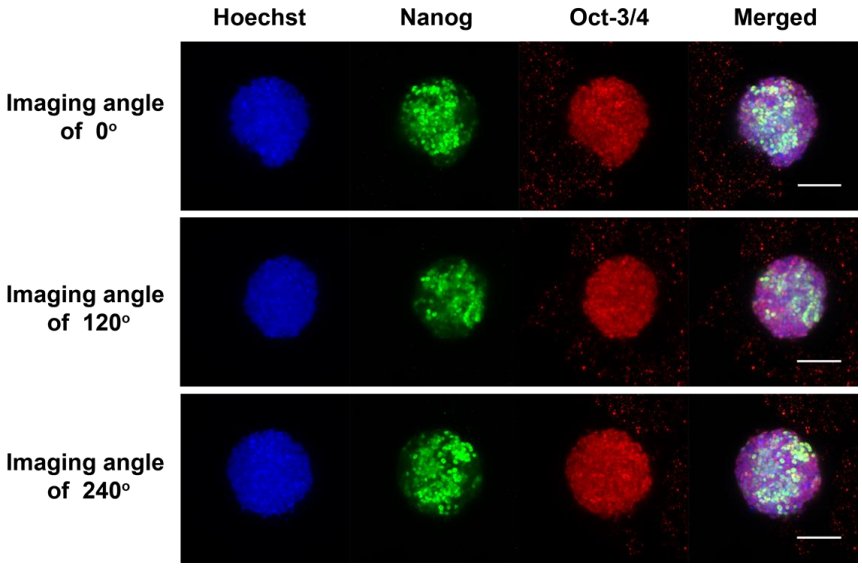

Figure 4-10. Lightsheet microscopy images of the day-5 stem cell aggregates recovered in Figure 4-9 B, C, D ii. Expression of Hoechst, Nanog, and Oct 3/4 which

are in blue, green, and red, respectively, along with a merged image are shown. A z-stack, with a step size of 5 μm, of the aggregate was captured at three different angles allowing for multiple areas of the aggregate to be imaged, and the maximum projection of each channel is shown. Imaging the aggregates from multiple views could not previously be performed for aggregates cultured in a microfluidic device. (Scale bar = 500 μm)

Shown by these sets of experiments, a powerful aspect of this platform is that it allows for imaging to be captured from more than one direction. Typically, to selectively recover aggregates for mutliview imaging, aggregates must be loaded and cultured in well plates, where single aggregates are loaded and the media is exchanged for each well for 5 days without disrupting or losing the aggregate. This is a tedious and very labor intensive process, which also does not allow for the same conditions from one aggregate to the next, due to the separation into different wells. Using our platform, we have the advantages of being able to individually recover aggregates, similar to what is possible in well systems, combined with the benefit of microfluidics where loading, media perfusion, and general culture procedures are streamlined and allow for the aggregates in the whole device to be exposed to the same environmental cues.

4.4 Conclusion

Although our method has the flexibility to be applied to different systems, there are a few limitations. Our list of limitations may not be exhaustive, however, it provides some bounds of this system. One limitation is the lower size limitation of the organism we are capable of recovering. For example, the concept of integrating a hydrogel solution into an array device would be difficult to incorporate with the cell trap array[199]. Due to the small dimensions of the device, where each trap is approximately 10 μm by 10 μm, and the restriction channel is 2 μm, the compression seal may cause for these small features to

collapse. Additionally, the cells are deformable and can withstand much lower pressure, as compared to the aggregates which are much larger. The much lower pressure is necessary to prevent the cells from leaving the traps through the restrictions channel. This would make integrating a hydrogel solution very difficult. Recovery of individual cells would also be very difficult due to the small scale. Another limitation is the complexity of the design. Because the device is sealed through compression, there must be sufficient PDMS surface to bond to the glass substrate. A failure to do so causes for leaking between channels when low pressure is applied. Lastly, a third limitation is the overall size of the microfluidic device that can be sealed using compression. If the device is too wide, the compression can only take place on the edges of the slide, and thus the device cannot be evenly compressed in the center causing for leaking to occur.

While there may be some limitations, the coupling of reversibly bonded array microfluidic devices with a hydrogel solution has increased the spectrum of experimental possibilities while maintaining the benefits of high-throughput microfluidics. The generalizability of the process was demonstrated through the application of this method to three different microfluidic devices with three different model systems at different size scales. Additional characterization of the selectively recovered animals can lead to correlation between what can be seen through microscopy and also what could be determined through end-point assays. Due to the simplicity of the system, adoption by various laboratories that do not currently have microfluidic expertise can fully embrace this technology with the current systems and set ups already in place. The ability to sort and selectively recover animals of interest without moving components or added software allows for a simpler experimental process that can lead to new conclusions. Because this

integrative approach can be applied to other microfluidic devices and organisms, the opportunities to explore untested hypothesis have broadened allowing for an innovative way to study complex systems.

CHAPTER 5. CONCLUSIONS AND FUTURE DIRECTIONS

5.1 Thesis Contribution

The goal of this thesis was to determine methods to better image, quantify, and characterize differences in *C. elegans* lipid droplet morphologies. The integration and modification of existing methods has been key to increasing the throughput, handling, and phenotype characterization of lipid droplets. Methods developed throughout this thesis provide a framework to increase the productivity and density of information available for lipid droplet phenotypes. The applications of these integrative platforms has provided the ability to begin answering biological questions as they pertain to lipid droplet morphologies, fat storage, and metabolism.

Chapter 2 describes the development of a platform that is capable of quantifying the lipid droplet size distribution in both clear high quality images, as well as low fidelity images. The power of analyzing low fidelity images lies in that lipid droplet phenotypes can also be classified in traditional epi-fluorescent microscopes which are the workhorse in a typical biological laboratory. This ability expands the number of scientists that are now able to conduct these experiments, even when an expensive high power microscope is not available. In addition to characterizing low fidelity images, the amount of time to quantify the lipid droplet size distribution was reduced by two orders of magnitude. Applying the principles of granulometry have allowed for a higher throughput method to calculate a semi-quantitative distribution that allows for characterization of phenotypes at the population level. In increasing the sample sizes that can be imaged for each condition, more comparisons can be accomplished in less time. The conclusions based on the phenotype

differences also hold more statistical power and higher confidence due to the larger sample sizes.

This method was compared to other segmentation methods, and although some methods may allow for quantification of circular objects, our modified granulometry method was the only one that could output a size distribution without any parameter optimization. The benefit of this parameter-free method is that the phenotype that is being quantified does not have to be pre-defined. Because parameters did not have to be optimized for each worm image, integrating this quantification method with microfluidics allowed for the first fully automated genetic screen for lipid droplet phenotypes. In this screen, a mutant was isolated that suppresses the *atlastin* mutation, where the lipid droplet morphology phenocopies that of wild type. This can lead to further information about gene-gene interactions in determining how *atlastin* functions.

To further demonstrate the ability of the modified granulometry algorithm to analyze more than circular objects, I demonstrated that the granulometry algorithm developed could also be used to differentiate between porosity phenotypes. In analyzing the endoplasmic reticulum of worms, it is very difficult to quantify a standard texture or mesh size because the phenotype is non-uniform. Reversing the polarity of the image allows for the pores to be quantified as objects, and a semi-quantitative porosity distribution can be calculated. This allowed for the difference between an *atlastin* mutant from a wild type mutant to be quantitatively differentiated, which had not been previously done. This now gives the opportunity to explore quantitative changes in endoplasmic reticulum phenotypes as well.

In Chapter 3, we used the quantitative method developed in Chapter 2 to further extend the reach of the lipid droplet characterization to changes due to differences in diet. With the availability of a knockout *E. coli* library, the effects of diet changes on fat storage in *C. elegans* can be more systematically tested. In applying existing microfluidic and microscopy technology to the quantitative method, I was able to conduct a pilot screen of the library to begin to determine dietary affects in fat storage. Due to subtle lipid droplet size changes from different diets, an analysis pipeline that quantified differences in populations was also developed. This gave the opportunity to study and find diets that contribute to changes in lipid droplet size distribution.

After determining the diets that contributed to the changes, further experiments were conducted to start to determine the metabolite changes that contributed to the lipid droplet changes. I found that the *E. coli* knockout, *prpC*, causes for an accumulation in propionic acid that contributes to a decrease in lipid droplet size. This information was further demonstrated by the reduction in lipid droplet size in animals that were fed the parent strain of the *E. coli* library with supplemented propionic acid. This can lead to more information about the pathways that lead to the reduction in lipid droplet size which may someday be able to be applied to humans as well. Propionic acid is significant in human diets as it has been linked to decreases in fatty acid content in the liver and plasma, where the increased production of propionic acid in the gut by microbiota may be beneficial in the prevention of obesity and type 2 diabetes[200]. The ability of this pilot screen to uncover metabolites that have been shown to cause a variation in fat content show that the screening of the whole library may lead to the discovery of different metabolite effects on diet not previously known.

Finally, in Chapter 4, we expand that ability of the microfluidic device used in Chapter 3 to allow for selective recovery of worms from a static device. Although recovery of worms from microfluidic devices have been previously performed, as it was in Chapter 2, the devices that are used for the recovery either do not allow precise animal recovery, or there is additional hardware and software needed to control fluid flow and recovery. The ability to perform a lipid droplet screen on a microscope without the addition of external valves or software would also be greatly beneficial to applying the methods to other laboratories. In sealing the worm array device with a compression seal instead of irreversibly plasma bonding the device to glass, it allows for the opening of the microfluidic device after imaging and culture. Filling the channels with a hydrogel prevents the worms from moving from their positions and thus precise recovery is possible. This static method allows for the imaging of over 100 worms per device, with selective recovery allowing for biologist to benefit from the high-throughput ability of microfluidics, without the expense and complexity of pressure valves and customized online software analysis.

This concept of a compression sealed array device with the addition of a hydrogel solution to allow for imaging and selective recovery of animals was also successfully applied to both *D. melanogaster* embryos and stem cell aggregates. *D. melanogaster* embryos can now be imaged using a microfluidic device, successfully recovered, and allowed to develop normally through larvae and fly stage. With stem cell aggregates, this opens up a new realm of experiments that before were very labor intensive and technically infeasible. Single aggregate cultures can be currently accomplished in independent wells, where they can be recovered but media exchange and culture are difficult, or in irreversibly bonded microfluidic devices that allow for ease in media exchange, but do not have the

ability to recover and analyze cell aggregates beyond imaging from a single plane. Using this compression sealing system with the integration of a biocompatible hydrogel to maintain the aggregates in place, it is now possible to use the benefit of microfluidics with the ease of media exchange and other factors, as well as lightsheet microscopy that allows for multiple views of the cell aggregate. This integrative method can also now allow for single aggregate analysis, such as qtPCR, after culture in a microfluidic device, which was not previously possible.

In summary, this thesis uses the microfluidic devices, automation techniques, and analysis methods in the lab and expands on their applicability, as well as integrates multiple methods to further study lipid droplets in *C. elegans*. The use of the developed techniques to other organisms studied in the lab also demonstrates the vast applicability and potential power of the method. Overall, the vision is that the quantitative approaches in this study and the device method developed can contribute to a new array of experiments possibilities that will lead to new innovations and biological discoveries.

5.2 Future Directions

In this section, I discuss the possibilities of the next direction for future work that compliments the work in this thesis. The focus is on the continued studies that can now be accomplished with the ground work laid in this thesis. This is by no means an exhaustive list of all the potential directions that these methods and approaches can take, but it does lead the discussion in what the potential next steps could be.

5.2.1 Genetic screen on endoplasmic reticulum phenotype using the modified granulometry algorithm

As an extension of what was shown in Chapter 2, conducting an automated forward genetic screen on the endoplasmic reticulum using the modified granulometry algorithm is now possible. Phenotypic differences between the *atlastin* mutation and wild type is difficult to quantify but can be somewhat discernible by eye. In using the algorithm developed, it is possible to sort potentially interesting phenotypes in an unbiased way. The endoplasmic reticulum is where lipid droplets are formed, so it is not surprising that *atlastin* affects both the endoplasmic reticulum and lipid droplets. More information about the *atlastin* mutation may be uncovered through further studying the variability in the endoplasmic reticulum phenotype through a suppressor screen similar to what was accomplished in Chapter 2.

To accomplish this experiment, criteria to discern between different phenotypes is necessary. The knowledge from this screen could increase the knowledge on how the *atlastin* mutation manifests and what genes contribute to a change in endoplasmic reticulum morphology. It would also be interesting to compare the differences in genetic variations that may cause differences in the endoplasmic reticulum as compared to differences in lipid droplet size.

5.2.2 Completing the Keio E. coli Consortium library diet screen on C. elegans

One of the clear next steps for the process developed in Chapter 3 is to complete the diet screen with the complete Keio library. The completion of the full library can be accomplished using the same procedures outlined in the paper. For the imaging time there

are approximately 40 plates, and the timeframe to image each plate is approximately 48 hours of loading in the device and imaging of approximately 50 worms. To complete the whole library, imaging for only a year is necessary, where it totals to 50 weeks of imaging, where imaging is conducted 8 hours a day and 5 days a week. Although a year may appear as a lengthy amount of time, this has been significantly reduced from what it would have been using traditional methods. One bottleneck is the imaging time. Although each worm takes approximately 4 seconds to image, the large number of conditions and worms per condition quickly multiplies. Advancements in imaging ability, such as a larger field of view where two worms can be imaged at a time or automated selection of the region of interest can potentially reduce this timeframe in the future.

An alternative step is to utilize a candidate method, and select specific knockouts that have previously caused changes to *C. elegans*. In literature, Watson, *et al.*, used the Keio *E. coli* library to determine dietary effects on life history traits[180]. They identified more than 20 knockouts that contributed to changes, and this could be a list to begin testing[180]. Of the knockouts they identified, two were studied in Chapter 3, and both showed dramatic effects on lipid droplet sizes. Continuing through the list of knockouts could be conducted in less than two weeks, and a vast amount of information can be determined from those experiments.

5.2.3 Determining biological implications of metabolite effects on lipid droplets

Additional research that can be continued from Chapter 3 is evaluating the lipid droplet morphology changes due to the addition of metabolites to the diet when fed certain knockouts. The two metabolites explored were vitamin B_{12} and propionic acid. Additional

metabolites to test include those investigated in Watson, *et al*[180]. Additionally, the identified knockouts that contributed to changes in lipid droplet morphology could be analyzed by mapping the genes onto bacterial metabolic networks[180]. The focus can be placed on genes that regulate metabolic operons, prioritizing genes encoding for metabolic enzymes, transporters, and transcription factors[180]. These metabolites can then be used to supplemented the diets. Experiments could also be conducted where instead of imaging the effects on the *dhs-28 C. elegans* mutant, a new experiment can be conducted using wild type worms. This would expand on the information available about the interaction between the diet, supplemented metabolite, and genetic composition of the worm.

5.2.4 The integrative compression seal and biocompatible hydrogel system increase potential for single animal analysis

In Chapter 4, I showed the use of a compression seal system to reversibly bond microfluidic devices incorporated with biocompatible hydrogels in order to selectively recover single animals.

Although various gels were explored in these applications, additional gels can be studied. For instance, the use of shear thinning gels may be advantageous as the properties suggest that at higher sheer the fluid will decrease in viscosity allowing for the fluid to flow through a device. Other biological applications or organisms may benefit from the use of shear thinning gels that may better suit the culture and imaging needs.

For *C. elegans*, there are existing devices that can sort and recover worms; however, the benefits of our system will enable easier experimental set up, with improved recovery and analysis. With this new integrative system, more scientists may be inclined to utilize

the worm array device instead of the typical agar pad imaging. Experiments, such as screens, can be conducted on microscopes that may not allow for customization due to proprietary software.

As for *D. melanogaster* and stem cell aggregates, the potential experiments that can be immediately accomplished using the methods discussed in Chapter 4 are performing PCR after imaging of the various single animals. In performing PCR, the expression of various genes can be correlated with the resulting phenotypes characterized during imaging. For *D. melanogaster*, more high-throughput imaging can be accomplished with the ability to perturb environmental factors, which cannot be easily accomplished when using agar pad imaging. For instance, the effect of oxygen or alcohol levels during different parts of developments can be evaluated through embryo imaging, as well as post-hatching larval and fly phenotype analysis.

As for stem cell aggregates, Emily Jackson-Holmes from the Lu lab will be continuing biological analysis and optimization in using the developed techniques in Chapter 4. Culture of single aggregates is very difficult in wells, so the ability to culture the aggregates for multiple days in devices allows for ease in culture as well as precise environmental control and media exchange. In using the integrative compression seal and hydrogel solution, these aggregates can now be extracted from the device, and imaging or qtPCR analysis can be conducted. Different differentiation protocols can be tested, and gene expression that correlates with fluorescent imaging patterns can be determined. As compared to what was possible before this approach, this increases the scope of experiments and strengthens conclusions about phenomenon that are occurring on the single aggregate level.

5.2.5 Concluding remarks

In general, with the work in this thesis I hope to empower scientists with methods that could be translatable between organisms and can change the way studies are conducted. The ability to have more efficient, and smarter experiments, will encourage the use of more integrative techniques to better support conclusions that can lead to new discoveries.

APPENDIX A. MODIFIED GRANULOMETRY ALGORITHM

A.1. Image stack conversion and preprocessing

Before preprocessing, acquired images stacks were converted to a single 2D image using the maximum intensity projection of captured focal planes. The converted image was then doubled in size using 2x2 bilinear interpolation and smoothed using an anisotropic diffusion filter, released in the public domain by David Lopes and available for download on MATLAB® Central File Exchange:

https://www.mathworks.com/matlabcentral/fileexchange/14995

Following smoothing, the image was processed using both top-hat and bottom-hat morphological operations; the bottom-hat transformation was subtracted from the sum of the top-hat transformation and the smoothed image. Both operations were performed using a structuring element size of 30 pixels, determined from empirical results. Next, image intensity of the processed image was adjusted using contrast-limited adaptive histogram equalization. This result was contrast adjusted once again to saturate one percent of both low and high intensity values before filling in holes in the image. Holes in this instance refer to dark pixel regions surrounded by lighter pixels.

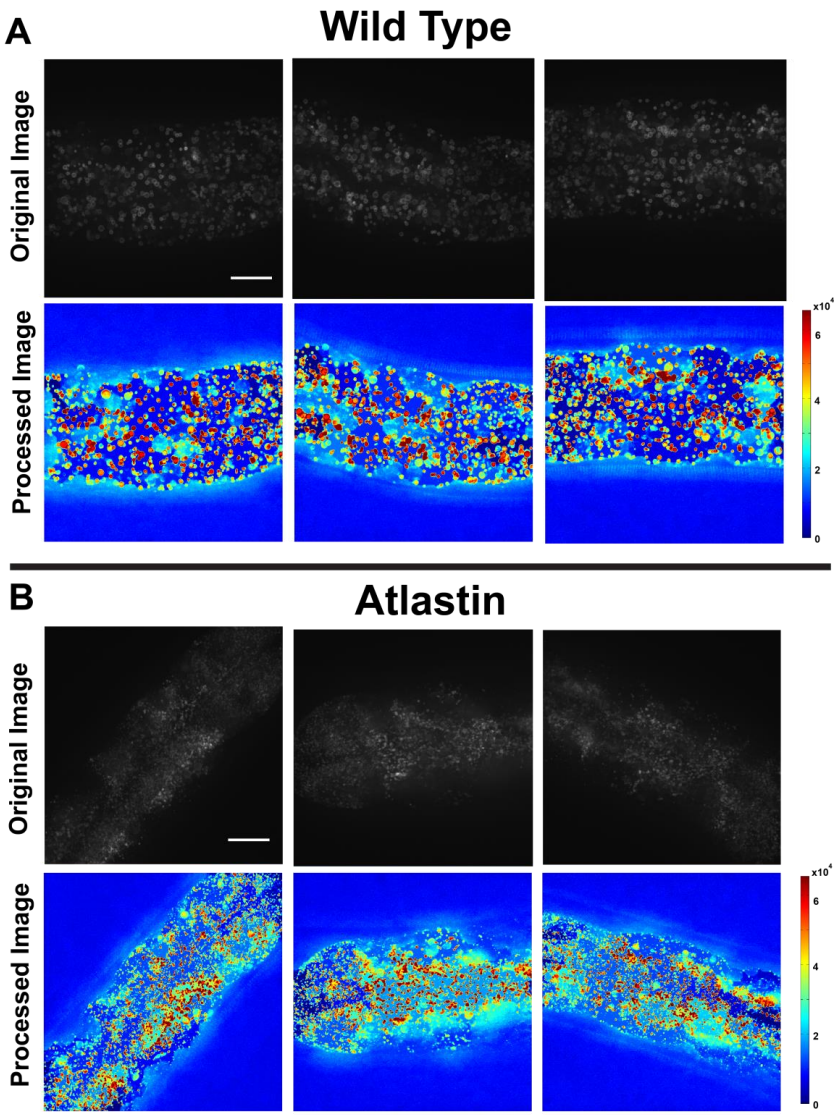

Figure 5-1. Example images of confocal microscopy images and the corresponding pre-processed image that will be used to undergo the granulometry morphological openings. A) Shows three different example images of confocal microscopy images in black and white of wild type worms. The images were pre-processed, and the corresponding images had a jet colormap applied to best show the variations in intensity. The color bar indicates the intensity in the 16 bit image. The brighter red spots correspond to lipids that have been enhanced through the pre-processing algorithm. B) Shows three different example images of confocal microscopy images in black and white of worms with the *atlastin (a015*) mutation. The images were pre-processed, and the corresponding images had a jet colormap applied to best show the variations in intensity. The color bar indicates the intensity in the 16 bit image. The brighter red spots correspond to lipids that have been enhanced through the pre-processing algorithm. (Scale bar = 10 µm)

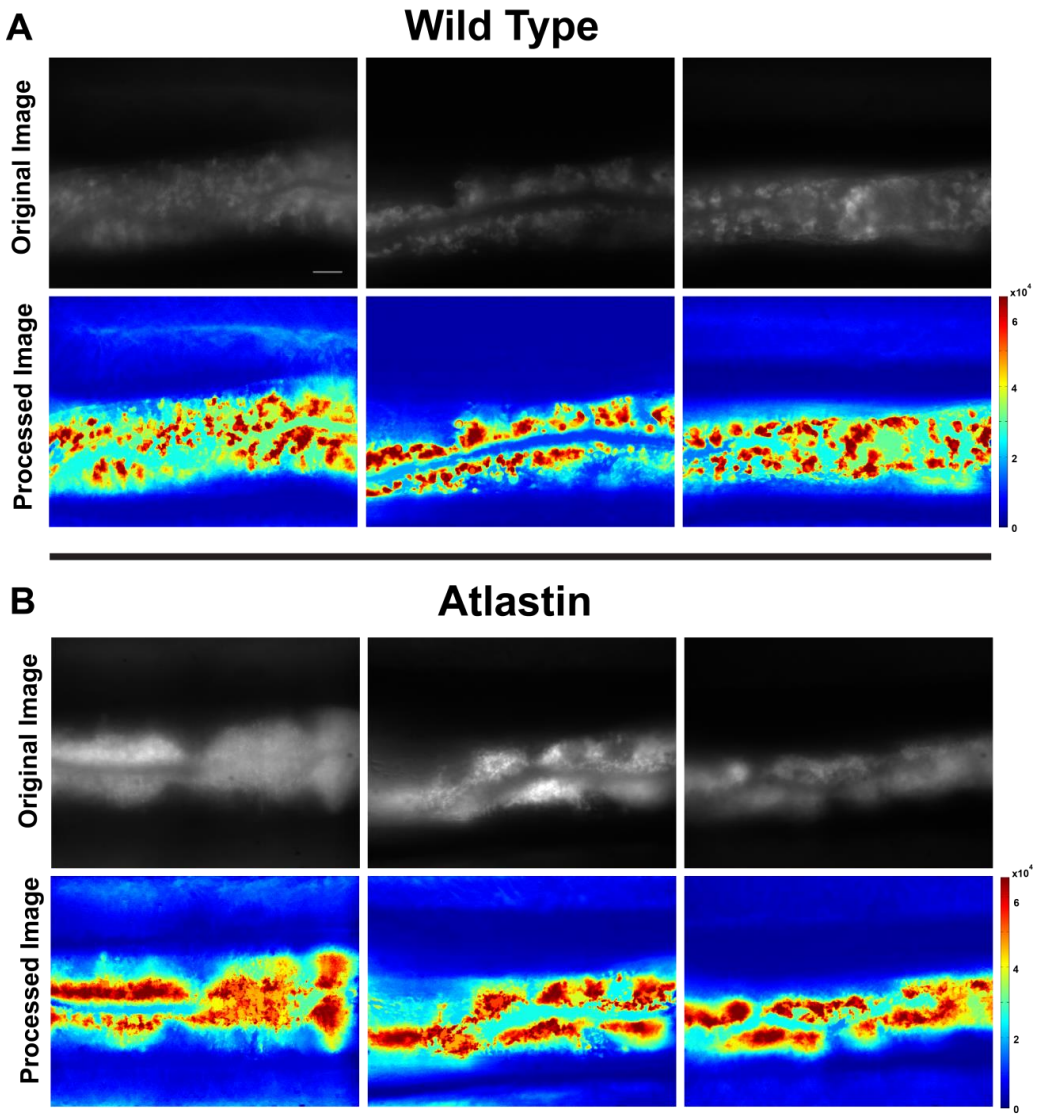

Figure 5-2. Example images of widefield microscopy images and the corresponding pre-processed image that will be used to undergo the granulometry morphological openings. A) Shows three different example images of widefield microscopy images in black and white of wild type worms. The images were pre-processed, and the corresponding images had a jet colormap applied to best show the variations in intensity. The color bar indicates the intensity in the 16 bit image. The brighter red spots correspond to lipids that have been enhanced through the pre-processing algorithm. B) Shows three different example images of widefield microscopy images in black and white of worms with the *atlastin (a015*) mutation. The images were pre-processed, and the corresponding images had a jet colormap applied to best show the variations in intensity. The color bar indicates the intensity in the 16 bit image. The brighter red spots correspond to lipids that have been enhanced through the pre-processing algorithm. (Scale bar = 10 µm)

A.2. Granulometry Algorithm

Granulometry is performed on preprocessed images using standard methods[91,201,202]. The normalized size distribution, $\Phi(\kappa)$, follows Eq. 1 below

$$\Phi(\kappa) = \frac{v[I] - v[I \circ \lambda_\kappa]}{v[I]} \quad \textbf{(1)}$$

where I represents the preprocessed image, v denotes the area or volume computed by taking the sum of all pixel intensities, $\circ$ is the morphological opening operation, λ is the disk structuring element used for morphological processing, and κ is the radius size of the structuring element ($k\epsilon[1,2,\dots,29]$). The normalized size density or pattern spectrum, $d\Phi(\kappa)$, is approximated from the difference of $\Phi(\kappa)$ for each λ_κ, and is seen in Eq. 2

$$d\Phi(\kappa) \approx \Phi(\kappa + 1) - \Phi(\kappa) \quad \textbf{(2)}$$

A.3. Size Analysis

Filtering and estimation of isolated lipids was performed in order to limit analysis to principle sizes. To isolate lipids of a specific size, morphological operations of the preprocessed image were subtracted from each other as in Eq. 3. Once isolated, a binary mask, $M(\kappa)$, was created from the resulting image to remove noise remaining after subtracting images processed by morphological operations of different sizes (Eq. 4). This mask was then applied to isolated lipids to preserve pixel intensity information while removing imaging artifacts, denoted as the filtered lipid image $F(\kappa)$ (Eq. 5).

$$L(k) = (I \circ \lambda_\kappa) - (I \circ \lambda_{k+1}) \quad \textbf{(3)}$$

$$M(\kappa) = \text{BOOL}\,\{L(\kappa)\} \circ \lambda_{\kappa} \quad \textbf{(4)}$$

$$F(\kappa) = L(\kappa) \times M(\kappa) \quad \textbf{(5)}$$

Using the processed lipid images, a filtered size density, $G(\kappa)$ (Eq. 6), was created by setting an empirical threshold (T) to one standard deviation over the mean of $d\Phi(\kappa)$ (Eq. 7). Values for $d\Phi(1)$ and $d\Phi(2)$ were ignored during threshold calculation and for $G(\kappa)$ as lipids in this range are non-existent according to smallest values observed in Klemm *et al*[164].

$$\mathrm{G}(k) = \begin{cases} 0, & d\Phi(\kappa) < T \\ \upsilon[F(\kappa)], & d\Phi(\kappa) \geq T \end{cases} \quad \textbf{(6)}$$

$$T = \overline{d\Phi} + \sigma_{d\Phi} \quad \textbf{(7)}$$

A.4. Data Normalization

The last steps of lipid analysis normalize the filtered size density by structuring element area to estimate the quantity of lipids present, $\boldsymbol{\Lambda(\kappa)}$, and by the sum of lipids detected during analysis to approximate the lipid distribution profile, $\boldsymbol{\Upsilon(\kappa)}$ (Eq. 9). In Eq. 8 below, $\boldsymbol{\alpha(\kappa)}$ represents the number of pixels present or area for each structuring element.

$$\Lambda(\kappa) = \frac{G(\kappa)}{a(\kappa)} \quad \textbf{(8)}$$

$$\Upsilon(\kappa) = \frac{\Lambda(\kappa)}{\sum \Lambda(\kappa)} \quad \textbf{(9)}$$

A.5. Example image depicting granulometry algorithm

Granulometry is performed through the series of sequential morphological openings. A morphological opening is composed of an erosion followed by a dilation of the image. In applying structuring elements of increasing size to perform the erosion and the subsequent dilation, the size information of the objects in the image can be obtained. An example using lipid droplet structures is shown in the following figure:

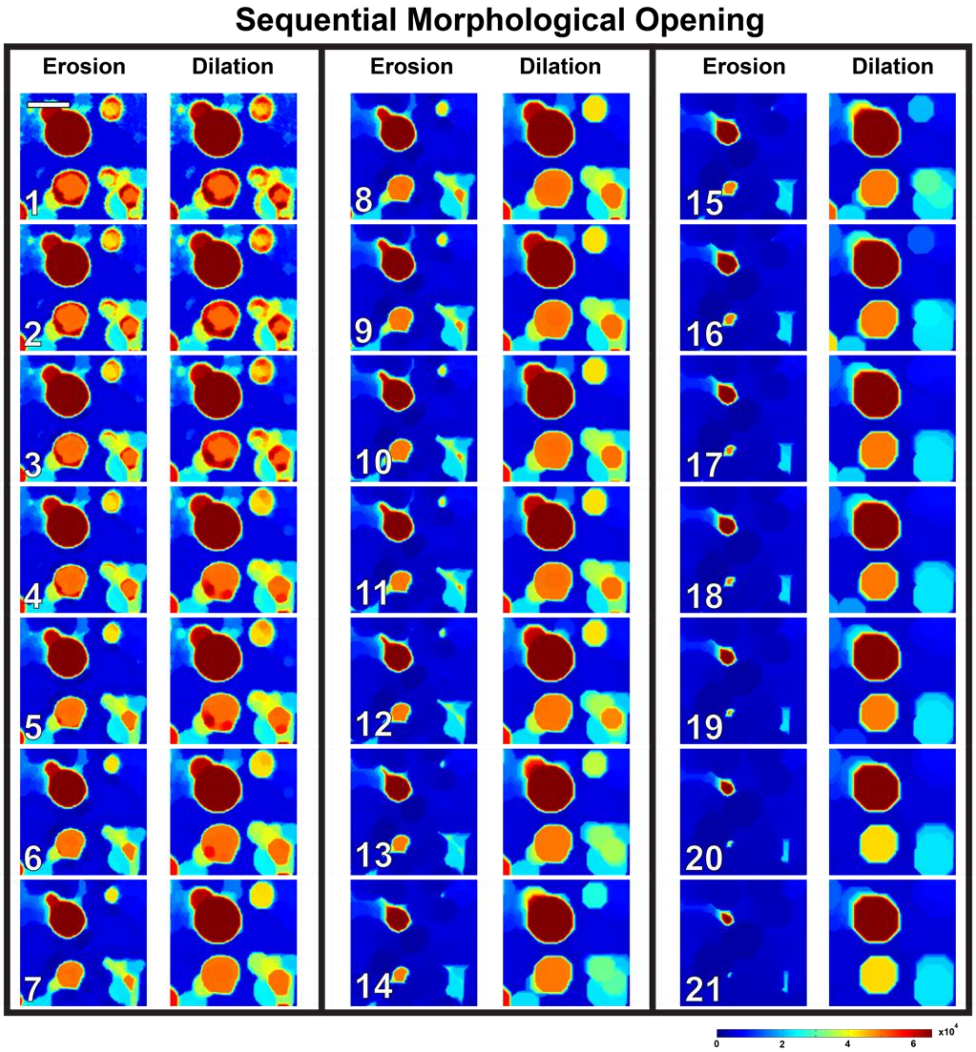

Figure 5-3. Sequential morphological opening example using region depicting the analysis of lipid droplets. Morphological openings are composed of sequential erosions and dilations. The numbers in each frame indicate the structuring element

disk radius size of the structuring element used to apply the erosion or dilation. The same structuring element is applied to the erosion and dilation paired images. The erosion applies the minimum value of the intensities within the structuring element when applied to the image per pixel. This eliminates structures that are smaller than the size of the structuring element disk. The sequential dilation applies the maximum value of the intensities within the structuring element of the same size, thus restoring the approximate size of the structures in the original image, however, the objects eliminated through the erosion cannot be dilated, thus the object is removed from the image. In determining the intensity decreases between each increasing structuring element radius disk size, it is possible to determine the size distribution of the objects in the image, which is what is used in the granulometry algorithm. (Scale bar = 50px = 3.2um)

APPENDIX B. GENETIC SUPPRESSOR SCREEN

B.1. *C. elegans* mutagenesis and forward genetic screens

Genetic manipulation of *C. elegans* is an important area of study that allows for the creation of novel mutants that advance the knowledge in various fields from synaptogenesis to metabolism. In this thesis, all mutagenesis was conducted by using the mutagen ethyl methane sulfonate (EMS), that when exposed causes random single nucleotide substitution from guanine pairs to thymine in the DNA[203]. The mutagen typically causes strong loss-of-function or null alleles, with 13% of the lesions as deletions or rearrangements of the chromosome[203]. Because *C. elegans* are hermaphroditic with a very low male population, soaking an animal in the L4 stage, prior to full gonad development causes for mutation in the offspring to occur due to the chemical infiltrating the germline, and different random mutations are seen in the progeny at a rate as high as 2.5×10^{-3} mutations/gene/generation[203].

To conduct the forward genetic screen, the mutagenized population is recovered, and two generations of progeny are cultured. In this second generation, or F2 populations, various mutations are then identified and scored in an attempt to find a novel phenotype that is relevant to the biological system being studied. Once an animal with an interesting mutation has been isolated, they are allowed to self, and the population is then re-screen to determine the mutation is still present. This population can then be sequenced to determine the exact mutation that caused the change in phenotype. Only one quarter of the screened

animals are homozygous with the mutation; therefore, to conduct a full-genome screen, typically over 100,000 animals must be phenotyped.

Screens can be conducted on a large scale by observing mutants with clear defects that affect phenotypes such as locomotion, which can be detected using lower magnification. Recovery of these mutants is easily done using a worm pick. The most difficult screens are those that involve small changes that must be observed using high magnification microscopes with complete immobilization to image and quantify the phenotype. For the purposes of this thesis, all screens that were conducted were identifying changes in lipid droplet phenotypes that are as small as 0.5 μm in diameter; therefore, high magnification and fluorescence were used to visualize and identify the desired mutants.

B.2. Protocol for mutagenesis

Briefly, worms are synchronized to the L4 stage. Worms are washed into a 50 mL conical tube with 4 mL of M9. In the hood, 20 μL of EMS is added to the tube with worms, and the tube is mixed using a shaker for approximately 1 minute. The tube is then place on a rotator causing the liquid to mix gently for 4 hours. The worms are aspirated into microcentrifuge tubes, and washed 3 times with M9, each time centrifuging for 30 seconds and removing the supernatant. The worms are then washed on to a plate with *E. coli* and are cultured for 30 to 60 minutes at room temperature. Healthy L4 worms are picked off of the original plate with P0s, and on to 25 different 10 cm plates seeded with *E. coli,* 10 worms are placed. These worms are cultured at 20^{o}C, and after 2 generations, the F2 population of worms are imaged.

B.3. Flow chart for automated imaging for genetic suppressor screen

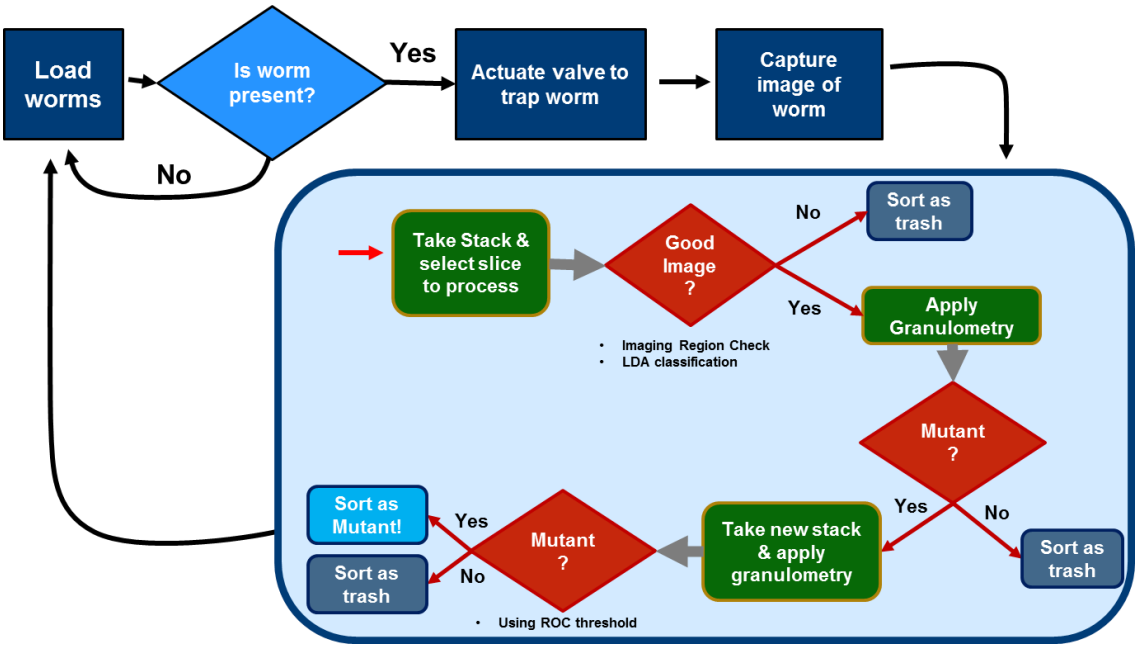

Figure 5-4. Worms loaded are imaged twice to verify that a mutant has been correctly phenotyped before sorting. To do this multiple steps occur where first a good image is determined using a region check where the majority of the region of interest has fluorescence. Next, the granulometry algorithm is applied and using the size range determined by the ROC threshold, the worm is sorted as mutant or trash.

APPENDIX C. DIET SCREEN

C.1. 2x YT media recipe used

900 mL of DI H_2O

16 g Bacto Tryptone

10 g Bacto Yeast Extract

5 g NaCl

Adjust pH to 7.0 with 5 M NaOH

Adjust to 1 L using Di H_2O

Sterilize in autoclave with liquid cycle for 45 minutes

C.2. Resulting LD size effect for diet of 96 clones from Plate 1 of Keio library

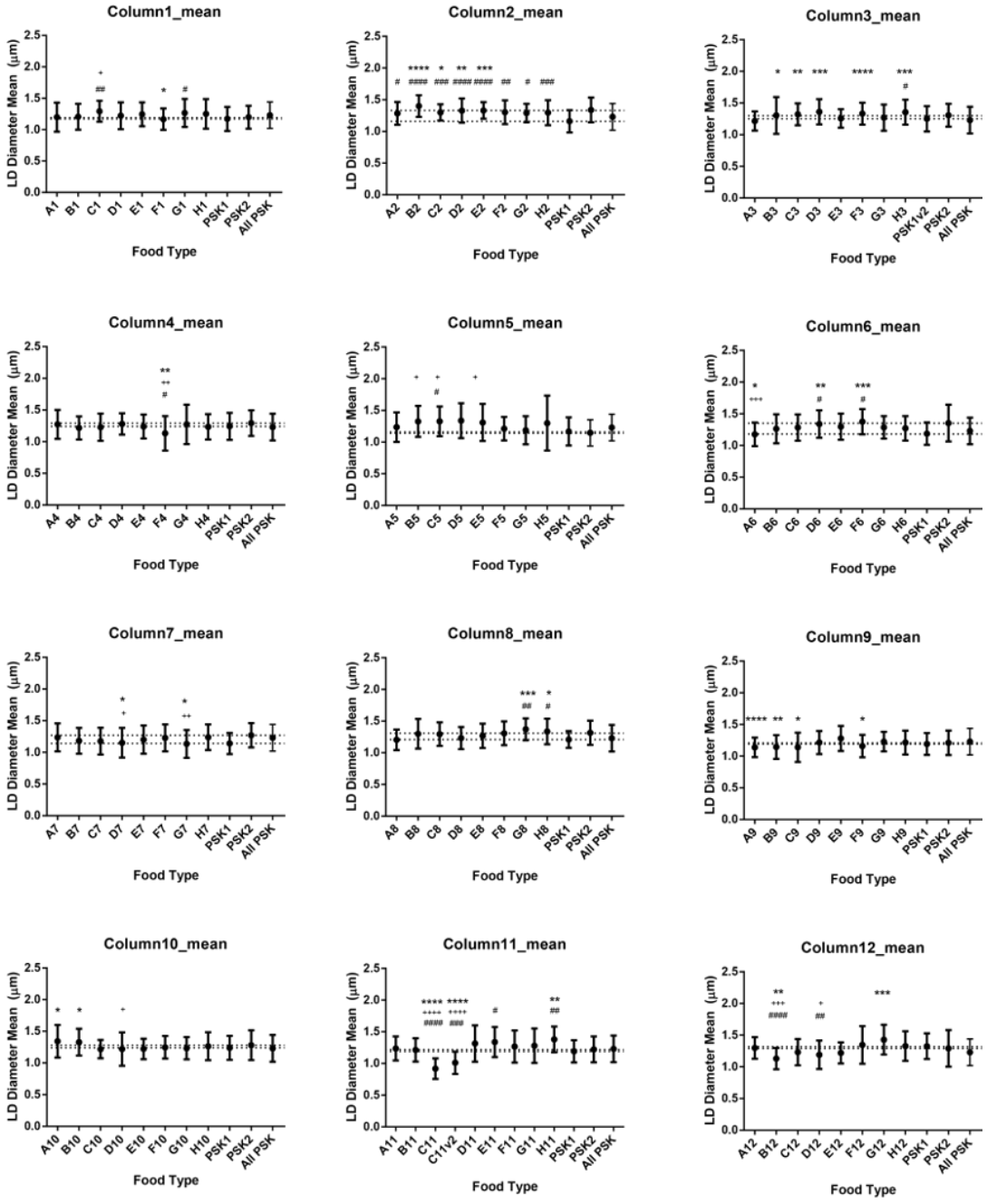

Figure 5-5. Mean lipid droplet size for each of the 96 conditions in Plate 1 of the Keio *E. coli* library.

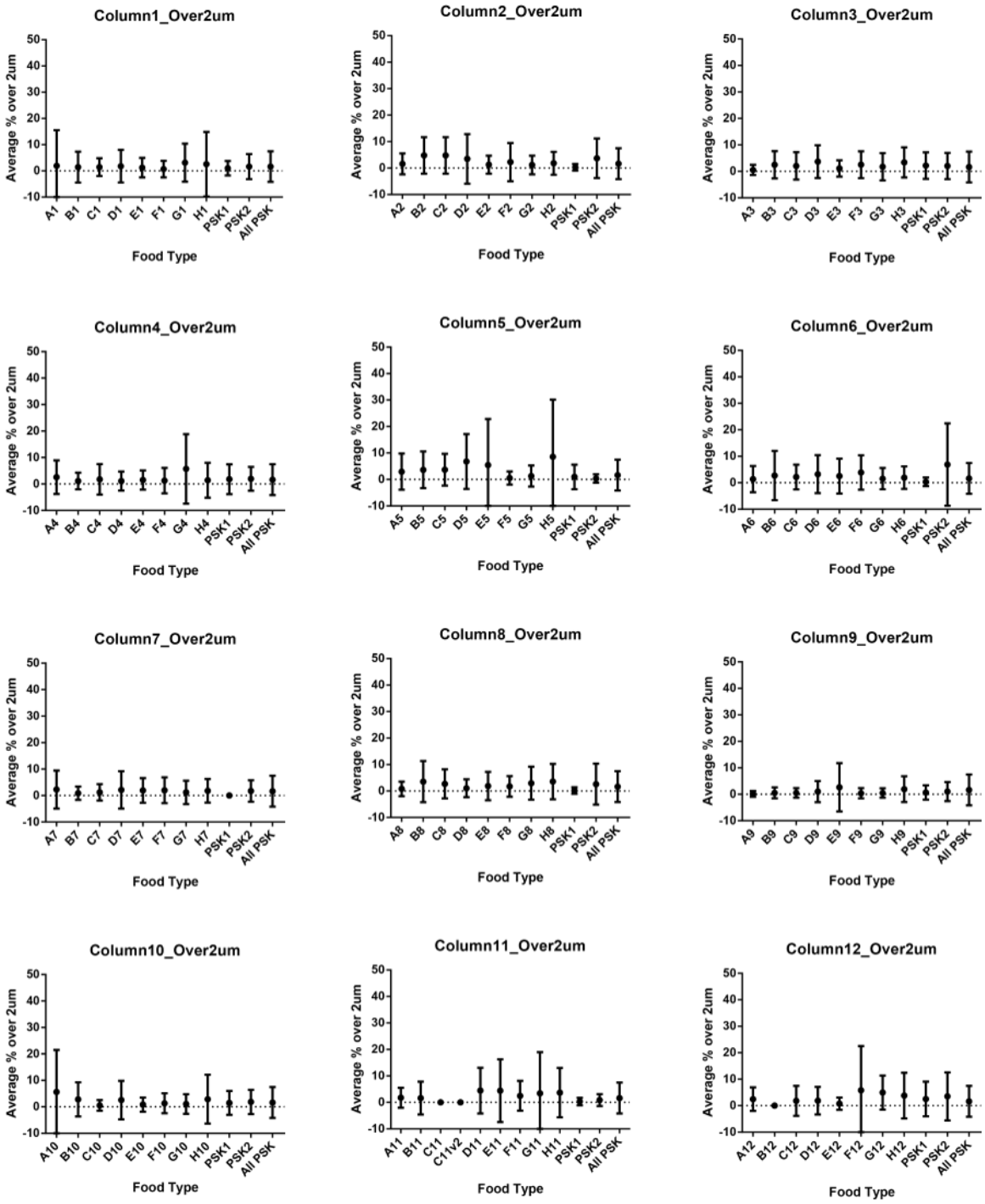

Figure 5-6. Percentage of lipid droplets with lipid droplet size over 2 μm for each of the 96 conditions in Plate 1 of the Keio *E. coli* library.

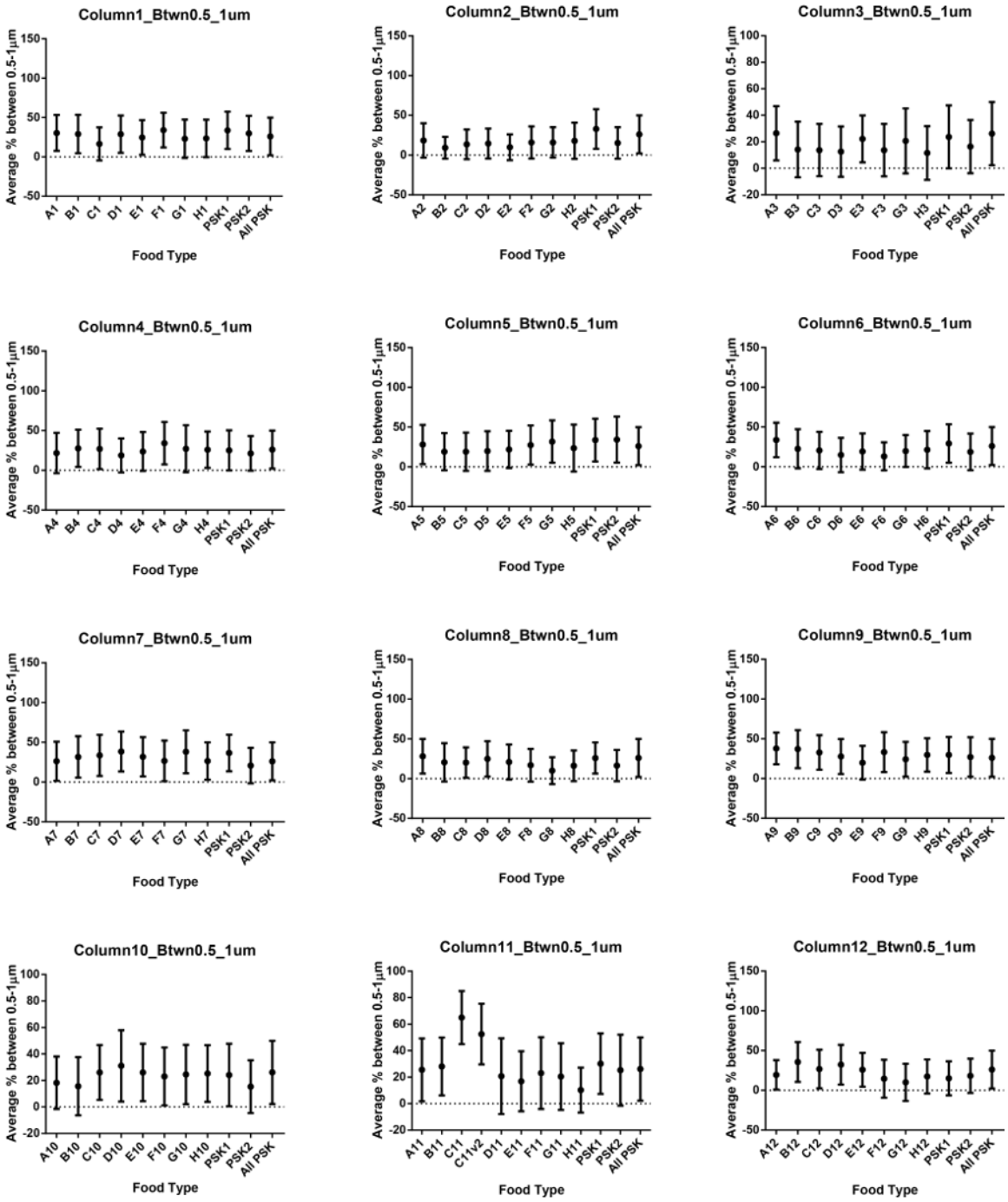

Figure 5-7. Percentage of lipid droplets between 0.5 to 1.0 µm for each of the 96 conditions in Plate 1 of the Keio *E. coli* library.

C.3. Genotype confirmation for genetic knockouts *tonB*, *btuR*, *prpC*, and *prpR*

A total of 5 sets of primers were used to confirm the knockout genotype of the *E. coli*. DNA amplification was conducted through PCR, and confirmation of a product was conducted through gel electrophoresis. The unique primer sets for each clone, and the primer set for the kanamycin cassette for k2 and kt were provided in literature[83,204].

Table 5-1. Primer Set

Gene	Forward Primer	Reverse Primer
tonB	ATTTAAAATCGAGACCTGGTTTTTCTACTGAAATGATTAT	CCTCCGGTCGGAGGCTTTTGACTTTCTGCTTACTGAATTT
prpR	AAACAAGACTAAACCCAATATTCGGTTTCTTAACTTTGCG	GATAAAGCGTTCGCGCTGCATTCGGCAGTTCAGCTTTTCA
prpC	CCGACAACAATCTCGACCCTACAAATGATAACAATGACGA	TACGTTTCCTTATTGTTATTCGTAGAGGTTTACTGGCGCT
btuR	GGCATGACCTTTGACGCCCAACCGGGCCGTAAACCAGGAA	CCGGACGTCATATCCGGCATTTTTACAGATTAATAATCGA
Kan Cassette	CGGTGCCCTGAATGAACTGC	CGGCCACAGTCGATGAATCC

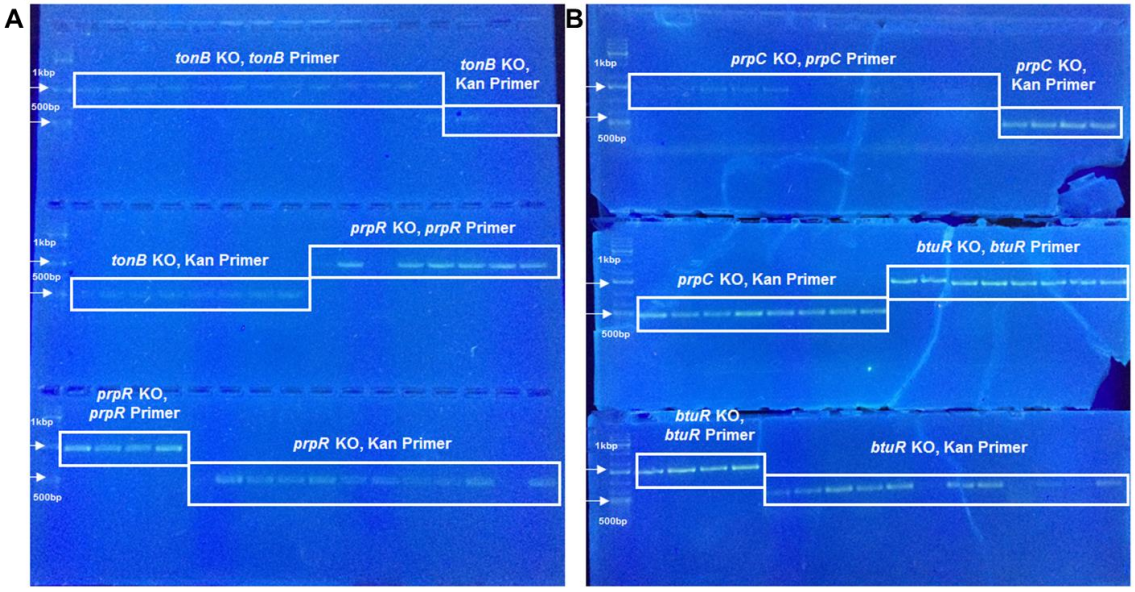

Figure 5-8. Gel electrophoresis results from single colony PCR DNA amplification using two different sets of primers for each of the 4 knockout strains studied: *tonB*, *prpR*, *prpC*, and *btuR*. A) Shows a 1.5% agarose gel with 48 different samples, where the knockouts *tonB* and *prpR* were assayed. B) Shows a 1.5%agarose gel with 48 different samples, where the knockouts *prpC* and *btuR* were assayed. Twelve independent single colonies were used and amplification was done with the knockout primer set or the kanamycin cassette primer set. Larger bands at

approximately 1000 bp were present when testing the knockout *E. coli* with the corresponding knockout primers. Smaller bands at approximately 500 bp were present when testing the knockout *E. coli* with the kanamycin cassette primers. The kanamycin cassette is 471bp, thus the corresponding gel size indicates that all of the knockouts have the correct kanamycin cassette. Because the knockout primers are unique to each gene, the larger bands indicate that the primers are properly amplifying the region that should contain the kanamycin cassette sequence. Confirmation of the kanamycin cassette sequence was then accomplished through sequencing the products from the 96 different PCR reactions corresponding to the 4 different knockouts with 12 single colonies with 2 different primer sets assayed.

The products from the PCR were purified using a the ZR-96 DNA Clean and Concentrator kit (Zymo Research, Co., Irvine, CA). A 96-well plate with the PCR products of the 4 different knockouts, where two different primer sets were used: either the primer set for the knocked out gene, or the kanamycin cassette primer set, and 12 different single colonies were selected for each strain. The purified DNA was then sequenced through external sequences services (Eurofins Genomics, a Eurofins MWG Operon company, Lousville, KY). The resulting sequences are depicted below, and confirm that the kanamycin cassette was present in the correct region, confirming the knockouts *btuR, tonB, prpC,* and *prpR* were correctly labeled in the library.

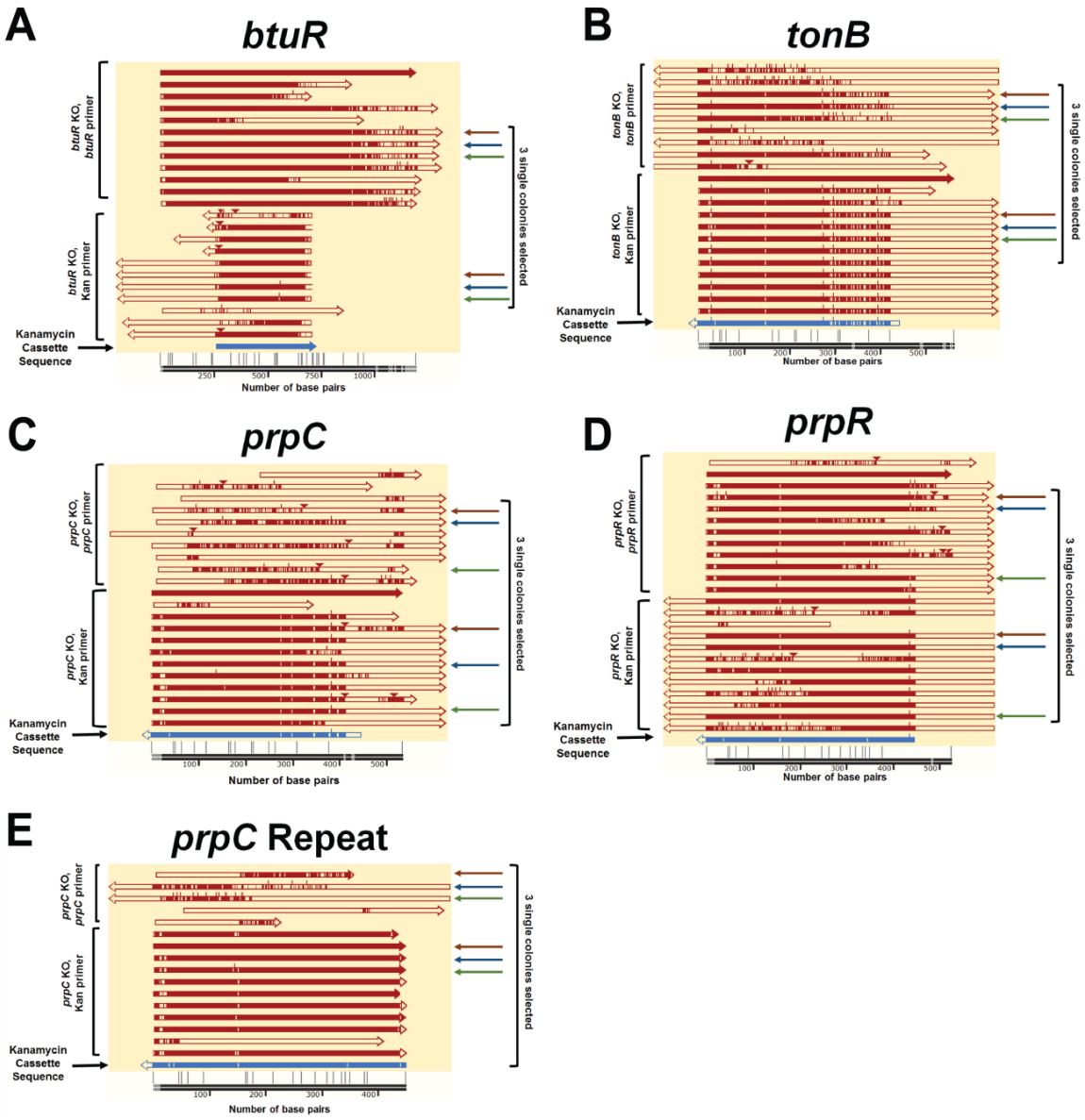

Figure 5-9. Sequencing results for the 4 knockout *E. coli* strains further investigated. Each horizontal line represents an individual sample that was sequenced. Each sample corresponds to an isolated single colony of each knockout. Red indicates that the sequences for the various samples are aligned and base pairs were identified in the sequencing process. A more solid red line indicates more base pair alignment with the sequences in the set. The portion indicated by the top bracket on the left corresponds to the samples that had the DNA of the knockout *E. coli* single colony amplified through PCR by using the primer set designated for this knockout gene. The bottom bracket on the left indicates the corresponding samples that had the DNA of the knockout *E. coli* single colony amplified through PCR by using the primer set designated for the kanamycin cassette used to create the Keio single gene knockout *E. coli* library (Ref). The blue bar indicates the sequence of the

kanamycin cassette region. The bottom axis corresponds to the range of the number of base pairs in the various sequences. On the right there are 2 sets of 3 arrows. The same color indicate that the same single colony was used for the DNA amplification with two different sets of primers. These 3 single colonies were then cultured and combined in order to repeat the supplementation experiments. This process was repeated for the 4 different knockouts investigated through the supplementation experiments: A) *btuR*, B) *tonB*, C) *prpC*, D) *prpR*. E) Indicates a repeat of the knockout *prpC* due to the variability in the sequencing results, however, sufficient base pairs aligned to determine this knockout was correctly labeled in the Keio single gene knockout *E. coli* library.

C.4. Repeated independent trials of supplementation experiments

Two additional independent trials were conducted where varied concentrations of the supplemented metabolite were added to NGM plates. This was conducted for both the two forms of vitamin B_{12} and propionic acid.

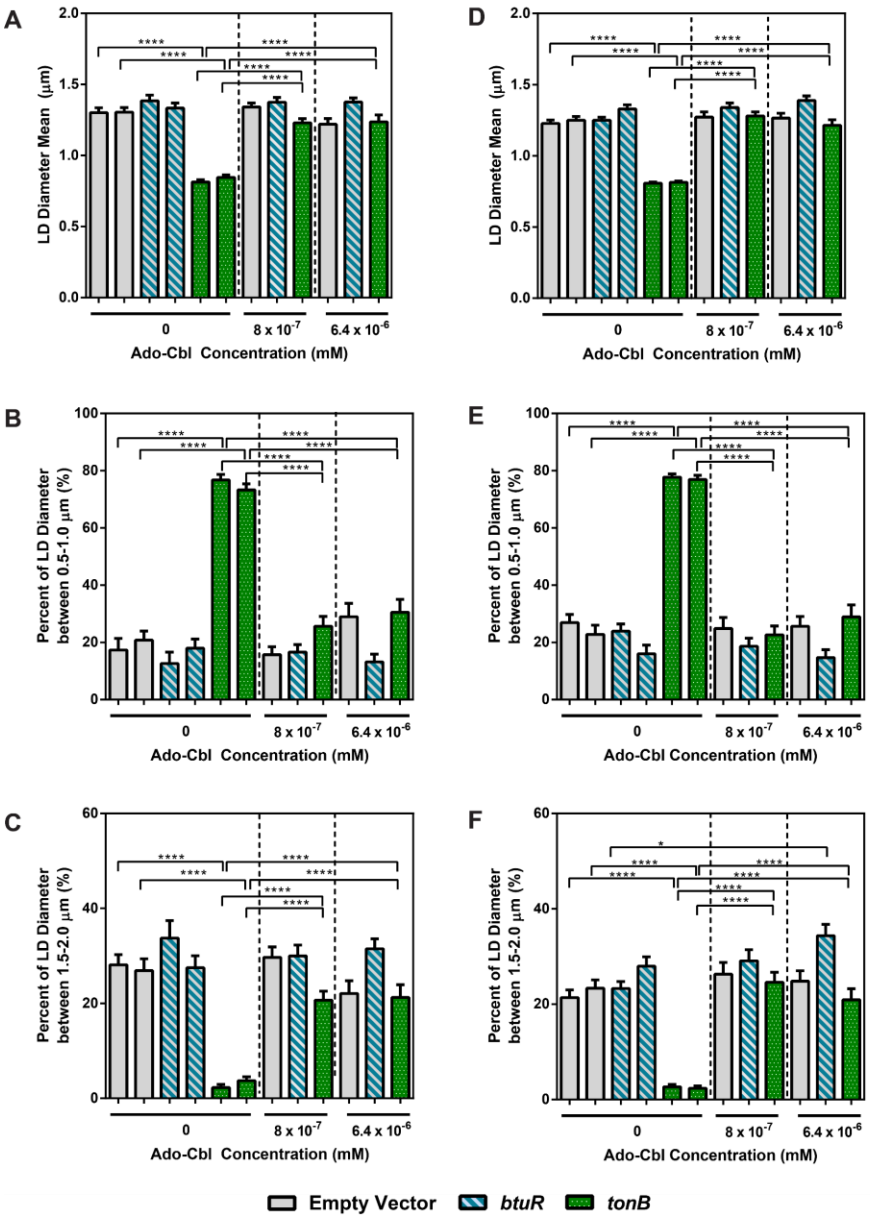

Figure 5-10. Results of two repeated experiments with supplemental metabolite enrichment of Ado-Cbl. A, D) Two different trials showing the mean lipid droplet

size for a population fed the various conditions, where the population fed *tonB* with no supplement had a decreased lipid droplet size, however when the plates is supplemented with either 8 x 10^{-7} mM or 6.4 x 10^{-6} mM Ado-Cbl, the population fed *tonB* has lipid droplets where the mean increases substantially, reaching similar size as the worms fed the empty vector without supplementation. B, E) Two different trials showing the average percentage of lipid droplets between 0.5 – 1.0 µm for a population fed the various conditions. Worms fed *tonB* have a significant increase in the amount of lipid droplets in this smaller size range as compared to the worms fed the empty vector. With the addition of metabolites, the percentage of smaller lipid droplets decrease to levels similar to the empty vector without supplementation. C, F) Two different trials showing the average percentage of lipid droplets between 1.5 – 2.0 µm for a population fed the various conditions. Worms fed *tonB* have a significant decrease in the percentage of lipid droplets in this larger size range, which compliments the results in B, E where the majority of the lipid droplets are in a smaller size range. When the plates are supplemented with Ado-Cbl, the percentage of LDs in this larger size range approximates that of the worms fed the empty vector. It can be inferred that the knockout *tonB* results in a diet deficient in vitamin B_{12} form of Ado-Cbl, and thus supplementation at the 8 x 10^{-7} mM or 6.4 x 10^{-6} mM level returns lipid droplet size and morphology to that of the empty vector which does not have this deficiency. (n> 30, * significance at p<0.05, ** significance at p<0.01, * significance at p<0.001, **** significance at p<0.0001)**

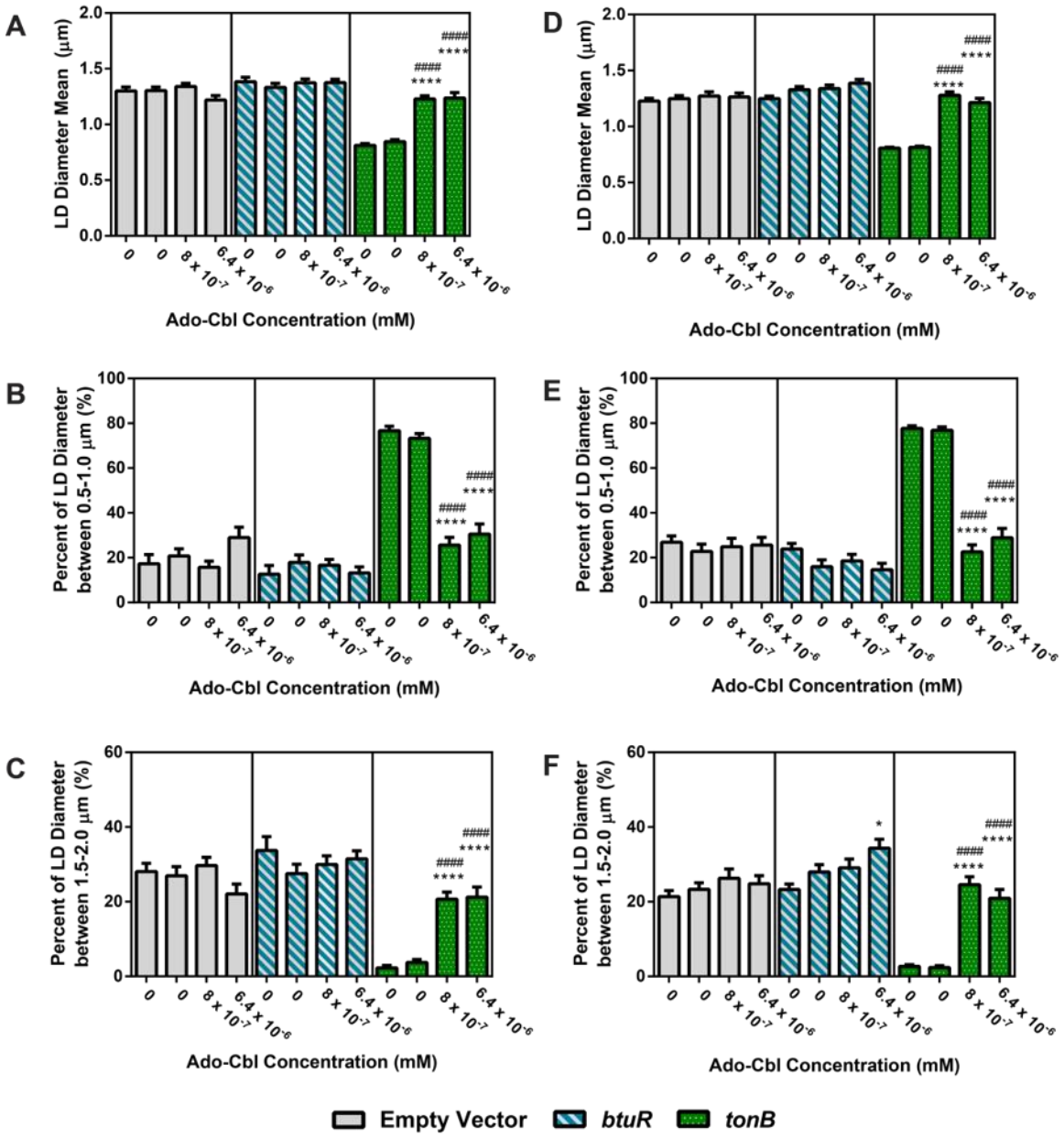

Figure 5-11. Results of the same two repeats grouped according to the various *E. coli* diets supplemented with Ado-Cbl. A, D) Two different trials showing the mean lipid droplet size for a population fed the various conditions, where the population fed *tonB* with supplementation was significantly different compared to the population fed *tonB* without supplementation. The other two diets did not contribute to a significant difference in mean as compared to the sets not supplemented. B, E) Two different trials showing the average percentage of lipid droplets between 0.5 – 1.0 µm for a population fed the various conditions. Worms fed *tonB* have a significant decrease in the amount of lipid droplets in this smaller size range as compared to the worms fed *tonB* without supplementation. C, F) Two different trials showing the average percentage of lipid droplets between 1.5 – 2.0

µm for a population fed the various conditions. Worms fed *tonB* with supplementation have a significant increase in the percentage of lipid droplets in this larger size range, which compliments the results in B, E. (n> 30, * significant difference versus the first set without supplementation (0 mM), # significant difference versus the second set without supplementation (0 mM). One symbol represents significance at p<0.05, two represents significance at p<0.01, three represents significance at p<0.001, and four represent significance at p<0.0001)

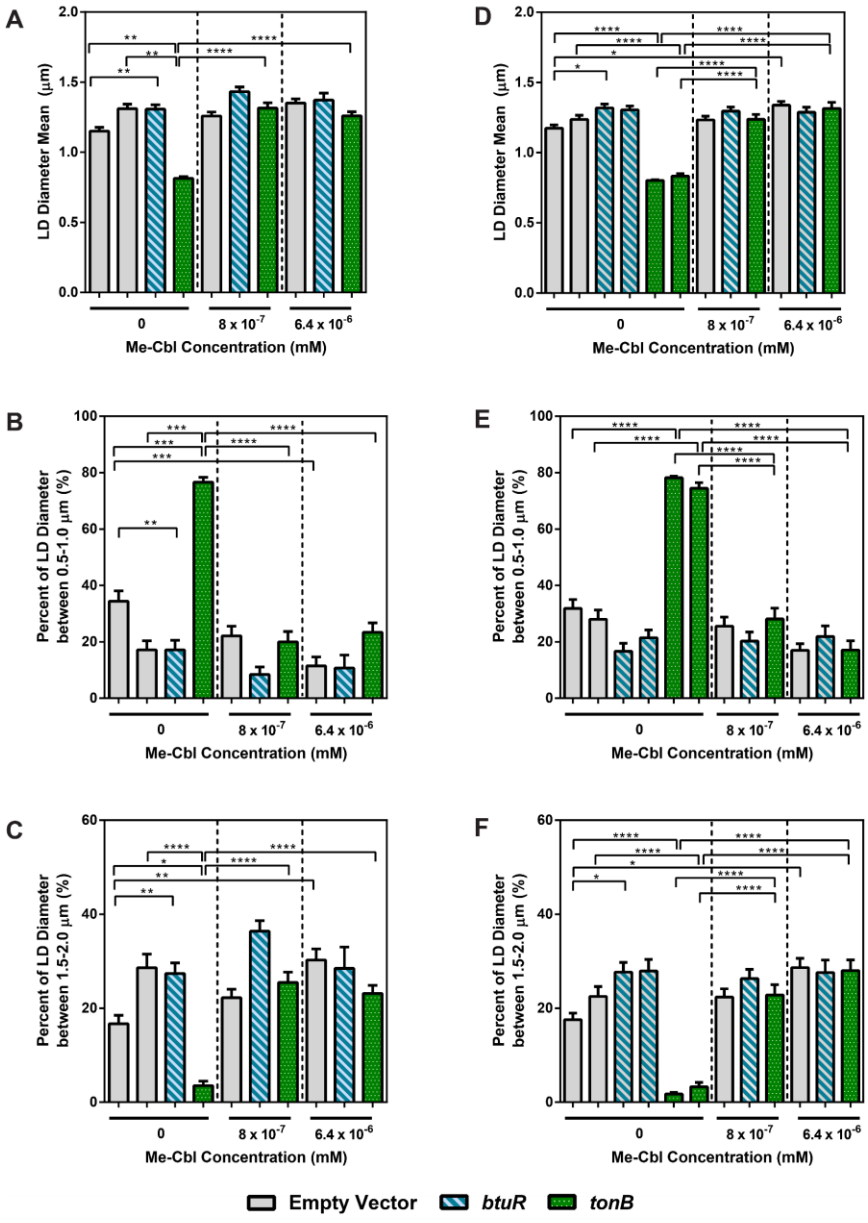

Figure 5-12. Results of two repeated experiments with supplemental metabolite enrichment of Me-Cbl. A, D) Two different trials showing the mean lipid droplet

size for a population fed the various conditions, where the population fed *tonB* with no supplement had a decreased lipid droplet size, however when the plates is supplemented with either 8 x 10^{-7} mM or 6.4 x 10^{-6} mM Me-Cbl, the population fed *tonB* has lipid droplets where the mean increases substantially, reaching similar size as the worms fed the empty vector without supplementation. B, E) Two different trials showing the average percentage of lipid droplets between 0.5 – 1.0 µm for a population fed the various conditions. Worms fed *tonB* have a significant increase in the amount of lipid droplets in this smaller size range as compared to the worms fed the empty vector. With the addition of metabolites, the percentage of smaller lipid droplets decrease to levels similar to the empty vector without supplementation. C, F) Two different trials showing the average percentage of lipid droplets between 1.5 – 2.0 µm for a population fed the various conditions. Worms fed *tonB* have a significant decrease in the percentage of lipid droplets in this larger size range, which compliments the results in B, E where the majority of the lipid droplets are in a smaller size range. When the plates are supplemented with Me-Cbl, the percentage of LDs in this larger size range approximates that of the worms fed the empty vector. It can be inferred that the knockout *tonB* results in a diet deficient in vitamin B_{12} form of Me-Cbl, and thus supplementation at the 8 x 10^{-7} mM or 6.4 x 10^{-6} mM level returns lipid droplet size and morphology to that of the empty vector which does not have this deficiency. (n> 30, * significance at p<0.05, ** significance at p<0.01, * significance at p<0.001, **** significance at p<0.0001)**

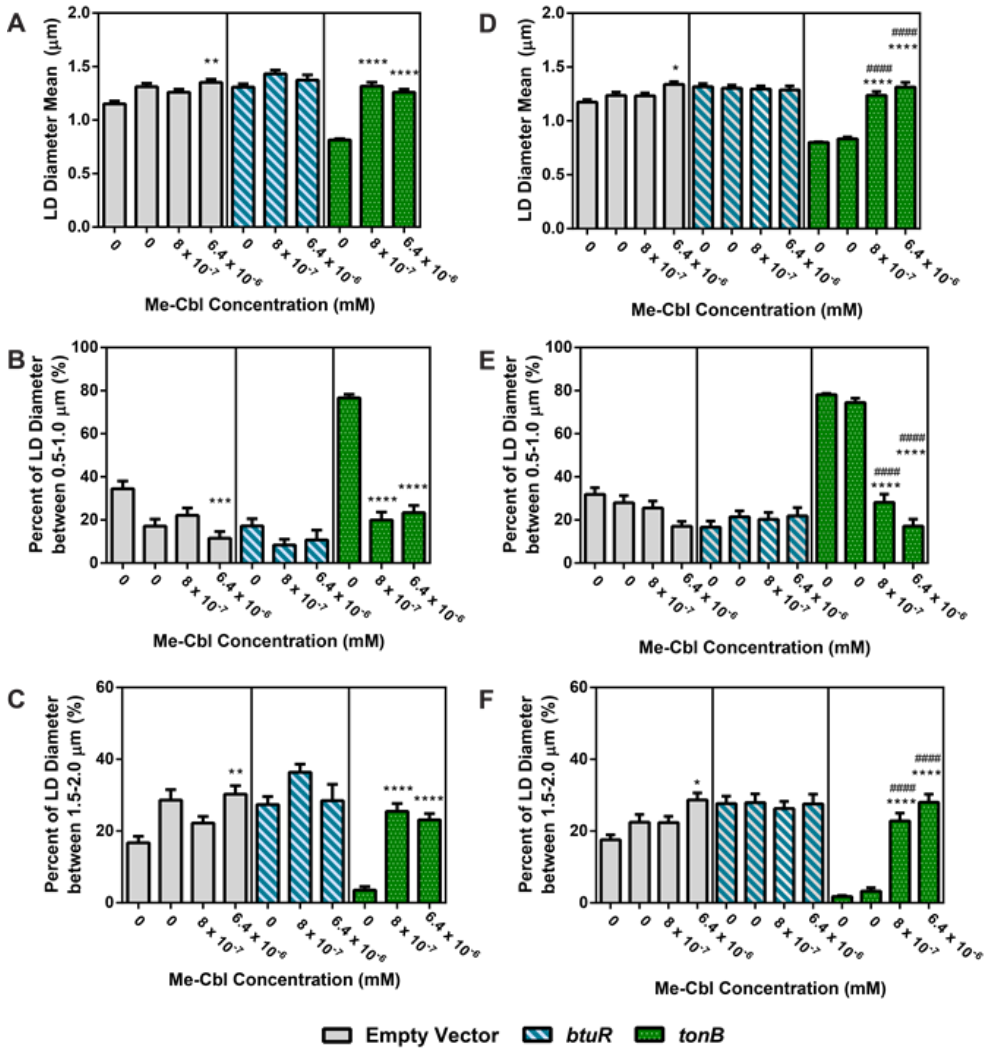

Figure 5-13. Results of the same two repeats grouped according to the various *E. coli* diets supplemented with Me-Cbl. A, D) Two different trials showing the mean lipid droplet size for a population fed the various conditions, where the population fed *tonB* with supplementation was significantly different compared to the population fed *tonB* without supplementation. The other two diets did not contribute to a significant difference in mean as compared to the sets not supplemented. B, E) Two different trials showing the average percentage of lipid droplets between 0.5 – 1.0 µm for a population fed the various conditions. Worms fed *tonB* have a significant decrease in the amount of lipid droplets in this smaller size range as compared to the worms fed *tonB* without supplementation. C, F) Two different trials showing the average percentage of lipid droplets between 1.5 – 2.0 µm for a population fed the various conditions. Worms fed *tonB* with supplementation have a significant increase in the percentage of lipid droplets in this larger size range, which compliments the results in B, E. (n> 30, * significant difference versus the first set without supplementation (0 mM), # significant difference versus the second set without supplementation (0 mM). One symbol represents significance at p<0.05, two represents significance at

p<0.01, three represents significance at p<0.001, and four represent significance at p<0.0001)

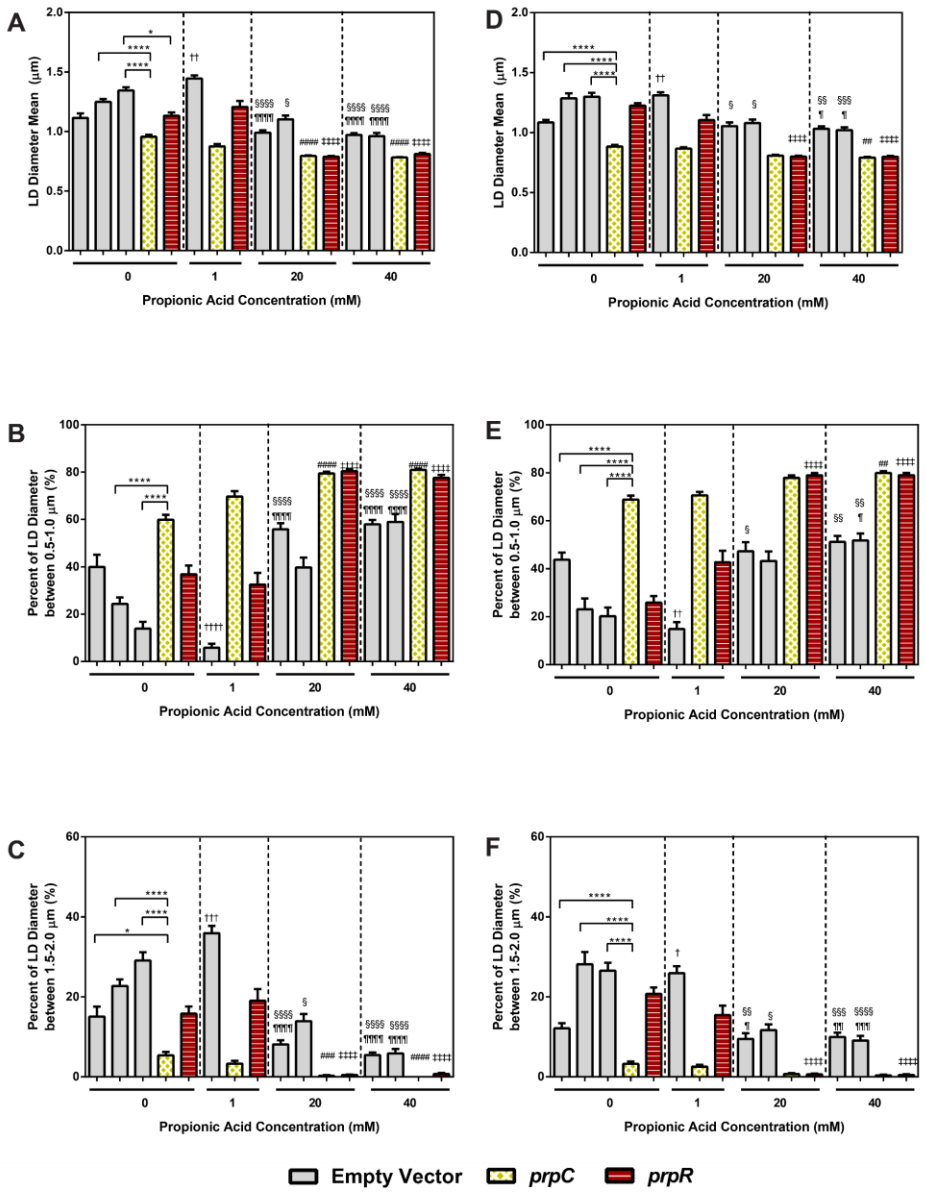

Figure 5-14. Results of two repeated experiments with supplemental metabolite enrichment of propionic acid. A, D) Two different trials showing the mean lipid droplet size for a population fed the various conditions, where the all three populations that were fed either the empty vector, *prpR*, or *prpC*, showed a significant reduction in LD size when fed 20 mM or 40 mM concentrations but not 1 mM. B, E) Two different trials showing the average percentage of lipid droplets between 0.5 – 1.0 µm for a population fed the various conditions. C, F) Two different trials showing the average percentage of lipid droplets between 1.5 – 2.0

µm for a population fed the various conditions. (n> 30; * significance level vs bracketed conditions, † significance level vs first empty vector 0 mM PA, ¶ significance level vs second empty vector fed 0 mM PA, § significance level vs third empty vector fed 0 mM PA, # significance level vs worms fed *prpC* with 0 mM PA, ‡ significance level vs worms fed *prpR* with 0 mM PA; 1 symbol = p<0.05, 2 symbols = p<0.01, 3 symbols = p<0.001, 4 symbols = p < 0.0001)

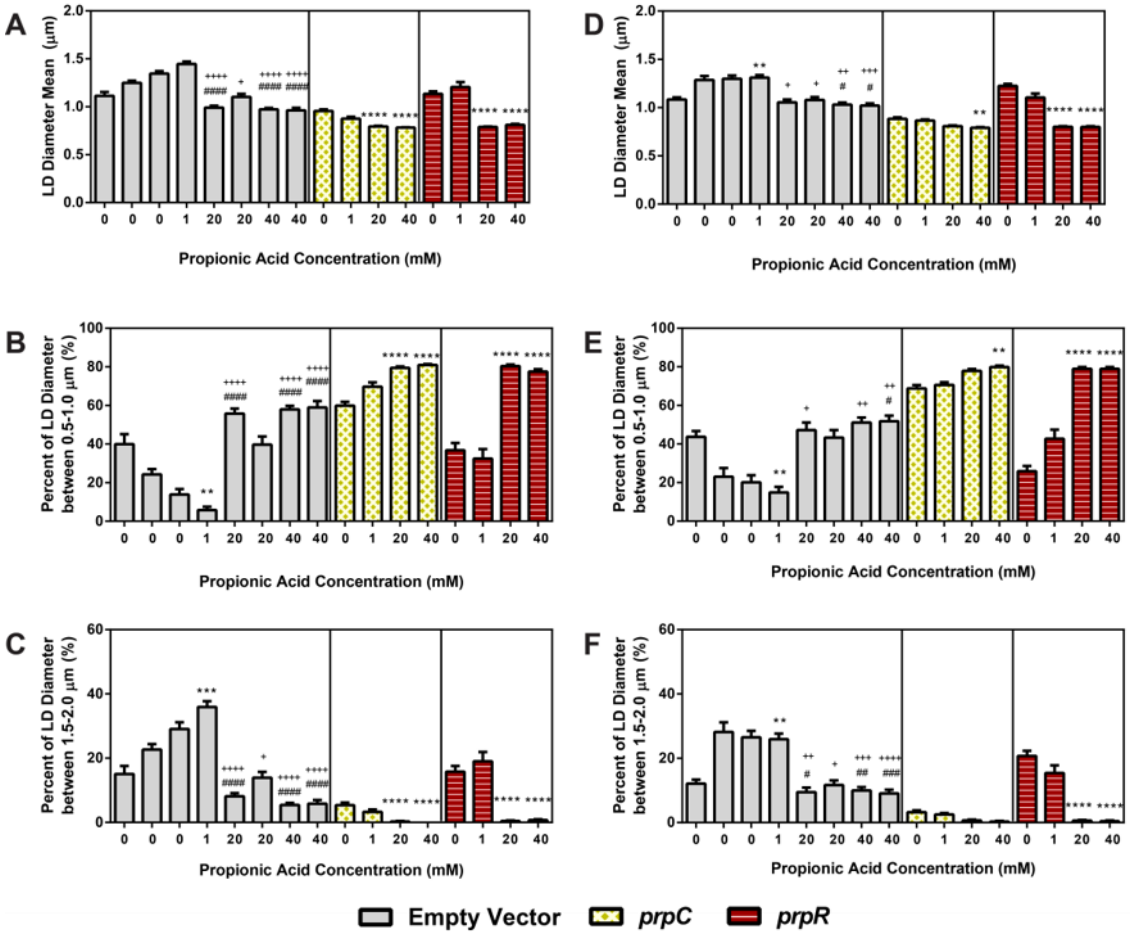

Figure 5-15. Results of the same two repeats grouped according to the various *E. coli* diets supplemented with propionic acid. A, D) Two different trials showing the mean lipid droplet size for a population fed the various conditions, where all diets, empty vector, *prpC*, and *prpR* show a significant decrease in lipid droplet mean diameter when supplemented at the 20 and 40 mM concentrations. B, E) Two different trials showing the average percentage of lipid droplets between 0.5 – 1.0 µm for a population fed the various conditions. Similar to the mean lipid droplet information, worms fed all three diets exhibited a statistically significant increase in droplets in the smaller size range of 0.5 to 1 µm indicating that the lipid droplets of each of the populations decreased in size with concentrations of 20 and 40 mM. C, F) Two different trials showing the average percentage of lipid droplets between 1.5

– 2.0 µm for a population fed the various conditions. Complimentary to the results in B, and E, in C and F we see that there is a significant decrease in the percentage of lipid droplets in the larger size range when supplemented with propionic acid as compared to no supplementation. (n> 30, * significant difference versus the first set without supplementation (0 mM), # significant difference versus the second set without supplementation (0 mM), + significant difference versus the third set without supplementation (0 mM). One symbol represents significance at p<0.05, two represents significance at p<0.01, three represents significance at p<0.001, and four represent significance at p<0.0001)

REFERENCES

1. Ogden, C. L., Carroll, M. D., Mcdowell, M. A. & Flegal, K. M. NCHS Data Brief Obesity Among Adults in the United States— No Statistically Significant Change Since 2003-2004 Highlights Data from the National Health and Nutrition Examination Survey NCHS Data Brief. (2003).

2. Gesta, S., Tseng, Y.-H. & Kahn, C. R. Developmental Origin of Fat: Tracking Obesity to Its Source. *Cell* **131,** 242–256 (2007).

3. Ashrafi, K. Obesity and the regulation of fat metabolism. *WormBook, ed. C. elegans Res. Community* 1–20 (2007). doi:10.1895/wormbook.1.130.1

4. Zhang, S. O., Trimble, R., Guo, F. & Mak, H. Y. Lipid droplets as ubiquitous fat storage organelles in C. elegans. *BMC Cell Biol.* **11,** 96 (2010).

5. Crane, M. M., Chung, K., Stirman, J. & Lu, H. Microfluidics-enabled phenotyping, imaging, and screening of multicellular organisms. *Lab Chip* **10,** 1509 (2010).

6. Chung, K., Crane, M. M. & Lu, H. Automated on-chip rapid microscopy, phenotyping and sorting of C. elegans. *Nat. Methods* **5,** 637–643 (2008).

7. Al-Lahham, S. H., Peppelenbosch, M. P., Roelofsen, H., Vonk, R. J. & Venema, K. Biological effects of propionic acid in humans; metabolism, potential applications and underlying mechanisms. *Biochim. Biophys. Acta - Mol. Cell Biol. Lipids* **1801,** 1175–1183 (2010).

8. Arora, T., Sharma, R. & Frost, G. Propionate. Anti-obesity and satiety enhancing factor? *Appetite* **56,** 511–515 (2011).

9. Brenner, S. The genetics of Caenorhabditis elegans. *Genetics* **77,** 71–94 (1974).

10. Kiontke, K. C. *et al.* A phylogeny and molecular barcodes for Caenorhabditis, with numerous new species from rotting fruits. *BMC Evol. Biol.* **11,** 339 (2011).

11. Altun, Z. F., Hall, D. H. *ATLAS OF C. elegans ANATOMY. WormAtlas* (2006).

12. White, J. G., Southgate, E., Thomson, J. N. & Brenner, S. The structure of the nervous system of the nematode Caenorhabditis elegans. *Philos. Trans. R. Soc. Lond. B. Biol. Sci.* **314,** 1–340 (1986).

13. Edgley, Mark, R. lab. What is C. elegans? WHAT IS CAENORHABDITIS ELEGANS AND WHY WORK ON IT? AN INTRODUCTION FOR THOSE UNFAMILIAR WITH 'THE WORM'. Available at: https://cbs.umn.edu/cgc/what-c-elegans. (Accessed: 21st February 2017)

14. Brenner, S. Nature's Gift to Science (Nobel Lecture). *ChemBioChem* **4,** 683–687 (2003).

15. Horvitz, H. R. Worms, Life, and Death (Nobel Lecture). *ChemBioChem* **4,** 697–711 (2003).

16. Sulston, J. E. Caenorhabditis elegans: The Cell Lineage and Beyond (Nobel Lecture). *ChemBioChem* **4,** 688–696 (2003).

17. Avery, L. & Horvitz, H. R. A cell that dies during wild-type C. elegans development can function as a neuron in a ced-3 mutant. *Cell* **51,** 1071–8 (1987).

18. Hedgecock, E. M., Sulston, J. E. & Thomson, J. N. Mutations affecting programmed cell deaths in the nematode Caenorhabditis elegans. *Science* **220,** 1277–9 (1983).

19. Fire, A. *et al.* Potent and specific genetic interference by double-stranded RNA in Caenorhabditis elegans. *Nature* **391,** 806–811 (1998).

20. Fire, A. Z. Gene silencing by double-stranded RNA. *Cell Death Differ.* **14,** 1998–2012 (2007).

21. Mello, C. C. Return to the RNAi World: Rethinking Gene Expression and Evolution (Nobel Lecture). *Angew. Chemie Int. Ed.* **46,** 6985–6994 (2007).

22. Chalfie, M., Tu, Y., Euskirchen, G., Ward, W. W. & Prasher, D. C. Green fluorescent protein as a marker for gene expression. *Science* **263,** 802–5 (1994).

23. Chalfie, M. GFP: Lighting Up Life (Nobel Lecture). *Angew. Chemie Int. Ed.* **48,** 5603–5611 (2009).

24. Corsi, A. K., Wightman, B. & Chalfie, M. A Transparent Window into Biology: A Primer on Caenorhabditis elegans. *Genetics* **200,** 387–407 (2015).

25. Kaletta, T. & Hengartner, M. O. Finding function in novel targets: C. elegans as a model organism. *Nat. Rev. Drug Discov.* **5,** 387–399 (2006).

26. Kenyon, C. J. The genetics of ageing. *Nature* **464,** 504–512 (2010).

27. Tissenbaum, H. A. & Guarente, L. Increased dosage of a sir-2 gene extends lifespan in Caenorhabditis elegans. *Nature* **410,** 227–230 (2001).

28. Ruvkun, G. *et al.* The Fork head transcription factor DAF-16 transduces insulin-like metabolic and longevity signals in C. elegans. *Nature* **389,** 994–999 (1997).

29. Kamath, R. S. *et al.* Systematic functional analysis of the Caenorhabditis elegans genome using RNAi. *Nature* **421,** 231–237 (2003).

30. Sawin, E. R., Ranganathan, R. & Horvitz, H. R. C. elegans Locomotory Rate Is Modulated by the Environment through a Dopaminergic Pathway and by Experience through a Serotonergic Pathway. *Neuron* **26,** 619–631 (2000).

31. Nagel, G. *et al.* Light Activation of Channelrhodopsin-2 in Excitable Cells of Caenorhabditis elegans Triggers Rapid Behavioral Responses. *Curr. Biol.* **15,** 2279–2284 (2005).

32. Li, Y. *et al.* High Concentration of Vitamin E Decreases Thermosensation and Thermotaxis Learning and the Underlying Mechanisms in the Nematode Caenorhabditis elegans. *PLoS One* **8,** e71180 (2013).

33. Zhang, Y., Lu, H. & Bargmann, C. I. Pathogenic bacteria induce aversive olfactory learning in Caenorhabditis elegans. *Nature* **438,** 179–184 (2005).

34. Grishok, A. *et al.* Genes and Mechanisms Related to RNA Interference Regulate Expression of the Small Temporal RNAs that Control C. elegans Developmental Timing. *Cell* **106,** 23–34 (2001).

35. Jacobson, M. D., Weil, M. & Raff, M. C. Programmed Cell Death in Animal Development. *Cell* **88,** 347–354 (1997).

36. Nonet, M. L., Grundahl, K., Meyer, B. J. & Rand, J. B. Synaptic function is impaired but not eliminated in C. elegans mutants lacking synaptotagmin. *Cell* **73,** 1291–1305 (1993).

37. Kraemer, B. C. *et al.* Neurodegeneration and defective neurotransmission in a Caenorhabditis elegans model of tauopathy. *Proc. Natl. Acad. Sci.* **100,** 9980–9985 (2003).

38. Maeder, C. I., San-Miguel, A., Wu, E. Y., Lu, H. & Shen, K. *In Vivo* Neuron-Wide Analysis of Synaptic Vesicle Precursor Trafficking. *Traffic* **15,** 273–291 (2014).

39. Balaban, R. S., Nemoto, S. & Finkel, T. Mitochondria, Oxidants, and Aging. *Cell* **120,** 483–495 (2005).

40. Schulz, T. J. *et al.* Glucose Restriction Extends Caenorhabditis elegans Life Span by Inducing Mitochondrial Respiration and Increasing Oxidative Stress. *Cell Metab.* **6,** 280–293 (2007).

41. Lee, S. S. DAF-16 Target Genes That Control C. elegans Life-Span and Metabolism. *Science (80-.).* **300,** 644–647 (2003).

42. Chiang, S. H. & MacDougald, O. A. Will fatty worms help cure human obesity? *Trends Genet.* **19,** 523–5 (2003).

43. McKay, R. M., McKay, J. P., Avery, L. & Graff, J. M. C elegans: a model for exploring the genetics of fat storage. *Dev. Cell* **4,** 131–42 (2003).

44. Jones, K. T. & Ashrafi, K. Caenorhabditis elegans as an emerging model for studying the basic biology of obesity. *Dis. Model. Mech.* **2,** 224–9 (2009).

45. Zhang, S. O. *et al.* Genetic and dietary regulation of lipid droplet expansion in Caenorhabditis elegans. *Proc. Natl. Acad. Sci. U. S. A.* **107,** 4640–5 (2010).

46. Ashrafi, K. *et al.* Genome-wide RNAi analysis of Caenorhabditis elegans fat regulatory genes. *Nature* **421,** 268–272 (2003).

47. Driscoll, M. Mounting Animals with Agar Pads. *WormAtlas* Available at: http://www.wormatlas.org/agarpad.htm. (Accessed: 21st February 2017)

48. San-Miguel, A. & Lu, H. Microfluidics as a tool for C. elegans research. *WormBook* 1–19 (2013). doi:10.1895/wormbook.1.162.1

49. Chung, K. *et al.* A microfluidic array for large-scale ordering and orientation of embryos. *Nat. Methods* **8,** 171–176 (2011).

50. Chung, K., Rivet, C. A., Kemp, M. L. & Lu, H. Imaging Single-Cell Signaling Dynamics with a Deterministic High-Density Single-Cell Trap Array. *Anal. Chem.* **83,** 7044–7052 (2011).

51. Albrecht, D. R. & Bargmann, C. I. High-content behavioral analysis of Caenorhabditis elegans in precise spatiotemporal chemical environments. *Nat. Methods* **8,** 599–605 (2011).

52. Whitesides, G. M. The origins and the future of microfluidics. *Nature* **442,** 368–373 (2006).

53. Crane, M. M., Chung, K. & Lu, H. Computer-enhanced high-throughput genetic screens of C. elegans in a microfluidic system. *Lab Chip* **9,** 38–40 (2008).

54. Hulme, S. E., Shevkoplyas, S. S., Apfeld, J., Fontana, W. & Whitesides, G. M. A microfabricated array of clamps for immobilizing and imaging C. elegans. (2007). doi:10.1039/b707861g

55. Lee, H. *et al.* A multi-channel device for high-density target-selective stimulation and long-term monitoring of cells and subcellular features in C. elegans. *Lab Chip* **14,** 4513–22 (2014).

56. Shah, N. R. & Braverman, E. R. Measuring Adiposity in Patients: The Utility of Body Mass Index (BMI), Percent Body Fat, and Leptin. *PLoS One* **7,** e33308 (2012).

57. Flegal, K. M., Carroll, M. D., Ogden, C. L. & Curtin, L. R. Prevalence and Trends in Obesity Among US Adults, 1999-2008. *JAMA* **303,** 235 (2010).

58. Farooqi, I. S. & O?Rahilly, S. Genetic factors in human obesity. *Obes. Rev.* **8,** 37–40 (2007).

59. Friedman, J. M. The Function of Leptin in Nutrition, Weight, and Physiology. 1–14

(2002).

60. Vann, K. How Is Excess Glucose Stored?

61. Mak, H. Y., Nelson, L. S., Basson, M., Johnson, C. D. & Ruvkun, G. Polygenic control of Caenorhabditis elegans fat storage. *Nat. Genet.* **38,** 363–368 (2006).

62. Fei, W., Du, X. & Yang, H. Seipin, adipogenesis and lipid droplets. *Trends Endocrinol. Metab.* **22,** 204–210 (2011).

63. Martin, S. & Parton, R. G. Lipid droplets: a unified view of a dynamic organelle. *Nat. Rev. Mol. Cell Biol.* **7,** 373–378 (2006).

64. Shamir, L., Wolkow, C. A. & Goldberg, I. G. Quantitative measurement of aging using image texture entropy. *Bioinformatics* **25,** 3060–3063 (2009).

65. Yen, K. *et al.* A Comparative Study of Fat Storage Quantitation in Nematode Caenorhabditis elegans Using Label and Label-Free Methods. *PLoS One* **5,** e12810 (2010).

66. Elle, I. C., Olsen, L. C. B., Pultz, D., Rødkaer, S. V. & Faergeman, N. J. Something worth dyeing for: Molecular tools for the dissection of lipid metabolism in *Caenorhabditis elegans*. *FEBS Lett.* **584,** 2183–2193 (2010).

67. Kinkel, A. D. *et al.* Oil red-O stains non-adipogenic cells: a precautionary note. *Cytotechnology* **46,** 49–56 (2004).

68. Greenspan, P., Mayer, E. P. & Fowler, S. D. Nile red: a selective fluorescent stain for intracellular lipid droplets. *J. Cell Biol.* **100,** 965–73 (1985).

69. Mullaney, B. C. & Ashrafi, K. C. elegans fat storage and metabolic regulation. *Biochim. Biophys. Acta - Mol. Cell Biol. Lipids* **1791,** 474–478 (2009).

70. Hellerer, T. *et al.* Monitoring of lipid storage in Caenorhabditis elegans using coherent anti-Stokes Raman scattering (CARS) microscopy. *Proc. Natl. Acad. Sci.* **104,** 14658–14663 (2007).

71. Wang, M. C., Min, W., Freudiger, C. W., Ruvkun, G. & Xie, X. S. RNAi screening

for fat regulatory genes with SRS microscopy. *Nat. Methods* **8,** 135–8 (2011).

72. Mak, H. Y. in *Methods in Cell Biology* **116,** 39–51 (2013).

73. Klemm, R. W. *et al.* A Conserved Role for Atlastin GTPases in Regulating Lipid Droplet Size. *Cell Rep.* **3,** 1465–1475 (2013).

74. Park, S. H., Zhu, P.-P., Parker, R. L. & Blackstone, C. Hereditary spastic paraplegia proteins REEP1, spastin, and atlastin-1 coordinate microtubule interactions with the tubular ER network. *J. Clin. Invest.* **120,** 1097–1110 (2010).

75. Fink, J. K. Hereditary spastic paraplegia: clinico-pathologic features and emerging molecular mechanisms. *Acta Neuropathol.* **126,** 307–328 (2013).

76. Nance, M. Hereditary Spastic Paraplegia. *NORD (National Organization for Rare Disorders)* Available at: https://rarediseases.org/rare-diseases/hereditary-spastic-paraplegia/. (Accessed: 21st February 2017)

77. Hu, J. *et al.* A Class of Dynamin-like GTPases Involved in the Generation of the Tubular ER Network. *Cell* **138,** 549–561 (2009).

78. Orso, G. *et al.* Homotypic fusion of ER membranes requires the dynamin-like GTPase Atlastin. *Nature* **460,** 978–983 (2009).

79. Rismanchi, N., Soderblom, C., Stadler, J., Zhu, P.-P. & Blackstone, C. Atlastin GTPases are required for Golgi apparatus and ER morphogenesis. *Hum. Mol. Genet.* **17,** 1591–1604 (2008).

80. Klemm, R. W. *et al.* A Conserved Role for Atlastin GTPases in Regulating Lipid Droplet Size. *Cell Rep.* **3,** 1465–1475 (2013).

81. Julien, C. *et al.* Conserved pharmacological rescue of hereditary spastic paraplegia-related phenotypes across model organisms. *Hum. Mol. Genet.* **25,** 1088–1099 (2016).

82. Brooks, K. K., Liang, B. & Watts, J. L. The Influence of Bacterial Diet on Fat Storage in C. elegans. *PLoS One* **4,** e7545 (2009).

83. Baba, T. *et al.* Construction of Escherichia coli K-12 in-frame, single-gene knockout mutants: the Keio collection. *Mol. Syst. Biol.* **2,** 2006.0008 (2006).

84. Jones, T. R. *et al.* Scoring diverse cellular morphologies in image-based screens with iterative feedback and machine learning. *Proc. Natl. Acad. Sci. U. S. A.* **106,** 1826–31 (2009).

85. Peng, H. Bioimage informatics: a new area of engineering biology. *Bioinformatics* **24,** 1827–36 (2008).

86. Bakal, C., Aach, J., Church, G. & Perrimon, N. Quantitative Morphological Signatures Define Local Signaling Networks Regulating Cell Morphology.

87. Widodo, A. & Yang, B.-S. Application of nonlinear feature extraction and support vector machines for fault diagnosis of induction motors. *Expert Syst. Appl.* **33,** 241–250 (2007).

88. Sophian, A., Tian, G. Y., Taylor, D. & Rudlin, J. A feature extraction technique based on principal component analysis for pulsed Eddy current NDT. *NDT E Int.* **36,** 37–41 (2003).

89. Braun, E., Geurten, B. & Egelhaaf, M. Identifying Prototypical Components in Behaviour Using Clustering Algorithms. *PLoS One* **5,** e9361 (2010).

90. Unnikrishnan, R., Pantofaru, C. & Hebert, M. Toward Objective Evaluation of Image Segmentation Algorithms. *IEEE Trans. Pattern Anal. Mach. Intell.* **29,** 929–944 (2007).

91. Matheron, G. (Georges). *Random sets and integral geometry*. (Wiley, 1974).

92. Geng, W., Cosman, P., Baek, J.-H., Berry, C. C. & Schafer, W. R. Quantitative Classification and Natural Clustering of Caenorhabditis elegans Behavioral Phenotypes.

93. Jain, A. K., Murty, M. N. & Flynn, P. J. Data clustering: a review. *ACM Comput. Surv.* **31,** 264–323 (1999).

94. Pal, N. R. & Pal, S. K. A review on image segmentation techniques. *Pattern*

Recognit. **26,** 1277–1294 (1993).

95. Blaschke, T. Object based image analysis for remote sensing. *ISPRS J. Photogramm. Remote Sens.* **65,** 2–16 (2010).

96. Pham, D. L., Xu, C. & Prince, J. L. Current Methods in Medical Image Segmentation. *Annu. Rev. Biomed. Eng.* **2,** 315–337 (2000).

97. Ding, L. & Goshtasby, A. On the Canny edge detector. *Pattern Recognit.* **34,** 721–725 (2001).

98. Heath, M. D., Sarkar, S., Sanocki, T. & Bowyer, K. W. A robust visual method for assessing the relative performance of edge-detection algorithms. *IEEE Trans. Pattern Anal. Mach. Intell.* **19,** 1338–1359 (1997).

99. Otsu, N. A Threshold Selection Method from Gray-Level Histograms. *IEEE Trans. Syst. Man. Cybern.* **9,** 62–66 (1979).

100. Wang, Q., Zhao, H., Wu, W. & Yuan, N. Algorithm for segmentation based on an improved three-dimensional Otsu's thresholding. in *Proceedings of 2012 2nd International Conference on Computer Science and Network Technology* 1737–1740 (IEEE, 2012). doi:10.1109/ICCSNT.2012.6526256

101. Vincent, L. & Soille, P. Watersheds in digital spaces: an efficient algorithm based on immersion simulations. *IEEE Trans. Pattern Anal. Mach. Intell.* **13,** 583–598 (1991).

102. Grau, V., Mewes, A. U. J., Alcaniz, M., Kikinis, R. & Warfield, S. K. Improved Watershed Transform for Medical Image Segmentation Using Prior Information. *IEEE Trans. Med. Imaging* **23,** 447–458 (2004).

103. D. N. Moriasi, D. N. *et al.* Model Evaluation Guidelines for Systematic Quantification of Accuracy in Watershed Simulations. *Trans. ASABE* **50,** 885–900 (2007).

104. Hough & P.V.C. METHOD AND MEANS FOR RECOGNIZING COMPLEX PATTERNS. (1962).

105. Ballard, D. H. GENERALIZING THE HOUGH TRANSFORM TO DETECT ARBITRARY SHAPES*. *Pattern Recognntt.* **11,** (1122).

106. Yuen, H., Princen, J., Illingworth, J. & Kittler, J. Comparative study of Hough Transform methods for circle finding. *Image Vis. Comput.* **8,** 71–77 (1990).

107. MATLAB. Find circles using circular Hough transform - MATLAB imfindcircles. Available at: https://www.mathworks.com/help/images/ref/imfindcircles.html. (Accessed: 21st February 2017)

108. Illingworth, J. & Kittler, J. A survey of the hough transform. *Comput. Vision, Graph. Image Process.* **44,** 87–116 (1988).

109. Matheron, G. Principles of geostatistics. *Econ. Geol.* **58,** 1246–1266 (1963).

110. Dinh, T. H. N. *et al.* Development of reversible bonding for microfluidic applications. *Microfluid. Nanofluidics* **19,** 751–756 (2015).

111. Bose, S. *et al.* Affinity flow fractionation of cells via transient interactions with asymmetric molecular patterns. *Sci. Rep.* **3,** 2329 (2013).

112. Situma, C. *et al.* Fabrication of DNA microarrays onto poly(methyl methacrylate) with ultraviolet patterning and microfluidics for the detection of low-abundant point mutations. *Anal. Biochem.* **340,** 123–135 (2005).

113. Anwar, K., Han, T. & Kim, S. M. Reversible sealing techniques for microdevice applications. *Sensors Actuators B Chem.* **153,** 301–311 (2011).

114. Le Berre, M., Crozatier, C., Velve Casquillas, G. & Chen, Y. Reversible assembling of microfluidic devices by aspiration. *Microelectron. Eng.* **83,** 1284–1287 (2006).

115. Rafat, M., Raad, D. R., Rowat, A. C. & Auguste, D. T. Fabrication of reversibly adhesive fluidic devices using magnetism. *Lab Chip* **9,** 3016 (2009).

116. Rasponi, M. *et al.* Reliable magnetic reversible assembly of complex microfluidic devices: fabrication, characterization, and biological validation. *Microfluid. Nanofluidics* **10,** 1097–1107 (2011).

117. Chong, SC (Chong, SC); Xie, L (Xie, L); Yobas, L (Yobas, L); Ji, HM (Ji, HM); Li, J (Li, J. Disposable polydimethylsioxane package for 'bio-microfluidic system'. *IEEE* **55th Elect,** 617–621 (2005).

118. Cai, D. & Neyer, A. Cost-effective and reliable sealing method for PDMS (PolyDiMethylSiloxane)-based microfluidic devices with various substrates. *Microfluid. Nanofluidics* **9,** 855–864 (2010).

119. Vézy, C., Haddour, N., Dempsey, N. M., Dumas-Bouchiat, F. & Frénéa-Robin, M. Simple method for reversible bonding of a polydimethylsiloxane microchannel to a variety of substrates. *Micro Nano Lett.* **6,** 871 (2011).

120. Wasay, A. & Sameoto, D. Gecko gaskets for self-sealing and high-strength reversible bonding of microfluidics. *Lab Chip* **15,** 2749–2753 (2015).

121. Khademhosseini, A. *et al.* Cell docking inside microwells within reversibly sealed microfluidic channels for fabricating multiphenotype cell arrays. *Lab Chip* **5,** 1380 (2005).

122. Eddings, M. A., Johnson, M. A. & Gale, B. K. Determining the optimal PDMS–PDMS bonding technique for microfluidic devices. *J. Micromechanics Microengineering* **18,** 67001 (2008).

123. Chen, Q. *et al.* Investigation and improvement of reversible microfluidic devices based on glass–PDMS–glass sandwich configuration.

124. Wittig, J. H., Ryan, A. F. & Asbeck, P. M. A reusable microfluidic plate with alternate-choice architecture for assessing growth preference in tissue culture. *J. Neurosci. Methods* **144,** 79–89 (2005).

125. Krajniak, J., Hao, Y., Mak, H. Y. & Lu, H. C.L.I.P.–continuous live imaging platform for direct observation of C. elegans physiological processes. *Lab Chip* **13,** 2963 (2013).

126. Krajniak, J. & Lu, H. Long-term high-resolution imaging and culture of C. elegans in chip-gel hybrid microfluidic device for developmental studies. *Lab Chip* **10,** 1862 (2010).

127. Hamilton, S. K. *et al.* Development of 3D hydrogel culture systems with on-demand

cell separation. *Biotechnol. J.* **8,** 485–495 (2013).

128. Cosson, S. & Lutolf, M. P. Hydrogel microfluidics for the patterning of pluripotent stem cells. *Sci. Rep.* **4,** 4462 (2014).

129. Zhang, X., Li, L. & Luo, C. Gel integration for microfluidic applications. *Lab Chip* **16,** 1757–1776 (2016).

130. Rinaudo, M. Main properties and current applications of some polysaccharides as biomaterials. *Polym. Int.* **57,** 397–430 (2008).

131. Balgude, A. Agarose gel stiffness determines rate of DRG neurite extension in 3D cultures. *Biomaterials* **22,** 1077–1084 (2001).

132. Armisen, Rafael, Galatas, F. *CHAPTER 1 - PRODUCTION, PROPERTIES AND USES OF AGAR. FAO Corporate Document Repository* (1988).

133. Low Melting Point Agarose - Thermo Fisher Scientific. Available at: https://www.thermofisher.com/order/catalog/product/16520050. (Accessed: 22nd February 2017)

134. Beebe, D. J. *et al.* Functional hydrogel structures for autonomous flow control inside microfluidicchannels. *Nature* **404,** 588–590 (2000).

135. Miyata, T., Asami, N. & Uragami, T. A reversibly antigen-responsive hydrogel. *Nature* **399,** 766–769 (1999).

136. Kazunori Kataoka, *,†, Hiroaki Miyazaki, ‡, Masayuki Bunya, ‡, Teruo Okano, § and & Sakurai§, Y. Totally Synthetic Polymer Gels Responding to External Glucose Concentration: Their Preparation and Application to On−Off Regulation of Insulin Release. (1998). doi:10.1021/JA982975D

137. Suzuki, A. & Tanaka, T. Phase transition in polymer gels induced by visible light. *Nature* **346,** 345–347 (1990).

138. TANAKA, T., NISHIO, I., SUN, S.-T. & UENO-NISHIO, S. Collapse of Gels in an Electric Field. *Science (80-.).* **218,** 467–469 (1982).

139. Hu, Z., Zhang, X. & Li, Y. Synthesis and Application of Modulated Polymer Gels. *Science (80-.).* **269,** 525–527 (1995).

140. Tanaka, T. *et al.* Phase Transitions in Ionic Gels. *Phys. Rev. Lett.* **45,** 1636–1639 (1980).

141. Peppas, N. A., Hilt, J. Z., Khademhosseini, A. & Langer, R. Hydrogels in Biology and Medicine: From Molecular Principles to Bionanotechnology. *Adv. Mater.* **18,** 1345–1360 (2006).

142. Gengyo-Ando, K. & Mitani, S. Characterization of Mutations Induced by Ethyl Methanesulfonate, UV, and Trimethylpsoralen in the Nematode Caenorhabditis elegans. *Biochem. Biophys. Res. Commun.* **269,** 64–69 (2000).

143. Escobar-Chávez, J. J. *et al.* APPLICATIONS OF THERMO-REVERSIBLE PLURONIC F-127 GELS IN PHARMACEUTICAL FORMULATIONS. *J Pharm Pharm. Sci* **9,** 339–358 (2006).

144. Alexandridis, P., Nivaggioli, T. & Hatton, T. A. Temperature Effects on Structural Properties of Pluronic P104 and F108 PEO-PPO-PEO Block Copolymer Solutions. *Langmuir* **11,** 1468–1476 (1995).

145. Kabanov, A. V, Batrakova, E. V & Alakhov, V. Y. Pluronic® block copolymers as novel polymer therapeutics for drug and gene delivery. *J. Control. Release* **82,** 189–212 (2002).

146. Khattak, S. F., Bhatia, S. R. & Roberts, S. C. Pluronic F127 as a Cell Encapsulation Material: Utilization of Membrane-Stabilizing Agents. *Tissue Eng.* **11,** 974–983 (2005).

147. Gong, C. Y. *et al.* Thermosensitive PEG–PCL–PEG Hydrogel Controlled Drug Delivery System: Sol–Gel–Sol Transition and In Vitro Drug Release Study. *J. Pharm. Sci.* **98,** 3707–3717 (2009).

148. Polk, A., Amsden, B., De Yao, K., Peng, T. & Goosen, M. F. A. Controlled Release of Albumin from Chitosan-Alginate Microcapsules. *J. Pharm. Sci.* **83,** 178–185 (1994).

149. Wilson, J. L., Najia, M. A., Saeed, R. & McDevitt, T. C. Alginate encapsulation

parameters influence the differentiation of microencapsulated embryonic stem cell aggregates. *Biotechnol. Bioeng.* **111,** 618–31 (2014).

150. Carpenter, A. E. *et al.* CellProfiler: image analysis software for identifying and quantifying cell phenotypes. *Genome Biol.* **7,** R100 (2006).

151. Cong, G. & Parvin, B. Model-based segmentation of nuclei. *Pattern Recognit.* **33,** 1383–1393 (2000).

152. Li, G. *et al.* 3D cell nuclei segmentation based on gradient flow tracking. *BMC Cell Biol.* **8,** 40 (2007).

153. Crane, M. M. *et al.* Autonomous screening of C. elegans identifies genes implicated in synaptogenesis. *Nat. Methods* **9,** 977–980 (2012).

154. Lee, H., Crane, M. M., Zhang, Y. & Lu, H. Quantitative screening of genes regulating tryptophan hydroxylase transcription in Caenorhabditis elegans using microfluidics and an adaptive algorithm. *Integr. Biol. (Camb).* **5,** 372–80 (2013).

155. Chung, K. & Lu, H. Automated high-throughput cell microsurgery on-chip. *Lab Chip* **9,** 2764–2766 (2009).

156. Husson, S. J. Keeping track of worm trackers. *WormBook* 1–17 (2012). doi:10.1895/wormbook.1.156.1

157. Bao, Z. *et al.* Automated cell lineage tracing in Caenorhabditis elegans. *Proc. Natl. Acad. Sci. U. S. A.* **103,** 2707–12 (2006).

158. Branson, K., Robie, A. A., Bender, J., Perona, P. & Dickinson, M. H. High-throughput ethomics in large groups of Drosophila. *Nat. Methods* **6,** 451–457 (2009).

159. Dankert, H., Wang, L., Hoopfer, E. D., Anderson, D. J. & Perona, P. Automated monitoring and analysis of social behavior in Drosophila. *Nat. Methods* **6,** 297–303 (2009).

160. Clarke, L. P. *et al.* MRI segmentation: methods and applications. *Magn. Reson. Imaging* **13,** 343–68 (1995).

161. C. elegans Sequencing Consortium. Genome sequence of the nematode C. elegans: a platform for investigating biology. *Science* **282,** 2012–8 (1998).

162. Hillier, L. W. *et al.* Genomics in C. elegans: so many genes, such a little worm. *Genome Res.* **15,** 1651–60 (2005).

163. Mak, H. Y. Lipid droplets as fat storage organelles in Caenorhabditis elegans: Thematic Review Series: Lipid Droplet Synthesis and Metabolism: from Yeast to Man. *J. Lipid Res.* **53,** 28–33 (2012).

164. Klemm, R. W. *et al.* A conserved role for atlastin GTPases in regulating lipid droplet size. *Cell Rep.* **3,** 1465–75 (2013).

165. Karunatillake, S. *et al.* A martian case study of segmenting images automatically for granulometry and sedimentology, Part 1: Algorithm. *Icarus* **229,** 400–407 (2014).

166. Karunatillake, S. *et al.* A martian case study of segmenting images automatically for granulometry and sedimentology, Part 2: Assessment. *Icarus* **229,** 408–417 (2014).

167. Lira, C. & Pina, P. Granulometry on classified images of sand grains. *J. Coast. Res. J. Coast. Res. SI* **64,** (2011).

168. Bruchon, J.-F. *et al.* Full 3D investigation and characterisation of capillary collapse of a loose unsaturated sand using X-ray CT. *Granul. Matter* **15,** 783–800 (2013).

169. Kim, H. Y., Maruta, R. H., Huanca, D. R. & Salcedo, W. J. Correlation-based multi-shape granulometry with application in porous silicon nanomaterial characterization. *J. Porous Mater.* **20,** 375–385 (2013).

170. Urbanski, J., Wochna, A. & Herman, A. Automated granulometric analysis and grain-shape estimation of beach sediments using object-based image analysis. *J. Coast. Res. J. Coast. Res. SI* **64,** (2011).

171. Lotufo, R. A., Rittner, L., Audigier, R., Machado, R. C. & Saúde, A. V. in 107–129 (Springer Berlin Heidelberg, 2010). doi:10.1007/978-3-642-15816-2_4

172. Yusai You & Huimin Yu. A separating algorithm based on granulometry for overlapping circular cell images. in *2004 International Conference on Intelligent*

Mechatronics and Automation, 2004. Proceedings. 244–248 (IEEE). doi:10.1109/ICIMA.2004.1384197

173. Vaccari, A. *et al.* Assessment of Wallerian degeneration by automated image analysis. in *2012 Conference Record of the Forty Sixth Asilomar Conference on Signals, Systems and Computers (ASILOMAR)* 1583–1587 (IEEE, 2012). doi:10.1109/ACSSC.2012.6489296

174. Habibzadeh, M., Krzyzak, A., Fevens, T. & Sadr, A. Counting of RBCs and WBCs in noisy normal blood smear microscopic images. in (eds. Summers, R. M. & van Ginneken, B.) 79633I (2011). doi:10.1117/12.878748

175. Jorgensen, E. M. & Mango, S. E. THE ART AND DESIGN OF GENETIC SCREENS: CAENORHABDITIS ELEGANS. *Nat. Rev. Genet.* **3,** 356–369 (2002).

176. Xia, Y. & Whitesides, G. M. SOFT LITHOGRAPHY. *Annu. Rev. Mater. Sci.* **28,** 153–184 (1998).

177. Cáceres, I. de C., Valmas, N., Hilliard, M. A. & Lu, H. Laterally Orienting C. elegans Using Geometry at Microscale for High-Throughput Visual Screens in Neurodegeneration and Neuronal Development Studies. *PLoS One* **7,** e35037 (2012).

178. Mak, H. Y. Personal Communication. (2016).

179. Lemieux, G. A. & Ashrafi, K. Insights and challenges in using *C. elegans* for investigation of fat metabolism. *Crit. Rev. Biochem. Mol. Biol.* **50,** 69–84 (2015).

180. Watson, E. *et al.* Interspecies Systems Biology Uncovers Metabolites Affecting C. elegans Gene Expression and Life History Traits. *Cell* **156,** 759–770 (2014).

181. Elle, I. C., Rødkær, S. V., Fredens, J. & Færgeman, N. J. A method for measuring fatty acid oxidation in C. elegans. *Worm* **1,** 26–30 (2012).

182. Watson, E. *et al.* Metabolic network rewiring of propionate flux compensates vitamin B12 deficiency in *C. elegans*. *Elife* **5,** (2016).

183. Zhang, S. O. *et al.* Genetic and dietary regulation of lipid droplet expansion in

Caenorhabditis elegans. *Proc. Natl. Acad. Sci. U. S. A.* **107,** 4640–5 (2010).

184. Khanna, A. *et al.* A genome-wide screen of bacterial mutants that enhance dauer formation in C. elegans. *Sci. Rep.* **6,** 38764 (2016).

185. Luo, H. *et al.* Production of 3-Hydroxypropionic Acid via the Propionyl-CoA Pathway Using Recombinant Escherichia coli Strains. *PLoS One* **11,** e0156286 (2016).

186. Stabler, S. P. & Allen, R. H. VITAMIN B12 DEFICIENCY AS A WORLDWIDE PROBLEM. *Annu. Rev. Nutr.* **24,** 299–326 (2004).

187. Deodato, F., Boenzi, S., Santorelli, F. M. & Dionisi-Vici, C. Methylmalonic and propionic aciduria. *Am. J. Med. Genet. Part C Semin. Med. Genet.* **142C,** 104–112 (2006).

188. Rosenblatt, D. S. *et al.* Altered vitamin B12 metabolism in fibroblasts from a patient with megaloblastic anemia and homocystinuria due to a new defect in methionine biosynthesis. *J. Clin. Invest.* **74,** 2149–2156 (1984).

189. Beylot, M. Effects of inulin-type fructans on lipid metabolism in man and in animal models. *Br. J. Nutr.* **93,** S163 (2005).

190. Porto, D. A., Rouse, T. M., San-Miguel, A. & Lu, H. in *Microfluidic Methods for Molecular Biology* 1–18 (Springer International Publishing, 2016). doi:10.1007/978-3-319-30019-1_1

191. Crane, M. M., Chung, K., Stirman, J. & Lu, H. Microfluidics-enabled phenotyping, imaging, and screening of multicellular organisms. *Lab Chip* **10,** 1509 (2010).

192. Crane, M. M. *et al.* Autonomous screening of C. elegans identifies genes implicated in synaptogenesis. *Nat. Methods* **9,** 977–980 (2012).

193. Foe, V. E. & Alberts, B. M. Studies of nuclear and cytoplasmic behaviour during the five mitotic cycles that precede gastrulation in Drosophila embryogenesis. *J. Cell Sci.* **61,** 31–70 (1983).

194. Ungrin, M. D., Joshi, C., Nica, A., Bauwens, C. & Zandstra, P. W. Reproducible,

Ultra High-Throughput Formation of Multicellular Organization from Single Cell Suspension-Derived Human Embryonic Stem Cell Aggregates. *PLoS One* **3,** e1565 (2008).

195. Aubry, G., Zhan, M. & Lu, H. From chip-in-a-lab to lab-on-a-chip: towards a single handheld electronic system for multiple application-specific lab-on-a-chip (ASLOC). **15,** (2014).

196. Levario, T. J., Zhao, C., Rouse, T., Shvartsman, S. Y. & Lu, H. An integrated platform for large-scale data collection and precise perturbation of live Drosophila embryos. *Sci. Rep.* **6,** 21366 (2016).

197. Kurusu, M. *et al.* Embryonic and larval development of the Drosophila mushroom bodies: concentric layer subdivisions and the role of fasciclin II. *Development* **129,** 409–19 (2002).

198. Callaini, G. & Marchini, D. Abnormal centrosomes in cold-treated Drosophila embryos. *Exp. Cell Res.* **184,** 367–74 (1989).

199. Chung, K., Rivet, C. A., Kemp, M. L. & Lu, H. Imaging Single-Cell Signaling Dynamics with a Deterministic High-Density Single-Cell Trap Array. *Anal. Chem.* **83,** 7044–7052 (2011).

200. Al-Lahham, S. H., Peppelenbosch, M. P., Roelofsen, H., Vonk, R. J. & Venema, K. Biological effects of propionic acid in humans; metabolism, potential applications and underlying mechanisms. *Biochim. Biophys. Acta - Mol. Cell Biol. Lipids* **1801,** 1175–1183 (2010).

201. Dougherty, E. R., Lotufo, R. A. & Society of Photo-optical Instrumentation Engineers. *Hands-on morphological image processing*. (SPIE, 2003).

202. Serra, J. Image Analysis and mathematical morphology. *London Acad. Press* (1982).

203. Fay, D. S. Classical genetic methods. *WormBook* 1–58 (2013). doi:10.1895/wormbook.1.165.1

204. Datsenko, K. A. & Wanner, B. L. One-step inactivation of chromosomal genes in Escherichia coli K-12 using PCR products. *Proc. Natl. Acad. Sci. U. S. A.* **97,** 6640–

5 (2000).

VITA

MARIA ELENA CASAS

Maria Elena was born in Miami, Florida in 1987 to Cuban immigrant parents. She attended the public school, Southwest Miami Sr. High School, where she graduated with the honor of Valedictorian. In 2010, she received her Bachelors of Science in Biomedical Engineering as *magna cum laude* from the University of Miami in Coral Gables, Florida. She then decided to pursue a graduate degree at the Georgia Institute of Technology and during her time there she earned several fellowships including the National Science Foundation Graduate Research Fellowship, and the Ford Foundation Pre-Doctoral Fellowship in 2012. She is the first person in her family to earn a doctorate.

When not working on research, Maria Elena was involved in the GT Salsa club where she taught *Casino* style salsa dancing, and competed with the chapters' dance team. She is also certified from the national guild of piano teachers. In addition to dancing and playing the piano, she enjoys rooting for the Miami Hurricanes and Georgia Tech Yellow Jackets, and sometimes the Florida Gators, as well. While at Georgia Tech, she also obtained her SCUBA certification being trained in the 1996 Olympics pool on campus. Along with her boyfriend, she loves playing with their affectionate yellow Labrador, Bentley, that is full of energy and a great companion. She especially enjoys traveling around the world with her boyfriend, tasting different cuisines and experiencing new cultures. She has now visited 4 continents and is looking forward to visiting them all.